SELENIUM CORONANDS AND THEIR METAL ION COMPLEXES

by

Xue Min Zhou

B.Sc., Shanghai Teachers' University, Shanghai, China, 1982

M. Sc., Shanghai Institute of Organic Chemistry

Academia Sinica, Shanghai, China, 1984

A THESIS SUBMITTED IN PARTIAL FULFILLMENT OF

THE REQUIREMENTS FOR THE DEGREE OF

DOCTOR OF PHILOSOPHY

in the Department

of

Chemistry

© Xue Min Zhou, 1993

SIMON FRASER UNIVERSITY

December 1993

APPROVAL

Name: Xue Min Zhou

Degree: Ph.D.

Title of Thesis: Selenium Coronands and their Metal Complexes

Examining Committee:

Chair: Dr. Sutton

Dr. I Gay (Professor)
Senior Supervisor

Dr. B.M. Pinto (Professor)
Committee Member

Dr. S. Holdcroft (Assistant Professor)
Committee Member

Internal Examiner: Dr. R.H. Hill (Assistant Professor)

External Examiner: Dr. M.D. Fryzuk (Professor)

Date Approved: _Dec 13, 1993_

PARTIAL COPYRIGHT LICENSE

I hereby grant to Simon Fraser University the right to lend my thesis, project or extended essay (the title of which is shown below) to users of the Simon Fraser University Library, and to make partial or single copies only for such users or in response to a request from the library of any other university, or other educational institution, on its own behalf or for one of its users. I further agree that permission for multiple copying of this work for scholarly purposes may be granted by me or the Dean of Graduate Studies. It is understood that copying or publication of this work for financial gain shall not be allowed without my written permission.

Title of Thesis/Project/Extended Essay:

Selenium Coronands and Their

Metal Ion Complexes

Author:

_____
(signature)

ZHOU, XUE MIN
(name)
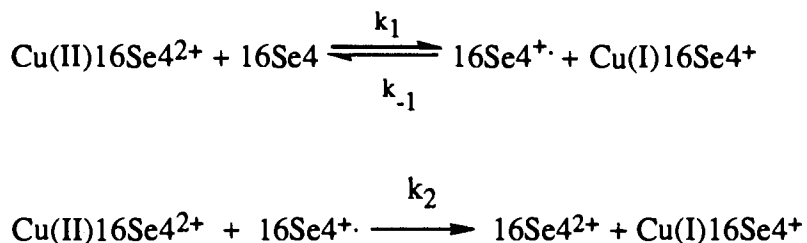
Dec. 8, 1993
(date)

ABSTRACT

The chemistry of selenium coronands and their metal ion complexes has been investigated.

New selenium coronands, namely, 3-hydroxyl-1,5-diselenacyclooctane (8Se2OH), cis-3,11-dihydroxyl-1,5,9,13-tetraselenacyclohexadecane (16Se4(OH)$_2$), 6,7,13,14-dibenzo-1,5,8,12-tetraselenacyclotetradecane (dibenzo-14Se4) and the mixed sulfur/selenium coronand, 1,5-diselena-9,13-dithiacyclohexadecane (16S2Se2) have been synthesized by a one-step or step-wise strategy. The compounds have been fully characterized by micro-analysis and spectroscopic methods (MS, IR, and ^{1}H and ^{13}C NMR). In addition, x-ray crystallography of the latter two selenium coronands indicates a gauche conformational preference about the C-Se bonds. The selenium coronands and two selenium coronand dications have been characterized by solid-state CP-MAS ^{13}C and ^{77}Se NMR spectroscopy.

The coordination and redox chemistry of selenium coronand metal complexes has been studied. Pd(II) and Cu(II) complexes of several selenium coronands have been synthesized and their x-ray structures been determined. The Pd(II) complexes have square planar configurations; the Cu(II) complexes have tetragonally distorted octahedral configurations. The structures of these complexes in solutions have been studied by UV-visible spectroscopy, and where applicable, ESR or NMR spectroscopic methods.

The Cu(II) complexes of 1,5,9,13-tetraselenacyclohexadecane (16Se4), cis-3,11-dihydroxyl-1,5,9,13-tetraselenacyclohexadecane (16Se4OH) and 1,5-diselena-9,13-dithiacyclohexadecane (16S2Se2) have been found to be unstable in certain organic solvents. The corresponding Cu(I) complexes from a spontaneous reduction reaction have been isolated and characterized by x-ray crystallography, the latter compounds have a tetrahedral configuration about the Cu atom. The presence of hydroxyl group substituents

in the coronands appears to increase the stability of the Cu(II) selenium coronand complex. The detailed kinetics and the mechanism of the spontaneous redox reaction of the Cu(II) complex of 1,5,9,13-tetraselenacyclohexadecane (16Se4) has been probed by uv-visible spectroscopy, electrochemistry and spectroelectrochemistry. The following mechanism has been proposed:

$$Cu(II)16Se4^{2+} + 16Se4 \underset{k_{-1}}{\overset{k_1}{\rightleftharpoons}} 16Se4^{+\cdot} + Cu(I)16Se4^+$$

$$Cu(II)16Se4^{2+} + 16Se4^{+\cdot} \overset{k_2}{\longrightarrow} 16Se4^{2+} + Cu(I)16Se4^+$$

Cyclic voltammetry of the Pd(II) and Cu(II) complexes has been carried out and the redox potentials or peak potentials have been determined.

Finally, the redox properties of the selenium coronands themselves have been investigated. Cyclic voltammetry, coulometry and spectroelectrochemistry have been used to characterize the radical cations and dications of various selenium coronands. The redox potentials of selenium coronands and the uv-visible absorption maxima (λ_{max}) of the corresponding radical cations have been measured. The λmax values are related to the strength of the two-center, three-electron bonds formed by dimerizations or by transannular interactions. Transannular interactions facilitate the oxidation of the selenium coronands on the electrode. Cyclic voltammetry, convolutional analysis, electrolysis, and spectroelectro-chemical methods have been used to investigate the fate of the radical cation (1,5,9,13-tetraselenacyclohexadecane$^{+\cdot}$, 16Se4$^{+\cdot}$) in solution. The results indicate that the radical cation forms a dimer with a parent molecule.

DEDICATION

To Ke Ma and Lulu.

ACKNOWLEDGMENTS

LIST OF ABBREVIATIONS

A	Electrode area
Å	Angstrom
C	Concentration
COSY	Chemical-shift correlated NMR spectroscopy
CP-MAS	Cross polarization and magic angle spinning
DMF	Dimethyl formamide
$\Delta S^{\ddagger}$	Standard entropy of activation
E	Potential
$E_{1/2}$	Half wave potential
ΔE_p	$|E_{pa}-E_{pc}|$ in cyclic voltammetry
$E^{o'}$	Formal potential of redox couple
E_{pa} & E_{pc}	Anodic and cathodic peak potential
$E_{p/2}$	Potential where $i = i_p/2$
ESR	Electron spin resonance spectroscopy
F	Faraday
ΔG	Gibbs free energy change in a chemical process
$\Delta G^{\ddagger}$	Standard Gibbs free energy of activation
h	Planck's constant
ΔH	Enthalpy change in a chemical process
$\Delta H^{\ddagger}$	Standard enthalpy of activation
i	Current
I(t)	Convolutive transform of current or semi-integral of current
i_{pa} & i_{pc}	Anodic and cathodic peak current
IR	Infrared spectroscopy
K	Equilibrium constant

k	Rate constant
k^o	Standard heterogeneous electron transfer rate constant
k_f	Heterogeneous rate constant for reduction ; homogeneous rate constant for "forward reaction"
k_{obs}	Observed rate constant
M	Concentration in molar
n	Number of electron involved in a redox reaction
NMR	Nuclear magnetic resonance
R	Gas constant
SCE	Saturated calomel electrode
ΔS	Entropy change in a chemical process
T	Temperature
t	Time
TEAP	Tetraethylammonium perchlorate
THF	Tetrahydrofuran
UV	Ultraviolet-visible spectroscopy
χ	Electronegativity or absolute electronegativity
δ	Chemical shift
ε	Extinction coefficient
η	Absolute hardness
λ_{max}	Absorption maximum wavelength
ν	Linear potential scan rate

TABLE OF CONTENTS

XI

LIST OF TABLES

LIST OF FIGURES

CHAPTER I
INTRODUCTION

1.1. Chalcogen Macrocycles

Chalcogen macrocycles have attracted tremendous interest recently[1-3]. There are two main areas of interest: 1) biochemical interests; 2) academic interests that may lead to industrial applications. The biochemical interest arose from the observation of thioether binding in biological systems such as d-biotin (involving tetrahydrothiophene)[4,5] and blue copper proteins such as plastocyanin and azurin (involving methionine)[6,7]. The relationship between structure and reactivity is of central interest. It is believed that the unusual optical and redox properties of blue copper proteins are the result of a distorted tetrahedral geometry in the active copper(II) center[8]. Vallee[9] and Williams[10] proposed that the high reactivity of all enzymes was due to the geometric constraints imposed on the reactive center by the surrounding protein matrix. However, proteins and enzymes are macromolecules that are relatively difficult to use to test the theory because for such a test one needs to have control of the active site structure. Hence, synthetic macrocycles are possible models for studying and understanding the chemical and biochemical processes in metalloenzymes or metalloproteins.

Macrocyclic ligand systems tend to provide a well-defined environment for the metal ion. The properties of the metal ions may be influenced by geometric deformation of the coordinating ligands. For example, when the geometry of a macrocyclic cavity is close to that preferred by the reduced ionic species a high standard potential results whereas a cavity geometry close to that of the oxidized state results in a lower standard potential[11]. Rorabacher and co-workers[3,7,12-15] have performed a thorough investigation of the relationship between redox reactivity and the structure of Cu and macrocyclic thioethers in an attempt to comprehend how the geometric environment of the coordination sphere would

affect the reactivity of the metal ions. Others applied the macrocyclic ligand approach to comprehend the unusual spectroscopic and electrochemical properties observed. For example, Addison has studied the effects of geometric arrangements of macrocyclic ligands and the different kinds of donor atoms on the spectroscopic properties (uv and ESR) of a number Cu(II) complexes of thia and/or aza, oxa macrocycles[16,17].

In addition to the biochemical interest, academic interest stems from the possible similarity between phosphines and thioethers in the formation of coordination bonds with transition metal ions. The finding that cyclic thioethers can bind to a range of transition metal ions[18,19] has promoted the development of the coordination chemistry of thioether ligands. Chalcogen macrocycles are expected to preferentially bind to transition metal ions, considering the "softness" of the chalcogen elements. The possible parallel between chalcogen and phosphines might bring up extensive and industrially useful coordination chemistry. As mentioned before, the synthetic macrocycles may provide means to control the stability, selectivity and reactivity of macrocyclic metal-ion complexes through ligation or dilation of the inner sphere of the complexes. Cooper and co-workers have significantly advanced in the synthesis, conformational analysis and coordination chemistry of macrocyclic polythia-ethers[2,20]. The relative stabilization of metal complexes has been linked to the degree of necessary conformational change from that of the uncomplexed ligand. Schröder and co-workers have made further progress in this area[1,21-29]. A tremendous amount work has been done in the chemistry of thia macrocycles and their transition metal ions complexes[2,3,14,19,30-39], in particular, the investigation of spectral, electrochemical, structural, kinetic and thermodynamic aspects of macrocyclic complex formation.

However, surprisingly, there is very little work on the selena macrocycles. To the best of our knowledge, prior to our work, the only large-ring selenides reported to date are cyclic oligomers of selenaformaldehyde (1)[40], diselenacyclophanes (2), 2,11-diselena[3.3](2,6)pyridinophane (3)[41-45], macrocyclic diselena ethers (4)[46], selenium

porphyrin derivatives (5)[47,48], tetraselena-3,4-benzocyclooctodecane (6)[49] and mixed selena oxa macrocyclic ethers (7)[49-52]. Among these publications only Hojjatie[41], Akabori[49] and Xu[52] reported the coordination chemistry of their selena macrocycles with transition metal ions. Therefore, the chemistry of selenium coronands and their metal ion complexes is really in its infancy.
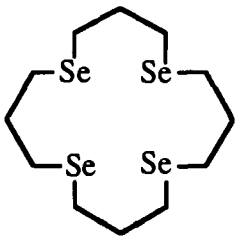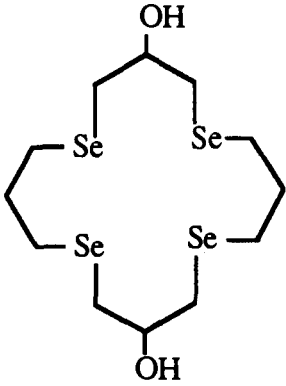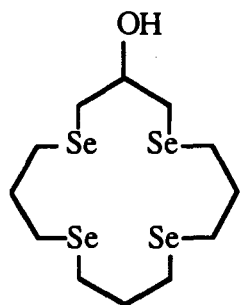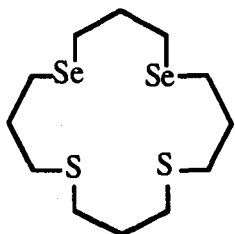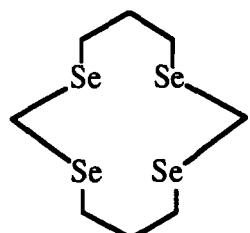
1.2. Definition and Nomenclature

During the development of the chemistry of macrocycles and their metal ions, new terminology and nomenclature have been introduced by their developers[53,54]. The terminology and nomenclature usually are abbreviations rather than the lengthy and cumbersome systematic naming. In order to avoid confusion, we would like to discuss some definitions of terms and nomenclature that are generally accepted by the chemistry community.
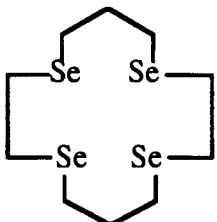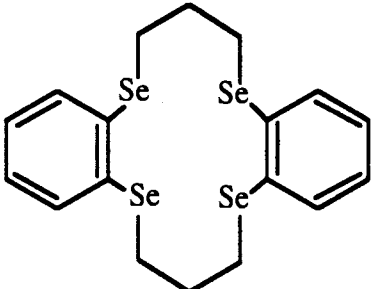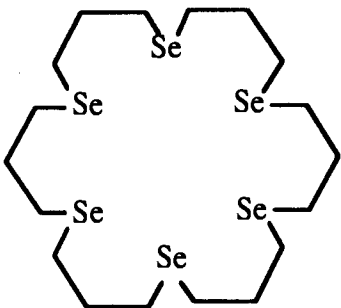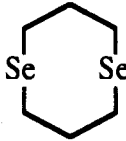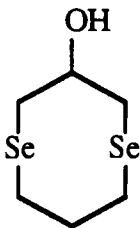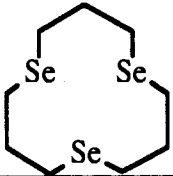
Coronands are multidentate monocyclic ligands with any type of donor atoms; the crown ethers refer to the cyclic oligomer-ethers containing exclusively oxygen as the donor atoms. The complexed coronands are called coronates[55]. Macrocycles are cyclic compounds with nine or more members (including all heteroatoms) and with three or more donor atoms[56,57]. According to this definition[56,57], the above mentioned macrocyclic diselena ethers and most of the selenacyclophanes may not be called macrocycles because they only involve two selenium atoms in a cyclic system.

The selenium coronands prepared in our group are named non-systematically by an extension of the crown nomenclature introduced by Pedersen[53]. Thus 1,5,9,13-tetraselenacyclohexadecane is called tetraselena-16-crown-4. This name is further abbreviated to 16Se4, in which the number 16 denotes the ring size and the number 4 denotes the selenium atoms. This nomenclature will be used elsewhere in the thesis. The relevant macrocyclic thioethers are also named by this convention[2]. Table 1.2.1 shows the structures of selenium coronands synthesized in our group and their names.

Table 1.2.1. Abbreviated Nomenclature for Selenium Coronands

No.	Selenium Coronands	Abbreviated Name	IUPAC Nomenclature
8		16Se4	1,5,9,13,tetraselena-cyclohexadecane
9		16Se4(OH)$_2$	3,11-dihydroxy-1,5,9,13-tetraselenacyclohexadecane
10		16Se4OH	3-hydroxy-1,5,9,13-tetra-selenacyclohexadecane
11		16S2Se2·	1,5-diselena-9,13-dithiacyclohexadecane
12		12Se4	1,3,7,9-tetraselenacyclo-dodecane

4

No.	Selenium Coronands	Abbreviated Name	IUPAC Nomenclature
13		14Se4	1,4,8,11-tetra-selenacyclotetradecane
14		dibenzo-14Se4	6,7,13,14-dibenzo-1,5,8,12-tetraselenacyclo-tetradecane
15		24Se6	1,5,9,13,17,21-tetraselenacyclotetracosane
16		8Se2	1,5-diselenacyclooctane
17		8Se2OH	3-hydroxy-1,5-diselena-cyclooctane
18		12Se3	1,5,9-triselenacyclo-dodecane

1.3. Our Research Interests in Selenium Coronands

Since donor atoms in a macrocycle directly bond to metal ions, the donor atoms have more influence on the stability and reactivity of the complexed transition metal ions. Thus, in addition to altering the sizes of macrocycles, altering the donor atoms also enables one to influence the properties and reactivity of the transition metal ions. In this regard, selenium coronands are attractive because of the large covalent radius and greater polarizability of selenium compared to oxygen and nitrogen. Would selenium coronands form complexes with transition metal ions? The answer is they likely would. In the literature, simple selenoether-transition metal complexes have been reported[58,59]. Table 1.3.1 lists the metal ions that have been reported to form complexes with selenoethers.

Table 1.3.1. **Metal Ions Reported to Form Complexes with Seleno Ethers**[58-64]

IVB	VB	VIB	VIIB		VIII		IB	IIB
Ti	V	Cr	Mn	Fe	Co	Ni	Cu	Zn
		Mo		Ru	Rh	Pd	Ag	
		W	Re	Os	Ir	Pt	Au	Hg

The presumption that selenium coronands would form complexes with transition metal can be rationalized by the concept of hard and soft acids and bases. Hard and soft acids and bases were originally defined as[65] :

soft base -- the donor atom is of high polarizability, low electronegativity, easily oxidized and associated with empty, low-lying orbitals.

hard base -- the donor atom is of low polarizability, high electronegativity, hard to reduce, and associated with empty orbitals of high energy and hence inaccessible.

6

soft acid -- the acceptor atom is of low positive charge, large size and has several easily excited outer electrons. Polarizable.

hard acids -- the acceptor atom is of high positive charge, small size and does not have easily excited outer electrons. Not polarizable.

For a general acid-base reaction

$$A + :B \rightleftharpoons A:B$$

there is an HSAB Principle[65] --- hard acids prefer to coordinate to hard bases and soft acids to soft bases --- to predict or understand the outcome of the reaction. The selenium atom has a large radius (r_{cov} = 1.12 Å)[66] , large polarizability and low electronegativity (χ_{Se} = 2.4, cf. χ_S = 2.5, χ_O = 3.5)[67]; therefore, it belongs to the soft base category. Selenium coronands should present a preference for coordination to transition metal ions, particularly with the low oxidation state transition metal ions.

Recent development of the concept of hard and soft acids and bases pioneered by Parr[68,69] allows us to compare the hardness of a base or acid in a quantitative manner. Parr and Pearson introduced a new concept, i.e., the absolute hardness (η_s) along with the absolute electronegativity (χ)[70]

$$\chi = -\left|\frac{\partial E}{\partial N}\right|_z = -\mu$$

$$\eta_S = 1 / 2 \left|\frac{\partial^2 E}{\partial N^2}\right|_z$$

where χ is the absolute electronegativity; μ is the electronic chemical potential; η_s is the absolute hardness; E is the electronic energy of a molecule, atom or ion; N is the number of electrons and Z is a fixed set of nuclear charges. The operational definitions[70] are

$$\chi = 1/2 (I_s + A_s)$$

$$\eta_s = 1/2 (I_s - A_s)$$

7

where I_s is the ionization potential of a species S and A_s is the electron affinity of a species S. Hard acids or bases have large η_s values, whereas soft acids and bases have small η_s. For example, atoms O, S and Se have the η_s values[70] of 6.08, 4.12 and 3.86 eV, respectively. Here, we can see that the S atom and Se atom have the comparable hardness or softness. In another example, the η_s values[70] for Cu^{2+}, Cu^+ and Pd^{2+} are 8.5, and 6.3 and 6.8 eV, respectively, which is consistent with that Cu^{2+} is a borderline acid whereas Cu^+ and Pd^{2+} are soft acids in comparison to Na^+ ($\eta = 21.1$)[71].

According to MO theory the first ionization potential of a molecule is simply the orbital energy of the HOMO, and the electron affinity is the orbital energy of the LUMO, with changes in sign[71]

$$I = -E_{HOMO}$$

$$A = -E_{LUMO}$$

Therefore, $-\chi$ is the average of the HOMO and LUMO energies and 2η is the gap between the HOMO and LUMO (Figure 1.3.1). A hard molecule or ion has a large gap between the HOMO and LUMO, and a soft molecule, or ion has a small gap.
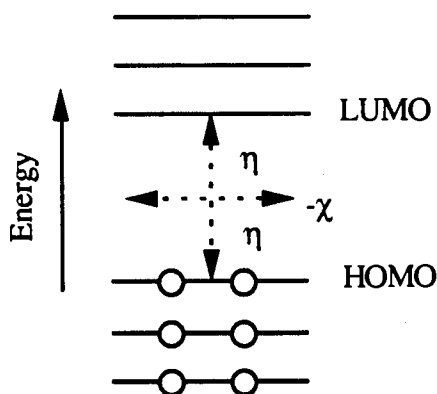
Figure 1.3.1. An orbital energy diagram showing χ and η for filled-shell molecule.

Thus, based on the HSAB principle we expect that selenium coronands should at least show a similar complexation ability with these transition metal ions (Cu(II), Cu(I) and Pd(II)) to their sulfur counterparts.

The introduction of selenium atoms into macrocycles adds an additional probe for structural characterization and dynamic processes of the complexes in solutions. Selenium-77 has a spin 1/2, a natural abundance 7.58% and a receptivity 2.98[59,72-74] with respect to carbon-13. Abel and co-workers[13] have investigated the pyramidal inversion at the selenium centers in Pt(II) complexes cis-[PtXMeSe(CH$_2$)$_2$SeMe](X = Cl, Br, I)$_2$ (see Figure 1.3.2) with NMR (^{1}H, ^{13}C, [77]Se, [195]Pt) studies and determined inversion barriers.
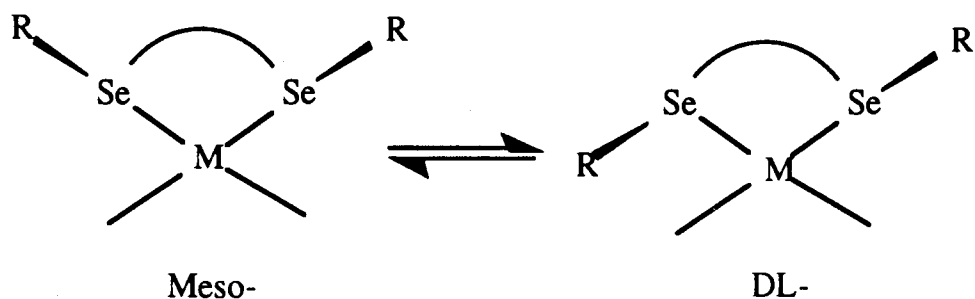
Figure 1.3.2. Meso and DL invertomers of a metal complex of a chelating diselenoether.

Lack of a proper synthetic route to prepare the selenium coronands might be one of the reasons for the little work on the chemistry of selenium coronands and their metal ion complexes in the past. However, Pinto and co-workers[75] have recently developed a synthetic route for selenium coronands (Scheme 1.1), in which Na/liquid NH$_3$ reduction of an α,ω-alkanebis(selenocyanate) to the bis(selenolate) followed by addition of dihaloalkanes gave mixtures of selenium coronands that were separated by chromatography.

Scheme 1.1

19a	R=H	**12a**	R=H, 13%	**20a**	R=H, 10%
19b	R=Me	**12b**	R=Me, 8%	**20b**	R=Me, 4%

8 40%   **15** 15%   **16** 17%

13 34%
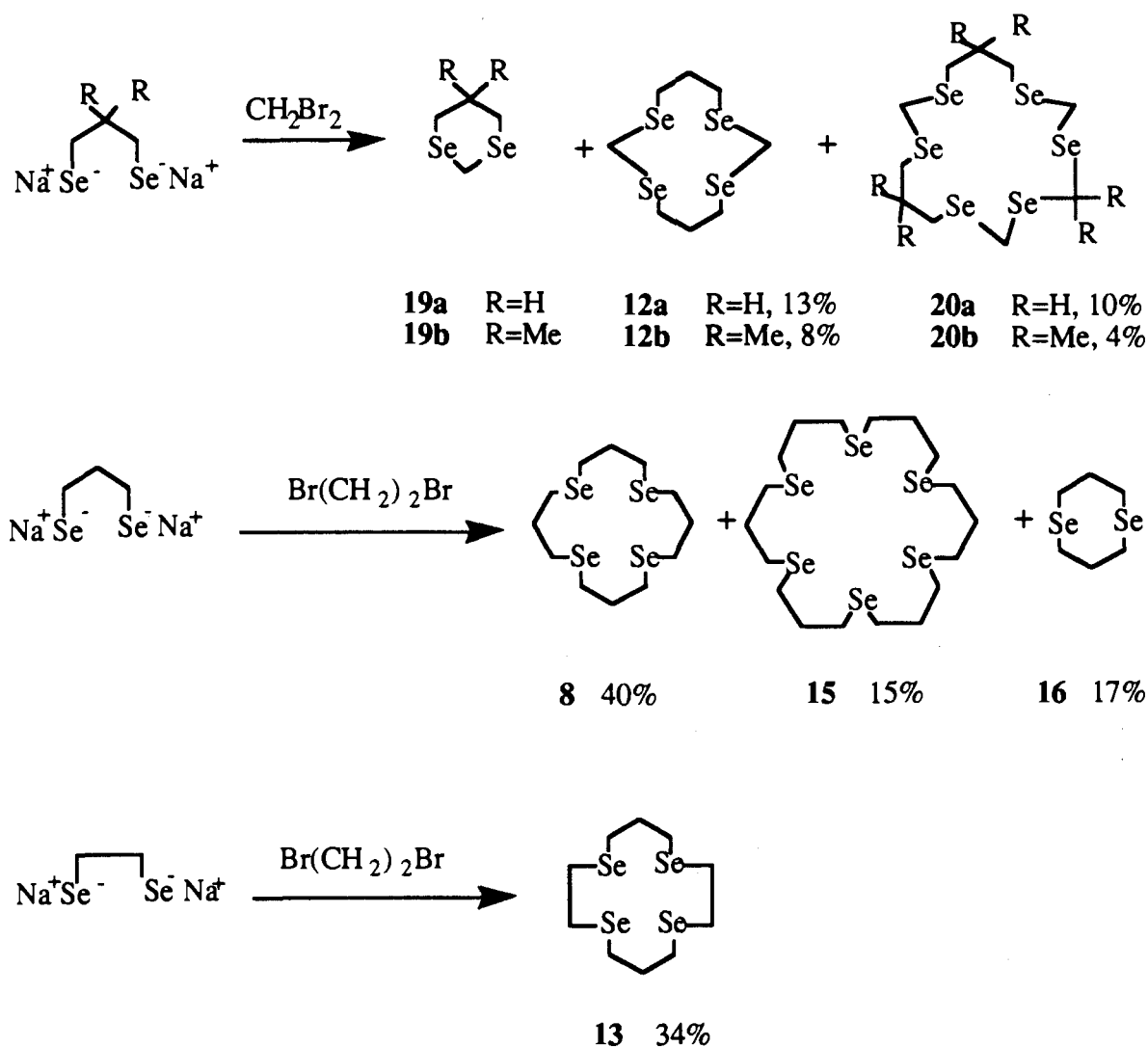
Conformational analyses of the solid state structure of these selenium coronands by x-ray crystallography[75] reveal that selenium coronands normally adopt exodentate conformations, that is, the selenium atoms usually tend to take a position in which they are pointing away from the macrocyclic ring. The placements are similar to those of thia macrocycles[76,77], but are different from those of crown ethers. It was also found that in coronands 12Se4 (**12**), 14Se4 (**13**) and 16Se4 (**8**) the selenium atoms occupy as many corner positions as possible. In such arrangements, C-Se-C-C sequences have the maximum number of *gauche* conformations about the Se-C bonds. The ramification is that

10

the ligands must reorganize to turn the selenium atoms inward to coordinate with a metal ion.

Thus, the coordination of metal ions will be a compromise between the bond strength of Se-M and the strain induced by the reorganization of the macrocyclic rings. Because selenium is a relatively weak σ-donor in comparison with P, N, and S, the macrocyclic effects might be diminished by this structural reorganization. The interplay of the exodentate preference in selenium coronands and the electronic requirements of the transition metal ions will likely render a rich coordination chemistry[59,72,78].

In preliminary experiments, Pinto et at[60], found an interesting redox reaction of a Cu(II) complex of 16Se4. During recrystallization of [Cu(16Se4)][SO_3CF_3]$_2$ (21), it was discovered that the copper (II) complex was spontaneously reduced to a copper(I) complex in THF and CH_3NO_2 solution. In CH_3CN solution this reduction was even faster, and 16Se4 dication crystallized from the solution[60]. Both reaction products were isolated and fully characterized. This redox reaction is probably a result of selenium's inherent redox property. In biological systems, the human body for example, selenium is a component of several enzymes involved in essential oxidation-reduction reactions[79]. One enzyme, glutathione peroxidase (GSH) appears to play a major role in the protection of red blood cells against the effects of hydrogen peroxide which is readily generated inside the cell.

Hence, we would like to know how the redox reaction occurs. What structural effects of the selenium coronands would affect this reaction and what is the probable reaction mechanism? To answer these questions further investigations are needed.

According to the findings in the redox chemistry of the Cu(II) thia complexes, the inner coordination sphere plays an important role in the determination of the stability and reactivity of the Cu(II) thia macrocycle complexes[35,80,81]. Also, the binding selectivity to the metal ions appears to increase for macrocycles with proper substituents[34,82-85]. Therefore, functionalized selenium coronands are the next logical candidates to answer the question of how ligand structure affects the properties of complexes. Furthermore, they

will also provide a way to explore the scope and limits of the synthetic route to the selenium coronands designed by Pinto et al[75] . New synthetic routes may be needed to obtain the selenium coronands with the required substituents. The newly synthesized selenium coronands together with other coronands can be used to prepare complexes of metal ions to study the coordination chemistry.

The redox chemistry of [Cu(16Se4)][SO$_3$CF$_3$]$_2$ (**21**) reveals that the selenium coronands are likely to be susceptible to oxidation. When a selenium coronand loses an electron it becomes a radical cation which can, in turn, be further oxidized to a dication. The radical cations are presumably stabilized by a two-center three-electron selenium-selenium bond that results from transannular interactions or intermolecular Se-Se interaction, as in the case of the sulfur congeners[86,87]. Preliminary results indicated that the radical cation of 16Se4 was stable enough in solutions to be detected by uv-visible spectroscopy under static conditions. The absorption is from the transitions between the bonding and anti-bonding orbitals of the two-center three-electron bonds[88]. Formation of two-center three-electron bonds in radical cations is documented in aliphatic thioethers[7,8,9,10]. However, compared to thioether radical cations there are very few examples of selenoether radical cations reported in the literature[89-93]. With the selenium coronands listed in Table 1.2.1 we can investigate the radical cations by uv-visible spectroscopy. From the uv-visible spectroscopic data, information about the bond strengths of these Se-Se bonds can be obtained from the absorption maxima. The radical cations can be generated by chemical and electrochemical methods. Electrochemistry techniques such as cyclic voltammetry and spectroelectrochemistry will be used to study the redox properties of the metal ion complexes of selenium coronands as well as of the ligands. The focus will be on the relationship between structure and redox properties such as the redox potential $E_{1/2}$ and the reversibility of the electrode reaction.

Finally, in order to propose a mechanism for the spontaneous electron transfer reaction of [Cu(16Se4)][SO$_3$CF$_3$]$_2$, kinetic studies are needed to determine the order of the

reaction with respect to the reactants and the stoichiometry of the reaction, and to identify reaction intermediates. The latter can be accomplished through the study of the redox properties of the selenium coronands.

Combining the above thoughts the research project was designed as follows:

1)   Continuation of the development of selenium coronands synthesis with focus on the coronands with functional groups.

2)   Characterization of the selenium coronands by solid-state CP-MAS NMR spectroscopy and x-ray crystallography.

3)   Preparation and characterization of the metal ion complexes of selenium coronands.

4)   Investigation of the redox properties of the selenium coronands and their metal complexes by various electrochemical methods such as cyclic voltammetry, electrolysis and spectroelectrochemistry.

5)   Study of the kinetics of the redox reaction of **21**.

1.4. Thesis Overview

In Chapter II of this thesis the synthesis of new and functionalized selenium coronands is presented. Based on the results from x-ray structures conformational analysis is discussed.

In Chapter III the structural characterization of selected selenium coronands and two dications of selena cyclic ethers by CP-MAS solid state NMR is presented.

In Chapter IV the redox chemistry of the selenium coronands is described, which includes characterization of the radical cations and dications of selenium coronands by uv-visible spectroscopy and various electrochemical techniques. The relationship between the absorption maxima as well as the redox potentials and the stability of the radical cations are discussed.

In Chapter V, the coordination chemistry of some selenium coronands and transition metal ions (Pd, Cu) complexes are discussed. The Chapter describes the preparation of complexes and their characterization by x-ray crystallography, uv-visible spectroscopy and, where applicable, ESR spectroscopy. The redox properties of the metal complexes of selenium coronands, obtained from cyclic voltammetric studies, are also discussed. The kinetic study of the redox reaction of the Cu(II) 16Se4 complex is presented and a mechanism is proposed.

Finally, in Chapter VI, a short summary on the main points in each Chapter is given.

In Chapter VII the detailed experimental procedures are given.

CHAPTER II
SYNTHESIS OF NEW AND FUNCTIONALIZED SELENIUM CORONANDS

2.1. Introduction

2.1.1. Synthetic Methods

The methodology for synthesizing selenium coronands depends on the nature of the targets. In Pinto's group, selenium coronands[75] were successfully prepared by reacting the sodium alkyl diselenolate with the appropriate dihalides. This procedure was also used to synthesize 8Se2OH (17) and 16Se4(OH)$_2$ (9). The advantage of this approach is that the synthesis is a one-step procedure (Scheme 2.1.1).

Scheme 2.1.1
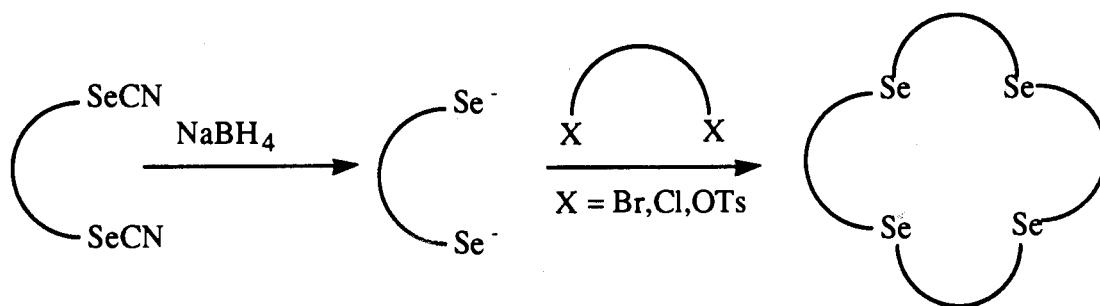
However, this approach failed in the synthesis of dibenzo-14Se4. Attempts to prepare dibenzo-14Se4 (14) through the one-step procedure resulted in 1,2-(1,3-trimethylenediseleno)benzene (22). Moreover, the one-step approach cannot be used in preparation of mixed donor-atom or selenium coronands containing an odd-numbered of heteroatoms. Hence, a stepwise synthetic approach is necessary. The concept of a

15

stepwise synthetic procedure is shown in Scheme 2.1.2. The key to the stepwise approach is replacing the 1,3-dibromopropane with a propane that has two functional groups on the 1 and 3 positions, one being more reactive than the other towards the nucleophile; hence, the self-cyclization problem can be circumvented. When the appropriate intermediate for the coronand is built up, the less reactive functional group (usually an OH group) is converted to a leaving group that reacts with the sodium alkyl diselenolate to complete the cyclization.

Spectroscopic methods such as IR, UV, MS and NMR spectroscopy were used for structural characterization along with microanalysis. In addition, solid state ^{13}C and ^{77}Se NMR spectroscopy were applied, when appropriate.

Scheme 2.1.2
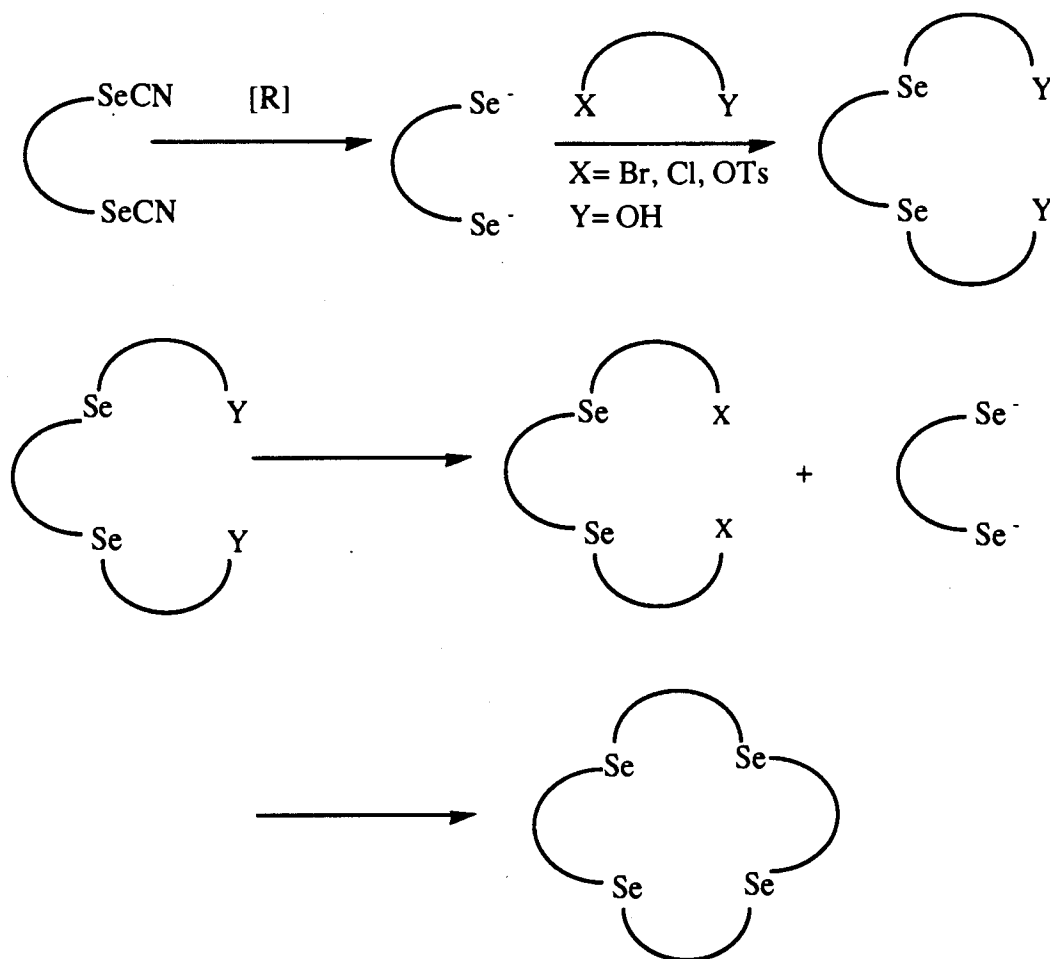
2.2. Results

2.2.1. Synthesis of 16Se4(OH)₂ (9) and 8Se2OH (17).

These two selenium coronands were synthesized by the one-step procedure (Scheme 2.2.1). Addition of 1,3-dibromopropane to sodium 2-hydroxy-1,3-propanediselenolate (37) in THF/EtOH yielded a mixture of 8Se2OH (17) and 16Se4(OH)₂ (9), which were isolated by flash column chromatography. The yields of 8Se2OH and 16Se4(OH)₂ were dependent on reaction temperatures. At 0 °C, mainly 8Se2OH (8Se2OH/16Se4(OH)₂, 36:2) was isolated, but at 40 °C the yield of 16Se4(OH)₂ increased (8Se2OH/16Se4(OH)₂, 23:12). The rest of the reaction mixture appeared to consist of polymeric material.

Scheme 2.2.1

Temperature	Yield	
	9	17
0 °C	2.7%	40%
40 °C	12%	23%

17
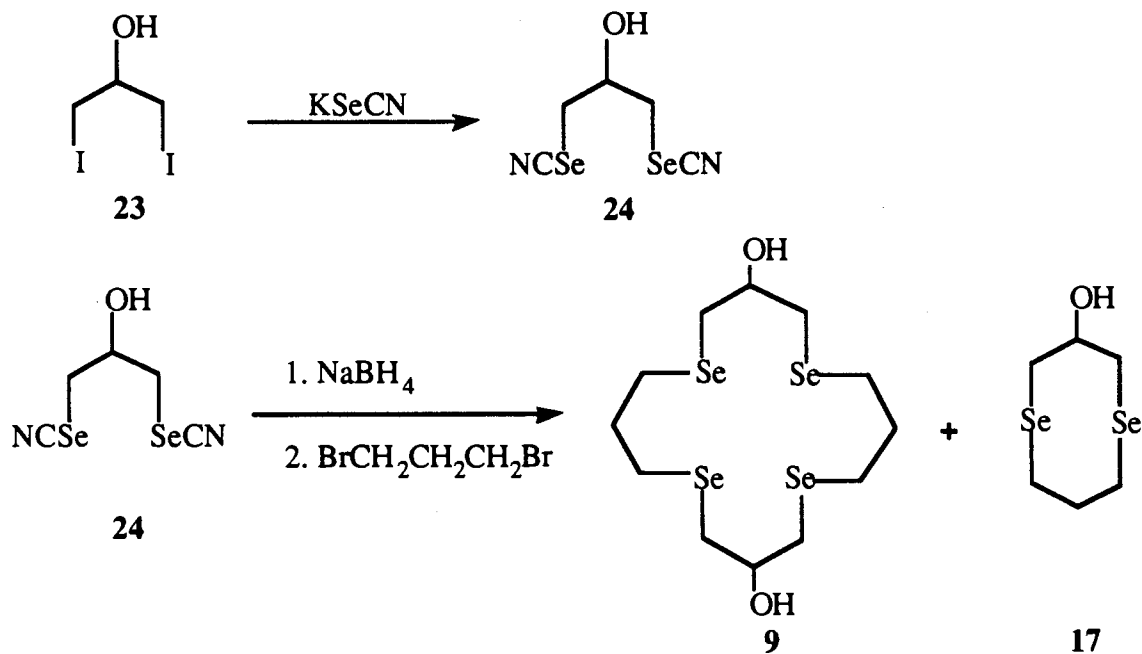
Products were characterized by microanalysis. More useful information for structure elucidation was obtained from the ^{1}H, ^{13}C NMR, IR and MS spectra. Table 2.2.1 and Table 2.2.2 list the ^{1}H, and ^{13}C NMR chemical shifts of **17** and **9** respectively Figure 2.2.1 and Figure 2.22 are illustrations of possible conformations for **17** and **9**, respectively. Figure 2.2.3 is a 2D ^{1}H-homonuclear chemical-shift correlated NMR spectrum of **17**.
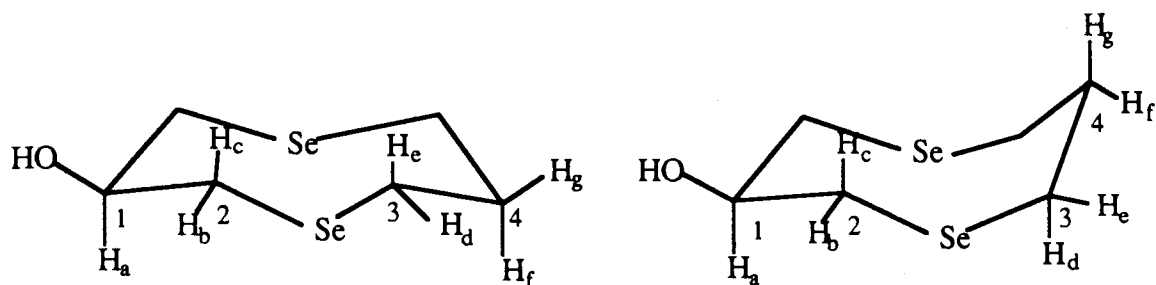
Figure 2.2.1. **Two possible conformations of 8Se2OH (17) (chair-chair and chair-boat conformations).**

Table 2.2.1. Solution ^{1}H and ^{13}C NMR Data for 8Se2OH (17)[a]

Proton	δ (ppm)[b] and J (Hz)	Carbon	δ (ppm)[c] (rel int)
H_a	3.98 s (br)	C_1	69.4 (1)
H_b	3.13-3.18; dd, J_{bc} = 13.8 Hz, J_{ba} = 3.00 Hz	C_2	30.2 (2)
H_c	2.96-3.03; dd, J_{cb} = 13.8 Hz, J_{ca} = 7.00 Hz		
H_d	2.79-2.86; ddd, J_{de} = 13.4 Hz, J_{dg} = 7.50 Hz, J_{df} = 3.75 Hz)	C_3	23.9 (2)
H_e	2.68-2.74; ddd, J_{ed} = 13.4 Hz, J_{ef} = 8.00 Hz, J_{eg} = 4.25 Hz		
H_f, H_g	2.32-2.48; dtt, J_{fg} = 13 Hz, J_{fd} 3.75 Hz, J_{fe} = 8.00 Hz, Jge = 4.25 Hz, Jgd = 7.50 Hz	C_4	30.8 (1)

a. In CDCl$_3$ and relative to TMS.

b. 400 MHz ^{1}H NMR.

c. 100 MHz ^{13}C NMR .
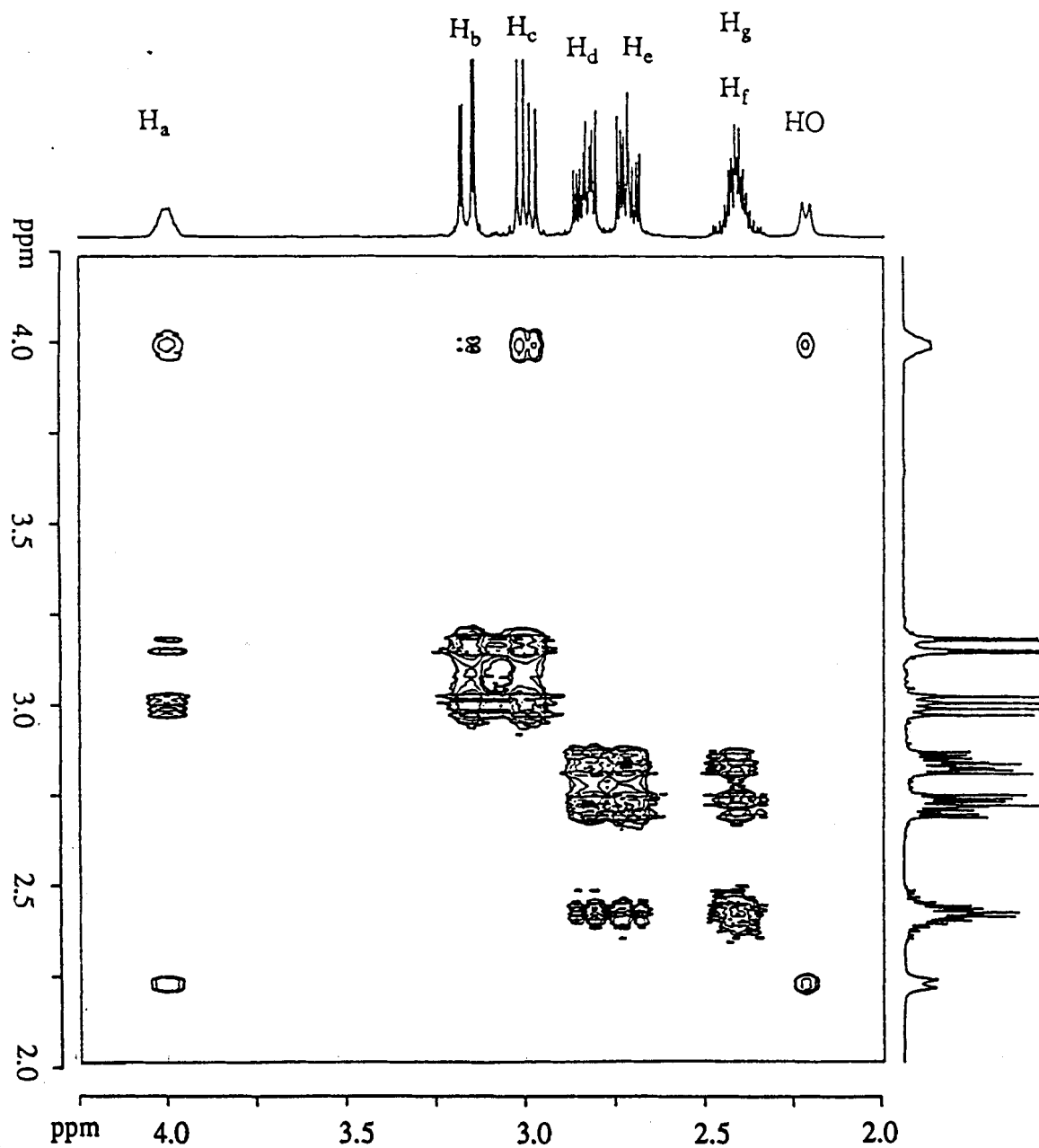
Figure 2.2.2. Two-dimensional COSY ^{1}H NMR spectrum of 8Se2OH (17) in CDCl$_3$.
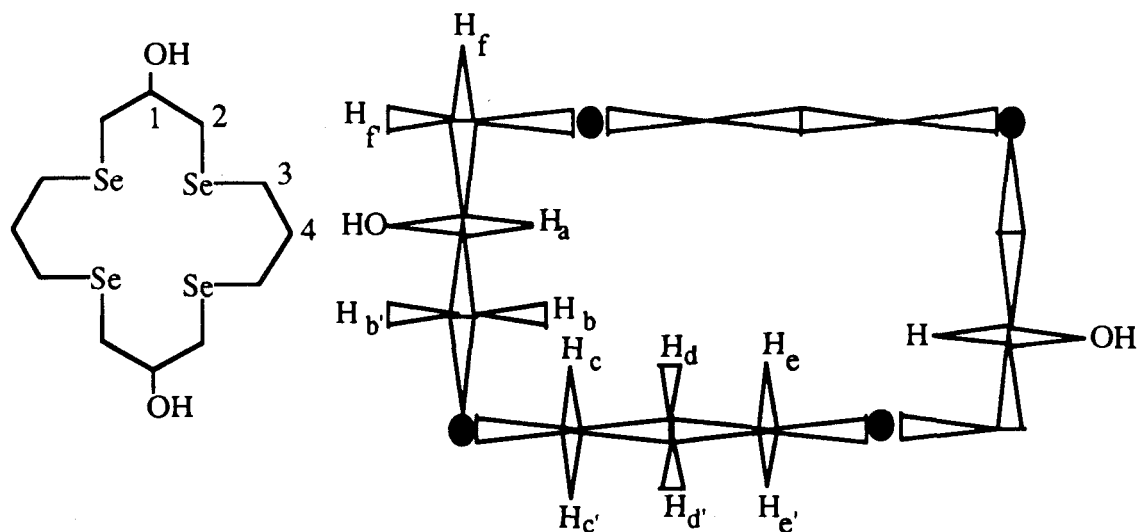
Figure 2.2.3. A proposed conformation of 16Se4(OH)$_2$ (9).

Table 2.2.2. Solution ^{1}H and ^{13}C NMR Data for 16Se4(OH)$_2$ (9)^a

Proton	δ (ppm)^b and J (Hz)	Carbon	δ (ppm)^c (rel int)
H$_a$	3.88 m; (rel int = 1)	C$_1$	70.1 (1)
H$_b$, H$_c$, H$_e$	2.86-2.91; m, (rel int = 3)	C$_2$	31.3 (2)
H$_{b'}$, H$_{c'}$, H$_{e'}$, H$_f$, H$_{f'}$	2.77-2.66; m, (rel int = 5)	C$_3$	24.3 (2)
H$_d$, H$_{d'}$	2.09, p, J = 6.4 Hz, (rel int = 2)	C$_4$	31.6 (1)

a. In CDCl$_3$ and relative to TMS.

b. 400 MHz ^{1}H NMR.

c. 100 MHz ^{13}C NMR .

2.2.2. Synthesis of Dibenzo-14Se4 (14)

Dibenzo-14Se4 (**14**) was synthesized by a stepwise procedure that is depicted in Scheme 2.2.2. The poly(1,2-diselenobenzene) (**26**), which was prepared according to a literature procedure[94] was reduced by $NaBH_4$ to give sodium 1,2-benzenediselenolate. As mentioned in the Introduction, the direct reaction of sodium 1,2-benzenediselenolate with 1,3-dibromopropane gave 1,2-(1,3-trimethylenediseleno)benzene (**22**), as the only product. Hence, 3-bromo-1-propanol was used to give 1,2-bis(3-hydroxy-1-propylseleno)benzene (**27**), which was isolated and transformed to a dichloro-compound. The dichlorocompound (**28**) was isolated and was reacted with sodium 1,2-benzenediselenolate to obtain **14**. The final coronand, as well as the intermediates, were isolated by flash silica column chromatography and characterized by microanalysis, IR, MS, ^{1}H NMR, and ^{13}C NMR spectroscopy. The structure of **14** was further characterized by x-ray crystallography, and ^{13}C solid state NMR spectroscopy. Figure 2.2.4 and Figure 2.2.5 show the x-ray molecular structures of dibenzo-14Se4 in two different conformations.

Besides the dichlorocompound **28**, the ditosylate of 1,2-bis(3-hydroxyl-1-propanylseleno)benzene was also made as the precursor for the cyclization step. However, the dichlorocompound was easier to isolate and purify.

Extension of the synthetic approach to synthesize analogs with only two-carbon bridges by reaction of sodium 1,2-benzenediselenolate with 1,2-bis(1-hydroxyethyleneseleno)benzene was totally unsuccessful. This likely arises because of the formation of the labile ethylene episelenonium ions which undergo extrusion of ethylene [95-97] as shown in Scheme 2.2.3.

Scheme 2.2.2

25

Na$_2$Se$_2$

DMF, 120 °C

26 85%

26

1. NaBH$_4$

2. ClCH$_2$CH$_2$CH$_2$OH

27 52%

27

Cl–S–Cl

CH$_2$Cl$_2$

28 46%

28

14 50%
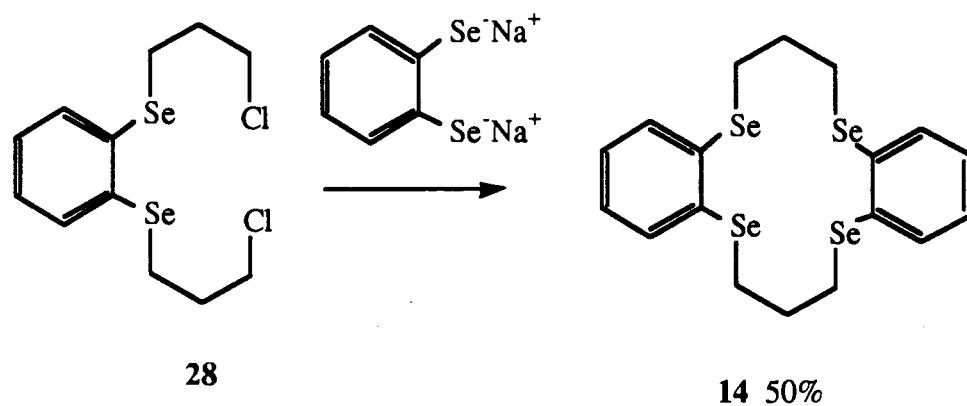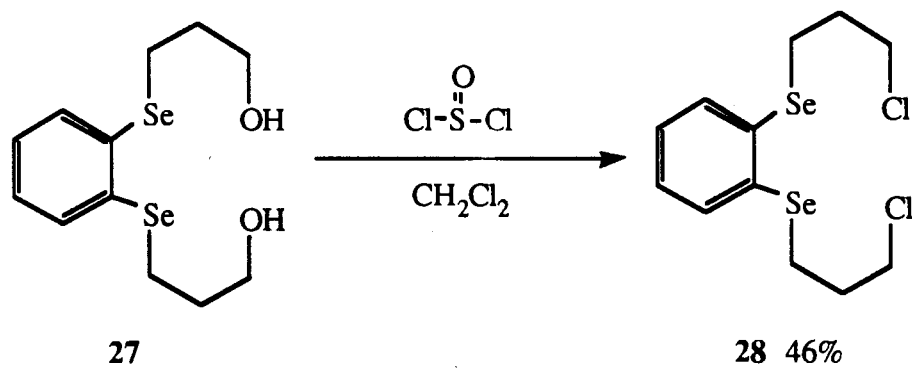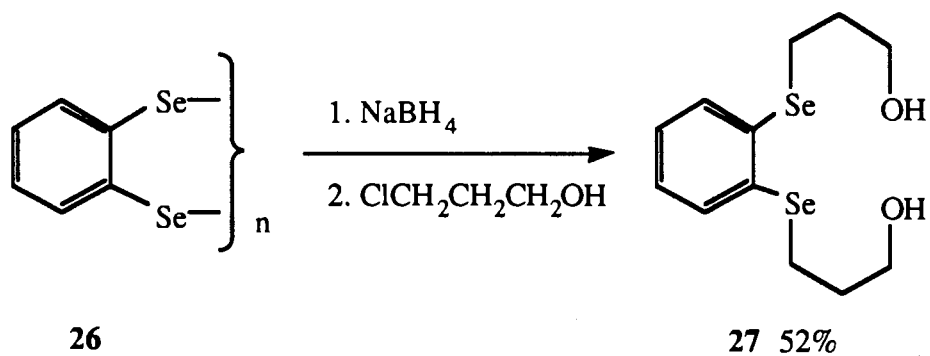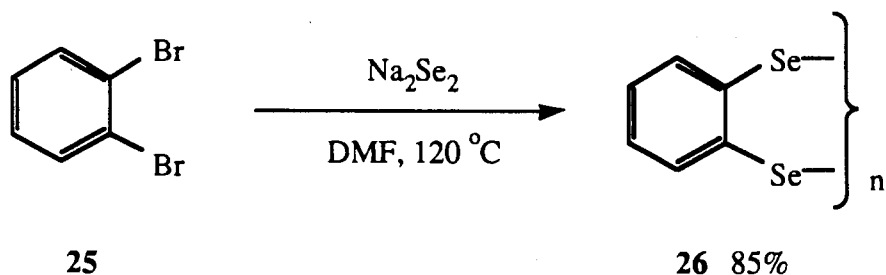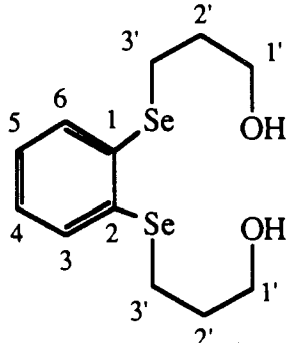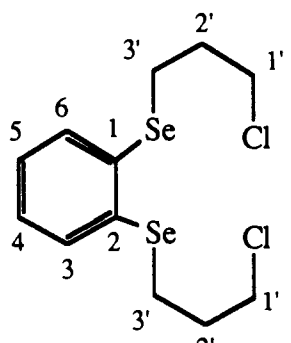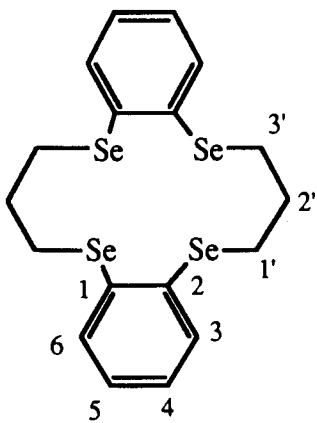
Table 2.2.3. Solution ^{1}H and ^{13}C NMR Data for Dibenzo-14Se4 (14) and Important Intermediates[a]

Compound	^{1}H	δ (ppm)[b] and J (Hz)	^{13}C	δ (ppm)[c] (rel int)
	H$_{1'}$	3.78; t, J = 6.61 Hz	C$_{1'}$	62.3 (1)
	H$_{2'}$	1.97; p, J = 6.61 Hz	C$_{2'}$	32.3 (1)
	H$_{3'}$	3.02; t, J = 6.61 Hz	C$_{3'}$	24.3 (1)
	H$_3$ H$_4$ H$_5$ H$_6$	7.11-7.46; m	C$_1$	134 (w)[d]
			C$_5$ C$_6$	127 (1), 132 (1)
	OH	2.72; m		
	H$_{1'}$	3.70; t, J = 6.29 Hz	C$_{1'}$	44.3 (1)
	H$_{2'}$	2.15; p, J = 6.56 Hz	C$_{2'}$	32.4 (1)
	H$_{3'}$	3.10; t, J = 6.89 Hz	C$_{3'}$	24.6 (1)
	H$_3$ H$_4$ H$_5$ H$_6$	7.17-7.80; m	C$_1$	134 (w)[d]
			C$_5$ C$_6$	127 (1), 132 (1)
	H$_{1'}$	3.02; t, J = 7.1 Hz	C$_{1'}$	27.0 (2)
	H$_{2'}$	1.98; p, J = 7.1 Hz	C$_{2'}$	29.3 (1)
	H$_3$ H$_4$ H$_5$ H$_6$	6.95-7.35; m	C$_1$	134 (weak)
			C$_5$ C$_6$	127 (2), 133 (2)

a. In CDCl$_3$ and relative to TMS.

b. 400 MHz ^{1}H NMR.

c. 100 MHz ^{13}C NMR.

Scheme 2.2.3

$$ArSeCH_2CH_2Cl \underset{+ Cl^-}{\overset{- Cl^-}{\rightleftharpoons}} \quad ArSe^+ \quad \longrightarrow \quad ArSeSeAr + CH_2{=}CH_2$$

$$ArSe^-$$

Scheme 2.2.4

29   30 (60%)

30   31   11 (22%)
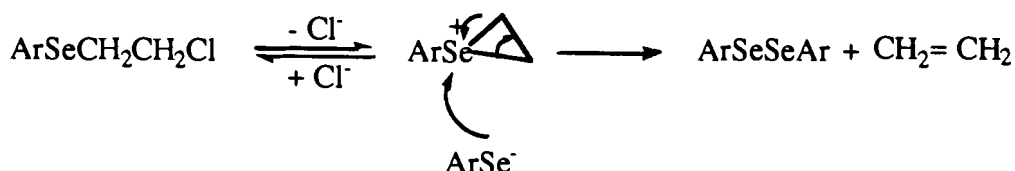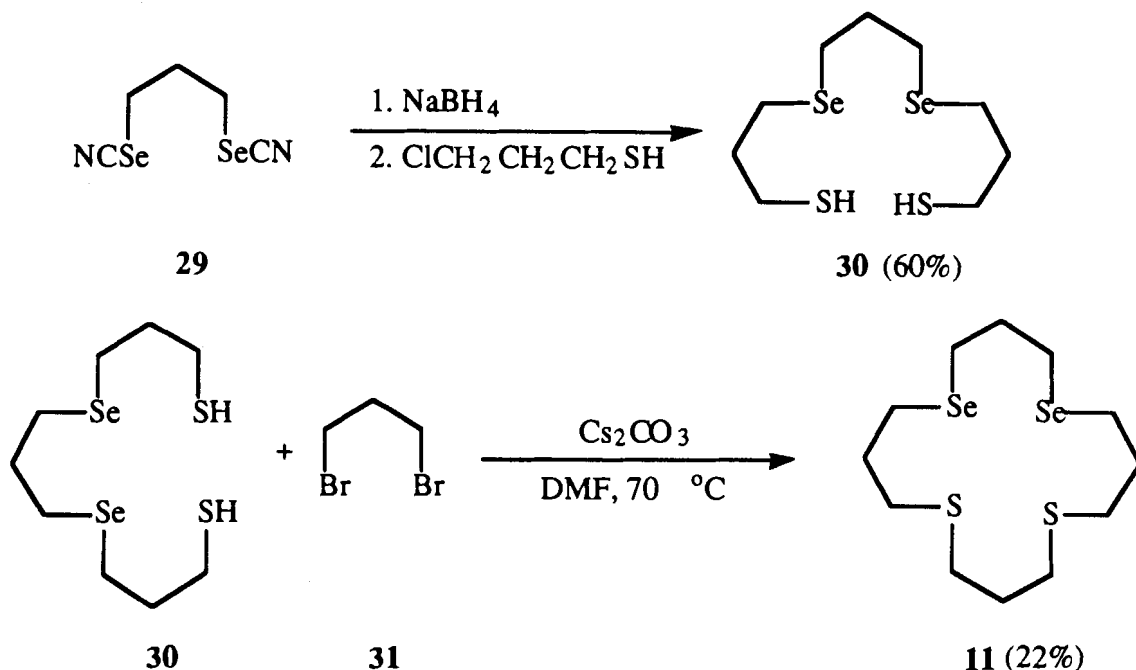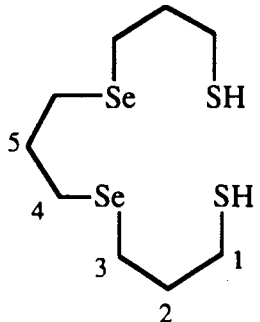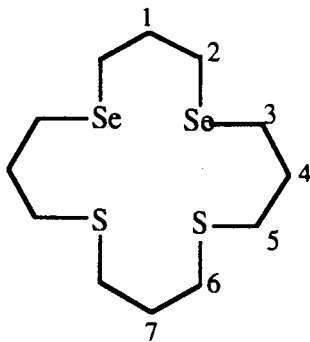
2.2.3. Synthesis of 16S2Se2 (11)

A stepwise synthetic route for preparation of 16S2Se2 is shown in Scheme 2.2.4. As such, we could use the existing starting material (1,3-propanediselenocyanate) and employ the method for preparing thiamacrocycles[98], i. e., alkyl dithiols reacted with dihalogenated or ditosylated alkyls in the presence of Cs_2CO_3 to complete the cyclization. Thus, 3-chloro-1-propanethiol was reacted with sodium 1,3-propanediselenolate to give the 5,9-diselenatridecane-1,13-dithiol (**30**). Compound **30** was isolated by flash column chromatography and characterized, then reacted with 1,3-dibromopropane to yield the

coronand, 16S2Se2, which was characterized by IR, UV, ^{1}H and ^{13}C NMR spectroscopy, microanalysis and x-ray crystallography. Figure 2.2.6 shows the x-ray structure of 16S2Se2.

Table 2.2.4.   **Solution ^{1}H and ^{13}C NMR Data for 16S2Se2 (11) and Important Intermediates[a]**

Compound	[1]H	δ (ppm)[b] and J (Hz),	[13]C	δ (ppm)[c] (rel int)
	H_1 H_3 H_4	2.88; p, J = 8.6 Hz	C_1	34.3 (2)
			C_2	24.4 (2)
	H_2	2.05; p, J = 8.6 Hz	C_3	23.7 (2)[d]
	H_5	1.53; p, 8.6 Hz	C_4	22.1 (2)[d]
			C_5	31.1 (1)
	H_1 H_4 H_7	1.97; p, J = 6.0 Hz	C_1 C_4 C_7	29.7 (1), 31.8 (1)
	H_2 H_3	2.87; t, J = 6.0 Hz	C_2	22.47 (2)
			C_3	23.7 (2)
	H_5 H_6	3.05; t, J = 6.89 Hz	C_5	31.8 (2)
			C_6	32.0 (2)

a. In CDCl$_3$ and relative to TMS.

b. 400 MHz ^{1}H NMR.

c. 100 MHz ^{13}C NMR .

d. satellite triplet was observed.

2.2.4. *Synthesis of 12Se3 (18)*

The coronand 12Se3 shown in Figure 2.2.7 was synthesized by a stepwise procedure by colleagues[99]. Its x-ray structure and selective bond distances, bond angles and torsion angles are listed in Table 2.2.7.
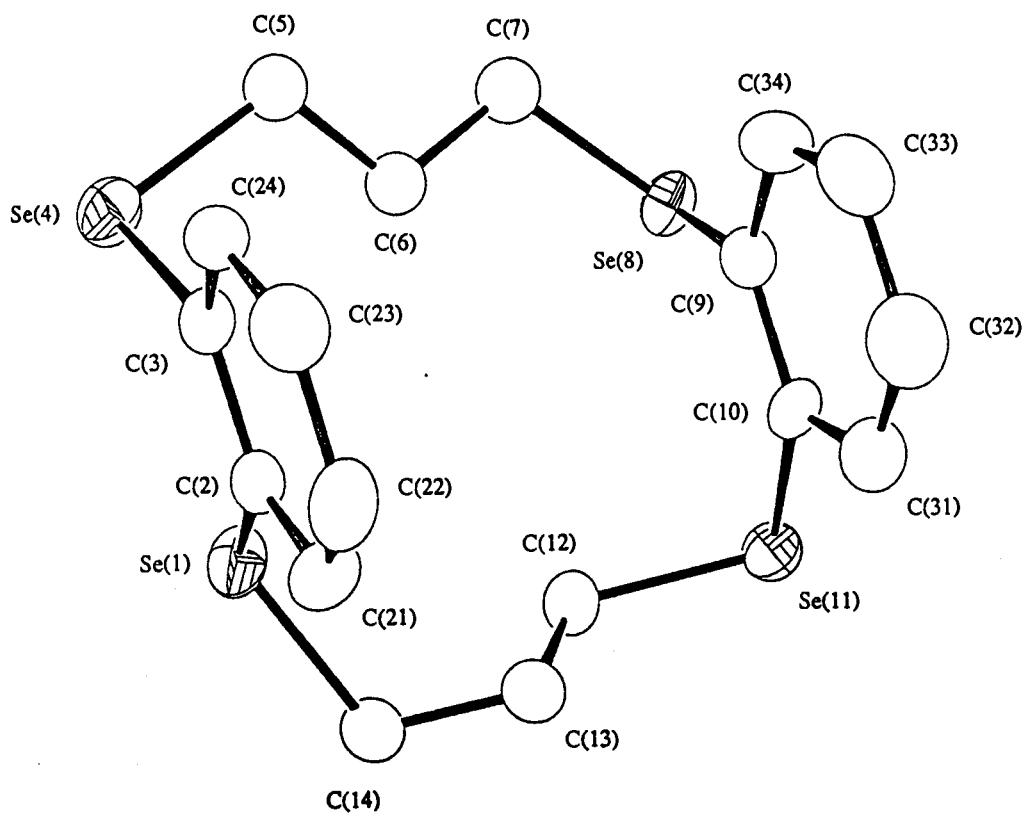
Figure 2.2.4. Molecular structure of dibenzo-14Se4 (14 a).
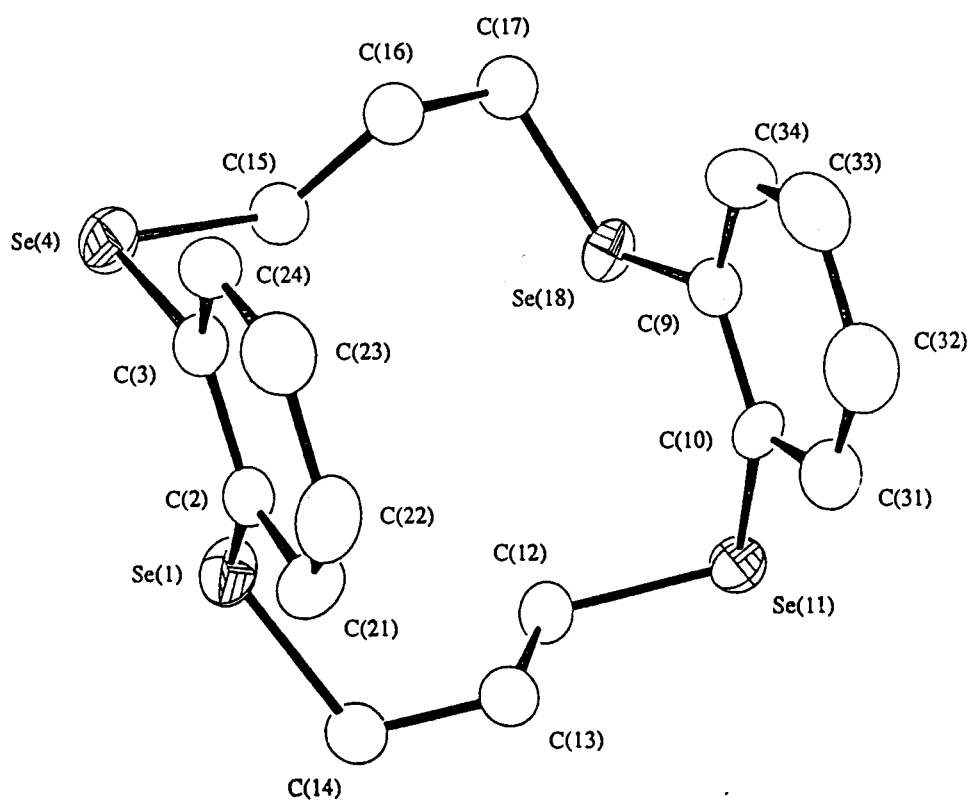
Figure 2.2.5. Molecular structure of dibenzo-14Se4 (14 b).
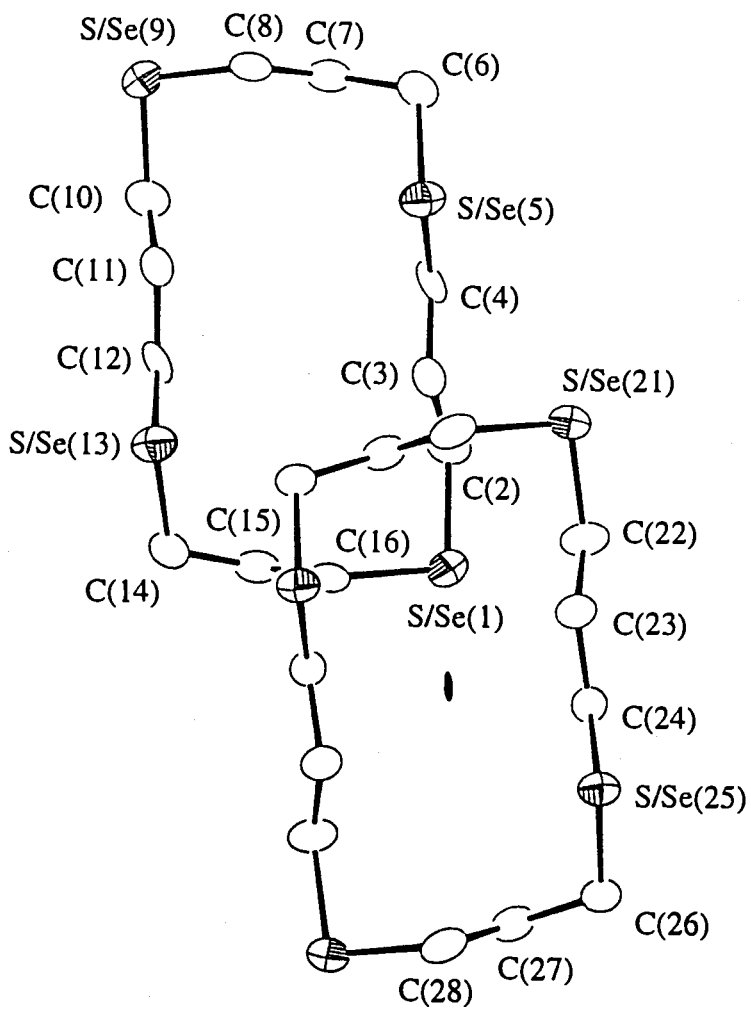
Figure 2.2.6. Molecular structure of 16S2Se2 (11).
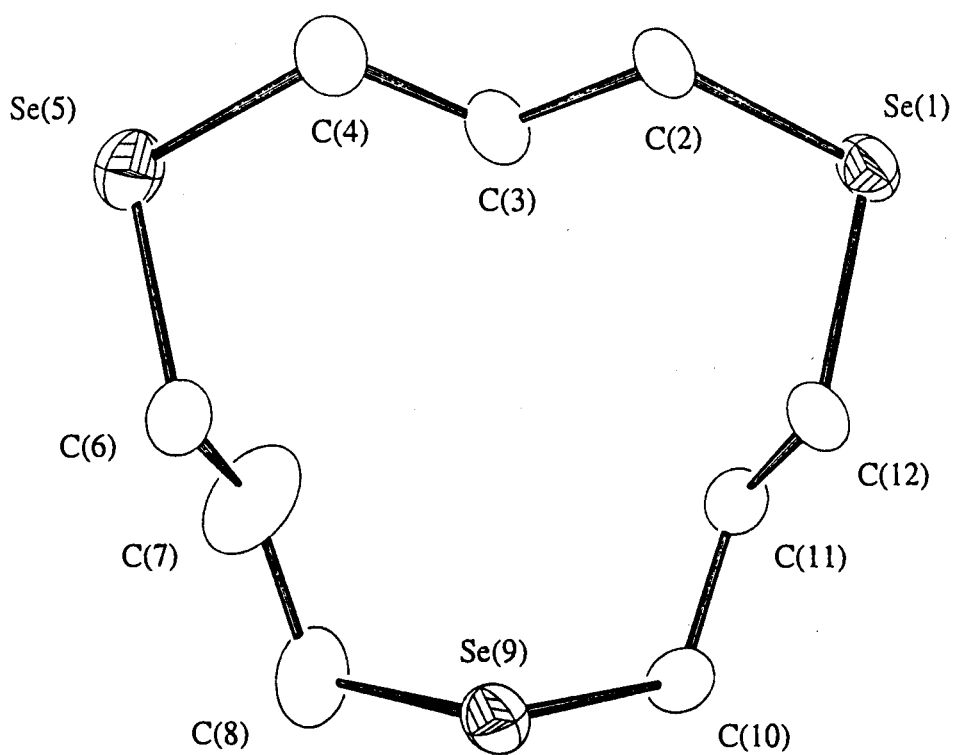
Figure 2.2.7. **Molecular structure of 12Se3 (18).**

Table 2.2.5. Selected Bond Distances (Å), Bond Angles and Torsion (°) Angles for Dibenzo-14Se4 (14) at 190 K

Bond Distances (Å)

Se(1)	C(2)	1.923 (6)		C(5)	C(6)	1.509 a
Se(1)	C(14)	1.963(7)		C(6)	C(7)	1.530
Se(4)	C(3)	1.923 (6)		C(15)	C(16)	1.535
Se(4)	C(5)	1.937		C(16)	C(17)	1.539
Se (4)	C (15)	2.000		C(9)	C(10)	1.397(8)
Se(8)	C(7)	1.959		C(9)	C(34)	1.387(8)
Se(8)	C(9)	1.949		C(10)	C(31)	1.389(9)
Se(18)	C(17)	1.962		C(12)	C(13)	1.516(9)
Se(18)	C(9)	1.878		C(13)	C(14)	1.511(9)
Se(11)	C(10)	1.920(6)		C(21)	C(22)	1.395(9)
Se(11)	C(12)	1.969(6)		C(22)	C(23)	1.368(9)
C(2)	C(3)	1.400(8)		C(23)	C(24)	1.387(9)
C(2)	C(21)	1.388(8)		C(31)	C(32)	1.399(9)
C(3)	C(24)	1.400(9)		C(32)	C(33)	1.395(9)
				C(33)	C(34)	1.372(10)

Bond Angles (°)

C(14)	Se(1)	C(2)	100.2(3)	C(10)	C(9)	Se(8)	120.8
C(5)	Se(4)	C(3)	99.1	C(10)	C(9)	Se(18)	119.1
C(15)	Se(4)	C(3)	97.6	C(34)	C(9)	Se(8)	119.7(5)
C(9)	Se(8)	C(7)	97.2	C(34)	C(9)	Se(18)	121.1(5)
C(9)	Se(18)	C(17)	99.6	C(34)	C(9)	C(10)	119.3(S)
C(12)	Se(11)	C(10)	98.0(3)	C(9)	C(10)	Se(11)	123.4(5)
C(3)	C(2)	Se(1)	118.2(4)	C(31)	C(10)	Se(11)	117.4(5)
C(21)	C(2)	Se(1)	122.5(5)	C(31)	C(10)	C(9)	119.2(6)
C(21)	C(2)	C(3)	119.3(6)	C(13)	C(12)	Se(11)	114.1(4)
C(2)	C(3)	Se(4)	121.9(4)	C(14)	C(13)	C(12)	111.2(6)

(continued)

continuation of:

Table 2.2.5. Selected Bond Distances (Å), Bond Angles and Torsion (°) Angles for Dibenzo-14Se4 (14) at 190 K

Bond Angles (°)

C(24)	C(3)	Se(4)	117.9(5)	C(13)	C(14)	Se(1)	115.7(5)
C(24)	C(3)	C(2)	120.0(6)	C(22)	C(21)	C(2)	120.2(6)
C(6)	C(5)	Se(4)	111.9	C(23)	C(22)	C(21)	120.3(7)
C(7)	C(6)	C(5)	111.1	C(24)	C(23)	C(22)	120.6(7)
C(6)	C(7)	Se(8)	111.4	C(23)	C(24)	C(3)	119.5(6)
C(16)	C(15)	Se(4)	114.8	C(32)	C(31)	C(10)	121.8(6)
C(17)	C(16)	C(15)	115.6	C(33)	C(32)	C(31)	117.4(7)
C(16)	C(17)	Se(18)	114.6	C(34)	C(33)	C(32)	121.3(7)
C(33)	C(34)	C(9)	120.9(6)				

Torsion Angles (°)

C(14)	Se(1)	C(2)	C(3)	161.9(5)	Se(1)	C(2)	C(3)	Se(4)	4.9(1)
C(5)	Se(4)	C(3)	C(2)	-103.2(5)	C(3)	Se(4)	C(5)	C(6)	63.9(4)
Se(4)	C(5)	C(6)	C(7)	175.0(8)	C(5)	C(6)	C(7)	Se(8)	169.8(8)
C(9)	Se(8)	C(7)	C(6)	-63.9(5)	C(7)	Se(8)	C(9)	C(10)	136.5(5)
Se(8)	C(9)	C(10)	Se(11)	-2.1(1)	C(12)	Se(11)	C(10)	C(9)	-81.8(4)
C(10)	Se(11)	C(12)	C(13)	-66.9(4)	Se(11)	C(12)	C(13)	C(14)	179.1(7)
C(12)	C(13)	C(14)	Se(1)	-64.5(4)	C(2)	Se(1)	C(14)	C(13)	-67.5(4)
C(14)	Se(1)	C(2)	C(21)	-18.2(4)	C(5)	Se(4)	C(3)	C(24)	82.6(4)
C(7)	Se(8)	C(9)	C(34)	-49.1(4)	C(12)	Se(11)	C(10)	C(31)	101.3(5)
Se(1)	C(2)	C(3)	C(24)	179.0(6)	C(21)	C(2)	C(3)	Se(4)	-175.0(7)
Se(8)	C(9)	C(10)	C(31)	174.8(7)	C(34)	C(9)	C(10)	Se(11)	-176.5(7)
Se(1)	C(2)	C(21)	C(22)	-179.5(7)	Se(4)	C(3)	C(24)	C(23)	176.2(7)
Se(8)	C(9)	C(34)	C(33)	-175.3(7)	Se(11)	C(10)	C(31)	C(32)	178.2(7)
C(21)	C(2)	C(3)	C(24)	-0.9(4)	C(3)	C(2)	C(21)	C(22)	0.4(4)
C(2)	C(3)	C(24)	C(23)	1.8(4)	C(34)	C(9)	C(10)	C(31)	0.4(4)
C(10)	C(9)	C(34)	C(33)	-0.7(4)	C(9)	C(10)	C(31)	C(32)	1.2(4)

(continued)

continuation of:

Table 2.2.5. Selected Bond Distances (Å), Bond Angles and Torsion (°) Angles for Dibenzo-14Se4 (14) at 190 K

Torsion Angles (°)

C(2)	C(21)	C(22)	C(23)	-0.7(4)	C(21)	C(22)	C(23)	C(24)	1.6(4)
C(22)	C(23)	C(24)	C(3)	-2.2(4)	C(10)	C(31)	C(32)	C(33)	-2.2(4)
C(31)	C(32)	C(33)	C(34)	1.8(4)	C(32)	C(33)	C(34)	C(9)	-0.4(4)
C(15)	Se(4)	C(3)	C(2)	-73.3(5)	C(3)	Se(4)	C(15)	C(16)	-65.2(7)
C(9)	Se(18)	C(17)	C(16)	-68.6(8)	C(17)	Se(18)	C(9)	C(10)	152.5(7)
Se(18)	C(9)	C(10)	Se(11)	12.2(2)	C(15)	Se(4)	C(3)	C(24)	112.5(6)
C(17)	Se(18)	C(9)	C(34)	-18.6(5)	Se(18)	C(9)	C(10)	C(31)	-170.9(7)
Se(18)	C(9)	C(34)	C(33)	170.3(7)	Se(4)	C(15)	C(16)	C(17)	-174.9(13)
C(15)	C(16)	C(17)	Se(18)	-64.4(9)					

a. Parameters for which no e.s.d.s are given were directly affected by restraints during refinement.

33

Table 2.2.6. Selected Bond Distances (Å), Bond Angles and Torsion Angles (°) for 16S2Se2 (11) at 200 K

Bond Distances (Å)

S/Se(1)	C(2)	1.938(13)	C(2)	C(3)	1.50(2)
S/Se(1)	C(16)	1.916(13)	C(3)	C(4)	1.54(2)
S/Se(5)	C(4)	1.904(12)	C(6)	C(7)	1.55(2)
S/Se(5)	C(6)	1.925(12)	C(7)	C(8)	1.49(2)
S/Se(9)	C(8)	1.868(13)	C(10)	C(11)	1.54(2)
S/Se(9)	C(10)	1.847(13)	C(11)	C(12)	1.52(2)
S/Se(13)	C(12)	1.883(12)	C(14)	C(15)	1.47(2)
S/Se(13)	C(14)	1.893(12)	C(15)	C(16)	1.52(2)
S/Se(21)	C(22)	1.884(12)	C(22)	C(23)	1.54(2)
S/Se(21)	C(28)	1.888(13)	C(23)	C(24)	1.53(2)
S/Se(25)	C(24)	1.909(12)	C(26)	C(27)	1.52(2)
S/Se(25)	C(26)	1.888(12)	C(27)	C(28)	1.51(2)

Bond Angles (°)

C(16)	S/Se(1)	C(2)	100.5(6)	C(11)	C(10)	S/Se(9)	114.4(10)
C(6)	S/Se(5)	C(4)	98.4(6)	C(12)	C(11)	C(10)	109.8(11)
C(10)	S/Se(9)	C(8)	101.2(6)	C(11)	C(12)	S/Se(13)	108.9(9)
C(14)	S/Se(13)	C(12)	97.8(6)	C(15)	C(14)	S/Se(13)	116.7(9)
C(28)	S/Se(21)	C(22)	99.6(6)	C(16)	C(15)	C(14)	113.6(11)
C(26)	S/Se(25)	C(24)	97.7(6)	C(15)	C(16)	S/Se(1)	115.0(9)
C(3)	C(2)	S/Se(1)	115.5(9)	C(23)	C(22)	S/Se(21)	113.5(9)
C(4)	C(3)	C(2)	110.0(11)	C(24)	C(23)	C(22)	110.8(10)
C(3)	C(4)	S/Se(5)	107.2(8)	C(23)	C(24)	S/Se(25)	108.4(8)
C(7)	C(6)	S/Se(5)	112.6(9)	C(27)	C(26)	S/Se(25)	115.8(9)
C(8)	C(7)	C(6)	113.7(11)	C(28)	C(27)	C(26)	112.9(11)
C(7)	C(8)	S/Se(9)	113.5(9)	C(27)	C(28)	S/Se(21)	114.6(9)

(continued)

Continuation of:

Table 2.2.6. Selected Bond Distances (Å), Bond Angles and Torsion Angles (⁰) for 16S2Se2 (11) at 200 K

Torsion Angles (⁰)

C(16)	S/Se(1)	C(2)	C(3)	59.0(6)
C(2)	S/Se(1)	C(16)	C(15)	64.9(6)
C(6)	S/Se(5)	C(4)	C(3)	-176.0(8)
C(4)	S/Se(5)	C(6)	C(7)	72.6(6)
C(10)	S/Se(9)	C(8)	C(7)	65.6(6)
C(8)	S/Se(9)	C(10)	C(11)	61.0(6)
C(14)	S/Se(13)	C(12)	C(11)	-173.9(8)
C(12)	S/Se(13)	C(14)	C(15)	72.4(7)
S/Se(1)	C(2)	C(3)	C(4)	-179.6(10)
C(2)	C(3)	C(4)	S/Se(5)	-172.0(10)
S/Se(5)	C(6)	C(7)	C(8)	63.1(7)
C(6)	C(7)	C(8)	S/Se(9)	-165.6(10)
S/Se(9)	C(10)	C(11)	C(12)	178.2(11)
C(10)	C(11)	C(12)	S/Se(13)	-173.1(10)
S/Se(13)	C(14)	C(15)	C(16)	62.8(7)
C(14)	C(15)	C(16)	S/Se(1)	-164.5(11)
C(28)'	S/Se(21)	C(22)	C(23)	-60.0(6)
C(22)	S/Se(21)	C(28)'	C(27)'	-62.0(6)
C(26)	S/Se(25)	C(24)	C(23)	173.9(8)
C(24)	S/Se(25)	C(26)	C(27)	-73.8(6)
S/Se(21)	C(22)	C(23)	C(24)	-179.8(11)
C(22)	C(23)	C(24)	S/Se(25)	169.6(10)
S/Se(25)	C(26)	C(27)	C(28)	-62.8(7)
C(26)	C(27)	C(28)	S/Se(21)'	166.7(11)

' indicates *2-x, y, 1.5-z*.

35

Table 2.2.7. Selected Bond Distances (Å), Bond Angles and Torsion Angles(°) for 12Se3 (18) at 190 K.

Bond Distances (Å)

Se(1)	C(2)	1.958(9)	C(2)	C(3)	1.515[a]
Se(1)	C(12)	1.956(7)	C(3)	C(4)	1.515
Se(5)	C(4)	1.963(7)	C(6)	C(7)	1.515
Se(5)	C(6)	1.962(8)	C(7)	C(8)	1.505
Se(9)	C(8)	1.923(9)	C(10)	C(11)	1.513
Se(9)	C(10)	1.961(8)	C(11)	C(12)	1.513

Bond Angles (°)

C(12)	Se(1)	C(2)	97.4(4)	C(7)	C(6)	Se(5)	109.7(6)
C(6)	Se(5)	C(4)	98.0(3)	C(8)	C(7)	C(6)	113.2(8)
C(10)	Se(9)	C(8)	100.6(4)	C(7)	C(8)	Se(9)	116.6(7)
C(3)	C(2)	Se(1)	113.9(6)	C(11)	C(10)	Se(9)	115.4(6)
C(4)	C(3)	C(2)	112.8(7)	C(12)	C(11)	C(10)	114.9(7)
C(3)	C(4)	Se(5)	112.2(6)	C(11)	C(12)	Se(1)	114.5(5)

Torsion Angles (°)

C(12)	Se(1)	C(2)	C(3)	-61.3(5)	C(2)	Se(1)	C(12)	C(11)	98.6(5)
C(6)	Se(5)	C(4)	C(3)	61.5(5)	C(4)	Se(5)	C(6)	C(7)	-102.6(6)
C(10)	Se(9)	C(8)	C(7)	-89.0(6)	C(8)	Se(9)	C(10)	C(11)	87.3(5)
Se(1)	C(2)	C(3)	C(4)	175.3(8)	C(2)	C(3)	C(4)	Se(5)	-171.6(8)
Se(5)	C(6)	C(7)	C(8)	173.0(9)	C(6)	C(7)	C(8)	Se(9)	-60.1(5)
Se(9)	C(10)	C(11)	C(12)	63.5(5)	C(10)	C(11)	C(12)	Se(1)	-172.7(8)

a Parameters for which no e.s.d.s are given were directly affected by restraints during refinement.

2.3. Discussion

8Se2OH (17). Sodium 2-hydroxyl-1,3-propanediselenolate can be prepared from the 2-hydroxy-1,3-propanediselenocyanate[100,101] by two reduction methods: one is by sodium in liquid ammonia; the other is by sodium borohydride[102]. Sodium borohydride as a reducing agent is preferred because it is easy to control the end-point of the reduction.

The 400 MHz ^{1}H NMR spectrum of 8Se2OH confirms that **17** has a cyclic structure (Figure 2.2.1). Geminal protons in the trimethylene groups have different chemical shifts. In a cyclic system, the geminal protons on the pseudoequatorial and pseudoaxial positions are in different chemical environments. The protons in the pseudoequatorial positions are in the deshielding zone (σ bond anisotropic effects[103]); therefore, the downfield chemical shifts are assigned to the pseudoequatorial protons and the upfield chemical shifts are assigned to the pseudoaxial protons. The proton (3.98 ppm) assigned to the carbon α to a hydroxyl group is supposed to be a multiplet because it has four neighboring protons on two adjacent carbons, but in the spectrum it appears as only a broad peak. Therefore, a 2-D NMR COSY experiment was run to unambiguously assign the spectrum. The off-diagonal peaks in the 2-D COSY ^{1}H NMR spectrum reveal (Figure 2.2.2) the coupling between H_a and H_b or H_c, which confirms that the resonance at 3.98 ppm is the proton (H_a) on the carbon α to the OH group.

8Se2OH **17** can have either a chair-chair or a chair-boat conformation (Figure 2.2.1). The energy barrier for inter conversion between these two conformations is low, as indicated by the disorder in the crystal structure of the complex $[Cu(8Se2OH)_2]^{2+}$ because of the interchanging between the chair-boat and chair-chair conformations (see Chapter 5). The energy difference between the chair-boat and the chair-chair conformation is also reported to be low for the sulfur congener; both conformations have been observed in the solid state structures of 8S2OH metal complexes[81,104]. Therefore, the NMR

spectrum is probably the average spectrum of the two rapidly interconverting conformations.

16Se4(OH)$_2$ (9). The ^{1}H NMR spectrum of **9** shows four sets of resonances. The pentet at high-field (2.07 ppm) is assigned to the protons on the CH$_2$ β to the Se atom; the pentet at low-field (3.88 ppm) is assigned to the protons on the hydroxyl substituted carbon. The remaining two mutiplets, integrating to a 3:5 ratio, occur between the two resonances. They are assigned to the CH$_2$ protons α to the Se atoms. If the molecule's structure has the symmetry shown in **9** in Scheme 2.2.1, the integral ratio of these two multiplets should be 1:1. However, if the coronand adopts a predominant conformation similar to 16Se4 in the solid-state, namely a [3535] quadrangle[75], as illustrated in Figure 2.2.3 (the numbers in the bracket designate the number of bonds on each side of the quadrangle), the integral ratio in the proton NMR spectrum of 16Se4(OH)$_2$ can be explained. In this conformation three protons, H$_b$, H$_c$ and H$_e$, are pointing inside the ring while the other five protons H$_f$, H$_{f'}$, H$_{b'}$, H$_{c'}$ and H$_{e'}$, are pointing outside the ring. These two groups of protons experience different chemical environments, and appear at different chemical shifts with a 3:5 integral ratio. Here, we only need to consider half of the molecule because the molecule has a C$_2$ axis perpendicular to the plane of the coronand. According to the x-ray crystal structure of [Cu{16Se4(OH)$_2$}](SO$_3$CF$_3$)$_2$, the two hydroxyl groups are on the same side of the macrocyclic ring (see Chapter 5).

Dibenzo-14Se4 (14). The molecular structure of the predominant (67.0(7)%) solid-state conformation of **14a** is shown in Figure 2.2.4. A second conformation **14b** (33.0(7)%) (Figure 2.2.5) replaces the chain C(5)-C(6)-C(7)-Se(8) with C(15)-C(16)-C(17)-Se(18) producing the observed disorder. The minor conformer differs from the major primarily in that C(15)-C(16)-C(17) is pivoted away from the C(5)-C(6)-C(7) positions, about an axis passing through Se(4), while the *anti* torsional arrangement for Se(4)-C(5)-C(6)-C(7) (175.0(8)°) is essentially retained in Se(4)-C(15)-C(16)-C(17) (-174.9 (13)°). This involves major conformational changes of two bond torsion angles.

The positive *gauche* arrangement, C(3)-Se(4)-C(5)-C(6) 63.9(4)°, changes to the negative *gauche* arrangement, C(3)-Se(4)-C-(15)-C(16)-65.2(7)°, while the approximately *anti* arrangement, C (5)-C(6)-C(7)-Se(8) 169.8(8)°, becomes the negative *gauche,* C(15)-C(16)-C(17)-Se(18)-64.4(9)°. Rationale for the occurrence of two such conformers of similar energy may be found in the following observations. The minor (33.0(7)%) conformer displays approximate two-fold symmetry for the molecule but has two nearly eclipsed arrangements: C(14)-Se(1)-C(2)-C(21)-18.2(4) ° and C(17)-Se(18)-C(9)-C(34)-18.6(5) °. These are associated with the most severe 'unimposed' intramolecular contacts *(i.e.* C(17)--C(34) 3.054(18) Å and C(14)--C(21) 3.147(10) Å). In the dominant (67.0(7)%) conformer this approximate molecular symmetry is destroyed and the latter torsion angle is 'relaxed' to C(7)-Se(8)-C(9)-C(34) -49.1(4)° (C(7)--C(34) 3.236(12) Å). Also two close Se--C intramolecular distances in the minor conformer (Se(1)--C(15) 3.489(16) Å and Se(18)--C(15) 3.476(11) Å) increase to 4.221(5) Å and 4.258(8) Å, respectively for Se(1)--C(5) and Se(8)--C(5) in the major conformer. At the same time, two intramolecular C--C contacts occur in the major conformer (C(3)--C(6) 3.331(10); C(6)--C(9) 3.313(9) Å) which were not significant in the minor conformer (C(3)--C(16) 3.427 (14) Å and C(9)--C(16) 3.464(16) Å). Selected bond distances and angles are given in Table 2.2.5. Differences in the lengths of chemically equivalent bonds involved in the disorder are not considered to be significant. An interesting feature of the compound is that the two arene rings are nearly coaxial. The dihedral angle between the planes of the arene rings is 6.0(3)°. An intriguing speculation is the possibility of forming chelating bis-arene metal complexes with this molecule. The arene rings' centroids are separated (intramolecularly) by 5.05 Å and the shortest inter-ring C--C distances range from 4.902(9) Å (C(21)--C(31)) to 5.253(9) Å (C(24)--C(34)). The rings are thus a little too far apart to make stable chelating bis-arene metal sandwich complexes without some conformational change in the Se(CH$_2$)$_3$Se chains but the molecule may be flexible enough to accommodate this.

Exodentate tendency is clearly demonstrated in dibenzo-14Se4. The lone pair electrons on selenium atoms are pointing out of the ring in both isomers. The explanation for this exodentate phenomenon is the *gauche* conformational preference around Se-C in the C-Se-C-C sequence. In both conformations, the molecule takes as many *gauche* conformations around the Se-C bonds as possible for the C-Se-C-C unit. Thus, **14a** has 9 *gauche*, 1 *anti* and 2 eclipsed conformations in the C-Se-C-C sequences, and **14b** has 8 *gauche*, 2 *anti* and 2 eclipsed conformations around Se-C bonds in the possible C-Se-C-C units. In contrast, dibenzo-14-crown-4[105], an oxygen analog, has 8 *anti*, 4 eclipsed and no *gauche* conformations around O-C bonds for C-O-C-C units.

The preference for a *gauche* conformation has also been observed in other selenium coronands[75] and in multithia macrocycles[2,36,76,77]. Cooper and co-workers[36] have explained the *gauche* preference in multithia macrocycles by means of the bond length difference between C-O (1.43 Å) and C-S (1.82 Å). The longer C-S bond diminishes the 1,4-interaction. Hence, the 1,4-interaction is likely to be less important for C-Se-C-C because the bond length for C-Se is about 1.94-1.96 Å[75].

With benzene groups fused to the macrocycle rings, it is more difficult for the coronand to reorganize through pseudorotation, the ramifications of which would be a decreased ability to coordinate with metal ions and electrochemical irreversibility for this coronand.

16S2Se2 (11). According to x-ray crystallographic results, the solid state structure of **11** (Figure 2.2.6) is similar to that of 16Se4 (**8**)[75]. It has a conformation of a [3535] quadrangle, in which one pair of Se and S atoms occupy the diagonal corners and the other pair of Se and S atoms are located at the two sides of the rectangle. The weighted-mean chalcogen atom site to carbon atom site 'bond distances' are reasonable (range: S/Se(9)-C(10) 1.847(13) Å to S/Se(1)-C(2) 1.938(13) Å) and display the expected correlation with the fractional selenium occupancy parameters. Typical Se-C distances are about 1.96 Å and S-C distances about 1.82 Å. The C-C bond distances in 16S2Se2 range

from 1.47(2) Å to 1.55(2) Å. The C-S/Se-C bond angles range from 97.7(6)° to 101.2(6)°; the C-C-S/Se angles from 107.2(8)° to 116.7(9)°; and the C-C-C angles from 109.8(11)° to 113.7(11)°.

The *gauche* preference around the C-E (E = S or Se) bond plays a role in dictating the coronand conformations, because by placing the Se or S atom at the corner maintains the C-Se/C-S bond in a *gauche* conformation. Although the [4444] conformation would have all C-Se-C-C sequences in *gauche* placement, the recent MNDO calculations[106] on the sulfur analog of 16Se4 suggest that the [3535] quadrangle conformer is slightly more stable (4 kJmol^{-1}) than the [4444] quadrangle conformer for 16S4.

12Se3 (18). The molecule **18** has no crystallographic symmetry but does have approximate local mirror (C_s or m) symmetry. The mirror passes through Se(9) and C(3). The analogous 12S3 compound[107] has been found to display two-fold rotational symmetry (C_2 or 2). Compound **18** is the only selenium coronand that shows a significant difference from its sulfur congener in terms of conformational preferences. In **18** every C-Se-C-C segment has the preferred gauche torsional arrangement whereas the molecule of 12S3 with C_2 symmetry has two anti C-S-C-C segments[107] and one gauche C-S-C-C segment. It seems that the Se-C bond in C-Se-C-C segment is more inclined to adopt a gauche conformation due to the longer Se-C bond lengths as compared to the S-C bond lengths.

In conclusion, we have successfully synthesized the selected selenium coronands containing different functional groups through a one-step or stepwise strategy. These functionalized selenium coronands can be used for further investigation of the substituent effects on metal ion complexes in terms of stability and reactivity. Also, the functional groups on the selenium coronands can serve as handles for further modifications or for attachment to polymers for developing new materials[108].

The information from x-ray crystallography indicates that the coronands display a preference for the *gauche* conformation about C-Se bond in C-Se-C-C sequences.

CHAPTER III
SOLID STATE NMR SPECTROSCOPY OF SELECTED SELENIUM CORONAND COMPOUNDS

3.1. Introduction

Solid-state NMR spectroscopy differs in several ways from solution NMR spectroscopy. For example, in the solid state molecules cannot tumble as freely as in solution so that the dipole-dipole interactions are not averaged, and as a consequence the peaks become broader and even indistinguishable in the worst case. Therefore, some special techniques such as magic angle spinning (MAS), cross polarization transfer (CP) and total suppression of spinning sidebands (TOSS) have been used in order to achieve high resolution NMR spectra. Here, we shall devote some effort to discuss the principles of these methods.

3.1.1. Magic Angle Spinning (MAS)

The broadening due to dipole-dipole interaction between two identical nuclei may be expressed[109] by Eq. 3.1.1

$$\nu_A = \nu_{Ao} \pm R/2(3\cos^2\theta - 1) \qquad (3.1.1)$$

Here, R is the splitting constant at $\theta = \pi/2$; θ is the angle between the external magnet direction and the internuclear vector; ν_{Ao} is the resonant frequency of nucleus A without dipole-dipole interaction.

In non-viscous solutions, the geometric factor $(3\cos^2\theta - 1)$ is averaged to zero by the isotropic molecular tumbling. Very narrow NMR lines are observed. In the situation of a powder sample, it has all the values of θ at random; hence, the corresponding

spectrum appears as a powder pattern. When the powder sample is turning around a conical path (Figure 3.1.1) the geometric factor $(3\cos^2\theta - 1)$ has the average value[109],

$$<3\cos^2\theta - 1> = 1/2 \; (3\cos^2\chi - 1)(3\cos^2\beta - 1) \qquad\qquad (3.1.2)$$

Here, χ is fixed for a single crystal but takes all possible values for a powder sample. β is the angle between the rotation axis and the applied magnetic field, which is the parameter one can adjust in an experiment. When $\beta = 54.7°$, $(3\cos^2\beta - 1) = 0$, and hence $<3\cos^2\theta - 1> = 0$ for all orientations. This situation is referred to as magic angle spinning (MAS) and $54.7°$ is called the magic angle. Ideally, magic angle rotation would remove the line broadening due to dipole-dipole interactions. However, in order to obtain a highly resolved solid-state NMR spectrum, the rotation rates must exceed the dipole-dipole coupling constants R (in Hz), which could be several tens of kHz and such speeds cannot be achieved in practice[109]. Thus, for dilute nuclei (^{13}C and ^{77}Se) high-power decoupling of protons is used to eliminate the line broadening due to heteronuclear dipole-dipole interactions. The high-power decoupling technique also increases the sensitivity for detecting the dilute nuclei (^{13}C and ^{77}Se).
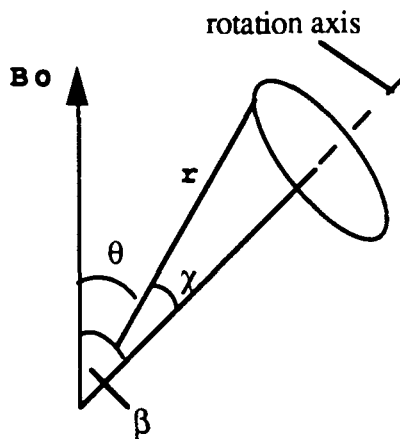
Figure 3.1.1. Macroscopic sample rotation at an angle to the applied magnetic field B_0, showing the geometric relationships involved.

43

Magic angle spinning can be used to eliminate the line broadening caused by chemical shielding anisotropy. In the general case, the observed shielding constant is denoted σ_{zz} and is expressed as[109]

$$\sigma_{zz} = \frac{1}{3} Tr\sigma + \sum_{j=i}^{3} (3\cos^2\theta_j - 1)\sigma_{jj} \qquad (3.1.3)$$

Where, Tr stands for the trace; θ_j is the angle between σ_{jj} and Bo; σ_{jj} are the principal components of the chemical shielding anisotropy tensor. The second term in Equation 3.1.3 contains a term similar to the dipolar interaction in Equation 3.1.1; therefore, this suggests that broadening by chemical shielding anisotropy can also be alleviated by the magic angle spinning technique.

Although in theory magic angle spinning can solve the broadening problems due to dipole-dipole interactions as well as chemical shielding anisotropy, in practice problems arise. In order to avoid interference from the spinning side-bands in the spectrum, the rate of spinning required has to be greater than the static bandwidth expressed in Hertz. In the case of ^{13}C NMR spectroscopy, the ^{13}C shielding anisotropy is 50 ppm for a sp^3 carbon and 100 ppm for a sp^2 carbon; therefore, a MAS speed of 3.7 kHz is needed for a B_0 of 3.5 T to eliminate the ^{13}C shielding anisotropy broadening. However, for ^{77}Se the shielding anisotropy of 1000 ppm requires a MAS speed 28 kHz for a B_0 of 3.5 T and this speed is experimentally unachievable.

When spinning rates are lower than the static spectrum width, the spinning side-bands would appear and cause difficulties in peak assignments. Two methods have been used to solve this difficulty. One is by running the spectrum at two different spinning rates. Since the position of spinning side-bands in the NMR spectrum is dependent on spinning rates, they can be distinguished from the resonance peak of the sample, which would remain at the same position for different spinning rates. Another method is called total suppression of sidebands (TOSS)[110]. The TOSS experiment is comprised of a

normal cross-polarization pulse sequence and a sequence of four 180º pulses. It is the additional sequence of four pulses that eliminates the sidebands, giving a spectrum with only isotropic peaks. However, care should be exercised when interpreting the peak intensities because TOSS experiments give spectra with distorted intensities.

3.1.2. Cross-Polarization

Both ^{13}C and ^{77}Se are nuclei of low sensitivity for NMR spectroscopy because of their low abundance, only 1.108% and 7.58% respectively[111]. Selenium-77 in particular has a detectability of only 5.2×10^{-4} relative to that of the proton[111]. Moreover, they have longer spin-lattice relaxation times than the proton does; consequently, the normal pulse methods are not very efficient and the sensitivity becomes a problem. This difficulty is solved by a technique called cross-polarization[109], in which the magnetization of dilute nuclei is derived from ^{1}H spins. We will use ^{13}C NMR spectroscopy as an example to describe the method.

The pulse sequence for cross-polarization, from a ^{1}H spin reservoir to ^{13}C spins, for solid-state NMR spectroscopy is depicted in Figure 3.1.2.

First, a 90º pulse is applied in the proton channel to bring the ^{1}H magnetization into the x-y plane, then the ^{1}H magnetization is spin-locked into the y direction of the rotating frame. At this point the radio-frequency in the ^{13}C channel is switched on, and the amplitude of the magnetic field is adjusted such that the Hartmann-Hahn matching condition is fulfilled;

$$\gamma_H B_{1H} = \gamma_C B_{1C} \qquad\qquad (3.1.4)$$

Here, γ_H, γ_C are the magnetogyric ratios for proton and carbon-13; B_{1H}, B_{1C} are r.f. magnetic fields for proton and carbon-13. Under this condition, the protons and carbons precess at equal rates in their respective rotating frames of reference and their effective

energies are comparable, thus allowing a rapid transfer of magnetization induced by the flip-flop term in the dipolar Hamiltonian.

From a thermodynamic perspective, the situation can be expressed[109] as

$$C_H B_o / T_L = C_H B_{1H} / T_s \qquad (3.1.5)$$

i.e.,

$$T_s = (B_{1H} / B_o) T_L \qquad (3.1.6)$$

Here, $C_H = 1/4 \gamma_H^2 (h/\pi)^2 N_H / k$; T_L is the lattice temperature; T_s is the spin temperature in the rotating frame; N_H is the total number of proton nuclei.. The term on the left of Equation 3.1.5 is the ^1H magnetization that is in equilibrium with the lattice in the laboratory frame; the term on the right is the magnetization in the rotating frame of reference. At this point the magnetization of the carbon nuclei in their rotating frame is zero, which is equivalent to an infinite spin temperature. Naturally, the spin energy will be repartitioned between the protons and the carbons to give a common spin temperature, T_s'.

$$C_H B_{1H}^2 / T_s = (C_H B_{1H}^2 + C_C B_{1C}^2) / T_s' \qquad (3.1.7)$$

Since the proton spins are abundant whereas ^{13}C spins are dilute, $C_c \ll C_H$, so T_s' $\approx Ts$. The protons lose a very small part of their total magnetization; the resulting magnetization of carbons is

$$M(^{13}C) = C_C B_{1C} / T_s' \approx C_C B_{1C} / T_s \qquad (3.1.8)$$

Substitution with Equations 3.1.4 and 3.1.6 gives

$$M(^{13}C) = C_C (\gamma_H / \gamma_C) B_o / T_L \qquad (3.1.9)$$

Comparison with the normal carbon magnetization at equilibrium in the laboratory frame

$$M_o(^{13}C) = C_C B_o / T_L \qquad (3.1.10)$$

shows a gain of $\gamma_H/\gamma_C \approx 4$. The enhanced magnetization in the carbon spins is detected by monitoring the FID following the cross-polarization.

The time duration of the pulse in the ^{13}C channel is called the contact time. Typical contact times are in the range of 0.5 - 5 ms. It is important to optimize the contact time, particularly for compounds that have low values of $T_{1\rho}(^1H)$ and only single contact operation is feasible.
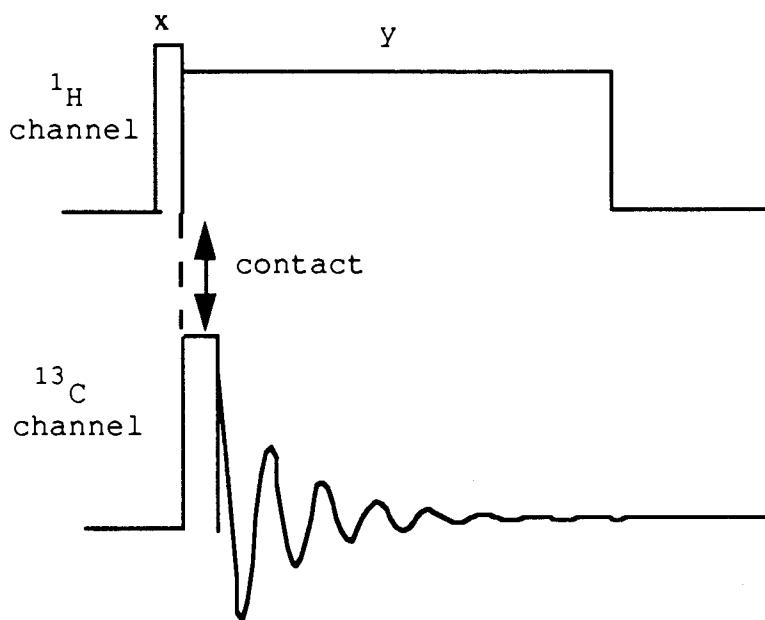
Figure 3.1.2. **The pulse sequence used to obtain cross-polarization from a proton spin reservoir to ^{13}C spins for solids.**

3.2. Results

The solid-state cross polarization-magic-angle spinning (CP-MAS) ^{77}Se and ^{13}C NMR spectral data for selected selenium coronands and dications, $8Se2(SO_3CF_3)_2$ and $16Se4(SO_3CF_3)_2$, are listed in Table 3.2.1.

Table 3.2.1. Solid-State NMR CP-MAS ^{77}Se and ^{13}C NMR Spectroscopic Data.

Compound	$\delta\ ^{77}Se^a$(rel int)	$\delta\ ^{13}C^b$(rel int)
16Se4(OH)$_2$	192 (1)	76.7 (1)
	155 ⎫	
	145 ⎬ (2)	37.7 (3)
9	134 ⎭	30.6 (2)
	113 (1)	
16Se4OH		71.7 (1)
	167 (1)	33.3 ⎫ (3)
10	131 (1)	33.0 ⎭
		28.7 (1)
		31.9 ⎫
	199 (1)	30.8 ⎬ (1,br complex)
16S2Se2	179 (1)	27.8 ⎭
	136 (1)	24.2 ⎫
11		22.1 ⎬ (1,br complex)
		19.2 ⎭
		204, 199
		192, 141
Dibenzo-14Se4		137, 130
		36.6
14		35.3
		28.2
12S3	277	33 (1)
18	196	27.3 (1)
16Se4(SO$_3$CF$_3$)$_2$	737 (1)	
	502 (1)	
32	419 (1)	
	173 (1)	
8Se2(SO$_3$CF$_3$)$_2$	810 (1)	52.7 (2)
	768 (1)	34.5 (1)
33		120 (br)

a. In ppm vs MeSeMe. *b.* In ppm vs TMS.
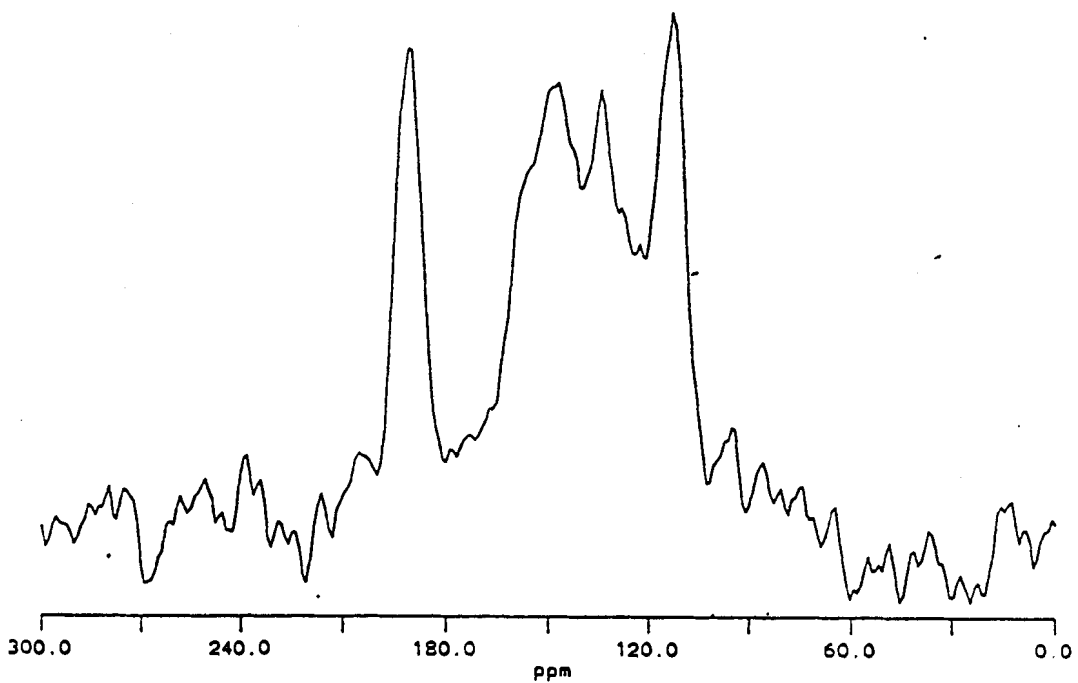
Figure 3.2.1. Solid-State CP-MAS ^{77}Se NMR spectrum of 16Se4(OH)$_2$ (9). The spectrum was recorded on a spectrometer operating at a field of 3.5 T.
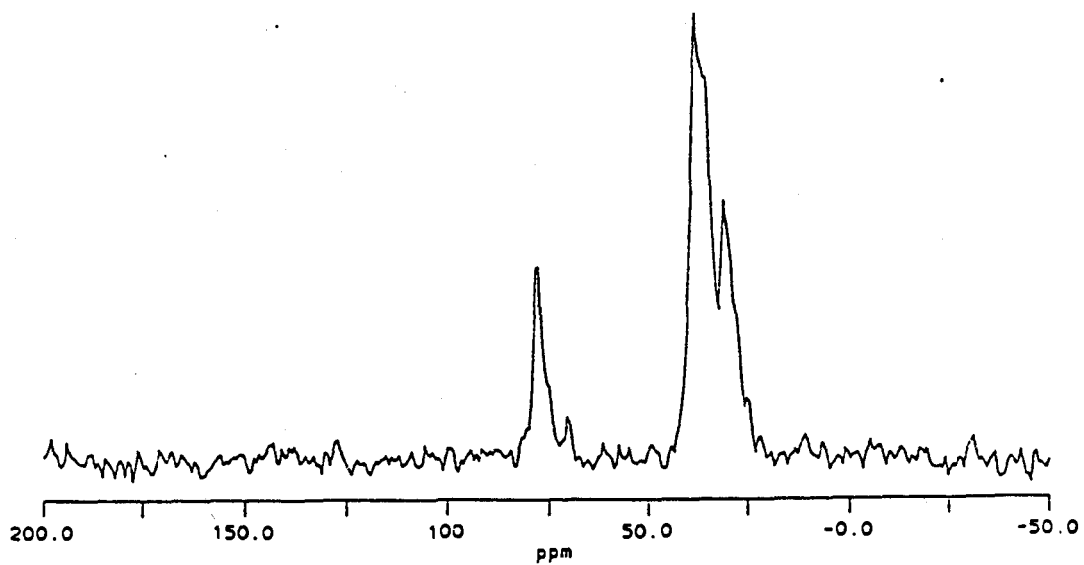
Figure 3.2.2. Solid-State CP-MAS ^{13}C NMR spectrum of 16Se4(OH)$_2$ (9). The spectrum was recorded on a spectrometer operating at a field of 3.5 T.
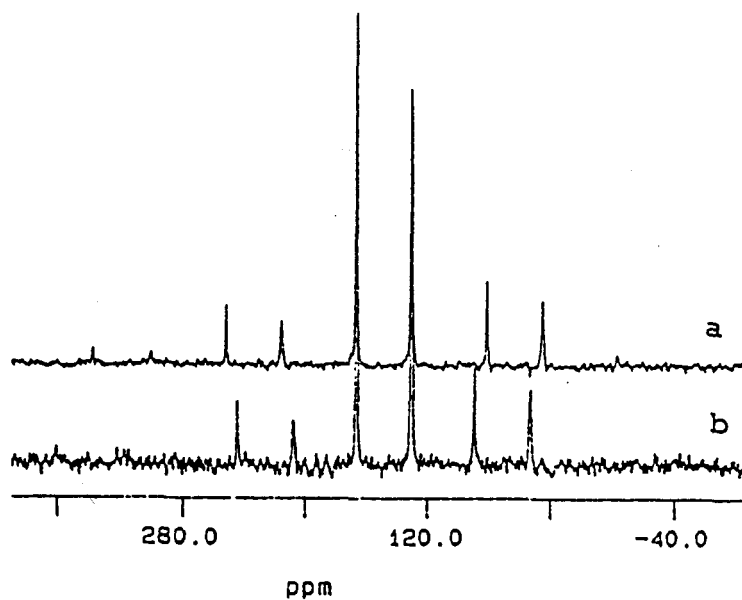
Figure 3.2.3. Solid-State CP-MAS ^{77}Se NMR spectra of 16Se4OH (10) at different spinning rates: (a) MAS rate = 2.4 kHz (b) MAS rate = 2.3 kHz. The spectra were recorded on a spectrometer operating at a field of 3.5 T.
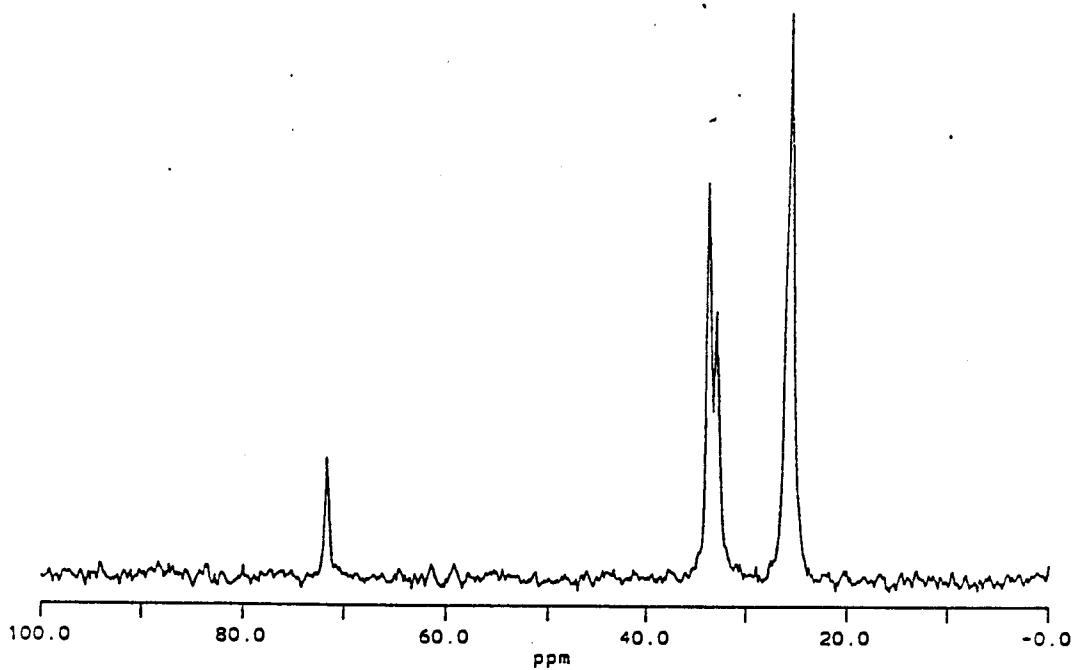
Figure 3.2.4. Solid-State CP-MAS ^{13}C NMR spectrum of 16Se4OH (10). The spectrum was recorded on a spectrometer operating at a field of 3.5 T.
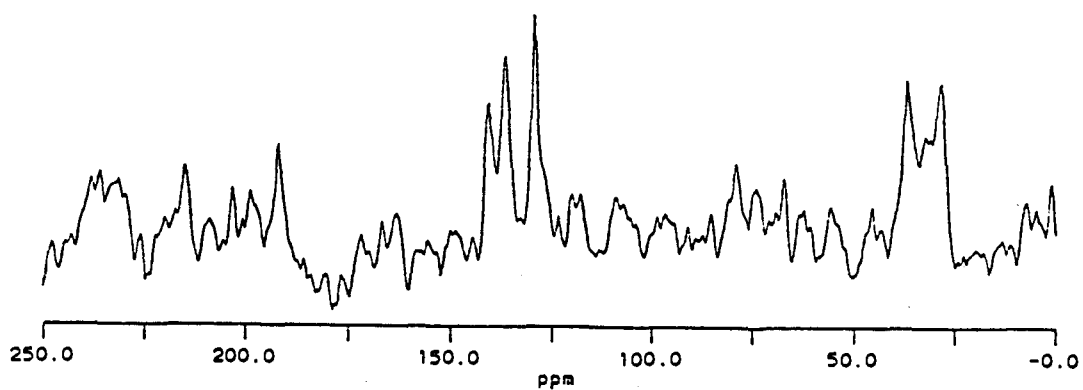
Figure 3.2.5. Solid-State CP-MAS ^{13}C NMR spectrum of dibenzo-
14Se4 (14). The spectrum was recorded on a spectrometer operating
at a field of 3.5 T.
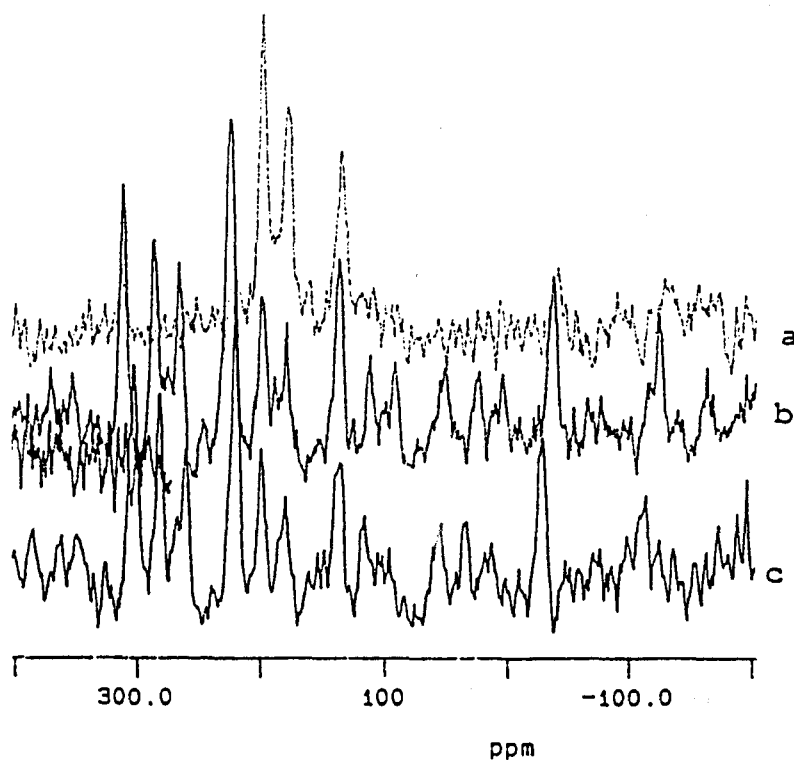
Figure 3.2.6. Solid-State CP-MAS ^{77}Se NMR spectra of 16S2Se2 (11). (a) TOSS spectrum; (b) MAS rate = 2.4 kHz; (c) MAS rate = 2.3 kHz. The spectra were recorded on a spectrometer operating at a field of 3.5 T.
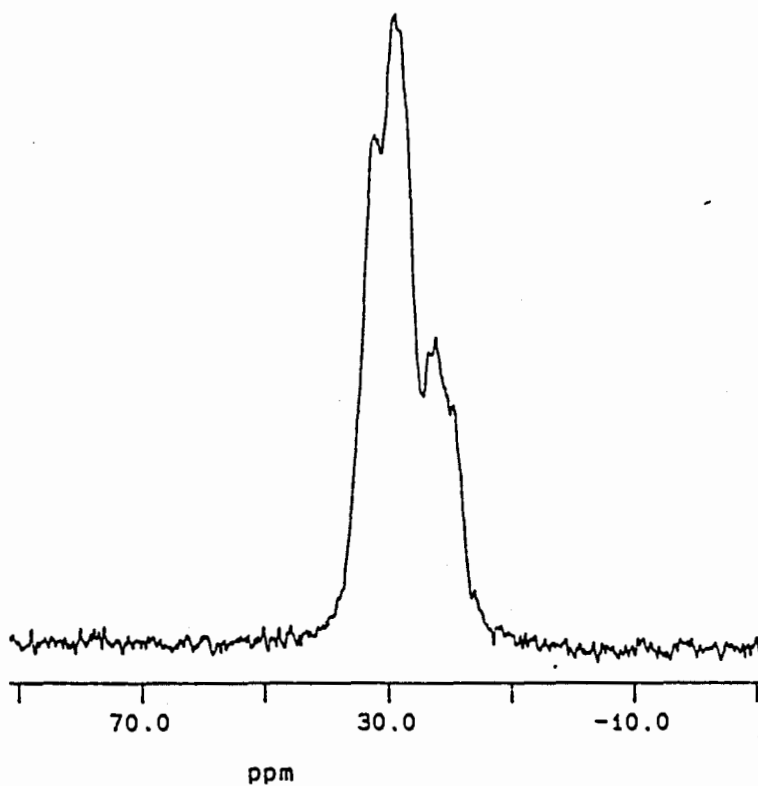
Figure 3.2.7. Solid-State CP-MAS ^{13}C NMR spectrum of 16S2Se2 (11). The spectrum was recorded on a spectrometer operating at a field of 3.5 T.
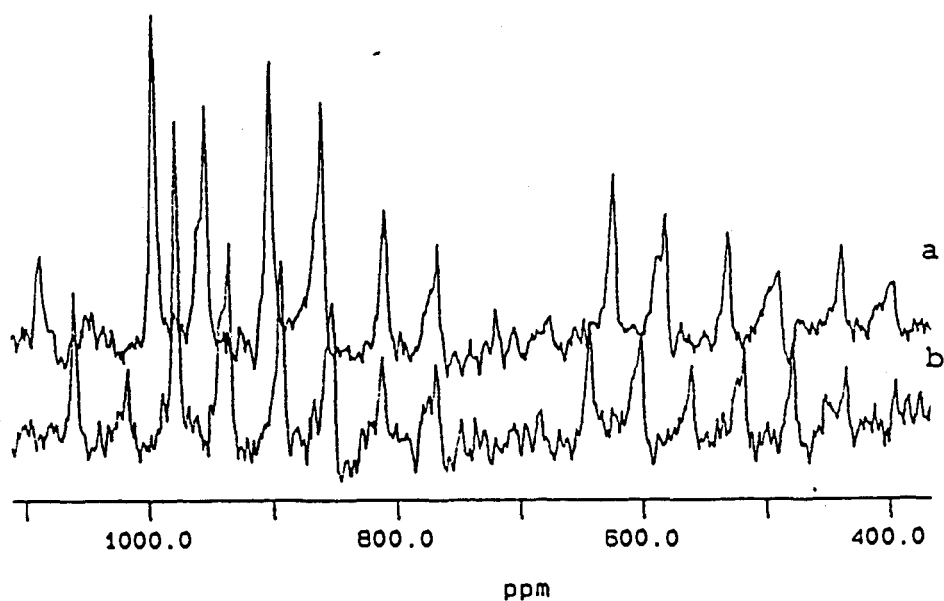
Figure 3.2.8. Solid-State CP-MAS ^{77}Se NMR spectra of 8Se2(SO_3CF_3)$_2$ (33) at different spinning rates. (a) MAS rate = 2.4 kHz; (b) MAS rate = 2.2 kHz. The spectra were recorded on a spectrometer operating at a field of 3.5 T.
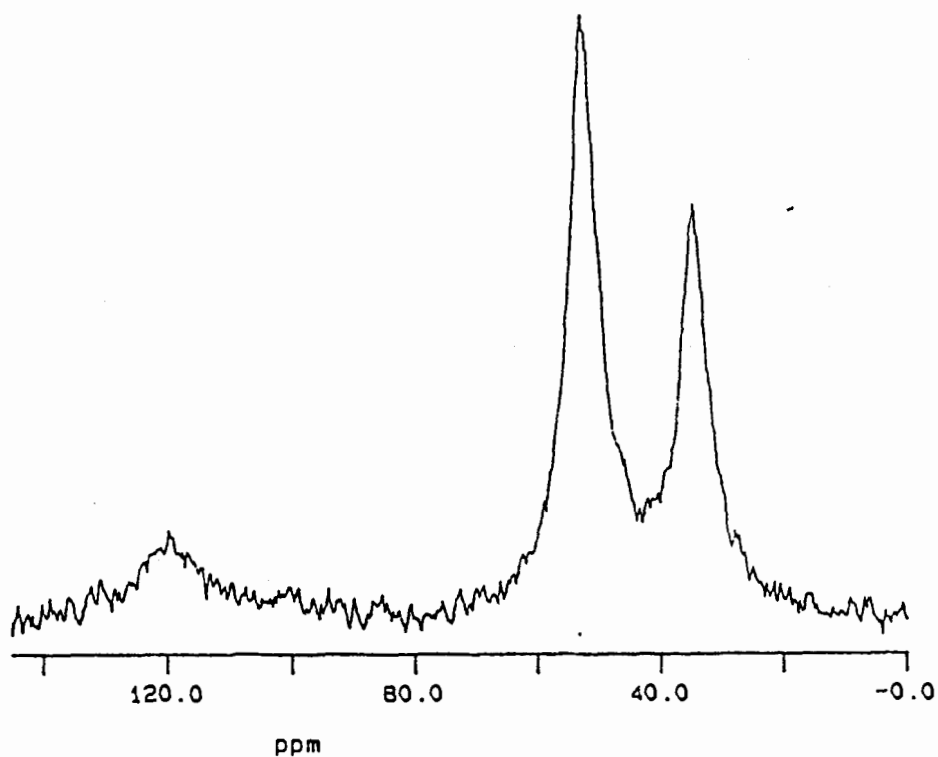
Figure 3.2.9. Solid-State CP-MAS ^{13}C NMR spectrum of 8Se2(SO$_3$CF$_3$)$_2$ (33). The spectrum was recorded on a spectrometer operating at a field of 3.5 T.
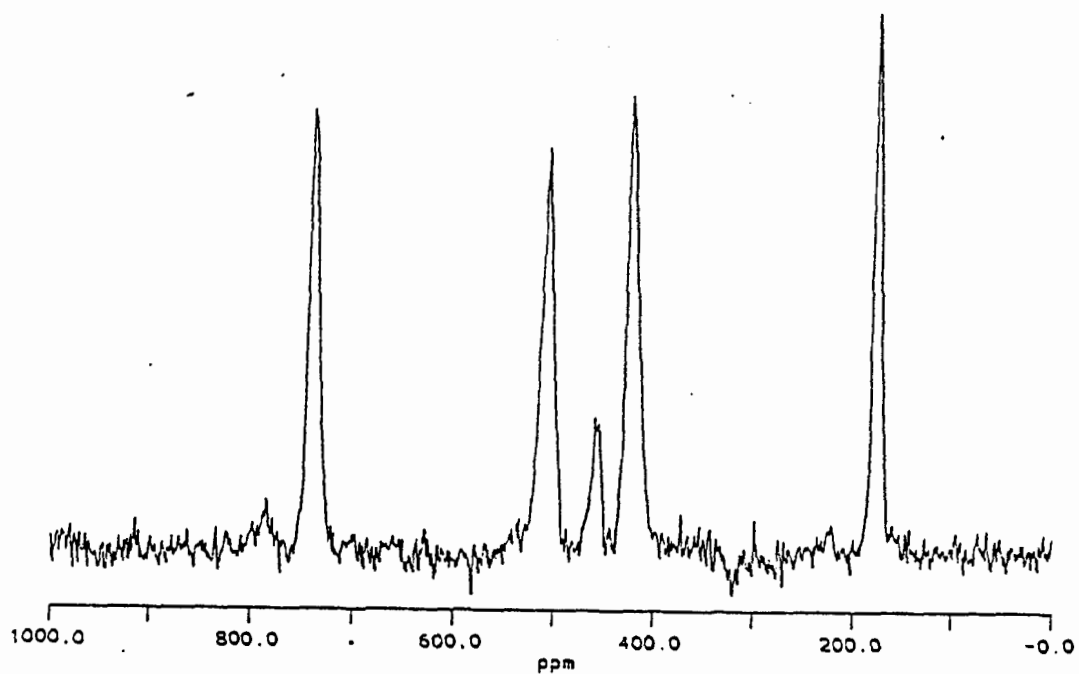
Figure 3.2.10. Solid-State CP-MAS ^{77}Se NMR spectrum of 16Se4-$(SO_3CF_3)_2$ (32). A small peak at about 450 ppm is a spinning sideband. The spectrum was recorded on a spectrometer operating at a field of 1.4 T.
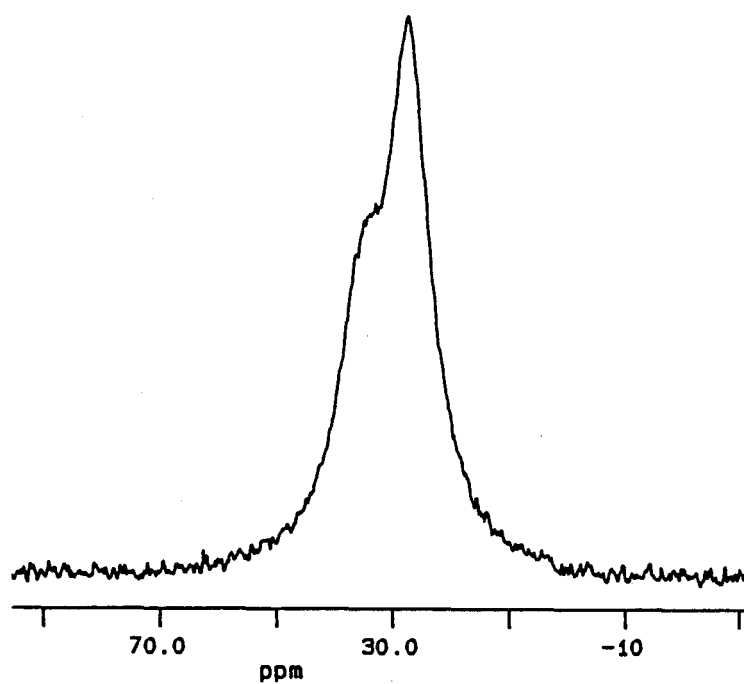
Figure 3.2.11. Solid-State CP-MAS ^{13}C NMR spectrum of 12Se3 (18). The spectrum was recorded on a spectrometer operating at a field of 3.5 T.
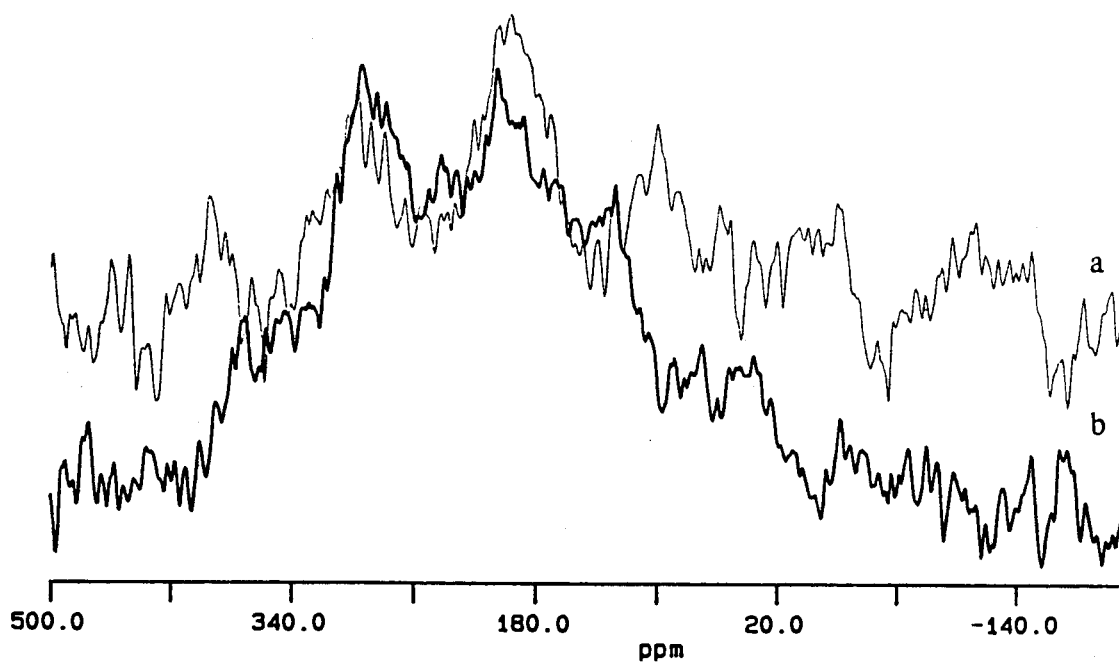
Figure 3.2.12. Solid-State CP-MAS ^{77}Se NMR spectra of 12Se3 (18) at different spinning rates. (a) MAS rate = 2850 Hz; (b) MAS rate = 2400 Hz. The spectra were recorded on a spectrometer operating at a field of 1.4 T.

3.3. Discussion

16Se4(OH)$_2$ (9). The CP-MAS solid-state ^{77}Se NMR spectrum of 16Se4(OH)$_2$ (9) (Figure 3.2.1) shows four resolved resonances with a relative area ratio of 1:2.2:1 if the middle two peaks were combined and treated as one peak. The CP-MAS ^{13}C NMR spectrum of 9 (Figure 3.2.2) shows three resolved peaks with relative intensity of 1:3:2. The peak at 76.7 ppm in the solid-state ^{13}C NMR spectrum is assigned to the carbons with hydroxyl groups. It is difficult to comment on other peaks because no x-ray structure is available for this molecule. In comparison with the solution ^{13}C NMR spectrum, the two spectra are similar, but the chemical shifts in the solid state spectrum are shifted about 6 ppm downfield. Also, in the solution ^{13}C NMR spectrum, the resonances of the CH$_2$ carbons α to the Se atoms are resolved into two sets; one is the resonance of the α-CH$_2$ in the trimethylene units with a hydroxyl substituent, the other is that of the α-CH$_2$ in the trimethylene units without a hydroxyl substituent.

16Se4OH (10). The CP-MAS ^{77}Se NMR spectrum of 16Se4OH (10) (Figure 3.2.3) shows two resonances with relative intensities of 1:1. According to the symmetry of 10 only two kinds of Se atoms that have different chemical environments are present. Hence, two resonances in the ^{77}Se NMR spectrum of 10 are consistent with the presence of one molecule in the asymmetric unit. The CP-MAS ^{13}C NMR spectrum of 10 (Figure 3.2.4) shows four peaks with relative intensities of 1:1.5:1.5:3. The resonance with chemical shift at 71.7 ppm is assigned to the carbon with a hydroxyl group substituent. Because no x-ray structure is available for this molecule, it is difficult to comment further.

Dibenzo-14Se4 (14). The CP-MAS ^{13}C NMR spectrum of dibenzo-14Se4 (14) (Figure 3.2.5) shows nine resonance peaks, accounting for nine unique carbon sites in the asymmetric unit. The spectrum is consistent with the assumption of one molecule with two-fold rotational symmetry in the asymmetric unit. Because the molecule does not

contain substituents that rotate freely and the relaxation time of the molecule is very long, it is difficult to run the MAS ^{77}Se NMR spectrum.

16S2Se2 (11). The CP-MAS ^{77}Se NMR spectrum of 16S2Se2 (11) (Figure 3.2.6) shows three resonance peaks with relative intensities of 1:1:1. By coincidence, the spectrum is consistent with the presence of one and a half molecules in the asymmetric unit. In fact, the crystal structure of **11** is disordered. Because of disorder the crystal has different Se/S arrangements, as shown in Figure 3.3.1. Therefore, Se atoms appear at all four positions and the structure displayed in x-ray crystallography is an average of these different conformers. In this case, six resonances would be observed in the ^{77}Se-MAS solid state NMR spectrum. It is necessary to point out that due to the procedure by which the coronand is synthesized, neither two Se atoms nor two S atoms would simultaneously appear in diagonal corner locations .
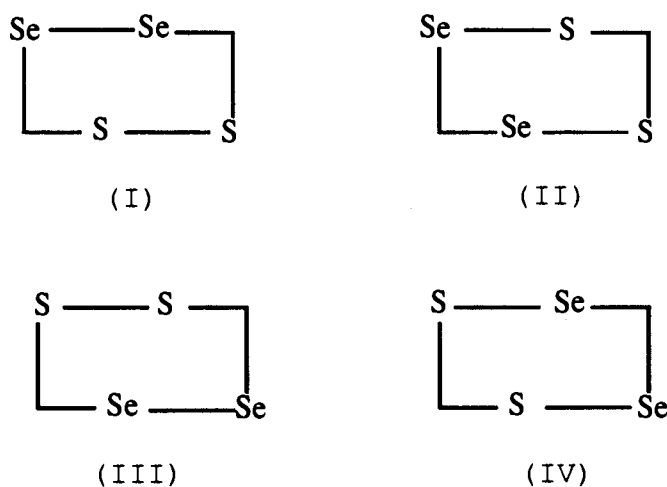
Figure 3.3.1. Different arrangements of Se and S atoms in 16S2Se2.

Unfortunately, the CP-MAS ^{13}C NMR spectrum shows two broad complex envelopes with only some resolved resonances, making it difficult to comment further.

12Se3 (18). The CP-MAS ^{13}C NMR spectrum (at ambient temperature) of 12Se3 (18) (Figure 3.2.11) shows two broadened resonance peaks with relative intensities

of 1:2, which is consistent with one molecule of **18** in the asymmetric unit. The broadness of the spectrum likely is the result of thermal motion. The x-ray structure of **18** (low temperature, 190 K) shows that the molecule has mirror symmetry. Even at this low temperature, the disorder results from the thermal motion of one trimethylene group. The CP-MAS ^{77}Se NMR spectrum of 12Se3 (**18**) (Figure 3.2.12) shows a very broad envelope with two resonances at 277 and 196 ppm, which are consistent with the presence of one molecule in the asymmetric unit. The broadness of this peak is probably due to the thermal motion of the molecule.

$8Se2(SO_3CF_3)_2$ (**33**). The CP-MAS ^{77}Se NMR spectrum of $8Se2(SO_3CF_3)_2$ (**33**) (Figure 3.2.8) shows two resonances in a 1:1 ratio. Severe spinning sidebands are concurrent with the NMR signals; however, the NMR signals are distinguishable from the sidebands by running the spectra at two different spinning speeds. The spectrum is consistent with the presumption that there are two independent Se atoms in an asymmetric unit as observed in the crystal structure of the **33** analog, $8S2(SO_3CF_3)_2$[112]. The recently published x-ray structure of $8Se2(SO_3CF_3)_2 \cdot CH_3CN$[113] also shows that there are two independent Se atoms in the asymmetric unit. The CP-MAS ^{13}C NMR spectrum of **33** (Figure 3.2.9) shows two strong resonances (34 and 52 ppm) in a ratio of 1:2, plus one weak resonance at low field (ca. 120 ppm). The weak resonance is assigned to the NMR resonance due to the trifluoromethyl group in $CF_3SO_3^-$. The peak at 52.7 ppm is assigned to the CH_2 group α to the Se atom; the positive charge on the selenium atoms causes a shift to lower field. The peak at 34.5 ppm is the resonance of the CH_2 β to the Se. Compared to the chemical shifts of $8Se2^{2+}$ from the solution ^{13}C NMR spectrum (36.11, 52.34 ppm), the solid-state ^{13}C chemical shifts are shifted downfield less than 2 ppm.

$16Se4(SO_3CF_3)_2$ (**32**). The CP-MAS ^{77}Se NMR spectrum of $16Se4(SO_3CF_3)_2$ (**32**) (Figure 3.2.10) shows four resonances of relative intensities 1:1:1:1. The spectrum is consistent with the presumption of one molecule in the asymmetric unit. We assigned the resonance at the lowest field to the Se(IV) atom because

63

it connects to two selenium atoms having positive charges. The upfield resonance peak is from the Se atom without a positive charge because the neutral selenium coronands have [77]Se chemical shifts around 150 ppm vs MeSeMe. The remaining two resonances are assigned to the Se atoms with positive charges.

CHAPTER IV
REDOX BEHAVIOR OF SELENIUM CORONANDS

4.1. Introduction

4.1.1. General

One of the unusual properties of selenium coronands is their susceptibility to oxidation. The chemically oxidized species of selenium coronands are radical cations, most of which are stable in solutions of dried and oxygen (O_2) free CH_3CN and can be detected by uv-visible spectroscopy. The study of selenium coronand redox behavior in this thesis comprises: 1) preparation of selenium coronand radical cations by chemical and electrochemical methods, 2) characterization of the radical cations by uv-visible spectroscopy and 3) investigation of redox properties of selenium coronands through various electrochemical techniques, the principles of which will be discussed shortly. For the selenium coronand 16Se4, chemical reactions that couple with the electrode reaction in solution have been pursued in order to obtain an insight into the reaction mechanism.

4.1.2. Preparation and Characterization of Selenium Coronand Radical Cations

The selenium coronand radical cations were prepared by two methods. The first method used nitrosyl tetrafluoroborate ($NOBF_4$) as an oxidizing agent to oxidize the corresponding coronand in CH_3CN through the following reaction

$$16Se4 + NOBF_4 \longrightarrow [16Se4^{+\cdot}]BF_4^- + NO\uparrow \qquad (4.1.1)$$
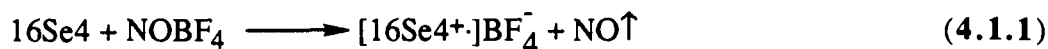
It is advantageous to use this reagent since the reduced product is a gas. Usually, a uv-visible spectrum was recorded immediately after the reactants were mixed.

The second method was to oxidize the selenium coronands electrochemically, i.e., to oxidize the selenium coronands through electrolysis. When the electrochemical method was used we utilized a technique that incorporates the uv spectroscopic method into the electrochemical method, which is termed spectroelectrochemistry. An optically transparent Pt electrode, the working electrode, is placed in a uv cell that is in the uv instrument beam path; therefore, the oxidized species produced on the electrode surface can be studied by uv spectroscopy.

In spectroelectrochemistry, when a potential step that is predetermined by cyclic voltammetry is applied on the electrodes, a flux of oxidized species is generated. Under the diffusion controlled condition and without further chemical reaction involved in the solution after oxidation, the relationship between absorbance of the oxidized species and the time is described by[114]

$$A = \frac{2\varepsilon_O C_O^* D^{\frac{1}{2}} t^{\frac{1}{2}}}{\pi^{\frac{1}{2}}} \qquad (4.1.2)$$

Where, ε_O is the molar absorptivity; C_O^* is the concentration of the substrate; D is the diffusion coefficient; t is the time. Plotting absorbance vs. the square root of time should give a straight line.

4.1.3. Cyclic Voltammetry

Cyclic voltammetry is the most powerful tool for examining an electroactive chemical substance or material. It is considered to be the electrochemical equivalent of spectrophotometry[115]. Cyclic voltammetry provides a means to observe the redox behavior rapidly over a wide potential range with ease; therefore, it is extensively applied in inorganic chemistry, organic chemistry and biochemistry[116]. Voltammetry is a term for experiments involving imposition of a potential on an electrode and measurement of the

resulting current. In cyclic voltammetry, the potential is scanned linearly from an initial potential towards either the anodic direction or cathodic direction, depending on the circumstance, then back to the initial potential. At the same time, the variation of current is recorded on a x-y plotter or an oscilloscope as a function of the scanning potential. One can vary rates of scanning or concentrations of substrate or both in order to obtain a full picture of the electrochemical properties of the substrate. Parameters such as peak current, peak potentials and the peak potential separations are used as criteria to determine the reversibility of the redox reaction.

Application of a linear potential sweep to a system where the electrode reaction is reversible should produce a pair of symmetric waves. The anodic and cathodic peak potentials as well as their separation should be independent of scan rates. The diagnostic criteria for reversibility of electrode reactions and the relationship of peak current with scan rate and concentrations of electroactive species at 25 $^{\circ}$C are listed in the following equations[117].

$$\Delta E_p = E_p^A - E_p^C = 59/n \text{ mV} \tag{4.1.3}$$

$$|E_p - E_{p/2}| = 57/n \text{ mV} \tag{4.1.4}$$

$$|i_p^A/i_p^C| = 1 \tag{4.1.5}$$

$$i_p = 2.69 \times 10^5 \, n^{3/2} \, A \, C_O^* D^{1/2} \upsilon^{1/2} \tag{4.1.6}$$

The half-wave potential $E_{1/2}$ is defined as

$$E_{1/2} = \frac{E_{pa} + E_{pc}}{2} \tag{4.1.7}$$

For a reversible couple, $E_{1/2}$ is centered between E_{pa} and E_{pc} and is related to the formal potential[114] $E^{o'}$ by

$$E_{1/2} = E^{o'} + \frac{RT}{nF} \ln(D_R/D_O)^{1/2} \tag{4.1.8}$$

Usually, $D_R = D_0$; hence, $E_{1/2} = E^{0'}$. Here, i_p is the peak current; $E_{p/2}$ is the half peak potential, that is, the potential at $1/2$ i_p; E_p is the peak potential, superscripts a and c denote anodic and cathodic events; υ is the potential sweep rate; A is the electrode area; D is the diffusion coefficient of the electroactive species and the subscripts O and R denote oxidation and reduction respectively; C_0 is the concentration of the electroactive species in bulk solution; n is the number of electrons involved in the electron transfer reaction.

Quasi-reversible reactions yield voltammograms with peak potential separations larger than 59 mV/n at 25 °C; the peak potentials as well as peak potential separations are scan rate dependent. When a reaction is totally irreversible, the peak of the reversal scan disappears; thus, only one peak should be observed.

4.1.4. Convolution Transformation

There is an alternative method of analyzing cyclic voltammetric data called convolution voltammetry[118-120] or semi-integral analysis[121,122]; which, in fact, are two equivalent approaches[114]. Instead of using parameters such as peak potentials and peak currents for analysis of cyclic voltammograms as described before, convolution voltammetry uses all the data contained in the cyclic voltammogram by transforming the whole curve prior to analysis. With the increasing accessibility of micro-computers, this method has become more and more common[123,124].

The transformation of cyclic voltammetric data is based on the convolution principle. Under semi-infinite linear diffusion conditions, the solution of the diffusion equation yields the following expression[121,122],

$$C_o(0,t) = C_o^* - \frac{1}{nFAD_o^{1/2}} \left[\frac{1}{\pi^{1/2}} \int_0^t \frac{i(u)}{(t-u)^{1/2}} du \right] \qquad (4.1.9)$$

where $C_o(0,t)$ is the concentration of the electroactive species O at the surface of the electrode; C_o^* is the initial concentration of species O; n is the number of electrons involved

in electron transfer; A is the area of the electrode; D_o is the diffusion coefficient and F is the Faraday constant. The expression is valid for any electrochemical technique. The term inside the bracket (Eq 4.1.9) is the convolution transform of i(t) which may be defined as

$$I(t) = \frac{1}{\pi^{1/2}} \int_o^t \frac{i(u)}{(t - u)^{1/2}} du \qquad (4.1.10)$$

$$C_o(0,t) = C_o^* - \frac{I(t)}{nFAD_o^{1/2}} \qquad (4.1.11)$$

Under purely diffusion-controlled conditions, $C_0(0,t) = 0$, I(t) reaches its maximum, I_l, given by

$$I_l = nFAD_o^{1/2}C_o^* \qquad (4.1.12)$$

The maximum value of this function, I_l, is independent of the manner in which the potential is obtained. The limiting value, I_l, is also independent of the reversibility of the electrode reaction. Thus,

$$C_o(0,t) = \frac{[I_l - I(t)]}{nFAD_o^{1/2}} \qquad (4.1.13)$$

and the concentration of the reduced species

$$C_R(0,t) = \frac{I(t)}{nFAD_o^{1/2}} \qquad (4.1.14)$$

If the electron transfer reaction is Nernstian, there is the expression[114]

$$E = E_{1/2} + \frac{RT}{nF} \ln \frac{I_l - I(t)}{I(t)} \qquad (4.1.15)$$

A plot of $\log \frac{I_l - I(t)}{I(t)}$ vs E will result in a straight line with a slope of 0.059/n at 25 °C.

4.1.5. *Controlled Potential Bulk Electrolysis*

Controlled potential bulk electrolysis or coulometry is widely used to determine the overall number of electrons involved in an electrode process.

$$Q = \int_0^{\infty} i_t dt = nFC^{\circ}V \tag{4.1.16}$$

Here, Q is the charge passed in electrolysis; V is the volume of electrochemical cell; i_t is the current; the rest of the terms are as defined before. Coulometry is also used to prepare a sufficient quantity of the reaction products. There are several aspects in which controlled electrolysis differs from cyclic voltammetry. In controlled potential electrolysis a large area electrode is used to ensure large changes in bulk solution concentration and the solution is stirred during electrolysis. Conventionally, electrolysis is conducted in a divided two-compartment cell in which the working electrode compartment is separated from the counter-electrode by means of a glass frit. Then, a known volume of solution containing a known concentration of electroactive species is introduced in the working electrode cell and a potential applied to the working electrode is set and maintained at a value at which the reaction under investigation proceeds at a mass transport limited rate. The potential usually is predetermined by cyclic voltammetry. The process of electrolysis is monitored through the current and its integral changes with time; usually, the electrolysis is terminated when the current drops to about 1% of its initial value.

4.2. Results

4.2.1. UV-visible Spectroscopy of Selenium Coronands

4.2.1.1. Radical Cations of Selenium Coronands Produced Chemically

Mixing of $NOBF_4$ and the given selenium coronand was performed by injecting an $NOBF_4$ solution with a syringe into the deoxygenated selenium coronand solution being stirred in a uv-cell. Recording of uv-visible spectroscopic measurements was started as soon as the $NOBF_4$ solution was added to the coronand solutions. The uv spectroscopic scanning was repeated at intervals based on the type of selenium coronand.

Each particular coronand radical cation had a characteristic absorption wavelength and the intensity of absorption increased quickly in about 2 minutes after $NOBF_4$ was added, indicating formation of the corresponding selenium coronand radical cation. After 2 min. the growth slowed down substantially.

Upon mixing with $NOBF_4$, 14Se4 (**13**), 12Se3 (**18**), 16Se4 (**8**), 16S2Se2 (**11**) and 16Se4(OH)$_2$ (**9**) gave rise to yellow colored solutions and the absorbance maxima of the solutions appeared at 274, 282, 320, 300 and 328 nm, respectively (see Table 4.2.1). The species were believed to be radical cations, because the CH_3CN solution of $NOBF_4$ and 16Se4 was ESR active.

Adding an $NOBF_4$ solution to coronands 8Se2 (**16**) and 24Se6 (**15**) in CH_3CN yielded yellow solutions. The absorbance maxima for the corresponding radical cations appeared at 428 and 318 nm respectively. It was very interesting that the absorption peaks of **16** and **15** decayed quickly over time, while the sulfur counterpart of 8Se2 was quite stable[87,125].

Coronand 12Se4 (**20**) and dibenzo-14Se4 (**14**) were not apparently oxidized by $NOBF_4$, because on mixing with $NOBF_4$ no new absorption peaks were observed.

The uv-visible absorption peak-positions of radical cations made from selenium coronands are shown in Table 4.2.1. It was interesting that the uv-visible absorption peak-positions of the radical cations made from selenium coronands 16Se4 and 16S2Se2 were found to be dependent on initial coronand concentrations.

Concentration Effects

In an experiment where the concentrations of 16Se4 and $NOBF_4$ were both 5.3×10^{-4} M, the absorption peak appeared at 320 nm, the intensity of which was growing until it reached a maximum. Subsequently, the peak decreased, and a new peak appeared at 256 nm. There was an isosbestic point at around 290 nm, indicating that there were at least two species present in the solution, and that the two species were interchangeable.

Further experiments revealed that peak variation was concentration dependent. $NOBF_4$ $(2 \times 10^{-5}$ M) in CH_3CN was added separately to 16Se4 solutions of concentrations: 1.87×10^{-4}, 2.81×10^{-4}, 3.75×10^{-4}, 4.68×10^{-4} and 5.62×10^{-4} M (Table 4.2.2). After the $NOBF_4$ was added, uv-visible spectra were recorded repetitively as a function of time for each concentration. At the lowest concentration of 16Se4 (1.87×10^{-4}), a 256 nm peak was observed, but the peak at 320 nm was almost absent (Figure 4.2.1). The absorption peak at 320 nm became more and more significant as the 16Se4 concentration increased. At the largest concentration, the peak at 320 nm first rose to a maximum and then fell; concurrently the 256 nm peak began to rise (Figure 4.2.2).

Table 4.2.1. Absorbance Maxima of Selenium Coronand Radical Cations

Parent Compound	Conc. of Parent Compound (M)[a]	Conc. of NOBF$_4$ (M)	λ_{max}(nm)
16Se4	5.60×10^{-4}	2.05×10^{-5}	322, 256
	1.87×10^{-4}	2.05×10^{-5}	256
16S2Se2	1.30×10^{-4}	4.0×10^{-5}	310, 274
	6.50×10^{-5}	4.0×10^{-5}	274
16Se4(OH)$_2$	2.00×10^{-4}	4.0×10^{-5}	332
	8.00×10^{-5}	4.0×10^{-5}	332
24Se6	1.77×10^{-4}	4.0×10^{-5}	320
	7.07×10^{-5}	4.0×10^{-5}	320
14Se4	9.87×10^{-4}	b	258
	9.87×10^{-5}	b	258
12Se3	1.27×10^{-4}	4.0×10^{-5}	280
	8.47×10^{-4}	4.0×10^{-5}	280
8Se2	4.67×10^{-4}	2.60×10^{-5}	420
	4.67×10^{-5}	2.60×10^{-5}	264
8Se2OH	1.62×10^{-4}	2.60×10^{-5}	404
	8.08×10^{-5}	2.60×10^{-5}	404

a. In CH$_3$CN solution.

b. Oxidized on an optically transparent electrode.

Table 4.2.2. Concentration Effects on the 16Se4 Radical Cation Absorbance Bands

[16Se4] (M)	[NOBF$_4$] (M)	Absorbance[a] (λ_{max} = 320 nm)	Absorbance[a] (λ_{max} = 256 nm)
1.87×10^{-4}	2.05×10^{-5}	0.024	0.22
2.81×10^{-4}	2.05×10^{-5}	0.036	0.21
3.75×10^{-4}	2.05×10^{-5}	0.065	0.32
4.68×10^{-4}	2.05×10^{-5}	0.11	0.34
5.62×10^{-4}	2.05×10^{-5}	0.21	0.45

a. The maximum value among the data.
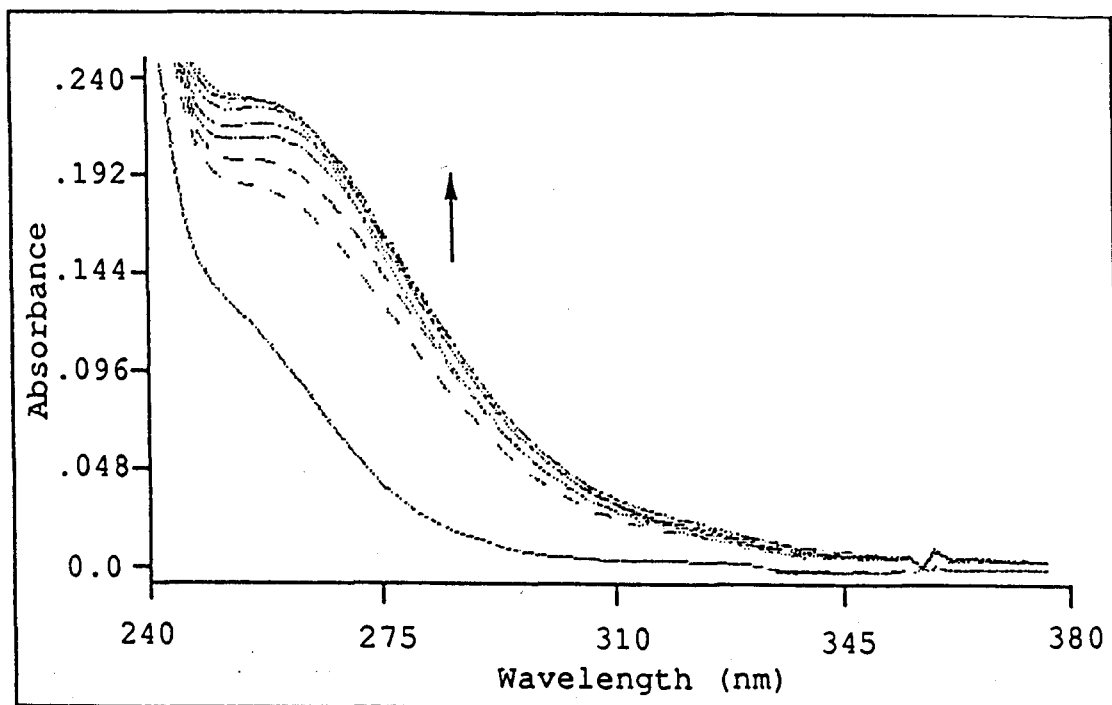
Figure 4.2.1. UV-visible spectra of 16Se4 (8) radical cation recorded as a function of time. The radical cation was prepared by mixing 16Se4 with $NOBF_4$ in CH_3CN: $[NOBF_4] = 2.05 \times 10^{-5}$ M; $[16Se4] = 1.87 \times 10^{-4}$ M. The spectra were taken at an interval of 300 seconds. The trace at the bottom is the original spetrum of 16Se4.
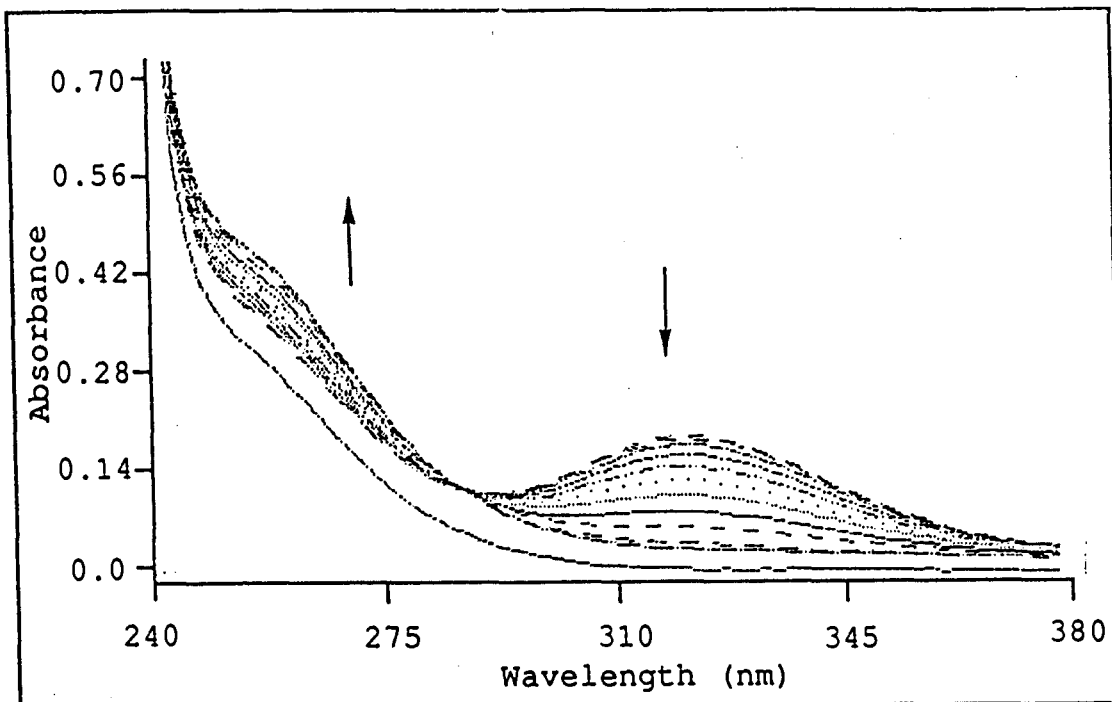
Figure 4.2.2. UV-visible spectra of 16Se4 (8) radical cation recorded as a function of time. The radical cation was prepared by mixing 16Se4 with NOBF$_4$ in CH$_3$CN: [NOBF$_4$] = 2.05 × 10^{-5} M; [16Se4] = 5.62 × 10^{-4} M. The spectra were taken at an interval of 300 seconds. The trace at the bottom is the original spetrum of 16Se4.

4.2.2. *Electrochemistry of Selenium Coronands*

4.2.2.1. *Cyclic Voltammetry*

16Se4 (8). A typical cyclic voltammogram of **8**, which was measured from a single scan with a platinum working electrode in a CH_3CN solution containing 1 mM of **8** (0.1 M) tetraethylammonium perchlorate (TEAP) as electrolyte, is shown in Figure 4.2.3

The initial potential was 0 V vs SCE which was chosen to avoid any electrolysis of 16Se4 (**8**) when the electrode was switched on. The potential was scanned linearly in the anodic direction as indicated by the arrow (Figure 4.2.3). When the potential was sufficiently positive to oxidize **8**, the anodic current increased, indicating that there was an electrode process corresponding to

$$16Se4 - e \longrightarrow 16Se4^{+\cdot} \qquad (4.2.1)$$

and the concentration of 16Se4 was subsequently diminished at the electrode surface. After passing the peak potential, the current dropped because the concentration of 16Se4 (**8**) at the electrode surface was depleted; however, the concentration of $16Se4^{+\cdot}$ at the electrode surface reached its maximum. As the potential scan continued towards the anodic direction, a second increase of current was observed, indicating a second electrode oxidation process corresponding to

$$16Se4^{+\cdot} - e \longrightarrow 16Se4^{2+} \qquad (4.2.2)$$

The potential scan direction was switched to the cathodic direction at 1.8 V. When the potential became negative enough, the $16Se4^{2+}$ that had been accumulating adjacent to the electrode was reduced by the electrode process

$$16Se4^{2+} + e \longrightarrow 16Se4^{+\cdot} \qquad (4.2.3)$$

76

This process caused the cathodic current to increase until the maximum was reached. At the same time, the concentration of $16Se4^{2+}$ adjacent to the electrode was decreased by the process; therefore, the cathodic current also began to decrease after the current maximum. As the potential was scanned towards the cathodic direction, the accumulated species $16Se4^{+\cdot}$ at the surface of the electrode was reduced through the electrode process

$$16Se4^{+\cdot} + e \longrightarrow 16Se4 \qquad\qquad (4.2.4)$$

The separations between anodic and cathodic peak potentials were scan rate dependent; the peak separations increased as the scan rate increased. This indicates that the electrode process is a quasi-reversible process. As scan rates exceeded 200 mV/s the second electrode redox reaction that relates the redox pair $16Se4^{2+}/16Se4^{+\cdot}$ became irreversible, as manifested by the disappearance of the second cathodic peak on the returning scan. On the other hand, slow scan rates also altered the appearance of the cyclic voltammogram. At the scan rate of 5 mV/s, the second oxidation peak as well as the cathodic peak disappeared; the current plateaued after the first oxidation peak, but the first cathodic peak was still observed on the returning scan. This may be the result of complications due to chemical reactions in solution.

Measurement of the cathodic current peak in the reversal scan is usually difficult because of the difficulty in determining the base line. Thus, the cathodic current peak was measured according to the method of Nicholson and Shain[120] in which cathodic peaks were measured to the extension of the anodic curve, correcting for the charging and the residual current. The ratio of cathodic and anodic currents was less than unity for the $16Se4^{2+}/16Se4^{+\cdot}$ pair, which also indicated a quasi-reversible system. Plotting i_{a1} or i_{a2} versus $\upsilon^{1/2}$ gave rise to straight lines, suggesting that the electrode reactions were diffusion controlled.

Table 4.2.3. Cyclic Voltammetric Data of Selenium Coronands (8, 9 and 18)[a,c].

υ	$E_{1/2}^{1}$ [b]	E_{pa1}	E_{pc1}	ΔE_{p1}	$E_{1/2}^{2}$ [b]	E_{pa2}	E_{pc2}	ΔE_{p2}
				16Se4 (8)				
10	0.569	0.638	0.500	.138	1.47	1.53	1.41	.12
20	0.563	0.650	0.475	.175	1.47	1.54	1.39	.15
50	0.544	0.663	0.425	.238	1.45	1.55	1.35	.20
100	0.519	0.675	0.363	.312	1.43	1.58	1.28	.30
200	0.545	0.789	0.300	.489	1.39	1.59	1.18	.41
				16Se4(OH)$_2$ (9)				
10	0.576	0.813	0.338	0.475	1.41	1.52	1.31	0.2000.
20	0.576	0.838	0.313	0.525	1.42	1.54	1.31	2300.37
50	0.540	0.828	0.215	0.577	1.38	1.57	1.19	90.600/
100	0.531	0.848	0.213	0.634	1.34	1.64	1.04	
200	0.525	0.888	0.163	0.725	/	1.64	/	
				12Se3 (18)				
20	.690	.800	.581	.22	1.69	1.80	1.58	.22
50	.680	.802	.550	.25	/	1.80	/	/
100	.680	.831	.519	.31	/	1.83	/	/
200	.680	.836	.483	.35	/	1.85	/	/

a. Measured with a stationary platinum electrode.

b. $E_{1/2}$ was obtained by taking $(E_{pa} + E_{pc})/2$.

c. Potential relative to SCE.

16Se4(OH)$_2$ (9). The cyclic voltammogram of **9** showed two quasi-reversible electrode redox reactions; each one involved a one electron transfer process as depicted in the following equations.

$$16Se4(OH)_2 - e \longrightarrow 16Se4(OH)_2^{+\cdot} \tag{4.2.5}$$

$$16Se4(OH)_2^{+\cdot} - e \longrightarrow 16Se4(OH)_2^{2+} \tag{4.2.6}$$
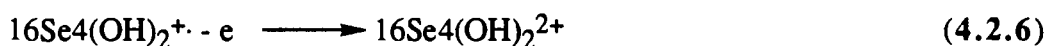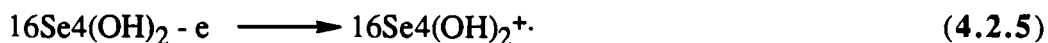
Similar to 16Se4 (**8**), the separation of anodic and cathodic peak potentials was dependent on scan rates so that increased scan rate caused increased separation between the anodic and cathodic peak potentials. As the scan rates increased, the second cathodic peak

in the returning scan became broader and broader and disappeared when the scan rate was increased to 200 mV/s.

12Se3 (18). The cyclic voltammogram of **18** was similar to that of 16Se4 (**8**), although the structure of **18** is quite different from that of 16Se4. However, the second reduction ($12Se3^{2+}/12Se3^{+\cdot}$) process became irreversible even when the scan rate was 50 mV/s, which was evidenced by the disappearance of the second cathodic peak in the returning scan. Also, the second redox potential ($E_{1/2}$) was higher than that of 16Se4 (**8**) and 16Se4(OH)$_2$ (**9**). The cyclic voltammetric data of these three selenium coronands are listed in Table 4.2.3.

8Se2 (16) and 8Se2(Me)$_2$ (40). Cyclic voltammograms of these two selenium coronands were almost the same; both showed only one pair of redox waves. In Figure 4.2.4 a cyclic voltammogram of 8Se2(Me)$_2$ (**40**) is shown. However, the results of a coulometric study indicated that the redox process on the electrode was a two-electron transfer process. Although the electrode process was quasi-reversible according to these criteria (in Eq 4.13-4.16), they gave the most reversible appearance — $\Delta Ep < 90$ mV at scan rate of 20 mV/s and $i_c/i_a = 1$ — among the cyclic voltammograms of selenium coronands examined. Furthermore, they had the lowest redox potentials by comparison to other selenium coronands; $E_{1/2}$ was 0.374 V and 0.408 V vs SCE for 8Se2 (**16**) and 8Se2(Me)$_2$ (**40**), respectively. The $E_{1/2}$ of 8Se2(Me)$_2$ (**40**) was higher than that of 8Se2 (**16**).

8Se2OH (17). The cyclic voltammogram of **17** showed a single pair of redox waves although the coulometric result suggested that the total process was a two-electron transfer process. Compared with 8Se2 (**16**) or 8Se2(Me)$_2$ (**40**), the oxidation wave of 8Se2OH (**17**) was broader. The separation of peak potentials was also larger for **17**. Moreover, $E_{1/2}$ of 8Se2OH (0.578 V vs SCE) was also higher than that of 8Se2 (**16**).

Cyclic voltammograms (Figure 4.2.5) obtained at various scan rates indicated that there were complications arising from chemical reactions in solution. At a scan rate of 200

mV/s, the oxidation wave became broadened as if it consisted of two waves. It is possible that the broadened wave resulted from different conformations of 8Se2OH in solution. When the scan rate was 20 mV/s, the oxidation wave had an onset at 0.5 V and reached a maximum at 0.688 V. However, the current did not diminish but rather leveled off when the scan passed the peak potential. The cyclic voltammogram at this point had the appearance of a steady state voltammogram. The cathodic wave on the reverse scan was well behaved. The i_c/i_a ratio was larger than unity for every scan rate. This indicated that the starting material was generated in solution by the chemical reaction 4.2.9.

$$8Se2OH - e \longrightarrow 8Se2OH^{+\cdot} \qquad (4.2.7)$$

$$8Se2OH^{+\cdot} - e \longrightarrow 8Se2OH^{2+} \qquad (4.2.8)$$

$$8Se2OH^{+\cdot} + 8Se2OH^{+\cdot} \longrightarrow 8Se2OH + 8Se2OH^{2+} \qquad (4.2.9)$$

14Se4 (13). The cyclic voltammogram of **13** (Figure 4.2.6) showed one pair of redox waves and the cathodic current peak on the reverse scan was apparently smaller than the anodic current peak. Peak potential separation was very large (about 700 mV) and the i_c/i_a ratio was less than unity. All these observations suggested a slow electrode process.

Table 4.2.4. Anodic Current Peak Potential of 14Se4 (13) at Different Initial Concentrations and Different Scan Rates

14Se4 (13)	E_{pa} (Volt vs SCE)[a]					
Conc. (M)	10 (mV/s)	20 (mV/s)	50 (mV/s)	100 (mV/s)	200 (mV/s)	500 (mV/s)
1.29×10^{-3}	0.858	0.868	0.878	0.868	0.908	0.938
2.55×10^{-3}	0.838	0.868	0.888	0.888	0.868	0.888
3.59×10^{-3}	0.838	0.858	0.878	0.888	0.928	0.948
4.28×10^{-3}	0.776	0.868	0.858	0.868	0.878	0.918

a. Measured with a stationary platinum electrode in CH_3CN with 0.1 M tetraethylammonium perchlorate electrolyte.

Increasing scan rates caused increased separation of peak potentials, i. e., the anodic peak potential shifted to the more positive direction whereas the cathodic peak potential shifted towards the more negative direction. When the potential scan was performed in a repetitive fashion, after the first scan that gave the normal cyclic voltammogram, the anodic peak potential shifted towards the more negative direction and the anodic current peak became sharper and greater. Meanwhile, the cathodic current peak shifted towards the more negative direction and became greater. However, this abnormality was eliminated by cleaning the surface of the working electrode with Al_2O_3 powder and wiping with a tissue paper after each scan. Evidently, some oxidized species that adsorbed on the working electrode was responsible for the observed behavior.

Cyclic voltammograms of 14Se4 (13) at different concentrations showed that the peak potential values tended to be less anodic as the concentrations became higher.

24Se6 (15). The cyclic voltammogram of **15** was similar to that of 14Se4 and only one pair of redox waves was observed. Increasing the scan rates caused the anodic peak to shift to a more anodic position.

16S2Se2 (11). Surprisingly, the cyclic voltammogram of **11** was quite different from that of 16Se4 (**8**); only one pair of redox waves was presented, although the two coronands were structurally very similar. Scanning the potential from 0 volt vs SCE toward the anodic direction at a scan rate of 100 mV/s gave a current response which reached a maximum at about 1 volt and the cathodic current peak appeared at 0.113 V in the returning potential scan. The separation of the potential peaks (ΔEp) was 0.847 V, showing that the electrode reaction was quasi-reversible. The potential peak separation increased with increasing scan rates.

When the scan rates were lower than 100 mV/s, the cathodic peak on the reverse scan disappeared. This suggested that the oxidized species of 16S2Se2 (**11**) in solution underwent homogeneous reactions which resulted in electrochemically inactive species within the potential scan ranges. The oxidation of 16S2Se2 was a diffusion controlled

electrode process because a plot of the anodic current peak versus the square root of the scan rate produced a straight line.

Dibenzo-14Se4 (14). The cyclic voltammogram of **14** showed a typical, irreversible cyclic voltammogram (Figure 4.2.7). Scanning from 0 V vs SCE towards the anodic direction and back only afforded a single anodic current peak at about 0.9 V. There was no cathodic current peak observed. The anodic peak potential shifted towards the more anodic direction as the scan rates increased. Plotting the anodic peak currents versus the square root of scan rates yielded a straight line, indicating that the oxidation process was diffusion controlled.

12Se4 (12). This coronand also produced an irreversible cyclic voltammogram. At a scan rate of 50 mV/s, an anodic current peak was observed at over 1 V. The anodic peak potential shifted towards the more anodic direction as the scan rate increased. A plot of the anodic peak currents versus the square root of scan rates yielded a straight line, indicating that the oxidation process was diffusion controlled.

Table 4.2.5. Cyclic Voltammetric Data for Oxidation of Selenium Coronands (16, 19, 17, 11, 13 and 15)

Compound	υ(mV/s)	$E_{1/2}{}^b$	$E_{pa}{}^c$	$E_{pc}{}^c$	i_c/i_a	ΔE_p
8Se2	20	.387	.485	.436	1.05	.049
	50	.386	.486	.436	1.00	.050
(16)	100	.381	.487	.434	1.01	.053
	200	.374	.489	.432	1.00	.057
8Se2(Me)$_2$	20	0.408	0.438	0.378	1.02	0.062
	50	0.418	0.468	0.358	1.00	0.108
(19)	100	0.413	0.468	0.358	.96	0.108
	200	0.428	0.498	0.358	1.01	0.108
8Se2OH	20	/	/	.454	1.12	/
	50	.578	.679	.476	1.20	0.203
(17)	100	.578	.710	.445	1.12	0.265
	200	.578	.757	.398	1.09	0.395
16S2Se2	20	/	0.870	/	/	/
	50	/	1.05	/	/	/
(11)	100	0.537	0.96	0.113	0.44	0.847
	200	0.549	1.11	-0.013	0.46	1.12
14Se4	20	.532	0.868	/	/	/
	50	.475	0.888	0.118	0.0645	0.770
(13)	100	.469	0.888	0.068	0.238	0.820
	200	.478	0.868	0.028	0.500	0.840
24Se6	20	.61	.781	.438	0.958	.343
	50	.61	.844	.375	0.947	.469
(15)	100	.56	.813	.313	0.960	.500
	200	.61	.938	.281	1.03	.600

a. Measured with a stationary platinum electrode in CH_3CN with 0.1 M TEAP electrolyte.

b. $E_{1/2}$ was obtained by taking $(E_{pa} + E_{pc})/2$.

c. Potential is in volt vs SCE.

In summary, redox potentials of the selenium coronands at low scan rate, 10 mV/s or 20 mV/s, are listed in Table 4.2.6.

Table 4.2.6. Summary of $E_{1/2}$ or E_p Values of Selenium Coronands[a].

#	Compound	$E_{1/2}$ or E_p [b,c] (V)
1	8Se2	0.378
2	8Se2Me$_2$	0.378
3	14Se4	0.468
4	16Se4	0.508 & 1.41
5	12Se4	1.57
6	24Se6	0.548
7	12Se3	0.518 & 1.63
8	8Se2OH	.578[d]
9	Dibezo-14Se4	.876
10	16Se4(OH)$_2$	.576 & 1.42
11	20Se5	0.523 & 0.925
12	16Se2S2	0.537[d]

a. Measured with a stationary platinum electrode in CH_3CN with 0.1 M TEAP.

b. $E_{1/2}$ was obtained by taking $(E_{pa} + E_{pc})/2$.

c. Potential is in volt vs SCE.

d. This $E_{1/2}$ was calculated from the cyclic voltammogram
   at a scan rate of 100 mV/s.
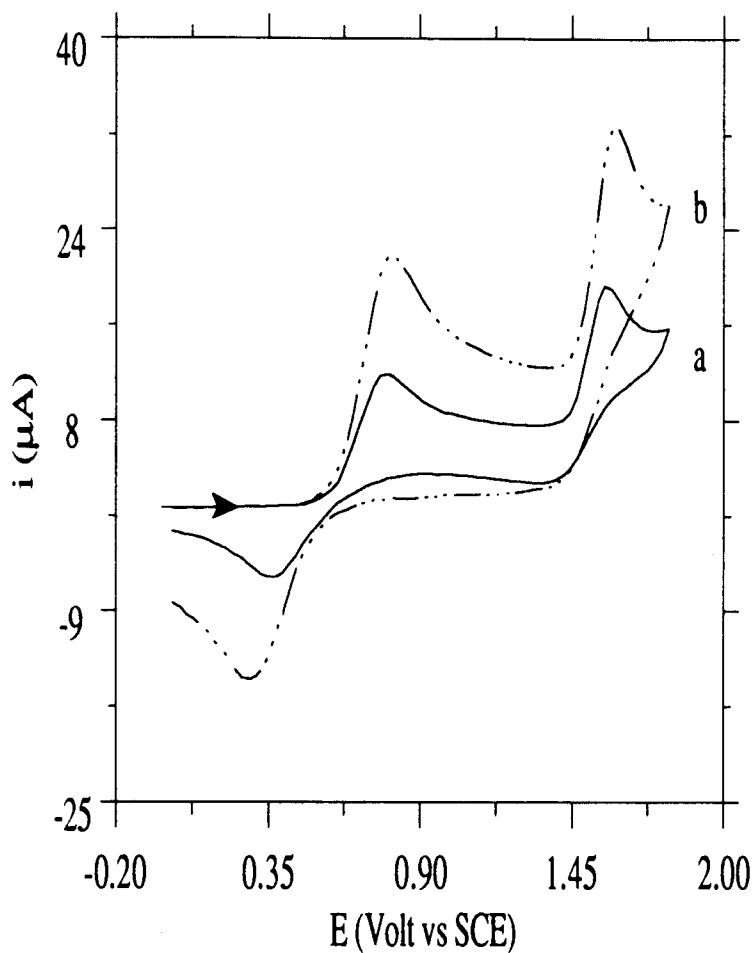
Figure 4.2.3. Cyclic voltammograms of 16Se4 (8) (1 mM) in CH_3CN at scan rates: (a) 50 mV/s; (b) 200 mV/s. Working electrode: Pt. Reference electrode: SCE. Electrolyte: 0.1 M tetraethylammonium perchlorate.
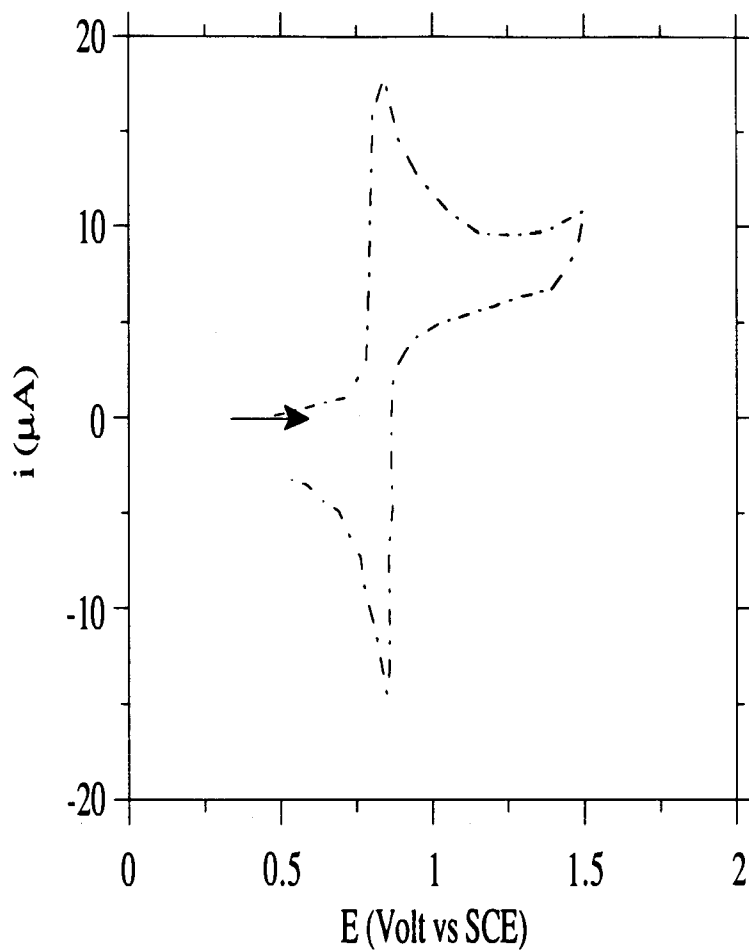
Figure 4.2.4. Cyclic voltammogram of $8Se2Me_2$ (40)(1 mM) in CH_3CN at scan rate 50 mV/s. Working electrode: Pt. Reference electrode: SCE. Electrolyte: 0.1 M tetraethylammonium perchlorate.
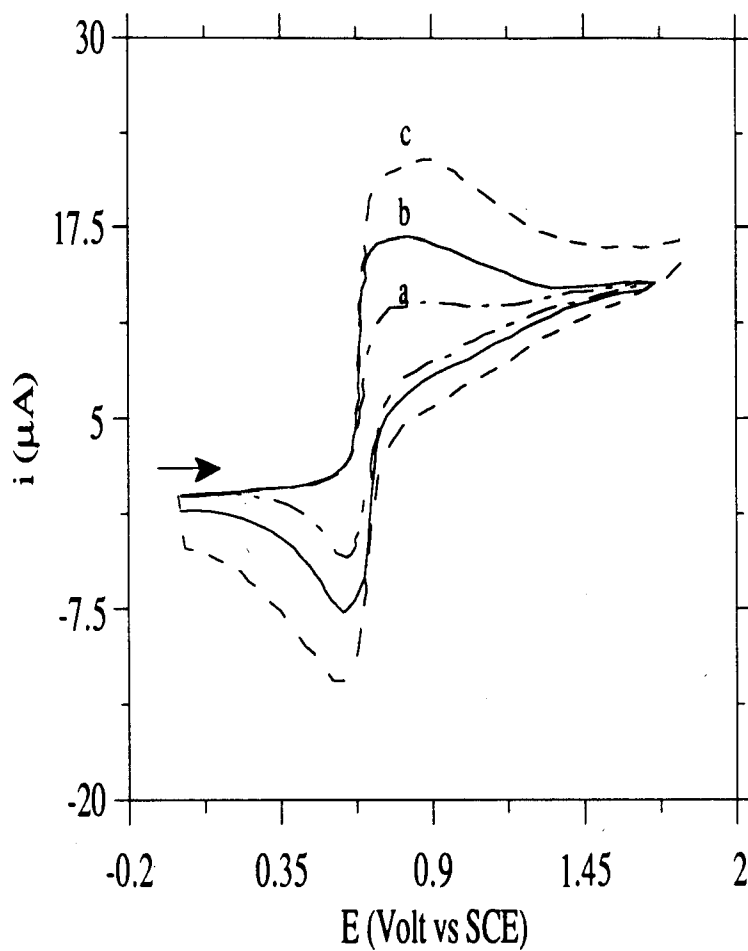
Figure 4.2.5. Cyclic voltammograms of 8Se2OH (17) (1 mM) in CH_3CN at various scan rates (upwards: 50, 100, 200 mV/s). Working electrode: Pt. Reference electrode: SCE. Electrolyte: 0.1 M tetraethylammonium perchlorate.
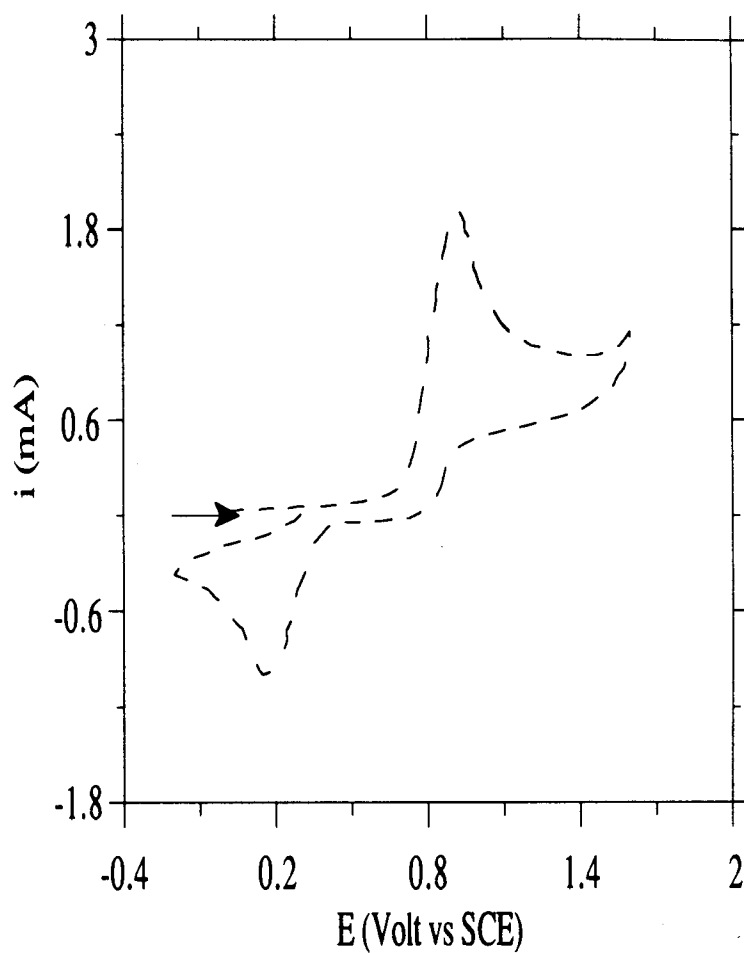
Figure 4.2.6. Cyclic voltammograms of 14Se4 (13) (1 mM) in CH₃CN at scan rate 100 mV/s. Working electrode: Pt. Reference electrode: SCE. Electrolyte: 0.1 M tetraethylammonium perchlorate.
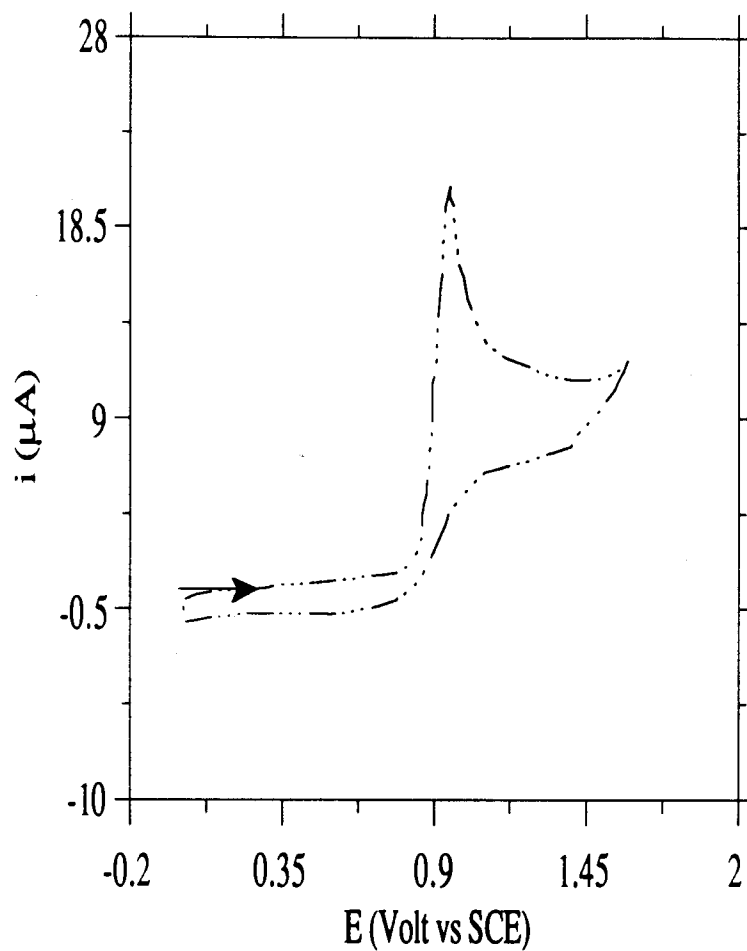
Figure 4.2.7. Cyclic voltammograms of Dibenzo-14Se4 (14) (1 mM) in CH$_3$CN at scan rate 100 mV/s. Working electrode: Pt. Reference electrode: SCE. Electrolyte: 0.1 M tetraethylammonium perchlorate.

4.2.2.2. Spectroelectrochemistry

The experimental setup of a three-electrode system for spectroelectrochemistry is shown in Figure 7.5.2 (see Chapter 7). The working electrode was an optically transparent platinum film electrode. The electrode was made by depositing a thin platinum film on a quartz glass plate so that the quartz glass plate became a Pt electrode and at the same time remained transparent to light. Over the uv-visible absorption range of interest (200 - 400 nm) the electrode had an absorbance of about 0.5. The electrode was placed in an ordinary uv-cell. The width of the electrode (quartz glass plate) covered the uv-cell window. The reference electrode was AgI/Ag. The counter electrode was a platinum wire that was sealed in a glass tube with a glass frit end to prevent the species generated on the counter electrode from interfering with the observation. Figure 4.2.8 shows the cyclic voltammogram of 16Se4 (**8**) recorded on the optically transparent platinum electrode, which shows that the electrode functions as an ordinary Pt electrode. However, the oxidation peaks of the cyclic voltammogram are shifted to the more anodic position because of the resistance of the optically transparent electrode (thin film of Pt metal), which causes the second oxidation peak to merge with the peak due to solvent oxidation.

Selenium coronand solutions were prepared in dried CH_3CN and placed in the uv-cell that was also an electrolysis cell. The solution contained 0.1 M tetraethylammonium perchlorate as electrolyte and was degassed with N_2. Then, a potential step that was predetermined by cyclic voltammetry of the corresponding selenium coronands was applied to the solution; at the same time, a spectrum was acquired.
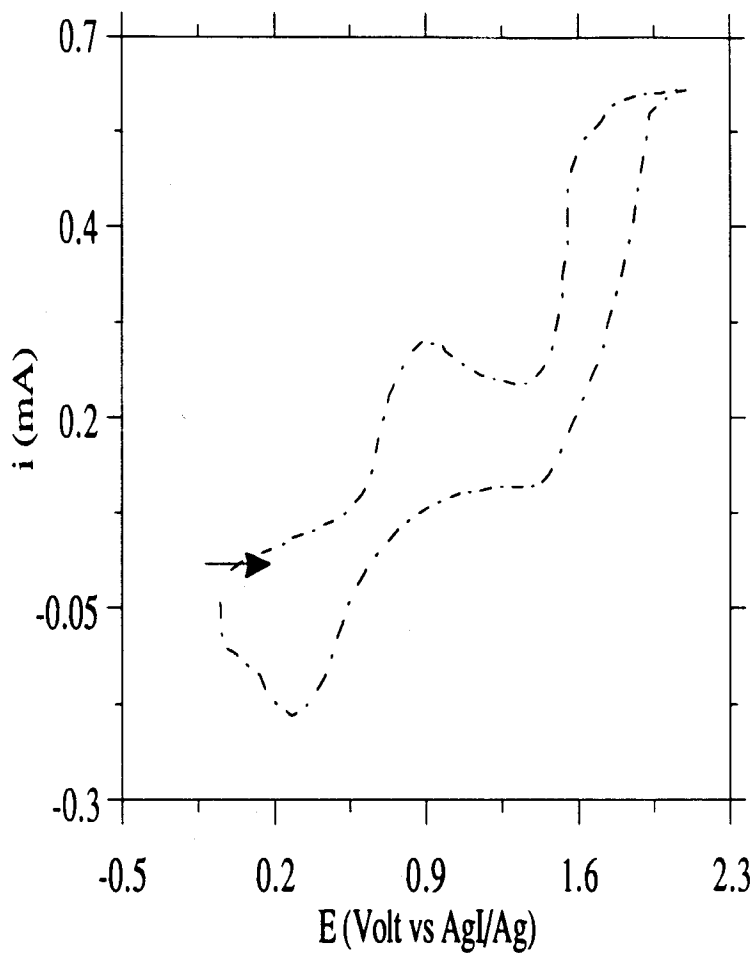
Figure 4.2.8. Cyclic voltammogram of 16Se4 (8) recorded on the Pt transparent film working electrode. [16Se4] = 1×10^{-3} M. Reference electrode: AgI/Ag. Electrolyte: 0.1 M tetraethylammonium perchlorate in CH_3CN. The arrow shows where the scan starts.

14Se4 (13). Coronand **13** was oxidized in a uv-cell at a potential of 1.2 V vs AgI/Ag. The absorbance maximum was at 260 nm. This is slightly different from the absorbance produced by $NOBF_4$ in CH_3CN solution of **13**, which appeared at 274 nm. We attributed this difference in absorbance maximum of the electrode-oxidized species to the oxidized species adsorbed on the electrode, since adsorption-induced abnormalities in cyclic voltammogram appearance were also discovered in experiments of cyclic voltammetry. Two concentrations of 14Se4 (**13**), 9.9×10^{-4} and 9.9×10^{-5} M, were tested and the absorbance band did not depend on concentration. A plot of the absorbance at 260 nm versus the square root of time gave rise to a straight line (Figure 4.2.9), which indicates that the electrolysis on the electrode is a diffusion-controlled process.

16Se4 (8). First, preliminary experiments were run in which the working electrode was a coiled platinum wire that was placed in the uv-cell. An CH_3CN solution of 16Se4 (1×10^{-4} M), with tetraethylammonium perchlorate (0.1 M), was electrolyzed in a uv cell. The counter electrode and reference electrode were as previously described. The applied potential was 1.2 V vs AgI/Ag. Under these conditions, it was found that initially, the absorption peak at 256 nm appeared first and grew faster than the absorption peak at 322 nm, although both peaks were observed. After 2000 seconds, the peak at 322 nm was of constant intensity while the peak at 256 nm continued to increase.

Next, an optically transparent platinum electrode was used as the working electrode. Again, a concentration-dependent phenomenon was observed (Figure 4.2.11). When the concentration of 16Se4 was about 10^{-4} M, only the peak at 256 nm was observed. A plot of absorbance versus the square root of time, according to Equation 4.1.2, yielded a straight line (Figure 4.2.10), indicating that the process is diffusion-controlled.

At a concentration of 16Se4 (**8**) of about 10^{-3} M, both peaks at 322 nm and 256 nm were observed. This indicates that the species absorbing at 322 nm is formed when **8** is in

high concentration. A plot of the logarithm of absorbance at 256 nm versus that of absorbance at 322 nm gave a straight line with a slope of about 1 (ca. 0.88, R = 0.99).

8Se2 (16). Oxidation of coronand 16 in CH_3CN with an applied potential of 0.5 V vs AgI/Ag also showed concentration-dependent absorbance maxima. Electrolysis of dilute 16 (1.86×10^{-4} M) produced only a 250 nm peak; electrolysis of concentrated 16 (1.86×10^{-3} M), gave two absorbance maxima at 250 nm and 428 nm. We attributed the 250 nm peak to the absorbance maximum of the 8Se2 dication, because a CH_3CN solution of $8Se2(SO_3CF_3)_2$ (25) has an absorbance maximum at 248 nm.
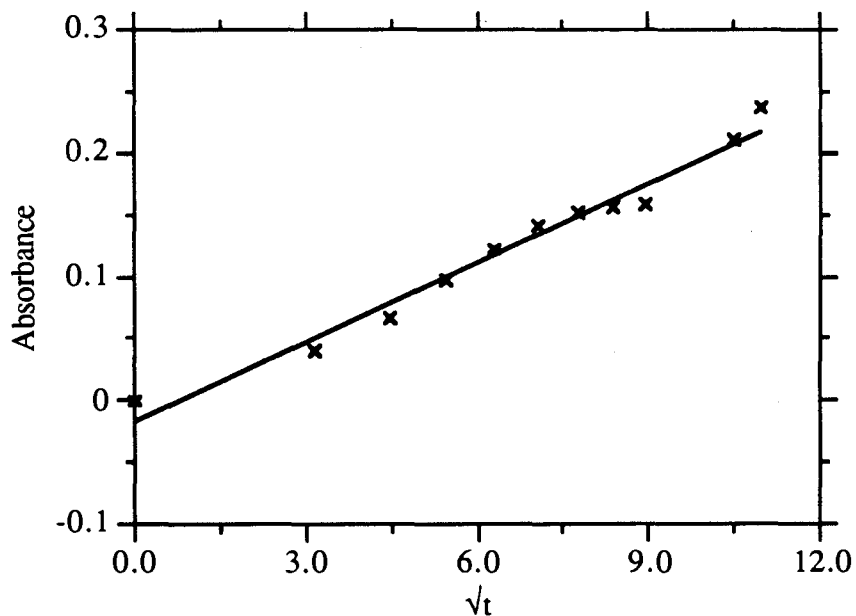
Figure 4.2.9. Plot of absorbance of 14Se4 radical cation (260 nm) versus $\sqrt{t}$. [14Se4] = 1.02×10^{-4} M. Counter electrode: Pt wire. Reference electrode: AgI/Ag. Electrolyte: 0.1 M tetraethylammonium perchlorate in CH_3CN.
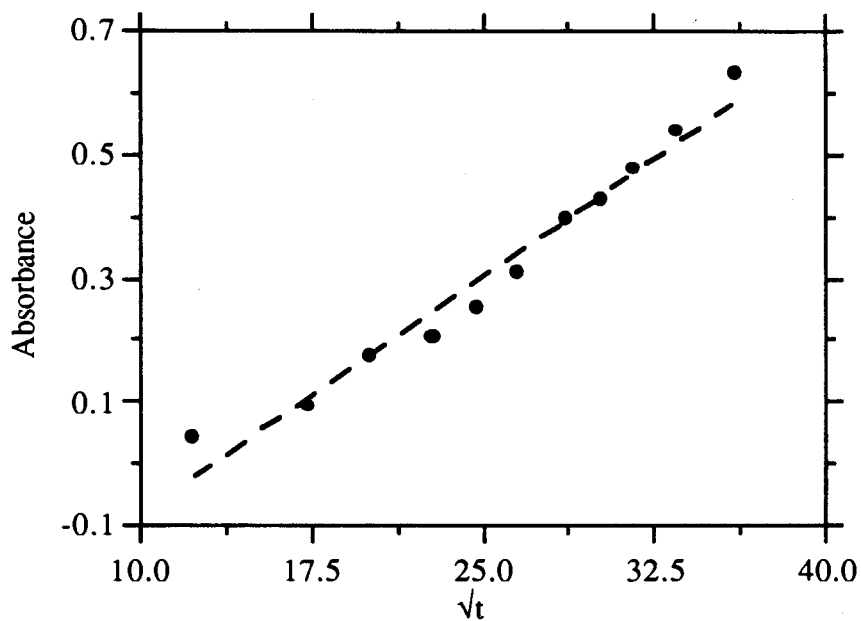
Figure 4.2.10. Plot of absorbance of 16Se4 radical cation (256 nm) versus $\sqrt{t}$. [16Se4] = 1.02×10^{-4} M. Counter electrode: Pt wire. Reference electrode: AgI/Ag. Electrolyte: 0.1 M tetraethyl-ammonium perchlorate in CH_3CN.
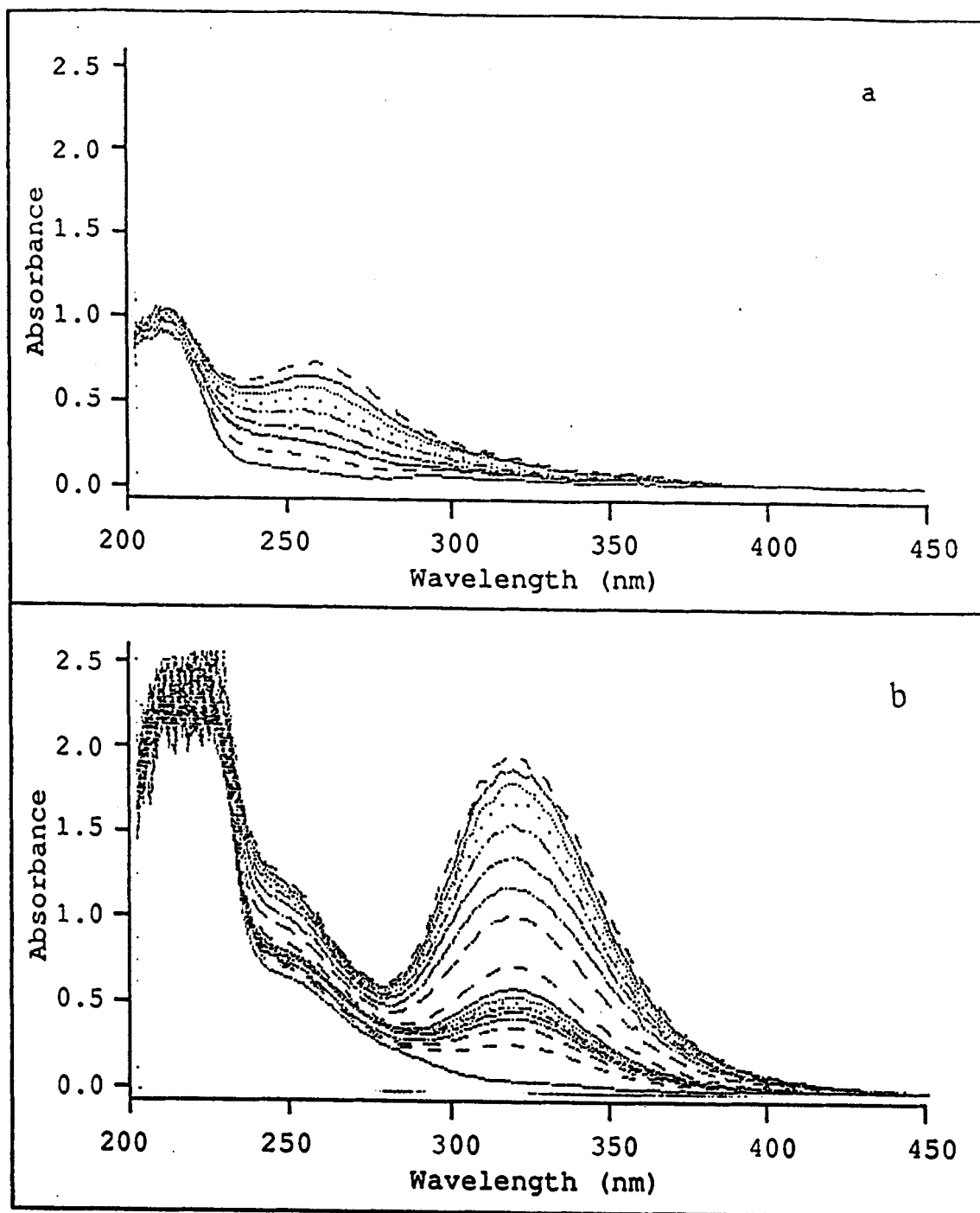
Figure 4.2.11. UV-visible spectra of 16Se4 (8) on a Pt transparent electrode. The applied potential was 1.2 V vs AgI/Ag. (a) [16Se4] = 1.02×10^{-4} M; (b) [16Se4] = 1.02×10^{-3} M. Electrolyte: 0.1 M tetraethylammonium perchlorate in CH_3CN.

4.2.2.3. *Chemical Reaction of 16Se4⁺· in Homogeneous Solution*

Since both the results from uv-spectroscopic and cyclic voltammetric studies suggested that the oxidized 16Se4 (16Se4⁺·) is involved in further chemical reactions in solution, we decided to carry out further investigations on the solution reactions of the radical cation by cyclic voltammetry.

Cyclic voltammograms of 16Se4 (**8**) with different initial concentrations in CH₃CN were recorded at various scan rates. In every case, as the scan rate increased both anodic current peaks shifted to more positive potentials, and both cathodic peaks shifted to more negative potentials. The extent of the shifts was more significant for the first redox pair than for the second redox pair. Also, the shifts exceeded those resulting from the uncompensated iR drop or charging current effects because the shifts and the separation of cathodic/anodic peak potential increment for ferrocene at various scan rates were small (5 mV). Thus, the anodic peak potential shifts resulted from the coupled solution chemical reactions that were yet to be defined.

The half peak width, $E_{pp/2}$, as calculated by $E_p^a - E_{p/2}$ for the first anodic peak became broadened (from $E_{pp/2} = 61$ mV to maximum $E_{pp/2} = 150$ mV) as the scan rate as well as concentration increased, where $E_{pp/2}$ was the potential at half peak current value. The half peak width, $E_{pp/2}$, of the second anodic peak was less affected by the variations of scan rate and concentration (from $E_{pp/2} = 70$ mV to maximum $E_{pp/2} = 90$ mV). The cathodic peak of the second redox waves became very broad as the scan rate increased and there was no clear peak that could be observed.

Because the second anodic peak was close to the solvent oxidation peak and there was no second cathodic peak at a fast scan rate (>200 mV/s), it was very difficult to determine i_a and i_c, parameters necessary for analyzing the system. Therefore, a potential scan range (0 - 1.2 V vs SCE) was chosen where only the first redox waves were shown

for further investigations. Figure 4.2.12 shows the cyclic voltammograms of 16Se4 at various scan rates in the potential range.

We observed the same phenomena of the anodic peak potentials shifting to the anodic direction and of separation of the associated anodic/cathodic peak potentials increasing as the scan rate increased. Also, in going from low to high concentrations of 16Se4, the first anodic peak shifted significantly to the more positive direction. Table 4.2.7 lists those scan-rate dependent, as well as concentration dependent, cyclic voltammetric parameters. Ratios of cathodic current peak to anodic current peak, i_c/i_a, were calculated with the equation derived by Nicholson[126].

$$\frac{i_c}{i_a} = \frac{(i_c)_0}{i_a} + \frac{0.485(i_{sp})_0}{i_a} + 0.086 \qquad (4.2.9)$$

Here, i_a is the anodic current; i_c is the cathodic current; $(i_c)_0$ is the uncorrected cathodic current with respect to the zero baseline; $(i_{sp})_0$ is the current at switching potential. At slow scan rates the recovery of i_c was low, but at high scan rates the recovery of i_c was high; at low concentrations of 16Se4 the recovery of i_c was high, but at high concentrations the recovery of i_c was low (Figure 4.2.13). A plot E_p vs $\log\upsilon$ and $\log C$ gave slopes of 55 ± 6.70 mV/decade and 126 ± 14.1 mV/decade respectively.

Table 4.2.7. Cyclic Voltammetric Data of The First Redox
Wave of 16Se4 (8)

Conc. (mM)	ν (V/s)	E_{pa} (mV)	$E_{pp/2}{}^a$ (mV)	E_{pc} (mV)	$\Delta E_p{}^b$ (mV)	$E_{1/2}{}^c$ (mV)	$\dfrac{i_a}{\nu^{1}/C}{}^d$	$\dfrac{i_c}{i_a}{}^e$
	0.01	630	61	450	180	540	36.4	0.70
	0.02	640	65	430	210	535	34.7	0.89
0.66	0.05	660	90	400	260	530	35.9	0.83
	0.1	670	100	380	290	525	32.4	0.90
	0.2	670	105	365	305	518	31.9	0.95
	0.5	780	160	280	500	530	27.2	0.94
	0.01	665	85	430	235	548	34.3	0.68
	0.02	670	85	410	260	540	34.7	0.78
1.2	0.05	690	90	365	325	528	32.9	0.81
	0.1	700	95	340	360	520	31.0	0.85
	0.2	735	110	300	405	518	29.6	0.87
	0.5	780	120	250	530	515	28.4	0.85
	0.01	710	100	410	300	560	29.4	0.69
	0.02	730	110	360	370	545	28.9	0.80
1.8	0.05	750	115	320	430	535	26.3	0.80
	0.1	775	135	290	485	533	24.8	0.88
	0.2	785	145	260	525	522	24.8	0.91
	0.5	800	140	210	590	505	24.5	0.91
	0.01	750	120	400	350	575	30.7	0.64
	0.02	750	120	370	380	560	28.4	0.78
2.2	0.05	770	125	320	450	545	25.7	0.82
	0.1	765	125	305	460	535	25.8	0.85
	0.2	780	140	279	501	530	25.1	0.93
	0.5	790	150	240	550	515	23.3	0.83

Continuation of

Table 4.2.7. Cyclic Voltammetric Data of The First Redox Wave of 16Se4 (8)

Conc. (mM)	v (V/s)	E_{pa} (mV)	$E_{pp/2}{}^{a}$ (mV)	E_{pc} (mV)	$\Delta E_p{}^{b}$ (mV)	$E_{1/2}{}^{c}$ (mV)	$\dfrac{i_a}{v^{1}/C}{}^{d}$	$\dfrac{i_c}{i_a}{}^{e}$
	0.01	740	110	440	300	590	29.4	0.61
	0.02	760	110	340	320	550	25.2	0.75
2.8	0.05	765	110	320	445	543	25.4	0.74
	0.1	775	95	289	486	532	24.6	0.80
	0.2	800	120	250	550	525	23.5	0.83
	0.5	900	180	140	760	520	21.4	0.87
	0.01	750	121	390	360	570	26.7	0.67
	0.02	770	120	350	425	560	25.2	0.70
3.3	0.05	775	117	320	455	547	24.3	0.74
	0.1	790	130	280	510	535	22.8	0.80
	0.2	810	140	240	570	525	23.1	0.87
	0.5	810	145	230	560	510	22.1	0.91

a. $E_{pp}/2 = E_{pa} - E_{p/2}$.

b. $\Delta E_p = E_{pa} - E_{pc}$.

c. $E_{1/2} = (E_{pa} + E_{pc})/2$.

d. in $\dfrac{\mu A}{(V/s)^{1/2}mM}$

e. The ratio of cathodic and anodic peak current for the first redox cycle.
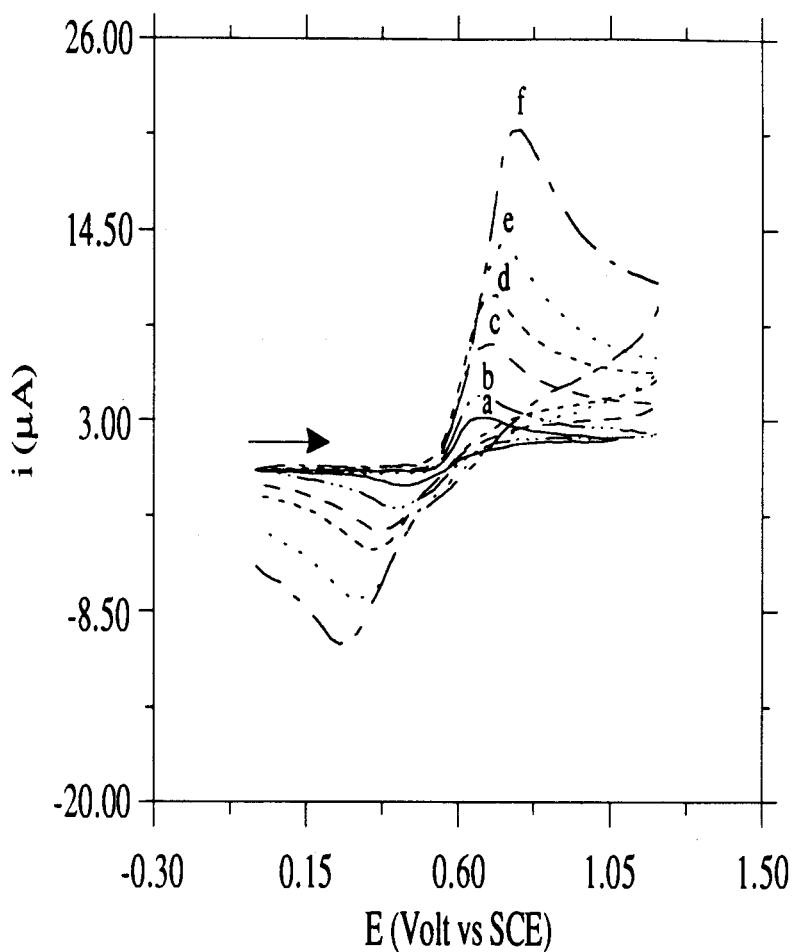
Figure 4.2.12. Cyclic voltammograms of 16Se4 (8) at various scan rates (10, 20, 50, 100, 200 and 500 mV/s) in CH_3CN. Working electrode: Pt. Reference electrode: SCE. Electrolyte: 0.1 M tetraethylammonium perchlorate.
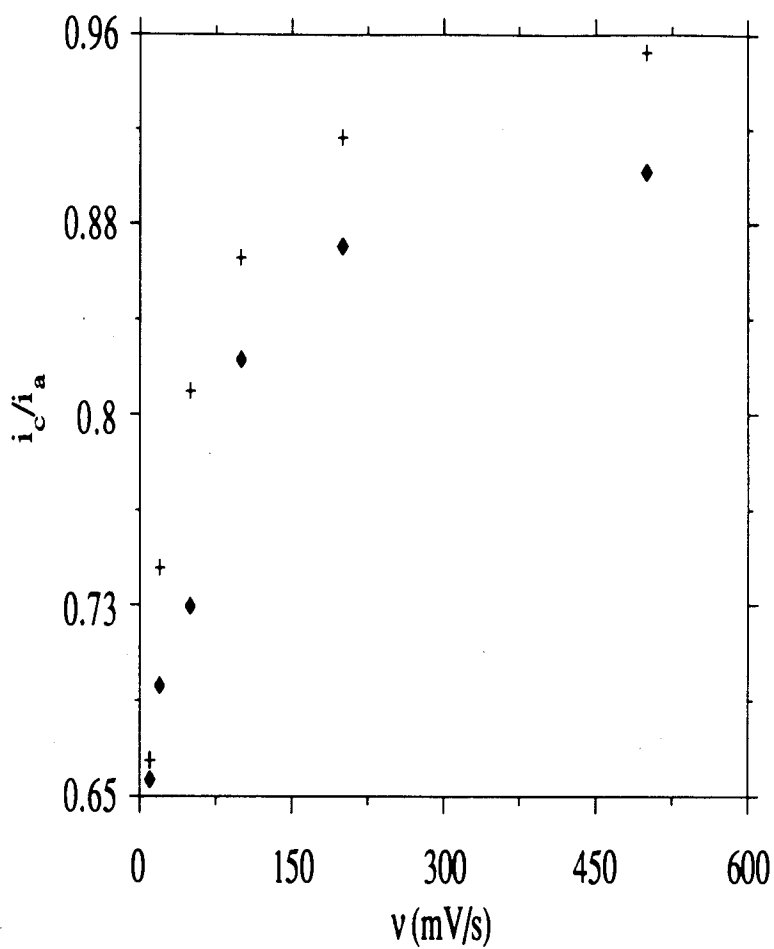
Figure 4.2.13. Plots of i_c/i_a vs scan rates. (+): [16Se4] = 1.2 mM; (♦): [16Se4] = 2.8 mM. Working electrode: Pt. Reference electrode: SCE. Electrolyte: 0.1 M tetraethylammonium perchlorate in CH_3CN.

4.2.2.4. Convolution Transformation

The convolution transformation of 16Se4 cyclic voltammetric data was carried out by a numerical integration technique on a personal computer based on the algorithm given in Equation 4.2.10[114]. Equation 4.2.10 was written in the BASIC computer program language.

$$I(k\Delta t) = \frac{1}{\pi} \sum_{j=1}^{j=k} \frac{\Gamma(k - j + \frac{1}{2})}{(k - j)!} \Delta t^{1/2} i(j\Delta t) \qquad (4.2.10)$$

where $I(k\Delta t)$ is the convolutive transformation (i.e., $I(t)$ in Equation 4.1.9) of the experimental $i(t)$(e.g., currents in cyclic voltammetry) that is expressed as $i(j\Delta t)$ in Equation 4.2.10; $\Gamma(x)$ is the Gamma function of x; k and j are depicted in Figure 4.2.14, $\Gamma(k-j+1/2)$ is the Gamma function.
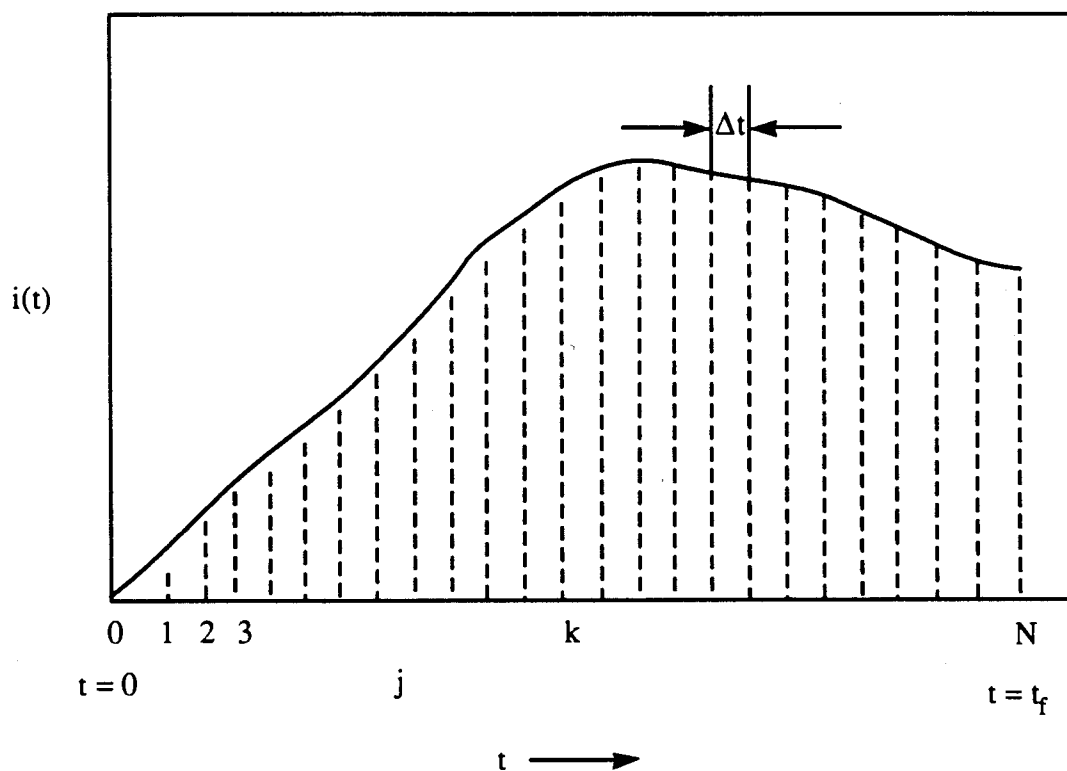
Figure 4.2.14. Illustration of i(t) vs t curve for digital evaluation of I(t).

102

In order to examine if the program was free of errors, we first conducted the convolution transformation on the cyclic voltammetric data of ferrocene in CH_3CN, because its cyclic voltammetric behavior is well known. Figure 4.2.15 shows the cyclic voltammogram of ferrocene as well as the corresponding convolution transformation voltammogram in which the convolution-transformed current function, I(t), is plotted as a function of the scanning potential, E. The advantage of the method can be seen immediately. For a reversible electron transfer system, such as ferrocene, the transformed current function, I(t), for the forward scan was superimposable on the transformed current function I(t) for the backward scan. A plot of E vs log $\frac{I_l - I(t)}{I(t)}$ was linear with a slope of 0.059/n. For a quasi-reversible reaction, however, the forward and backward I(t) curves would not superimpose.

The cyclic voltammogram data of the redox pair 16Se4 /16Se4$^{+\cdot}$ were then substituted in Equation 4.2.10 and calculated on the personal computer. The results are shown in Figure 4.2.16 and Figure 4.2.17. These plots showed that the redox system was not reversible in general because none of the forward and backward curves were superimposable. Furthermore, I_l was scan rate dependent; at the lowest scan rate the I(t) function attained its largest value. However, I(t) did not actually reach a limiting value but continued to increase with time as long as the applied potential was greater than $E_{1/2}$. This indicates two possibilities: convection or more likely indirect oxidation of 16Se4 from $(16Se4)_2^{+\cdot}$ to 16Se4$^{+\cdot}$ and 16Se4 through dissociation. Figure 4.2.16 shows that from a to f the reduction of the oxidized product is a time dependent phenomenon: faster scans resulted in more recovery, as manifested by the overlapped curves (I(t)) of forward and backward scans at the starting point of convolution voltammetry; slower scans gave rise to less recovery shown by parted curves of forward and backward at the starting point of convolution voltammetry. Concentration effects were also shown by the convolution transformation: more recovery of 16Se4 was achieved at the reversal scan for low initial

16Se4 concentration, consistent with the observation of the i_c/i_a ratio from cyclic voltammetry.
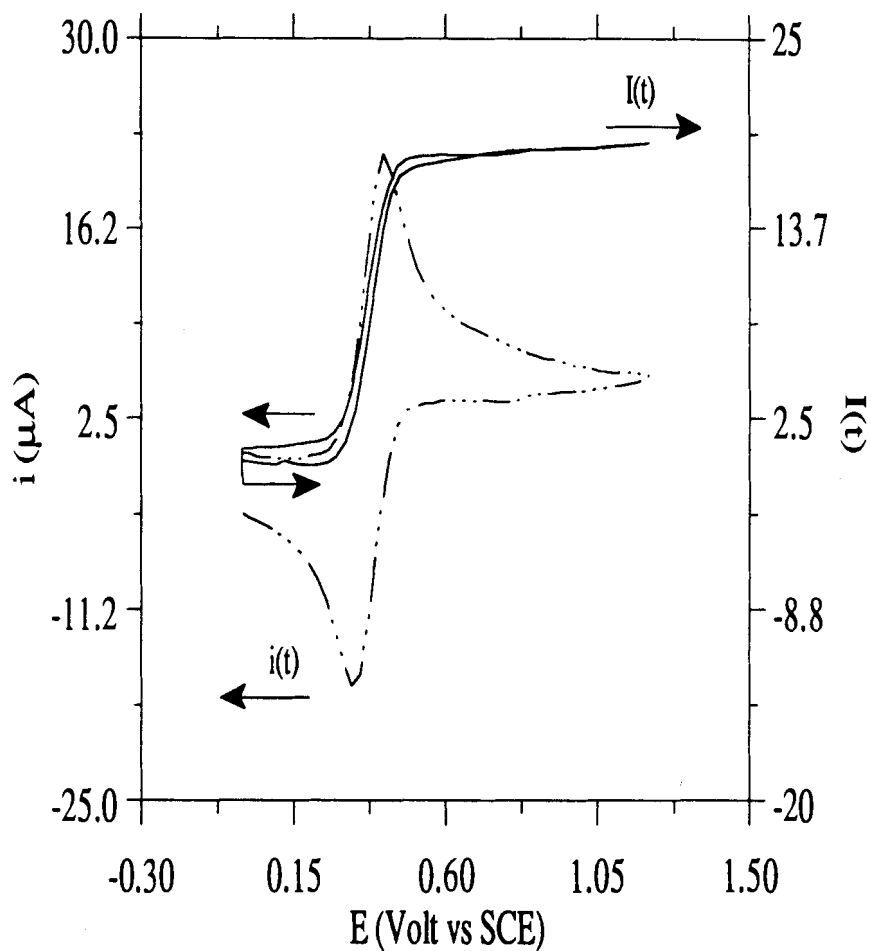
Figure 4.2.15. Cyclic voltammogram and convolution transformation of ferrocene (1 mM) at scan rate 100 mV/s in CH_3CN. Working electrode: Pt. Reference electrode: SCE. Supporting electrolyte: 0.1 M tetraethylammonium perchlorate.
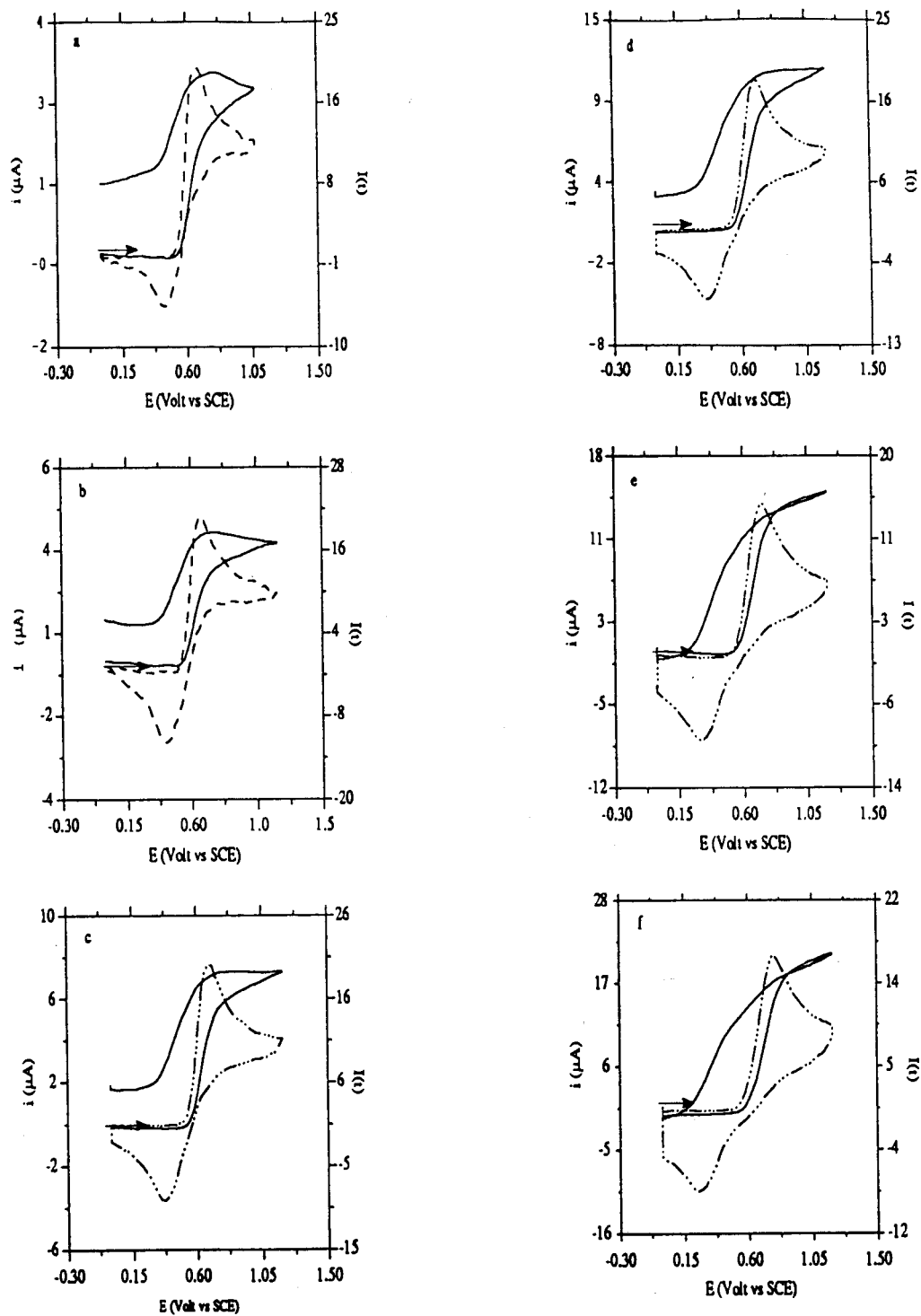
Figure 4.2.16. Convolution transformation of voltammograms of 16Se4 (8) for the first redox pair. Concentration of 16Se4 1.2 mM. a) 0.01 V/s; b) 0.02 V/s; c) 0.05 V/s ; d) 0.1 V/s ; e) 0.2 V/s ; f) 0.5 V/s.

105
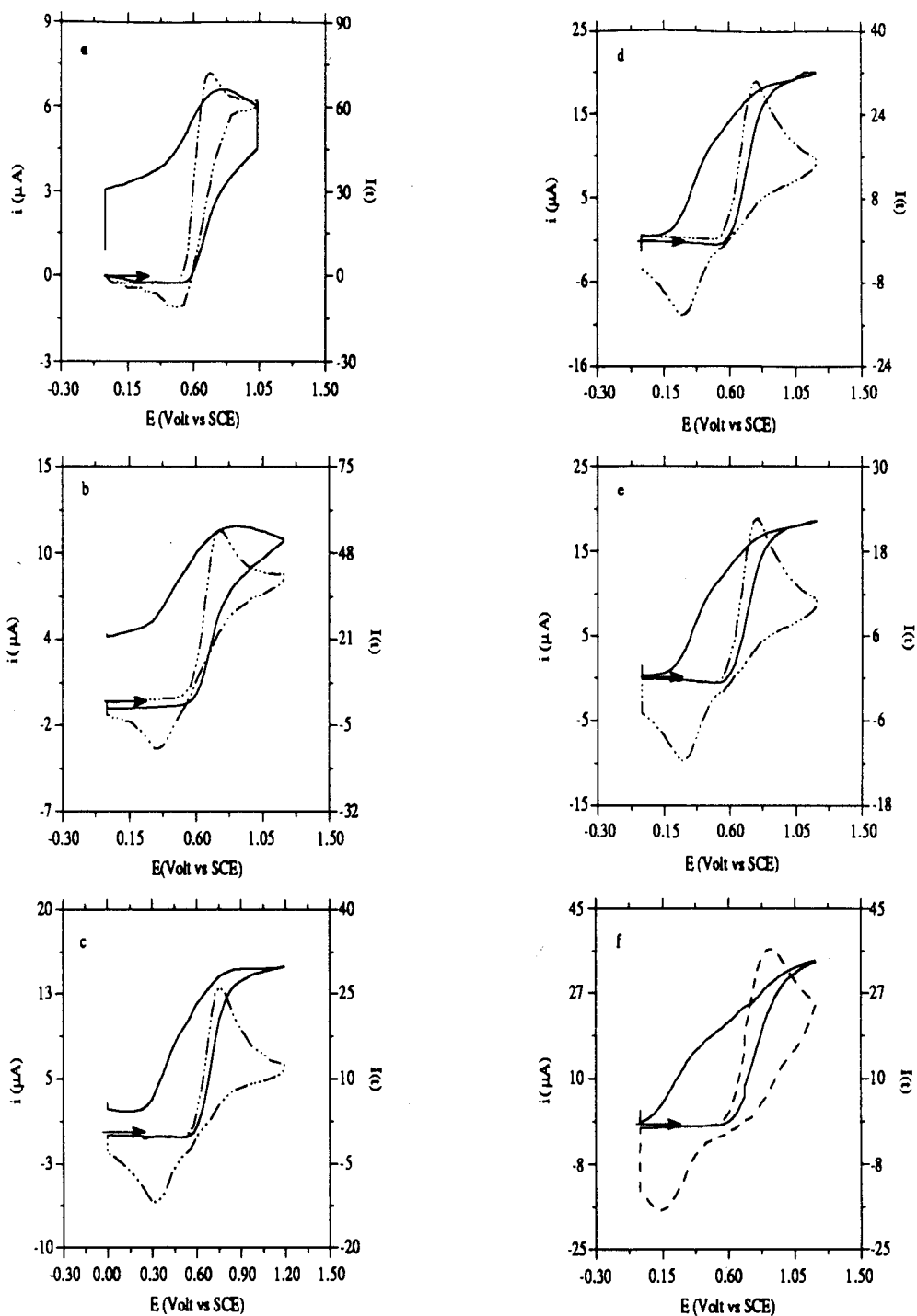
Figure 4.2.17. Convolution transformation of voltammograms of 16Se4(8) for the first redox pair. Concentration of 16Se4 2.8 mM. a) 0.01 V/s; b) 0.02 V/s; c) 0.05 V/s ; d) 0.1 V/s ; e) 0.2 V/s ; f) 0.5 V/s.

4.2.2.5 . Coulometric Studies

16Se4. Electrolysis of 16Se4 was carried out in a two-compartment electrochemical cell. 16Se4 was electrolyzed by a pair of Pt gauze electrodes in dry and O_2 free CH_3CN solution with tetraethylammonium perchlorate (0.1 M) as electrolyte and a saturated calomel electrode (SCE) as the reference electrode. Two applied potentials (0.8 and 1.8 V vs SCE) were used in the electrolysis experiments. The applied potentials were chosen such that the former would oxidize 16Se4 to the radical cation (one electron-transfer), and the latter would oxidize 16Se4 to the dication (two-electron transfer), as determined by cyclic voltammetry. The progress was monitored with a coulometer and an x-y plotter that plotted currents as a function of time or a multi-meter that showed the currents.

At an applied potential of 0.8 V, 16Se4 was quickly oxidized, forming a yellow solution. When the amount of charge indicated by the coulometer equaled an overall one-electron transfer, the electrolysis process stopped as indicated by a constant reading on the meter.

The solution being electrolyzed was monitored by uv-visible spectroscopy, by withdrawing the solution into a uv cell with a syringe. When 20% of the total amount of electric charge had passed through the solution, the electrolyte had an absorbance maximum at 322 nm; when 42% of the total amount of electric charge had passed through the solution, the electrolyte had two absorption peaks at 322 nm and 256 nm respectively; when the amount of electric charge corresponding to a one-electron transfer had passed through the solution, the 256 nm peak became the major peak and the 322 nm was merely a tail to the 256 nm peak.

When the applied potential was raised to 1.8 V after one-electron transfer, the electrolysis resumed until the amount of charge corresponded to an overall two-electron transfer oxidation. At this point, the 16Se4 had been oxidized to $16Se4^{2+}$. The color of

the solution became light yellow. In a separate experiment, the applied potential was 1.8 V and the amount of electric charge passed through the solution corresponded to an overall two-electron oxidation process.

The uv-visible spectrum of the electrolyte, on which the applied potential was raised from 0.8 to 1.8 V and the electrolysis resumed, showed that the 322 nm peak reappeared. When the amount of charge corresponding to a two-electron transfer reaction had passed through the solution, both the 256 nm peak and 322 nm peaks were observed, but the 256 nm peak was more intense, which was consistent with the uv-visible spectrum of $16Se4^{2+}$ (**24**) in CH_3CN.

Cyclic Voltammetry of 16Se4 (8) Under Electrolysis

Cyclic voltammograms were run on 16Se4 (**8**) solutions that were being electrolyzed with an applied potential of 1.2 and 1.8 V. The experiments were carried out in the same cell in which electrolysis was performed; however, two sets of working electrodes were used. One-set was a pair of Pt gauze electrodes for electrolysis; the other was a Pt micro-electrode for cyclic voltammetry.

First, an CH_3CN solution of 16Se4 was electrolyzed with an applied potential of 1.2 V. The solution was monitored by uv-visible spectroscopy from time to time. Initially, there were absorption peaks at 320 nm as well as 256 nm, then only the 256 nm peak was seen. At that point, the cyclic voltammetric scan was started. Several experiments were performed in which different initial potentials were used as the starting points for the cyclic voltammetric scans.

The resulting cyclic voltammograms are shown in Figure 4.2.18. For comparison, the cyclic voltammogram of 16Se4 under normal conditions, i. e., neutral 16Se4 solution, is also shown.

In the first experiment, the initial potential of the cyclic voltammetric scanning was 0 V vs SCE. At this potential, $16Se4^{+\cdot}$ produced by electrolysis was reduced to 16Se4 at

the vicinity of the micro-electrode, but the bulk solution was still $16Se4^{+\cdot}$. The cyclic voltammogram obtained from the electrolyzed 16Se4 solution was almost the same as that recorded from the neutral 16Se4 solution except that the first oxidation current peak was slightly smaller and appeared at a more anodic position than the former. Because the cyclic voltammetry was performed on a $16Se4^{+\cdot}$ solution that had an absorbance maximum at 256 nm, the experimental result indicated that the species absorbing at 256 nm was the radical cation and that it could be reversibly reduced to neutral 16Se4.

In another experiment, the initial potential for the cyclic voltammetric scan was 1 V vs SCE. At this initial potential, the cyclic voltammetric scan was on the radical cation $16Se4^{+\cdot}$. Scanning towards the anodic direction at a scan rate of 50 mV/s produced an anodic current peak at 1.6 V, which was at the same position as the second anodic current peak in the cyclic voltammogram measured from the unelectrolyzed 16Se4 solution. Then, at 1.8 V, the potential scan direction was reversed towards the cathodic direction. Consequently, a cathodic current peak appeared at the position (0.4 V) where the current peak related to $16Se4^{2+}/16Se4^{+\cdot}$ appeared under normal conditions. This result meant that the second anodic current peak corresponding to $16Se4^{2+}/16Se4^{+\cdot}$ was caused by oxidation of the species that absorbed at 256 nm in the uv-visible spectrum.

In the third experiment, the potential scan was started from 1.2 V towards the cathodic direction until 0 V, then the scan was switched towards the anodic direction until 1.8 V, and subsequently, the scan was reversed back to 1.2 V. The scan was carried out at three different scan rates. The resulting cyclic voltammograms were similar to the previous ones, but the cathodic current peak shifted to a more cathodic position and the anodic current peak was weaker. At the slow scan rate there was no first anodic current peak, an indication of a chemical reaction that consumed 16Se4.

Cyclic voltammograms of a 16Se4 solution that was being electrolyzed at an applied potential of 1.8 V vs SCE were different from those of a neutral 16Se4 solution. Scanning from 1.8 V to 0 V and back showed two close cathodic peaks at 0.381 and 0.279

V. The cathodic current peak at 0.381 V was only observed when the scan rate was over 50 mV/s and appeared as a shoulder of the cathodic current peak at 0.279 V. When the scan was switched at 0 V and scanned towards the anodic direction, there were two peaks observed at 1.17 V and 1.49 V respectively with lower currents. Because the 16Se4 dication was moisture sensitive and it was very difficult to exclude moisture from the solvent, the cyclic voltammograms from the 16Se4 solution that was being electrolyzed were presumably those of the decomposed 16Se4 dication.

Electrolysis of Other Selenium Coronands

Controlled electrolysis on other selenium coronands, 8Se2OH, 14Se4 and 16S2Se2 in CH_3CN has been carried out as well. The selenium coronands were electrolyzed at applied potentials that were determined by the cyclic voltammetry of each coronand. When the potentials were applied, all of them yielded yellow solutions. Although these selenium coronands showed only one pair of redox waves in cyclic voltammograms, the amount of charge that passed through the solution of each coronand equaled an overall two-electron transfer process.
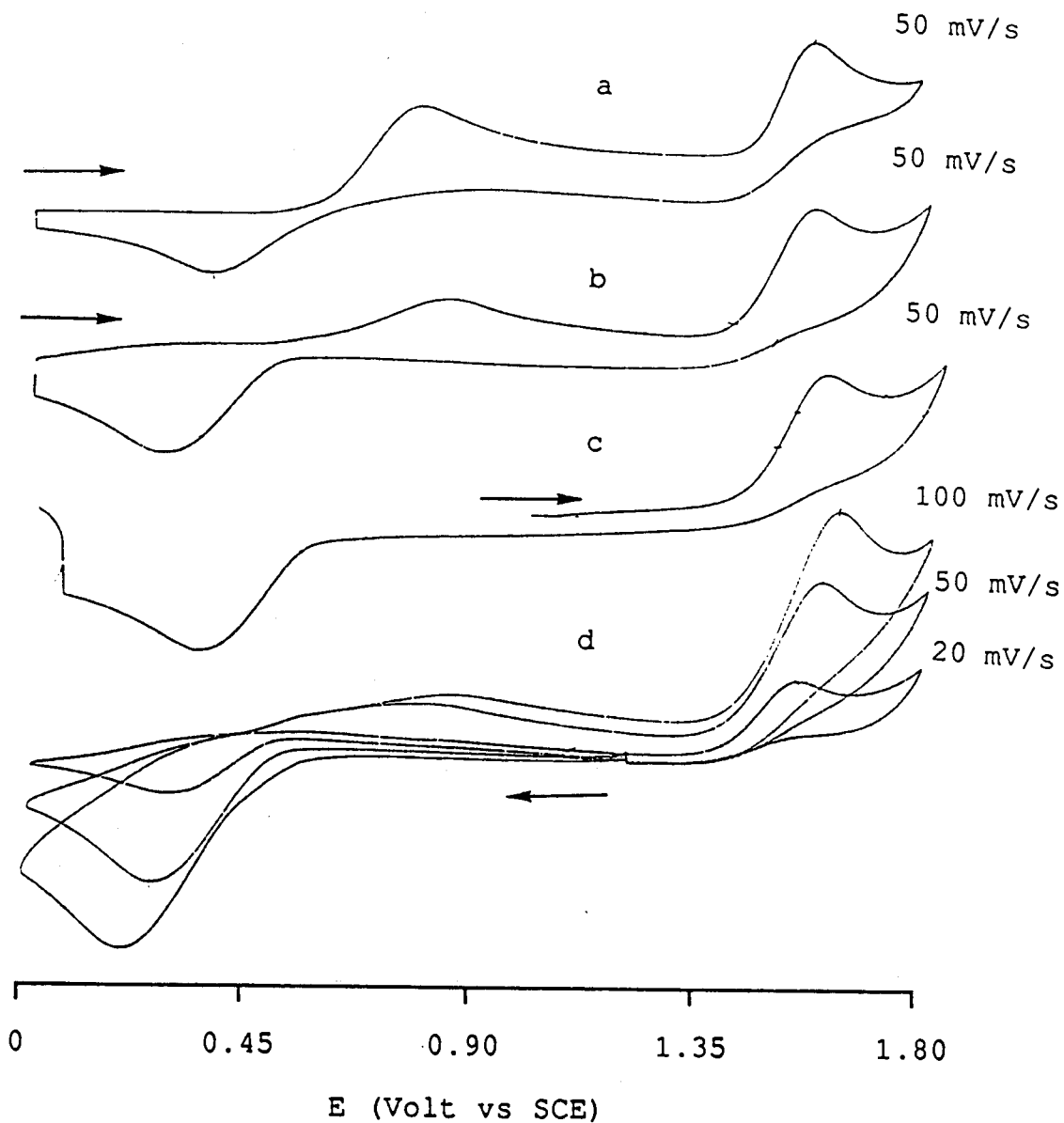
Figure 4.2.18. Cyclic voltammograms of 16Se4 (8) (1×10^{-3} M) under electrolysis. (a) without electrolysis; (b) under electrolysis; initial scanning potential of 0 V; (c) under electrolysis; initial scanning potential of 1 V; (d) under electrolysis; initial scanning potential of 1.2 V.

4.3. Discussion

4.3.1. Radical Cations

The one-electron oxidation of selenium coronands by means of $NOBF_4$ or electrolysis yields radical cations of the corresponding selenium coronands. According to frontier molecular orbital theory, an open electronic shell encountering a neutral closed shell will result in covalent stabilization from the interaction between their frontier MO's. For neutral selenium coronands, every selenium atom has two doubly occupied non-bonding orbitals (HOMO), but for the oxidized selenium atom the higher energy non-bonding orbital is singly occupied (SOMO). Therefore, it is reasonable to propose that the doubly and singly occupied non-bonding orbitals would interact with one another to give bonding (σ) and anti-bonding (σ^*) molecular orbitals which are occupied by a total of three electrons. The single electron is located in the σ^* orbital (see Figure 4.3.2).

$$(4.3.1)$$
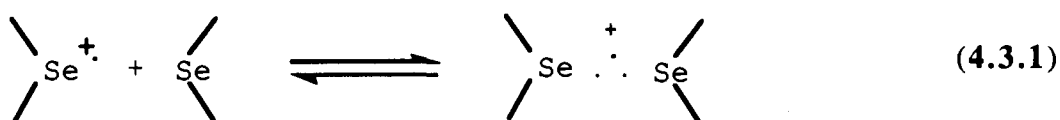
In the literature[127,128], this type of interaction is termed a two-centered three-electron (2c/3e) interaction, giving rise to a two-centered three- electron bond. Numerous compounds containing lone-pair electrons have been found that form radical cations stabilized by 2c/3e bonds through intramolecular, intermolecular and transannular interactions, as long as the HOMO-LUMO interactions are available.

Norman and co-workers[129] first reported that a dimeric cation $[R_2SSR_2]^{+\cdot}$ was formed from an ESR flow system in which dimethyl sulfide and tetrahydrothiophene were oxidized with titanium(III)-hydrogen peroxide in aqueous solution. Asmus studied the oxidation of thioethers[88,127,130-137], alkyl disulfides and iodides[138,139] with hydroxyl

radicals generated by pulse radiolysis and characterized the products by uv-visible spectroscopy. They attributed the new absorption bands to the σ-σ* transition of 2c/3e sulfur-sulfur bonds. Moreover, they have discovered that 2c/3e bonds formed between sulfur and other lone-pair donors such as N, O, Cl, Br, I, and even between RI-IR+.[140].

Asmus also found a concentration effect on the absorbance maxima of S-S 2c/3e bonds. The oxidized dithioether, 1,4-dithiane, formed two different species depending on the concentration: at concentrations greater than 10^{-3} M, the visible spectrum showed a λ_{max} near 500 nm, which is typical for dimeric cations; at lower concentrations the λ_{max} was at 660 nm, which was thought to be from a 1,4-dithiane radical cation with an intramolecular S-S bond[127].

Musker and co-workers[86,141] have found that the radical cation from 1,5-dithiacyclooctane has a very long lifetime (several days). This long life-time is attributed to the transannular interaction within the cyclooctane that had the proper geometrical arrangements to form such bonds. The x-ray crystal structure of the 8S2 dication[92,112] showed that such bonds exist.

There are examples of radical cations that involve 2c/3e bonds other than sulfur. Nelson and co-workers[142] have studied radical cations formed from alkylated hydrazines. The unpaired electron was thought to be in a π* orbital. Alder et al[143], have synthesized and studied a series of multiply bridged diamines whose lone pairs were pointing toward each other. As a consequence, oxidation resulted in an intramolecular 2c/3e bond that was a partial σ bond between two nitrogen atoms.

The first example of an alkyl selenium radical cation was found by William and co-workers[89]. The radical cation was formed by irradiating the single crystal of dimethyl selenide with γ-rays, and the resulting species was studied by ESR spectroscopy. Based on the hyperfine interaction splitting pattern they suggested the following dimeric radical cation (Figure 4.3.1) to account for thirteen equivalent splitting lines. At the time when we had prepared the crystal of 8Se2 dication, Furukawa et al[38] published their findings on the

radical cation and dication of 8Se2. In a recently published paper[113], the x-ray molecular structure of 8Se2 dication shows that a single bond has formed between the two Se atoms.

The stabilization effects due to a two-center three-electron σ bond can be understood by Hückel molecular orbital theory[128], as depicted in Figure 4.3.2, where two electrons are in the bonding orbital and one electron is in the anti-bonding orbital. The net contribution is bonding favored if the overlap integral is ignored. According to recent calculations[144], the bond strength can vary anywhere between 1 - 2 kcal/mol (for complexes of second and third row hydrides with noble gases) and 50 kcal/mol (for HF·····FH)[145]. The energy difference between bonding and anti-bonding orbitals is 2β, here β is the Hückel Coulomb integral, which dictates the electron promotion from the highest doubly occupied to the singly occupied molecular orbital. Thus, the uv-visible absorption bands are correlated to the strength of the 2c/3e bonds. If the overlap integral, S, is considered[146], the energy of the molecular orbitals becomes

$$E_\sigma = \frac{\alpha - \beta S}{1+S}$$
(4.3.2)

$$E_\sigma^* = \frac{\alpha - \beta S}{1-S}$$
(4.3.3)

The bonding level is stabilized by an amount proportional to 1/(1+S). The anti-bonding level is destabilized by an amount proportional to 1/(1-S). Because S >0, the anti-bonding level is more destabilized than the bonding level is stabilized. Thus, the interaction between two orbitals is not always bonding favored.
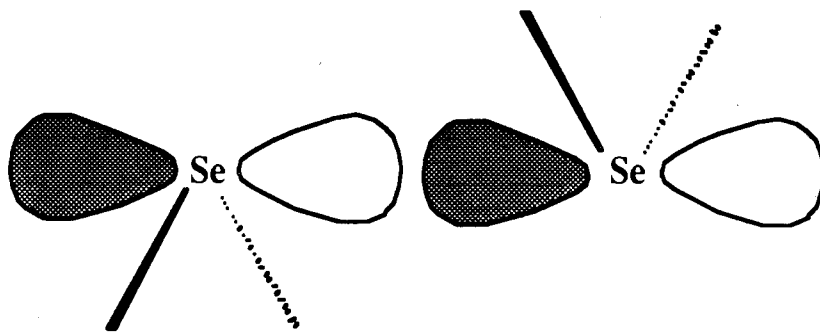
Figure 4.3.1. Anti-bonding orbital of $(Me_2Se)_2^{+\cdot}$ dimeric radical
cation.
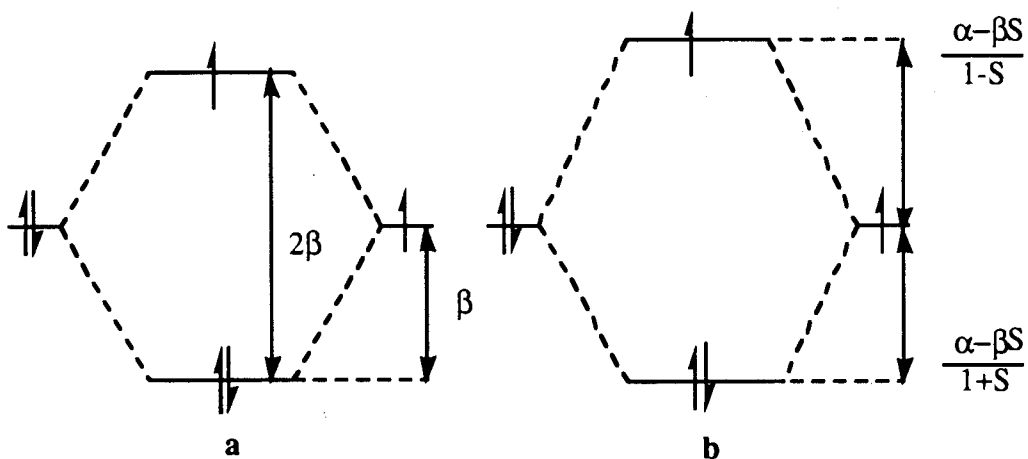
Figure 4.3.2. Orbital diagrams for two-center three-electron
interactions.(a) Overlap integral is not considered; (b) Overlap
integral is considered.

Our experimental results from the spectroscopic investigation of selenium coronand radical cations have shown that most radical cations are relatively stable at room temperature. This is the first time that selenium coronand radical cations have been detected in static conditions to the best of our knowledge. We assigned the uv-visible absorption bands of the oxidized selenium coronands to σ - σ^* transitions resulting from the 2c/3e selenium-selenium bonds. The geometrical accessibility of the interacting selenium atoms within the molecule has been unequivocally confirmed by x-ray crystallography[60]. The distances between the selenium atoms in the crystal structure are 2.669 and 2.592 Å, that is, within the sum of covalent atomic radii of selenium[147,148].

The observed concentration-dependent uv-visible absorption bands for the oxidized species of 16Se4 or 16S2Se2 have shown that there are two different radical cation species. For 16Se4, we attribute the 320 nm peak to a σ-σ^* transition of the dimeric radical cation in which the 2c/3e bond is formed through intermolecular interactions of the oxidized selenium in 16Se4 with the neutral selenium from another 16Se4 because the dimer forms only at high concentrations. The absorption band at 256 nm, that becomes the only absorption band at low concentrations of 16Se4, is attributed to a σ - σ^* transition of the 2c/3e bond formed through intramolecular (transannular) interactions.

It had been discovered previously that selenium atoms in the selenium coronand 16Se4 are exodentate[75]; the lone pair electrons are pointed out from the ring, so that the molecule adopts as many of the preferred C-Se gauche conformations as possible. Hence, it is more favored to form a 2c/3e bond through dimerization at high concentrations. At lower concentrations, there is not enough neutral 16Se4 available to form a dimeric radical cation; only a monomeric radical cation is observed. Besides, the intramolecular 2c/3e bonds are more stable for 16Se4 and 16S2Se2; therefore, the species absorbing at 320 nm eventually converts to the species that absorbs at 256 nm. The lack of concentration effects for the radical cations of other selenium coronands indicates that in those radical cations the stabilization contributions are most likely from transannular interactions.

Based on Hückel theory, the absorbance maxima of radical cations correlate with the strength of the 2c/3e bond. One of the factors which controls the strength of a covalent bond is the extent of p orbital overlap along the interaction coordinate. Accordingly, the energy difference between the σ and σ* levels, and hence the position of the absorbance maximum of a σ-σ* transition, is expected to depend on the distance between the two interacting atoms[149,150]. All selenium coronand radical cations investigated so far absorb at 350-260 nm except those derived from eight-membered ring selenium coronands (400 nm). This indicates a large energy splitting between the σ and σ* energy levels. Such effectiveness in the overlap between the interacting orbitals of selenium atoms can be attributed to the flexibility of the macrocyclic ring.

In principle, all compounds containing atoms with lone pairs can form two center three-electron (2c/3e) bonds of the type depicted in Equation 4.3.1. However, in the literature, the radical cations derived from sulfides which consist of small ring or acyclic di- and trithiaethers are not stable enough to be observed under static conditions in solution and hence the technique of pulse radiolysis was applied for their investigation. In addition, the absorbance maxima of these multithioethers are around 500 to 650 nm[128], an indication that the overlap is not effective. Only 8S2 is an exception. 8S2 is an eight-membered ring compound and the overlap between S atoms is good; therefore, it is relatively stable and can be detected by absorption spectroscopy (λmax is 428 nm, which is almost the same as that of 8Se2) under the static condition. Asmus has proposed that because radical cation complexes are in equilibrium (as shown in Eq 4.3.1) the intermolecular distance and the extent of p-orbital overlap cannot be considered as constant. Therefore, it seems reasonable to expect a greater degree of molecular mobility in intermolecular radical cation complexes as compared to intramolecular radical cation complexes.

Structural requirements for overlap between two lone-pair orbitals are clearly demonstrated. Selenium coronands 12Se4 and dibenzo-14Se4 cannot form radical cations stable enough to allow the observation of uv-visible absorptions under the experimental

conditions, because forming intramolecular two-center three-electron bonds for these two coronands will result in highly strained rings. Our results indicate that the intramolecular selenium-selenium 2c/3e bonds are more important in stabilizing the radical cations.

UV-visible spectroscopic data of the dication 8Se2 provides information on the character of the third unpaired electron. This species absorbs at 248 nm indicating a further splitting between the σ and σ^* energy levels as a result of removing an electron from an anti-bonding orbital, as compared with the radical cation 8Se2$^{+\cdot}$ (428 nm). The dication of 16Se4 has two absorbance maxima. That indicates that there may be more than one electron configuration for the compound or that the two Se-Se bonds may have different bond strength.

Results of the cyclic voltammetric study on selenium coronands demonstrated that the stabilization contribution from transannular interactions is a balance between the strength of the newly formed bond and the ring strain resulting from the new bond. These are two opposing effects. In order to have maximum overlap of orbitals to form a stable covalent bond, the molecule needs some structural reorientation so that the involved heteroatoms can be brought in to bonding distances. However, this structural reorientation may compress some bond angles and dihedral angles, and introduce ring strain that may attenuate or even cancel the stability contributed by the transannular interactions. These effects are reflected in the results of cyclic voltammetry.

Based on the appearance of the cyclic voltammograms three groups can be identified: (a) those which have one redox cycle wave; (b) those which have two redox cycle waves; and (c) those which have one irreversible wave (although they may be in the same group, individual selenium coronands still show some differences in the extent of reversibility). These differences can be understood by examining the structures of these selenium coronands.

8Se2 and 8Se2(Me)$_2$ belong to the first group and show the most reversible electrode behavior among the selenium coronands. Both selenium coronands show lower

redox potentials ($E_{1/2}$) that can be attributed to the Se-Se transannular interaction forming a two-centered three-electron covalent bond[88,133]. Evidence has shown that thia- or selena-heterocyclic rings which can have transannular interactions to achieve extra stabilization possess low redox potentials[151,152], e.g., 8S2, 5-methyl-1-thia-5-azacyclooctane [86,141,152,153] and 5H,7H-dibenzo[b,g][1,5]selenathiocin[93,154].

Because the single electron is in the anti-bonding orbital, removal of the second electron electrochemically should not be more difficult than removal of the first one, unless massive structural reorganization is involved. This was observed for 8Se2. Although only one pair of redox waves is observed for each compound, the results of controlled electrolysis reveal that the oxidation is a two-electron transfer process. This means that the second redox potential is the same as or lower than the first one ($E_1^O \geq E_2^O$)[155]. According to the x-ray structure of 8Se2 dication, no significant structural change is needed in order to form the Se-Se σ bond. The redox potentials of substituted selenium coronands, 8Se2(Me)$_2$ and 8Se2OH, are higher than that of 8Se2. The differences may be attributed to the interactions between the substituents with the Se-Se bonds, which attenuate the transannular interaction. For 24Se6, considering the size of the ring, forming a Se-Se bond within the molecule probably involves significant structural reorientation; therefore, it has a higher redox potential. If one uses resonance structures to represent the transannular interaction within the molecule, Figure 4.3.3 shows that 14Se4 has cyclopentane-type and cyclobutane-type interactions. The latter will increase the ring strain and is not a favorable contribution. This explains why the electron transfer on the electrode is quasi-reversible with a large peak potential separation. For 12Se4 and dibenzo-14Se4, such transannular interactions would produce highly strained rings, which outweigh the stabilizing contributions from the transannular interactions. Therefore, irreversible redox cyclic voltammograms are observed.
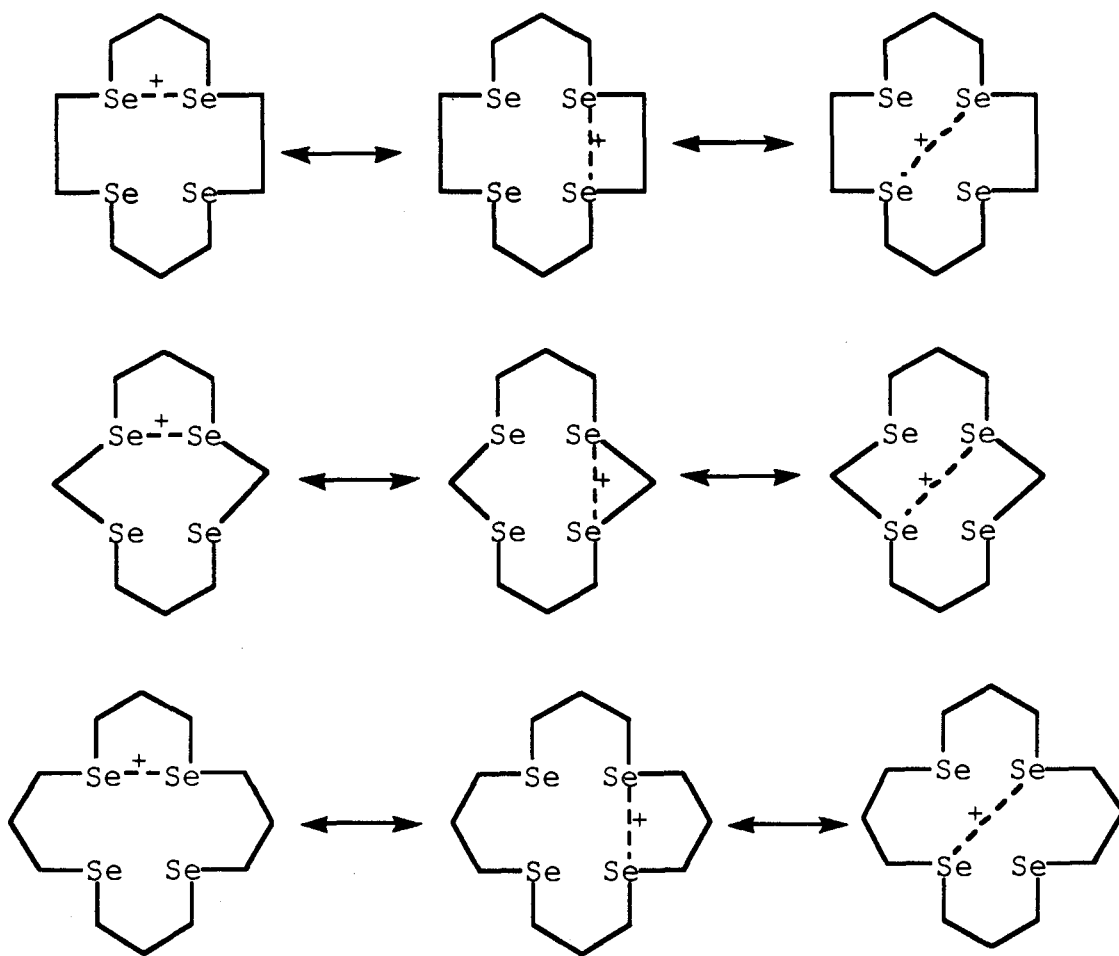
Figure 4.3.3. Resonance structures for radical cations of 14Se4, 12Se4 and 16Se4.

As mentioned earlier, the reversibility as shown by the cyclic voltammogram is an indicator of the ease of the electrode process. For a quasi-reversible electrode reaction, the separation of peaks is a function of a dimensionless parameter Ψ which correlates with the electron transfer rate constant[114]

$$\Delta E_p = f(\Psi) \qquad (4.3.4)$$

$$\Psi = \frac{k^o(RT)^{1/2}}{(nFD\pi\upsilon)^{1/2}} \qquad (4.3.5)$$

Here, k^o is the standard rate constant for an electron transfer couple (cm s^{-1}) (k^o is a hetero-electron transfer rate constant; it has a unit of distance); n is the number of electrons involved in the overall electrode reaction; F is the Faraday constant; R is the gas constant; υ is the potential scan rate; D is the diffusion coefficient and T is the temperature in Kelvin. Thus, for selenium coronands at a given scan rate, the separation of the peaks on the cyclic voltammograms is directly correlated with the standard rate constant of electron transfer on the electrode.

It is conceivable that for 8Se2 (**16**) which involves the least structural reorientation, the electron transfer is fast on the electrode and the peak separation is small. On the other hand, 14Se4 and 24Se6 need major conformational rearrangement; thus, electron transfer is slow and the peak separation is larger.

Cyclic voltammograms of 16Se4 (**8**), 16Se4(OH)$_2$ (**9**) and 12Se3 (**18**) suggest that the processes consist of two consecutive one-electron transfer steps and the second redox potential is higher than the first one. Taking 16Se4 (**8**) as an example, comparison of the x-ray structures of 16Se4 (**8**) and 16Se4 dication indicates that there are significant structural differences. The crystal structure of **8** shows a rectangular conformation with two selenium atoms located at the diagonal corners. In this conformation the macrocycle has most of the C-Se bonds in the preferential gauche conformations[75]. However, this conformation is drastically changed in the 16Se4 dication in which three selenium atoms

121

are bonded linearly[60]. In such an arrangement, the positive charges are on the two outside selenium atoms to achieve the best separation. The fourth selenium atom interacts with the central selenium atom with van der Waals forces so that the positive charges are dispersed among the four selenium atoms. In solution this is also likely to be the case, and probably the positive charge in the 16Se4 radical cation is delocalized among the selenium atoms, as suggested by Asmus[127,133] for the case of the sulfur analogs. This likely results in significant changes in the conformation of 16Se4 and hence a higher redox potential for the second electron transfer step.

4.3.2. Homogeneous Reaction of 16Se4 (8)

The results of coulometry on 16Se4 show how the dication of 16Se4 (8) is formed. There are two possible routes to the dication of **8**. One is by consecutive oxidation of 16Se4$^{+\cdot}$; i. e., 16Se4 is first oxidized to 16Se4$^{+\cdot}$, then to 16Se4^{2+}, as shown in Equation 4.3.4 and 4.3.5. The other is through disproportionation of 16Se4$^{+\cdot}$ in solution after the first oxidation step, as shown in the following equations.

$$16Se4 - e \longrightarrow 16Se4^{+\cdot} \tag{4.3.6}$$

$$16Se4^{+\cdot} + 16Se4^{+\cdot} \rightleftharpoons 16Se4^{2+} + 16Se4 \tag{4.3.7}$$
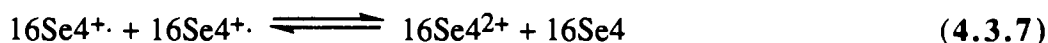
At the applied potential of 0.8 V, which is higher than the first oxidation peak potential (E_{ap}^{1}) that oxidizes 16Se4 (8) to 16Se4$^{+\cdot}$ but lower than the second oxidation peak potential (E_{ap}^{2}) that oxidizes 16Se4$^{+\cdot}$ to 16Se4^{2+}, no 16Se4^{2+} should be produced electrochemically because the potential is not enough to oxidize 16Se4$^{+\cdot}$. Therefore, at that potential the total number of electrons involved in the reaction should be one. However, if there were a disproportionation reaction, the total number of electrons involved in the reaction would be two even if the potential was not enough to oxidize 16Se4$^{+\cdot}$ to 16Se4^{2+} because 16Se4 could be regenerated through reaction (4.3.7).

The experimental result revealed that only one electron is involved in the electrolysis at a potential of 0.8 V vs SCE, and two electrons are involved at a potential of 1.8 V, which unequivocally suggested that the whole process of oxidizing 16Se4 to 16Se4^{2+} was a two-step oxidation, and each step was a single electron transfer process. The redox potentials of 16Se4 also imply that disproportionation is not important. The equilibrium constant K of the reaction (Eq. 4.3.7) can be calculated as follows,

$$\ln K = \frac{F}{RT} (E^2_{1/2} - E^1_{1/2}) \qquad (4.3.8)$$

where K is the equilibrium constant of the disproportionation reaction; $E^1_{1/2}$ and $E^2_{1/2}$ are the redox potentials of the first and second step electrode reactions; and the other symbols have the usual meanings. Substituting $E^1_{1/2}$ and $E^2_{1/2}$ of 16Se4 gives

$$\ln K = \frac{F}{RT} (E^1_{1/2} - E^2_{1/2})$$

$$= \frac{96500}{8.31*298}(0.508 - 1.41) = -35.1 \qquad (4.3.9)$$

$$K = 5.71 \times 10^{-16}.$$

Thus, the disproportionation reaction is not favored.

The electrolyzed 16Se4 solution prepared by electrolysis of the 16Se4 solution at 1.2 V vs SCE has an absorbance maximum at 256 nm, which is presumably an absorption due to a 16Se4 radical cation. The cyclic voltammetry on this solution gave rise to similar cyclic voltammograms as those from an 16Se4 solution, indicating that the species which absorbs at 256 nm is the radical cation (monomeric) which can be further oxidized to the dication at a higher potential or reduced to the neutral 16Se4 at a more negative potential.

What is the species that has an absorbance maximum at 320 nm? When 16Se4 loses one electron to the electrode, the resulting species, the radical cation, is a reactive intermediate. The radical cation of 16Se4 would undergo further reactions. Experimental

results of both cyclic voltammetry and spectroscopy of 16Se4 indicate that there are chemical reactions involved after the electron transfer reaction. The chemical reaction after the oxidation of 16Se4 is likely a dimerization reaction because concentration effects are observed.

In electrochemistry, if a chemical reaction occurs following the electron transfer it is termed an EC system [126]. The first letter designates the electron transfer, and the second, the following chemical reaction. Because of the following reaction, the concentration of the oxidized species $16Se4^{+\cdot}$ at the vicinity of the electrode changes and the cyclic voltammogram of 16Se4 may be consequently changed should the time scale of the reaction be comparable to that of cyclic voltammetry. The time window of the cyclic voltammetry can be adjusted by changing scan rates and the concentrations of 16Se4.

The concentration-dependent phenomenon indicates the following reaction is a second order reaction. Combined with the information from uv-visible spectroscopy as well as that from cyclic voltammetry, the system may be depicted as follows.

Scheme 4.3.1

$$16Se4 - e \rightleftharpoons [16Se4^{+\cdot}] \qquad\qquad (4.3.10)$$

$$[16Se4^{+\cdot}] + 16Se4 \underset{k_{-1}}{\overset{k_1}{\rightleftharpoons}} (16Se4)_2^{+\cdot} \quad 320\ nm \qquad (4.3.11)$$

$$[16Se4^{+\cdot}] \underset{k_{-2}}{\overset{k_2}{\rightleftharpoons}} 16Se4^{+\cdot} \quad 256\ nm \qquad\qquad (4.3.12)$$

$$(16Se4)_2^{+\cdot} \overset{k_f}{\longrightarrow} 16Se4^{+\cdot} + 16Se4 \qquad (4.3.13)$$
$$320\ nm \qquad\qquad 256\ nm$$

$$16Se4^{+\cdot} - e \rightleftharpoons 16Se4^{2+} \qquad\qquad (4.3.14)$$

124
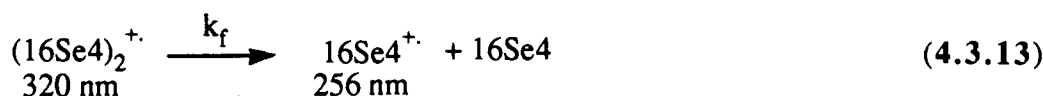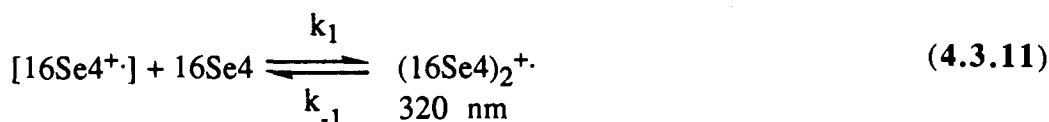
In this scheme, [16Se4$^{+\cdot}$] is the 16Se4 radical cation immediately after being formed on the electrodes which undergoes either dimerization with another 16Se4 or structural reorganization through transannular interaction. The absorption peak at 256 nm is assigned to the 16Se4 radical cation that is in monomeric form because only this species is observed in the uv-visible spectrum when the concentration of 16Se4 is dilute, no matter whether the oxidant is NOBF$_4$ or a Pt electrode. The [16Se4$^{+\cdot}$] reacts with a neutral 16Se4 to form a dimeric radical cation that is assigned to the absorption peak at 320 nm. At low concentrations of 16Se4, the reaction 4.3.13 is slow; therefore, the ratio of cathodic to anodic peaks (i_c/i_a) is close to unity. However, at high concentrations of 16Se4, the reaction 4.3.13 becomes important; hence, the value of i_c/i_a deviates from unity. The dependence of the ratio of i_c/i_a on the potential scan rates is also explained. At the fast scan rates the reduction of the radical cation is predominant and results in a larger i_c/i_a ratio, whereas at slow scan rates the chemical reaction competes with the electron transfer reaction and leads to a smaller i_c/i_a ratio.

The peak potential shifts in the cyclic voltammograms of 16Se4 also indicate a chemical reaction following the electrode oxidation. The cyclic voltammetric response for such a reaction system is dependent on both the rate of electron transfer on the electrode and the rate of chemical reaction. Two dimensionless parameters (Λ and λ) can be used to define such a system[114].

$$\Lambda = \frac{k^{\circ}}{v^{1/2}} \left(\frac{RT}{DnF}\right)^{1/2} \qquad (4.3.15)$$

$$\lambda = \frac{k_f}{v} \frac{RT}{nF} \qquad (4.3.16)$$

Here, k$^\circ$ is the rate of electron transfer on the electrode; υ is the scan rate; D is the diffusion coefficient of the substrate; k_f is the rate of chemical reaction and the other symbols have their normal meaning. Based on the combination of Λ and λ values, Saveant has defined the EC system in different zones[156]. For example, a reversible electron transfer coupled

with an irreversible chemical reaction would remain as a reversible cyclic voltammogram when the value of λ is small ($\lambda < -1$); however, when λ is large($0.5 < \lambda < 5.5$) the anodic peak potential would shift with increasing υ according to

$$E_p = E_{1/2} - \frac{RT}{nF} 0.78 + \frac{RT}{2nF} \ln \lambda \qquad (4.3.17)$$

so that the wave shifts towards positive potentials by about 30/n mV (at 25 °C) for a tenfold increase in υ. For a quasi-reversible electrode reaction ($\Lambda \neq \infty$) coupled with an irreversible chemical reaction, increasing the scan rate by tenfold, the peak potential shift would be 59/n mV (at 25°C). Therefore, peak potentials can be used as diagnostic parameters to analyze the chemical reaction following the electrochemical step. In addition, for a second-order chemical reaction the concentration dependence of the corresponding cyclic voltammograms is also a diagnostic parameter: with decreasing substrate concentrations, reversible current-voltage curves are observed even at low sweep rates.

Quantitative evaluation of the rate constant is possible with the aid of calculated working curves[126,157,158]. There are established methods[126] to estimate the rate constants of chemical reactions involved in electrode reactions. Through theoretical calculations Nicholson[157,159-161] established the working curve for the subsequent reaction as shown in Figure 4.3.4 where i_c/i_a is plotted versus $\ln(k\tau)$, where τ is the time in seconds from $E_{1/2}$ to the switching potential and k is the rate constant for the chemical reaction. The working curve implies that for an EC system a constant value of the parameter $k\tau$ corresponds to a constant i_c/i_a ratio.

Assuming Equation 4.3.14 is the rate-determining step, and Equations 4.3.12 and 4.3.13 are in equilibrium, the overall rate of the chemical reactions can be expressed as

$$\frac{d[(16Se4)_2^{+\cdot}]}{dt} = k_f \frac{K_1}{K_2} [16Se4]\{[16Se4^{+\cdot}]\} \qquad (4.3.18)$$

$$k_{obs} = k_f \frac{K_1}{K_2} [16Se4] \qquad (4.3.19)$$

Where K_1 and K_2 are the equilibrium constants of the reactions 4.3.12 and 4.3.13. Comparison of the concentration of 16Se4$^{+\cdot}$ with that of 16Se4, indicates that the concentration of 16Se4 is in excess and is constant during the reaction. Thus, the system can be further simplified as a pseudo-first order chemical reaction. From the experimental data, i. e., the ratios of cathodic peak current to anodic peak current i_c/i_a, $k_{obs}\tau$ values were determined on the working curve. Then, the k_{obs} values for various concentrations of 16Se4 were obtained from the slope by plotting $k_{obs}\tau$ as a function of τ, as shown in Figure 4.3.5. A plot of k_{obs} versus the concentrations of the 16Se4 is shown in Figure 4.3.6, in which the error bars are 20%.

Two major sources may cause the errors in this estimation. One is from the determination of the τ values. This is because, in the sense of electrochemistry, the system of interest is not a reversible one; $E_{1/2}$ calculated by $(E_{pc} + E_{pa})/2$ (at a scan rate of 20 mV/s) might not be a true $E_{1/2}$, although Rorabacher has noted that the $E_{1/2}$ values of a series of Cu(II) thia-macrocyclic compounds, which are determined by $(E_{pc} + E_{pa})/2$ from cyclic voltammograms of slow scan rates, are close to those determined by potentialstatic measurements (of ~±10% error)[162]. The uncertainty in $E_{1/2}$ results in the uncertainty in the values of τ. Nicholson et al[157,159-161] pointed out that this method is sensitive to the values of τ. Another source of error is from the determination of i_{pc}/i_{pa}, especially when the concentrations of 16Se4 are low, which is probably why the first point (at the left end of the x-axis) in Figure 4.3.6 deviates from linearity, and it is not used in the determination of the $k_f\frac{K_1}{K_2}$ value. The value of $k_f\frac{K_1}{K_2}$ is found to be 2.1 ± 0.6 s^{-1}M^{-1} from the slope of the plot of k_{obs} versus the concentrations of 16Se4 (Figure 4.3.6).

In conclusion, the radical cations of selenium coronands were prepared chemically and electrochemically and identified by uv-visible spectroscopy. Cyclic voltammetry of these selenium coronands was carried out in CH_3CN. The relatively reversible behavior on electrodes and the stability of the radical cations are attributed to the formation of a two-center three-electron bond within a radical cation (transannular interaction) or between a

radical cation and a neutral coronand. 16Se4 has been studied in detail. Its whole process of cyclic voltammetry with two redox pairs consists of two single electron transfer processes with $E^1_{1/2}$ 0.503 V and $E^2_{1/2}$ 1.41 V respectively. Therefore, the disproportionation of the radical cation of 16Se4 to form 16Se4^{2+} can be ruled out. Scheme 4.3.2 summarizes the electrode processes of 16Se4 and 16Se4$^{+\cdot}$ as well as the homogeneous reactions of 16Se4$^{+\cdot}$ in CH$_3$CN solution.

Scheme 4.3.2

$$16Se4 \underset{+e}{\overset{-e}{\rightleftharpoons}} [16Se4^{+\cdot}] \underset{-16Se4}{\overset{+16Se4}{\rightleftharpoons}} (16Se4)_2^{+\cdot}$$

322 nm

Transannular interactions

$$16Se4^{+\cdot} \underset{+e}{\overset{-e}{\rightleftharpoons}} 16Se4^{2+}$$

256 nm   322 & 256 nm
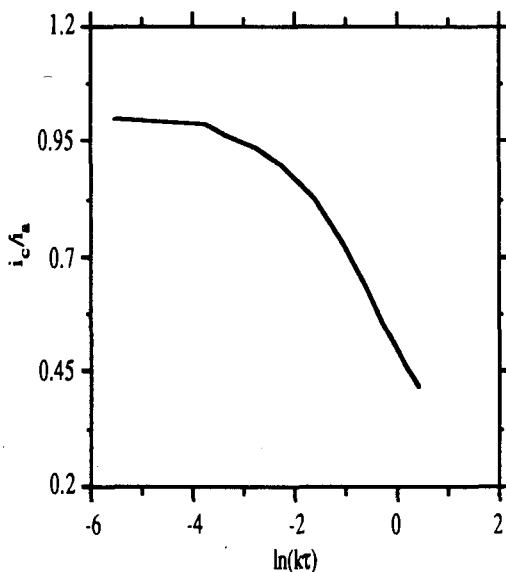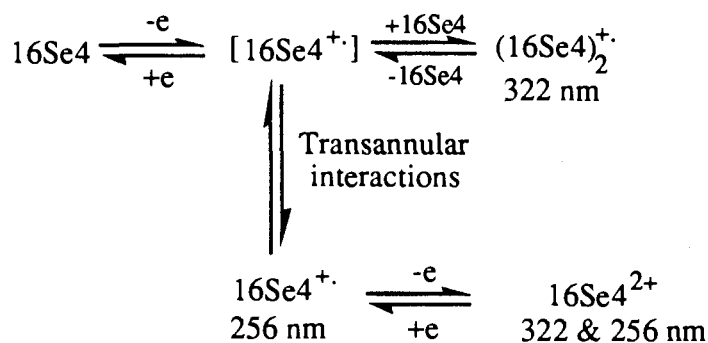
Figure 4.3.4. Working curve for a chemical reaction following an electrode reaction (EC).

128
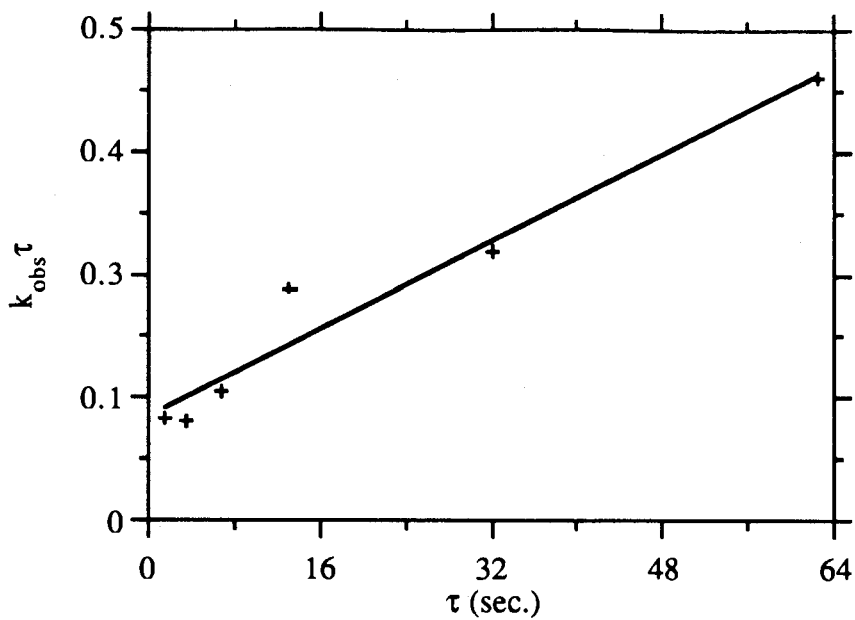
Figure 4.3.5. Plot of k_{obs} vs τ.
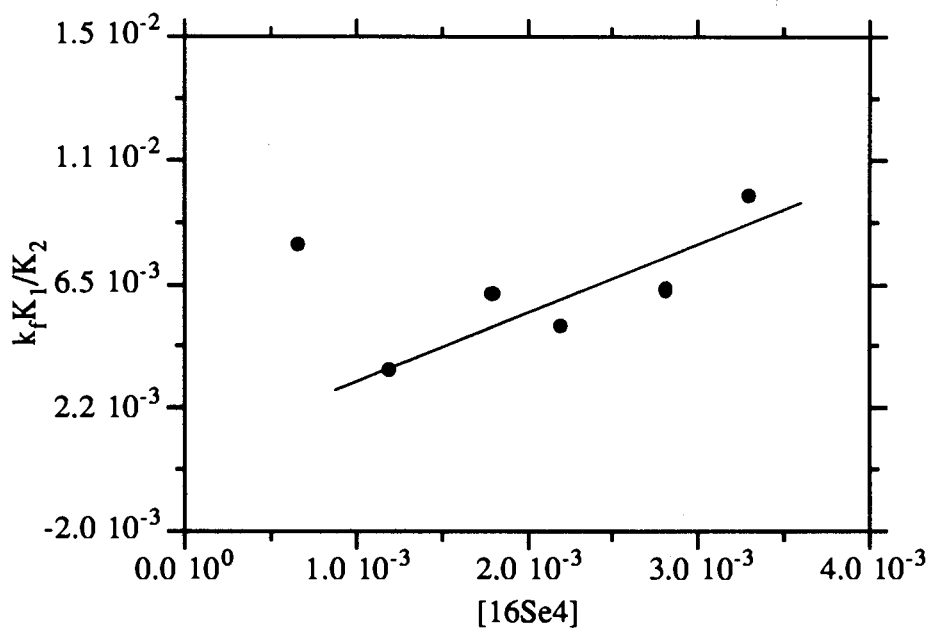
Figure 4.3.6. Determination of K_1/K_2k_f.

129

CHAPTER V
METAL ION COMPLEXES OF SELENIUM CORONANDS

5.1. Introduction

Investigation of the coordination chemistry of selenium coronands in this thesis focuses on their complexation with Cu(II) and Pd(II) ions. It includes the preparation of the complexes and their structural characterization by micro-analysis, x-ray crystallography and spectroscopic methods (uv-visible, ESR and NMR). Cyclic voltammetry is used for the study of the redox properties of the complexes.

Although x-ray crystallography gives the most unambiguous structural information about the complexes in the solid state, in solution the complexes may exist in some other forms. Besides, a good quality single crystal is not always available. Hence, uv-visible spectroscopy is a very useful means for characterization of the complexes in solution. The complexes of selenium coronands and metal ions have a strong absorption (e.g., peaks around 460 nm for Cu(II) complexes) which is assigned to the charge transfer transition between ligands and the metal ions[12]. The absorption is strong and characteristic for particular a metal ion, which makes it particularly useful to identify the complexes, determine the composition of the complexes and follow the reaction progress in solution.

The cyclic voltammetric study of the Pd(II) and Cu(II) complexes gives their redox potentials or peak potentials. The information about electron transfer on electrodes (Pt or carbon electrode) would be obtained in terms of reversible, quasireversible and irreversible processes through analysis of the cyclic voltammograms of the complexes. From the shape of the cyclic voltammograms, information about intermediates or conformational changes of the complexes during the electron transfer reaction could be obtained[162].

As indicated before, the complex [Cu(16Se4)][SO$_3$CF$_3$]$_2$ (21) is not stable in organic solvent[60]. It undergoes a spontaneous redox reaction to give the corresponding

130

Cu(I) complex and dication of 16Se4. This redox reaction is unique to Cu(II) complexes of selenium coronands, because the Cu(II) complexes of the sulfur analogs are stable[163,164]. Kinetics of the redox reaction has been studied, from which the rate law and stoichiometry of the reaction have been established. A mechanism for the redox reaction has been proposed.

5.2. Complexes of Pd(II) and Selenium Coronands

5.2.1. Results

5.2.1.1. Preparation of Pd(II) Complexes of Some Selenium Coronands

Pd(II) and selenium coronand complexes were prepared by direct insertion of Pd^{2+} ion into selenium coronands[18], i.e., by mixing $PdCl_2$ with the corresponding selenium coronands (16Se4 and 24Se6) in CH_3CN, in the presence of excess $NaBF_4$. The mixed solution was stirred and filtered into a vial. Crystals of the complexes were formed by allowing ether vapor to diffuse into the above solution and were isolated by filtration.

[Pd(16Se4)][BF$_4$]$_2$ (34) was prepared by the method as described above, and was isolated as yellow crystals. When the stirring time was short, the anion exchange was not complete, and [Pd(16Se4)]ClBF$_4$ (35) was also isolated as red crystals.

X-ray crystal structures of the cation of 34 (Figure 5.2.1) and 35 (Figure 5.2.2) show that both 34 and 35 contain the complex cation [Pd(16Se4)]$^{2+}$ in which Pd is centrally bound by the four Se atoms in a square-planar arrangement. In either case the configuration of the complex cation can be described as c,c,c[165] (i.e. the non-bonding electron pairs of all four Se atoms are directed towards one side of the coordination plane). In the case of 34 a crystallographic mirror plane bisects the molecule, passing through atoms Pd, C(1) and C(9). In both cases, however, the cation has approximate mm (C_{2v}) symmetry. The molecular conformation (characterized by the bond and torsion angles

given in Tables 5.2.1 and 5.2.2) can be described as having alternate chair and boat forms of the fused six-membered metallocyles about Pd. In **34**, the Pd atom deviates from the precise plane of the four Se atoms by 0.045(2) Å, while in **35** the Pd atom is 0.2422(5) Å from the best least-squares plane through the four Se atoms which themselves deviate slightly (±0.032(1) Å) from coplanarity. Curiously, all the non-hydrogen atoms of the cation lie on the same side of the Se4 plane in both structures.

UV-visible absorption measurements were made on the solutions that were prepared by dissolving the crystals of **34, 35** in CH_3CN separately. Both complexes **34, 35** formed yellow solutions. The UV-visible spectra of **34** and **35** were similar; λ_{max}(nm(ε)): **34**, 314 (26758), 210 (8409); **35**, 314 (19949), 210 (6548).

$[Pd_2(24Se6)Cl_2][BF_4]_2$ (**36**). Ligand 24Se6 (**15**) and $PdCl_2$ in a 1:2 ratio were mixed in an CH_3CN solution and the corresponding binuclear Pd complex was obtained as yellow crystal with empirical formula $[Pd_2(24Se6)Cl_2][BF_4]_2$ (**36**).

Selected bond distances and angles for the complex cation ($[Pd_2(24Se6)Cl_2]$) are listed in Table 5.2.3 and the molecule is shown in Figure 5.2.3. While the cation has no crystallographic point symmetry it roughly approximates m (C_s) molecular point symmetry where the Pd, Cl, Se(5) and Se(17) atoms lie approximately in the local mirror plane. This approximate symmetry is exemplified by the sequence of C-Se-C-C and Se-C-C-C bond torsion angles around the 24Se6 ring which define its conformation. Qualitatively this sequence can be described as $AG^-G^+G^+AG^-AAG^+G^+G^-AAG^+G^-G^-AAG^+AG^-G^-G^+A$ (where A represents *anti* and G^+ and G^- represent positive and negative *gauche* relationships) starting with the C(4)-Se(5)-C(6)-C(7) (*anti*) and proceeding counter-clockwise around the ring as shown in Figure 5.2.3. The configuration might be described as *UDU,DUD* (*U* and *D* denote the non-bonding electron pairs of Se atoms pointing up or down of the coordination plane) to describe the stereochemical arrangements of the selenium atoms' lone pairs of electrons. The four six-membered metallocyles are all in approximate chair conformations.

Both Pd environments are approximately square planar but show significant pyramidal distortion. The two square planes have a relative dihedral of approximately 48° and the chlorine atoms protrude from opposite sides of the 24Se6 ring, similarly to those in the complex cation[23] $[Pd_2Cl_2([18]aneN_2S_4)]^{2+}$. There are no intramolecular interactions either between the palladium atoms or between a palladium atom and the chlorine atom bound to the other Pd atom.

UV-visible absorption measurements were made on a yellow solution that was prepared by dissolving the crystal of **36** in CH_3CN; $\lambda_{max}(nm(\varepsilon))$: 366 (4837), 294 (24838), 216 (13145).
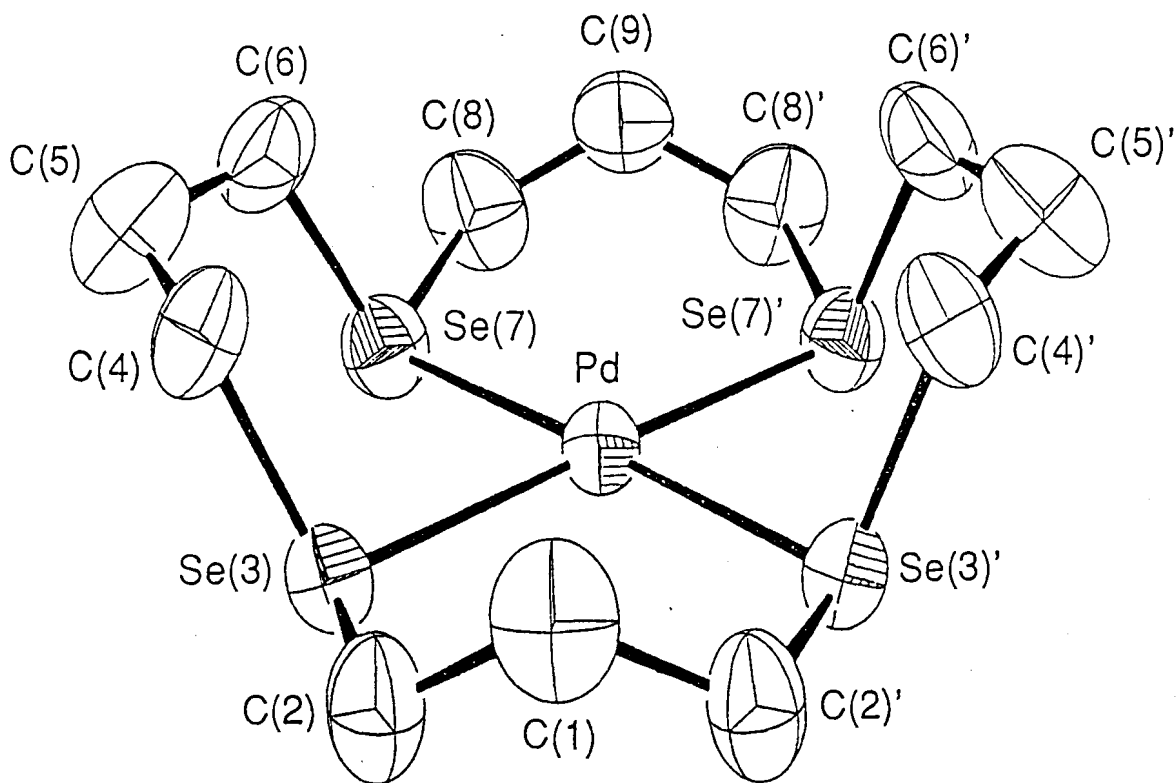
Figure 5.2.1. The molecular structure of $[Pd(16Se4)][BF_4]_2$ (34) from x-ray crystallography. 50% enclosure thermal ellipsoids are shown. Hydrogen atoms have been omitted for clarity.
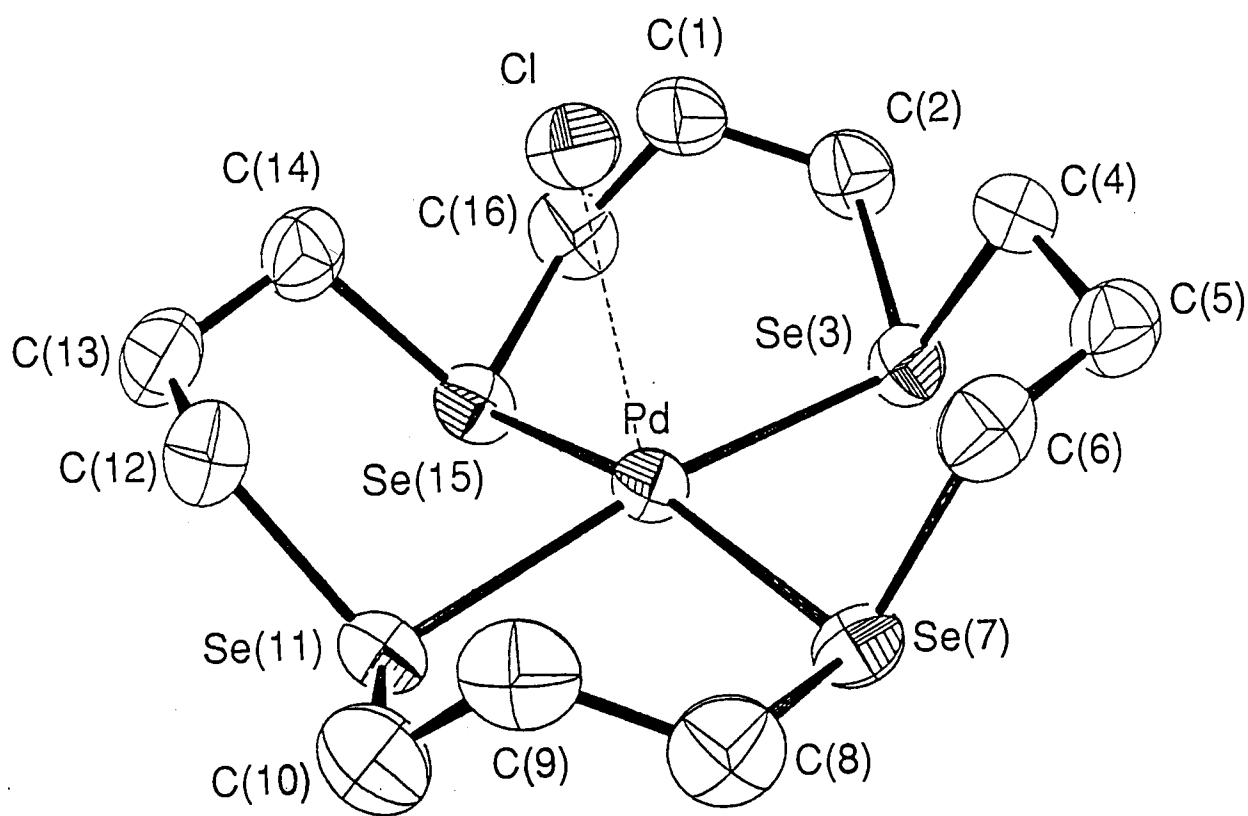
Figure 5.2.2. The molecular structure of [Pd(16Se4)Cl][BF$_4$] (35) from x-ray crystallography. 50% enclosure thermal ellipsoids are shown. Hydrogen atoms have been omitted for clarity.
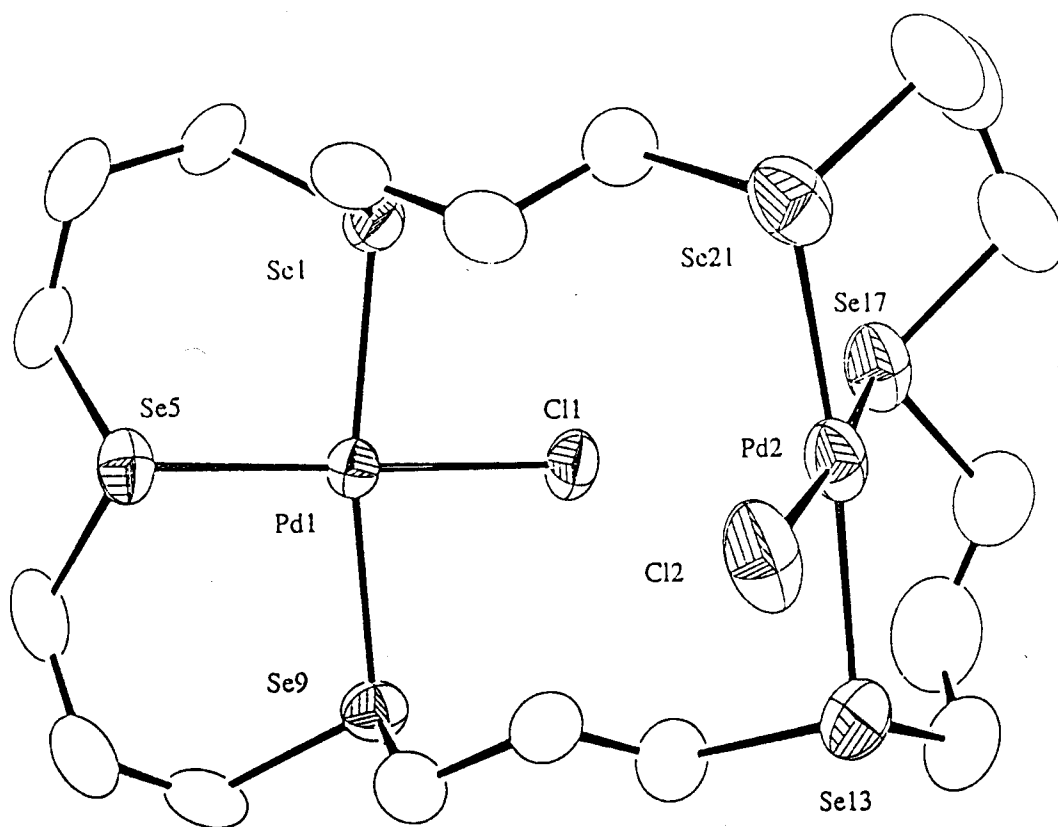
Figure 5.2.3. The molecular structure of $[(PdCl)_2(24Se6)]^{2+}$ (36). 50% enclosure thermal ellipsoids are shown. Hydrogen atoms have been omitted for clarity.

Table 5.2.1. Selected Bond Distances (Å) , Bond Angles and Torsion Angles (°) for [Pd(16Se4)]$^{2+}$ (34)

Bond Distances (Å)

Pd	Se(3)	2.423(1) {2.429}[a]	Pd	Se(7)	2.432(1) {2.438}
Se(3)	C(2)	1.94(1)	Se(7)	C(6)	1.96(1)
Se(3)	C(4)	1.94(1)	Se(7)	C(8)	1.945(9)
C(1)	C(2)	1.45(1)	C(5)	C(6)	1.51(2)
C(4)	C(5)	1.52(1)	C(8)	C(9)	1.51(1)

Bond Angles (°)

Se(3)	Pd	Se(3)'[b]	98.67(7)	C(4)	Se(3)	Pd	99.5(3)
Se(7)	Pd	Se(3)	81.27(4)	C(4)	Se(3)	C(2)	98.6(5)
Se(7)	Pd	Se(3)'	177.90(7)	C(6)	Se(7)	Pd	100.3(4)
Se(7)	Pd	Se(7)'	98.71(7)	C(8)	Se(7)	Pd	112.3(3)
C(2)	Se(3)	Pd	112.8(3)	C(8)	Se(7)	C(6)	98.1(5)
C(1)	C(2)	Se(3)	119.2(10)	C(2)	C(1)	C(2)'	119.4(17)
C(5)	C(4)	Se(3)	111.9(8)	C(6)	C(5)	C(4)	118.4(11)
C(5)	C(6)	Se(7)	113.4(8)	C(8)	C(9)	C(8)'	112.2(14)
C(9)	C(8)	Se(7)	116.8(9)				

Torsion Angles (°)

C(2)	Se(3)	C(4)	C(5)	-168.4(10)
C(2)'	C(1)	C(2)	Se(3)	-74.2(9)
C(4)	Se(3)	C(2)	C(1)	-78.7(8)
Se(3)	C(4)	C(5)	C(6)	-67.8(8)
Se(3)	Pd	Se(7)	C(6)	68.9(4)
Se(3)	Pd	Se(7)	C(8)	172.1(3)
Se(3)'	Pd	Se(3)	C(2)	7.6(3)
Se(3)'	Pd	Se(3)	C(4)	111.1(3)
Se(7)	Pd	Se(3)	C(2)	-174.6(4)
Se(7)	Pd	Se(3)	C(4)	-71.0(3)
C(4)	C(5)	C(6)	Se(7)	65.5(8)

continued......

137

continuation of

Table 5.2.1. Selected Bond Distances (Å) , Bond Angles and Torsion Angles (°) for [Pd(16Se4)]²⁺ (34)

Torsion Angles (°)

C(8)	Se(7)	C(6)	C(5)	173.2(10)
C(6)	Se(7)	C(8)	C(9)	76.1(7)
Se(7)	C(8)	C(9)	C(8)'	82.0(8)
Se(7)'	Pd	Se(7)	C(6)	-113.3(4)
Se(7)'	Pd	Se(7)	C(8)	-10.0(3)
Pd	Se(3)	C(2)	C(l)	25.5(6)
Pd	Se(3)	C(4)	C(5)	76.6(7)
Pd	Se(7)	C(6)	C(5)	-72.2(7)
Pd	Se(7)	C(8)	C(9)	-28.6(5)

a The values in { } include a correction for rigid-body thermal motion for the non-hydrogen atoms of the complex cation.

b ' = x, 1/2-y, z.

Table 5.2.2. Selected Bond Distances (Å) , Bond Angles and Torsion Angles (°) for [Pd(16Se4)]Cl⁺ (35)

Bond Distances (Å)

Pd	Se(3)	2.4560(7) {2.460}a	Pd	Se(ll)	2.4395(7) {2.444}
Pd	Se(7)	2.4583(7) {2.463}	Pd	Se(15)	2.4430(7) {2.447}
Se(3)	C(2)	1.973(6)	Se(ll)	C(10)	1.944(6)
Se(3)	C(4)	1.959(5)	Se(ll)	C(12)	1.962(5)
Se(7)	C(6)	1.958(6)	Se(15)	C(14)	1.965(5)
Se(7)	C(8)	1.965(5)	Se(15)	C(16)	1.944(6)
C(l)	C(2)	1.500(8)	C(8)	C(9)	1.487(8)
C(l)	C(16)	1.516(8)	C(9)	C(10)	1.502(8)
C(4)	C(5)	1.523(7)	C(12)	C(13)	1.504(8)
C(5)	C(6)	1.517(8)	C(13)	C(14)	1.510(8)

continuation of

Table 5.2.2. Selected Bond Distances (Å) , Bond Angles and Torsion Angles (°) for [Pd(16Se4)]Cl+ (35)

Bond Angles (°)

Se(7)	Pd	Se(3)	84.89(2)	Se(15)	Pd	Se(3)	96.14(2)
Se(11)	Pd	Se(3)	170.03(3)	Se(15)	Pd	Se(7)	166.97(2)
Se(11)	Pd	Se(7)	95.63(2)	Se(15)	Pd	Se(11)	81.12(2)
C(2)	Se(3)	Pd	111.6(2)	C(10)	Se(11)	Pd	112.2(2)
C(4)	Se(3)	Pd	102.4(2)	C(12)	Se(11)	Pd	102.2(2)
C(4)	Se(3)	C(2)	94.5(3)	C(12)	Se(11)	C(10)	94.6(3)
C(6)	Se(7)	Pd	102.0(2)	C(14)	Se(15)	Pd	100.5(2)
C(8)	Se(7)	Pd	110.9(2)	C(16)	Se(15)	Pd	110.8(2)
C(8)	Se(7)	C(6)	95.1(3)	C(16)	Se(15)	C(14)	96.1(3)
C(16)	C(1)	C(2)	113.8(5)	C(10)	C(9)	C(8)	115.2(5)
C(1)	C(2)	Se(3)	116.2(4)	C(9)	C(10)	Se(11)	116.5(4)
C(5)	C(4)	Se(3)	112.4(4)	C(13)	C(12)	Se(11)	114.5(4)
C(6)	C(5)	C(4)	114.0(5)	C(14)	C(13)	C(12)	115.3(5)
C(5)	C(6)	Se(7)	113.5(4)	C(13)	C(14)	Se(15)	112.1(4)
C(9)	C(8)	Se(7)	117.7(4)	C(1)	C(16)	Se(15)	114.7(4)

Torsion Angles (°)

C(10)	Se(11)	C(12)	C(13)	-173.3(6)
C(12)	C(13)	C(14)	Se(15)	70.6(5)
C(16)	C(1)	C(2)	Se(3)	-72.6(5)
C(2)	Se(3)	C(4)	C(5)	-172.5(5)
C(4)	C(5)	C(6)	Se(7)	75.0(4)
C(6)	Se(7)	C(8)	C(9)	92.5(5)
C(8)	C(9)	C(10)	Se(11)	-78.9(5)
C(4)	Se(3)	C(2)	C(1)	-100.3(5)
Se(3)	C(4)	C(5)	C(6)	-74.7(4)
C(8)	Se(7)	C(6)	C(5)	173.4(5)

continued......

continuation of

Table 5.2.2. Selected Bond Distances (Å) , Bond Angles and Torsion Angles (°) for [Pd(16Se4)]Cl⁺ (35)

Torsion Angles (°)

Se(7)	C(8)	C(9)	C(10)	76.4(5)
C(12)	Se(ll)	C(10)	C(9)	-88.9(5)
Se(ll)	C(12)	C(13)	C(14)	-67.7(5)
C(16)	Se(15)	C(14)	C(13)	169.0(6)
C(14)	Se(15)	C(16)	C(l)	75.6(4)
Pd	Se(3)	C(2)	C(l)	5.0(3)
Pd	Se(3)	C(4)	C(5)	74.2(3)
Pd	Se(7)	C(6)	C(5)	-73.9(4)
Pd	Se(7)	C(8)	C(9)	-12.5(3)
Se(15)	Pd	Se(3)	C(2)	30.8(2)
Se(15)	Pd	Se(ll)	C(10)	-166.3(2)
Se(3)	Pd	Se(15)	C(14)	-121.3(2)
Se(3)	Pd	Se(7)	C(6)	61.7(2)
Se(7)	Pd	Se(3)	C(2)	-162.3(2)
Se(7)	Pd	Se(ll)	C(10)	26.5(2)
Se(ll)	Pd	Se(15)	C(14)	68.3(2)
Se(ll)	Pd	Se(7)	C(6)	-128.3(2)
C(2)	C(l)	C(16)	Se(15)	88.3(5)
Se(7)	Pd	Se(3)	C(4)	-62.3(2)
Se(15)	Pd	Se(3)	C(4)	130.7(2)
Se(3)	Pd	Se(7)	C(8)	162.0(2)
Se(ll)	Pd	Se(7)	C(8)	-28.0(2)
Se(7)	Pd	Se(ll)	C(12)	126.7(2)
Se(15)	Pd	Se(ll)	C(12)	-66.1(2)
Se(3)	Pd	Se(15)	C(16)	-20.6(2)
Se(ll)	Pd	Se(15)	C(16)	169.1(2)
Pd	Se(ll)	C(10)	C(9)	16.3(3)
Pd	Se(ll)	C(12)	C(13)	72.8(4)
Pd	Se(15)	C(14)	C(13)	-78.4(4)
Pd	Se(15)	C(16)	C(l)	-28.1(3)

a The values in { } include a correction for rigid-body thermal motion for the non-hydrogen atoms of the complex cation.

Table 5.2.3. Selected Bond Distances (Å) , Bond Angles and Torsion Angles (°) for [(PdCl)$_2$(24Se6)]$^{2+}$ (36)

Bond Distances (Å)

Pd(1)	Se(1)	2.428(1)	Pd(2)	Se(13)	2.428(1)
Pd(1)	Se(5)	2.372(1)	Pd(2)	Se(17)	2.364(1)
Pd(1)	Se(9)	2.428(1)	Pd(2)	Se(21)	2.421(1)
Pd(1)	Cl(1)	2.343(2)	Pd(2)	Cl(2)	2.351(3)
Se(1)	C(2)	1.961(9)	C(2)	C(3)	1.53(1)
Se(1)	C(24)	1.963(9)	C(3)	C(4)	1.52(1)
Se(5)	C(4)	1.96(1)	C(6)	C(7)	1.51(1)
Se(5)	C(6)	1.953(9)	C(7)	C(8)	1.53(1)
Se(9)	C(8)	1.934(9)	C(10)	C(11)	1.52(1)
Se(9)	C(10)	1.954(9)	C(11)	C(12)	1.50(1)
Se(13)	C(12)	1.961(9)	C(14)	C(15)	1.51(2)
Se(13)	C(14)	1.97(1)	C(15)	C(16)	1.48(2)
Se(17)	C(16)	1.97(1)	C(18)	C(19)	1.50(2)
Se(17)	C(18)	1.94(1)	C(19)	C(20)	1.51(1)
Se(21)	C(20)	1.96(1)	C(22)	C(23)	1.49(1)
Se(21)	C(22)	1.954(9)	C(23)	C(24)	1.52(1)

Bond Angles (°)

Se(5)	Pd(1)	Se(1)	92.34(4)	Se(17)	Pd(2)	Se(13)	97.77(5)
Se(9)	Pd(1)	Se(1)	169.83(4)	Se(21)	Pd(2)	Se(13)	170.71(5)
Se(9)	Pd(1)	Se(5)	96.62(4)	Se(21)	Pd(2)	Se(17)	90.77(5)
Cl(1)	Pd(1)	Se(1)	85.61(7)	Cl(2)	Pd(2)	Se(13)	84.63(9)

continuation of

Table 5.2.3. Selected Bond Distances (Å) , Bond Angles and Torsion Angles (^{o}) for [(PdCl)$_2$(24Se6)]$^{2+}$ (36)

Bond Angles (^{o})

Cl(1)	Pd(1)	Se(5)	174.68(7)	Cl(2)	Pd(2)	Se(17)	174.37(8)
Cl(1)	Pd(1)	Se(9)	85.05(7)	Cl(2)	Pd(2)	Se(21)	86.54(9)
C(2)	Se(1)	Pd(1)	110.1(3)	C(12)	Se(13)	Pd(2)	104.5(3)
C(24)	Se(1)	Pd(1)	102.6(3)	C(14)	Se(13)	Pd(2)	113.9(4)
C(24)	Se(1)	C(2)	99.6(4)	C(14)	Se(13)	C(12)	97.7(5)
C(4)	Se(5)	Pd(1)	104.6(3)	C(16)	Se(17)	Pd(2)	108.0(4)
C(6)	Se(5)	Pd(1)	106.9(3)	C(18)	Se(17)	Pd(2)	104.0(3)
C(6)	Se(5)	C(4)	94.1(4)	C(18)	Se(17)	C(16)	95.5(5)
C(8)	Se(9)	Pd(1)	113.1(3)	C(20)	Se(21)	Pd(2)	110.8(4)
C(10)	Se(9)	Pd(1)	103.6(3)	C(22)	Se(21)	Pd(2)	103.0(3)
C(10)	Se(9)	C(8)	96.3(4)	C(22)	Se(21)	C(20)	99.9(5)
C(3)	C(2)	Se(1)	117.0(6)	C(15)	C(14)	Se(13)	115.2(8)
C(4)	C(3)	C(2)	114.7(8)	C(16)	C(15)	C(14)	115.7(13)
C(3)	C(4)	Se(5)	114.8(7)	C(15)	C(16)	Se(17)	115.0(8)
C(7)	C(6)	Se(5)	112.6(6)	C(19)	C(18)	Se(17)	112.3(8)
C(8)	C(7)	C(6)	113.0(8)	C(20)	C(19)	C(18)	115.1(10)
C(7)	C(8)	Se(9)	118.1(7)	C(19)	C(20)	Se(21)	118.7(8)
C(11)	C(10)	Se(9)	113.4(6)	C(23)	C(22)	Se(21)	110.2(6)
C(12)	C(11)	C(10)	113.2(8)	C(24)	C(23)	C(22)	114.9(8)
C(11)	C(12)	Se(13)	112.9(7)	C(23)	C(24)	Se(1)	110.1(6)

continued......

142

continuation of

Table 5.2.3. Selected Bond Distances (Å), Bond Angles and Torsion Angles (°) for $[(PdCl)_2(24Se6)]^{2+}$ (36)

Torsion Angles (°)

Se(5)	Pd(1)	Se(1)	C(2)	-44.4(3)	Se(5)	Pd(1)	Se(1)	C(24)	60.9(3)
Cl(1)	Pd(1)	Se(1)	C(2)	140.5(3)	Cl(1)	Pd(1)	Se(1)	C(24)	-114.2(3)
Se(1)	Pd(1)	Se(5)	C(4)	50.1(3)	Se(1)	Pd(1)	Se(5)	C(6)	149.0(3)
Se(9)	Pd(1)	Se(5)	C(4)	-134.8(3)	Se(9)	Pd(1)	Se(5)	C(6)	-35.8(3)
Se(5)	Pd(1)	Se(9)	C(8)	25.7(3)	Se(5)	Pd(1)	Se(9)	C(10)	-77.3(3)
Cl(1)	Pd(1)	Se(9)	C(8)	-159.4(3)	Cl(1)	Pd(1)	Se(9)	C(10)	97.6(3)
Se(17)	Pd(2)	Se(13)	C(12)	-82.7(3)	Se(17)	Pd(2)	Se(13)	C(14)	22.8(4)
Cl(2)	Pd(2)	Se(13)	C(12)	92.2(3)	Cl(2)	Pd(2)	Se(13)	C(14)	-162.3(4)
Se(13)	Pd(2)	Se(17)	C(16)	-29.6(4)	Se(13)	Pd(2)	Se(17)	C(18)	-130.3(3)
Se(21)	Pd(2)	Se(17)	C(16)	154.0(4)	Se(21)	Pd(2)	Se(17)	C(18)	53.4(3)
Se(17)	Pd(2)	Se(21)	C(20)	-42.8(3)	Se(17)	Pd(2)	Se(21)	C(22)	63.2(3)
Cl(2)	Pd(2)	Se(21)	C(20)	142.1(3)	Cl(2)	Pd(2)	Se(21)	C(22)	-111.8(3)
Pd(1)	Se(1)	C(2)	C(3)	53.5(5)	C(24)	Se(1)	C(2)	C(3)	-53.9(6)
Pd(1)	Se(1)	C(24)	C(23)	70.9(5)	C(2)	Se(1)	C(24)	C(23)	-175.8(8)
Pd(1)	Se(5)	C(4)	C(3)	-73.1(6)	C(6)	Se(5)	C(4)	C(3)	178.3(8)
Pd(1)	Se(5)	C(6)	C(7)	68.9(5)	C(4)	Se(5)	C(6)	C(7)	175.5(8)
Pd(1)	Se(9)	C(8)	C(7)	-40.3(5)	C(10)	Se(9)	C(8)	C(7)	67.4(6)
Pd(1)	Se(9)	C(10)	C(11)	-59.4(5)	C(8)	Se(9)	C(10)	C(11)	-175.0(8)
Pd(2)	Se(13)	C(12)	C(11)	-52.8(5)	C(14)	Se(13)	C(12)	C(11)	-170.0(8)
Pd(2)	Se(13)	C(14)	C(15)	-39.5(6)	C(12)	Se(13)	C(14)	C(15)	70.2(8)
Pd(2)	Se(17)	C(16)	C(15)	61.6(7)	C(18)	Se(17)	C(16)	C(15)	168.3(11)
Pd(2)	Se(17)	C(18)	C(19)	-78.7(6)	C(16)	Se(17)	C(18)	C(19)	171.1(9)

143

continuation of

Table 5.2.3. Selected Bond Distances (Å), Bond Angles and Torsion Angles (°) for [(PdCl)$_2$(24Se6)]$^{2+}$ (36)

Torsion Angles (°)

Pd(2)	Se(21)	C(20)	C(19)	48.2(6)	C(22)	Se(21)	C(20)	C(19)	-59.9(7)
Pd(2)	Se(21)	C(22)	C(23)	71.4(5)	C(20)	Se(21)	C(22)	C(23)	-174.4(8)
Se(1)	C(2)	C(3)	C(4)	-66.4(6)	C(2)	C(3)	C(4)	Se(5)	78.5(7)
Se(5)	C(6)	C(7)	C(8)	-87.2(8)	C(6)	C(7)	C(8)	Se(9)	69.8(7)
Se(9)	C(10)	C(11)	C(12)	-61.6(6)	C(10)	C(11)	C(12)	Se(13)	-167.7(10)
Se(13)	C(14)	C(15)	C(16)	71.6(9)	C(14)	C(15)	C(16)	Se(17)	-86.7(10)
Se(17)	C(18)	C(19)	C(20)	79.6(8)	C(18)	C(19)	C(20)	Se(21)	-62.4(7)
Se(21)	C(22)	C(23)	C(24)	170.7(10)	C(22)	C(23)	C(24)	Se(1)	66.2(6)

5.2.1.2. Determination of the Complex Composition by UV-visible Spectroscopy

Although the results of microanalysis as well as crystallography revealed that Pd(II) formed a 1:1 complex with 16Se4 and a 2:1 complex with 24Se6 in the solid state, it is necessary to investigate whether the solution compositions of these complexes retain the same metal ion to ligand ratio as in the solid state. It is particularly interesting to know if 24Se6 still remains bound to two Pd(II) ions. Thus, uv-visible absorption spectroscopy was applied to investigate the composition of the complexes in solution.

There are two methods which can be used, 1) the continuous change method; 2) the molar ratio method, for the investigation of the complex compositions.

5.2.1.2.1. The Continuous Change Method[166,167]

For a complex formed from a metal ion M and a ligand L in solution, the equilibrium may be written as

$$M + nL = ML_n \qquad\qquad (5.2.1)$$

where n is the molecular ratio. If the concentrations of M and L are the same and have the initial concentration m, then on mixing x ml of L with (1-x) ml of M (where x is less than unity), the concentration of the species in solution will be given by

$$C_M = m*(1-x) - C_{ML_n} \qquad\qquad (5.2.2)$$

$$C_L = xm - nC_{ML_n} \qquad\qquad (5.2.3)$$

where C_M and C_L are the concentrations for M and L at equilibrium. These concentrations are also related to each other by the equilibrium equation of the complex

$$KC_M C_L^n = C_{ML_n} \qquad\qquad (5.2.4)$$

where K is the stability constant. For a plot of C_{MLn} vs. x, the condition for a maximum is

$$dC_{MLn}/dx = 0 \qquad (5.2.5)$$

Differentiating equations (5.2.2) and (5.2.3) with respect to x and combining the resulting equations with equations (5.2.2), (5.2.3), (5.2.4) and (5.2.5) gives

$$n = \frac{x}{(1-x)} \qquad (5.2.6)$$

The molar absorptivity ε is related to the absorbance A by the Lambert Beer relationship

$$A = \varepsilon l c \qquad (5.2.7)$$

Where c is the concentration in mole/liter and l is the length that the light passes through the solution. Hence, for the mixture

$$A = l*(\varepsilon_1 C_M + \varepsilon_2 C_L + \varepsilon_3 C_{MLn}) \qquad (5.2.8)$$

where ε_1, ε_2 and ε_3 are the molar absorptivities for M, L and ML_n. If no reaction had occurred on mixing, the absorbance A' would have been

$$A' = l*[\varepsilon_1 m(1-x) + \varepsilon_2 mx] \qquad (5.2.9)$$

Hence

$$A - A' = l*[\varepsilon_1 C_M + \varepsilon_2 C_L + \varepsilon_3 C_{MLn} - \varepsilon_1 m(1-x) - \varepsilon_2 mx] \qquad (5.2.10)$$

In most cases the ligand does not absorb at the wavelength where the complex absorbs; therefore, when $\varepsilon_3 > \varepsilon_1$ there is a maximum for this differential absorbance (A - A'). When $\varepsilon_3 < \varepsilon_1$ there is a minimum for this differential absorbance (A - A'). By plotting A - A' vs. x, the value of x corresponding to the maximum or minimum value of A-A' can be determined and n can thus be calculated with equation (5.2.6).

Two stock solutions of the same concentrations were prepared, i.e., a stock solution of $Pd(BF_4)_2$ that was prepared by stirring $PdCl_2$ with excess $NaBF_4(1:1.6)$ in CH_3CN and a stock solution of 16Se4 or 24Se6 in CH_3CN. From these two stock solutions, a series of solutions were prepared by combining x ml of $Pd(BF_4)_2$ stock solution with (10-x) ml of 16Se4 or 24Se6 stock solution in 10-ml volumetric flasks. Thus, the sum of Pd^{2+} and ligand concentrations was always equal to the concentration of stock solutions for each flask. The prepared solutions were left for 10 hours at room temperature so that the complexation between $Pd(II)^{2+}$ and the selenium coronands could reach equilibrium.

The uv-visible absorption spectra of the series of solutions were measured, and the absorbance at the λmax for the particular complex was recorded. The absorbance of the solution containing only 16Se4 or 24Se6 was zero at these wavelengths. Thus, The resultant A-A' value was determined by subtracting the absorbance of the solution with only Pd^{2+} from that of the mixed solutions at the wavelength of interest. Plots of (A-A') vs. x/10 were prepared, and the values of x corresponding to the maxima on the graphs appeared at x = 0.5 and 0.64 for 16Se4 and 24Se6, respectively (Figure 5.2.4). Hence, the value of n was calculated according to Equation (5.2.6); the ligand to Pd(II) ratio in the complexes was 1 : 1 for 16Se4 and Pd(II) and 1:2 for 24Se6 and Pd(II) respectively.
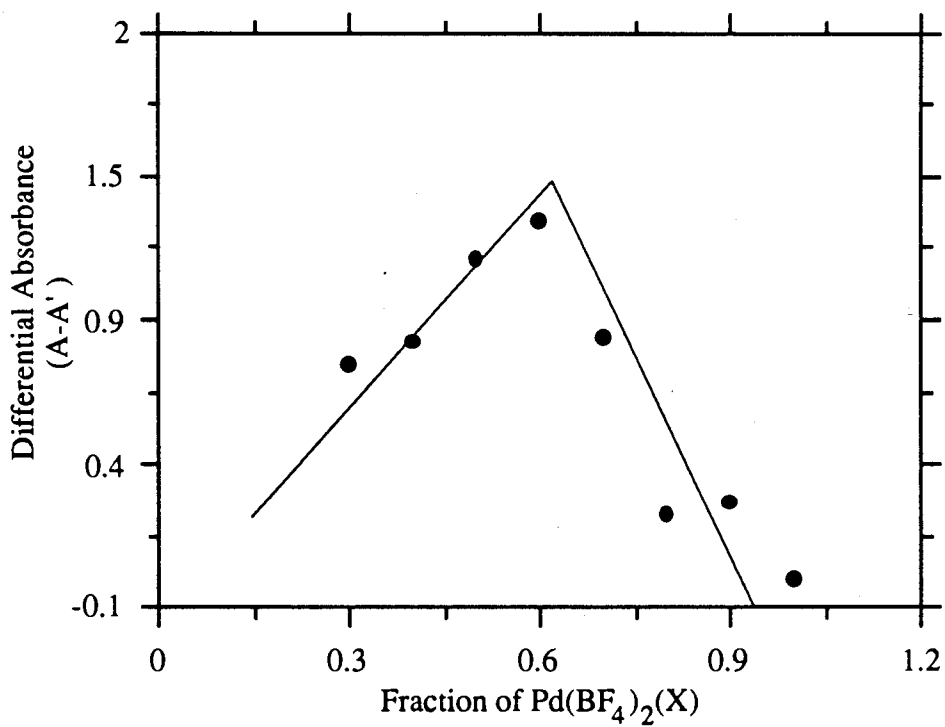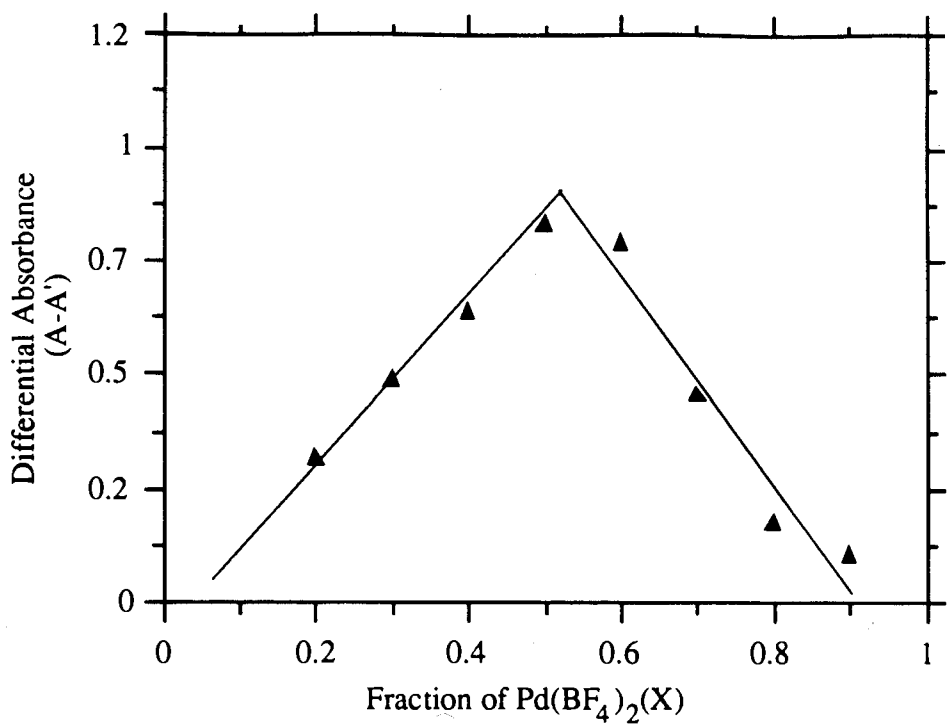
Figure 5.2.4. Job plots: a) Pd(II) and 16Se4 ; b) Pd(II) and 24Se6.

5.2.1.2.2. *The Molar Ratio Method*[168]

In this method a series of solutions are prepared, in which the metal ion and ligand are mixed in ratios of 1, 2, 3, ..., 10. The solutions are measured by uv-visible spectroscopy. The absorbance at the absorbance maximum wavelength (λmax) corresponding to a particular complex is plotted against the ratio of the metal ion and ligand as in Figure 5.2.5. The composition of the complex will be determined at the turning point P. This method should be applied to complexes with large stability constants, because for a complex with a small stability constant the turning point would be a blur and the composition of the complex determined from such a plot would be doubtful.

A series of Pd(II) and 16Se4 (**8**) solutions was prepared, in which the concentration of Pd(II) was constant but the concentration of 16Se4 was varied so that the solutions had 16Se4 to Pd(II) ratios of 0.25, 0.49, 0.74, 0.98, 1.96 and so on.

UV-visible absorption spectra of these solutions were measured at different temperatures. The absorbance maximum (310 nm) of $[Pd(16Se4)]^{2+}$ from the solutions with different 16Se4 to Pd(II) ratios are listed in Table 5.2.4.

The absorbance was plotted versus the ratio of Pd(II) and 16Se4 (Figure 5.2.5). As the ratio of 16Se4/Pd(II) increased, the absorbance at 310 nm increased accordingly. When the ratio of 16Se4/Pd(II) became 1 the increment slowed. Then, the absorbance reached a maximum (A_∞) as the ratio of 16Se4/Pd(II) passed over 1. Continuing to increase the 16Se4 to Pd(II) ratio did not increase the absorbance. This indicates that the Pd(II) ion is completely complexed by 16Se4. The composition of the complex was found to be 1:1 by drawing a vertical line from the turning point P to the abscissa. From the above graph the stability constant of the complex $[Pd(16Se4)]^{2+}$ was determined according to the following equilibrium equations:

$$Pd^{2+} + 16Se4 \rightleftharpoons [Pd(16Se4)]^{2+} \qquad (5.2.11)$$

$$\frac{[Pd(16Se4)^{2+}]}{[Pd^{2+}][16Se4]} = K \qquad (5.2.12)$$

$$\frac{[Pd(16Se4)^{2+}]}{[Pd^{2+}]} = K[16Se4] \qquad (5.2.13)$$

$$\ln\frac{[Pd(16Se4)^{2+}]}{[Pd^{2+}]}] = \ln K + \ln[16Se4] \qquad (5.2.14)$$

The values of $\frac{[Pd(16Se4)^{2+}]}{[Pd^{2+}]}$ and $[16Se4]$ were determined by

$$\frac{[Pd(16Se4)^{2+}]}{[Pd^{2+}]} = \frac{A}{A_{\infty}-A} \qquad (5.2.15)$$

$$[16Se4] = C_{Pd^{2+}} * (\frac{[L]}{[M]} - \frac{A}{A_{\infty}}) \qquad (5.2.16)$$

Here, A_{∞} is the maximum absorbance; A is the absorbance; $C_{Pd^{2+}}$ is the initial concentration of Pd^{2+}. By plotting $\ln\frac{[Pd(16Se4)]^{2+}}{[Pd^{2+}]}$ versus $\ln[16Se4]$, the stability constants at the various temperatures were determined as the intercepts. From the stability constants at the various temperatures, the values for the enthalpy change and the entropy change were also calculated as $\Delta H = 48.8 \pm 0.76$ kJ/mol and $\Delta S = -67.8 \pm 3.4$ J/mol.

Table 5.2.4. Absorbance at 310 nm at Different Temperatures

$\dfrac{[16\mathrm{Se4}]}{[\mathrm{Pd}^{2+}]}$	Absorbance (10.0 °C)	Absorbance (20.0 °C)	Absorbance (27.5 °C)	Absorbance (35.0 °C)
0.25	0.0200	0.0160	0.0200	0.0100
0.49	0.192	0.180	0.170	0.180
0.74	0.598	0.581	0.570	0.560
0.98	0.725	0.716	0.700	0.693
1.96	0.775	0.758	0.740	0.732
3.92	0.790	0.780	0.761	0.759
7.89	0.775	0.760	0.740	0.732
$\ln K$[a]	12.5 ± 0.73	11.5 ± 0.71	11.4 ± 0.71	10.8 ± 0.71

a. The absorbance at $[16\mathrm{Se4}]/[\mathrm{Pd}^{2+}] = 3.92$ was chosen as A_∞. The first two points at the low 16Se4 to Pd^{2+} ratio were not used for calculation of $\ln K$ (see discussion for reason).
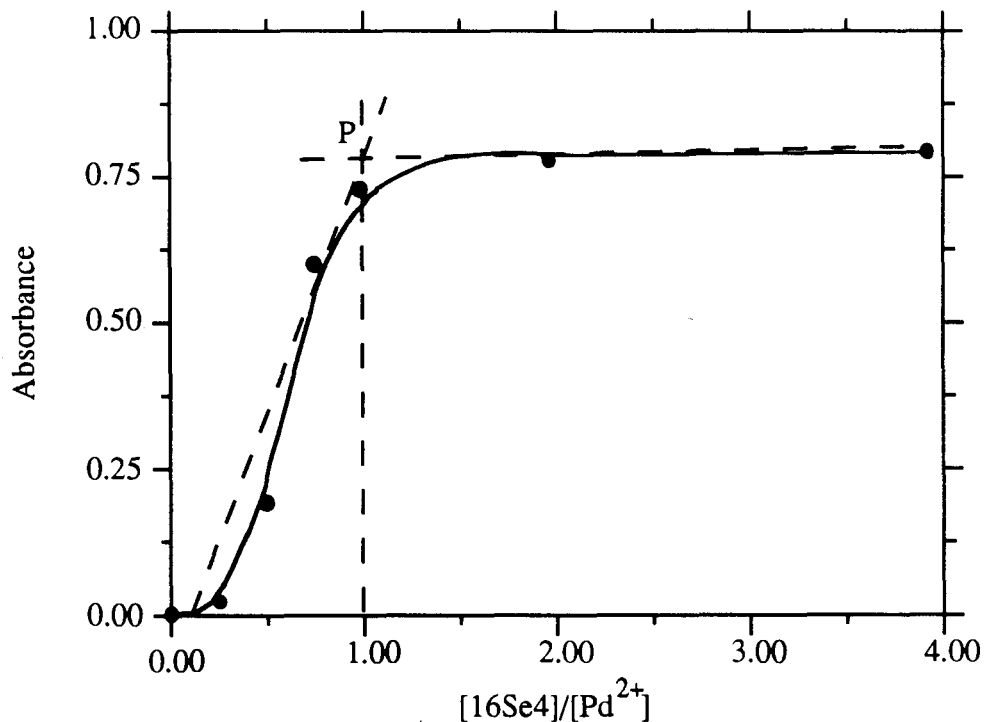
Figure 5.2.5. The plot of absorbance (310 nm) versus $[16\mathrm{Se4}]/[\mathrm{Pd}^{2+}]$.
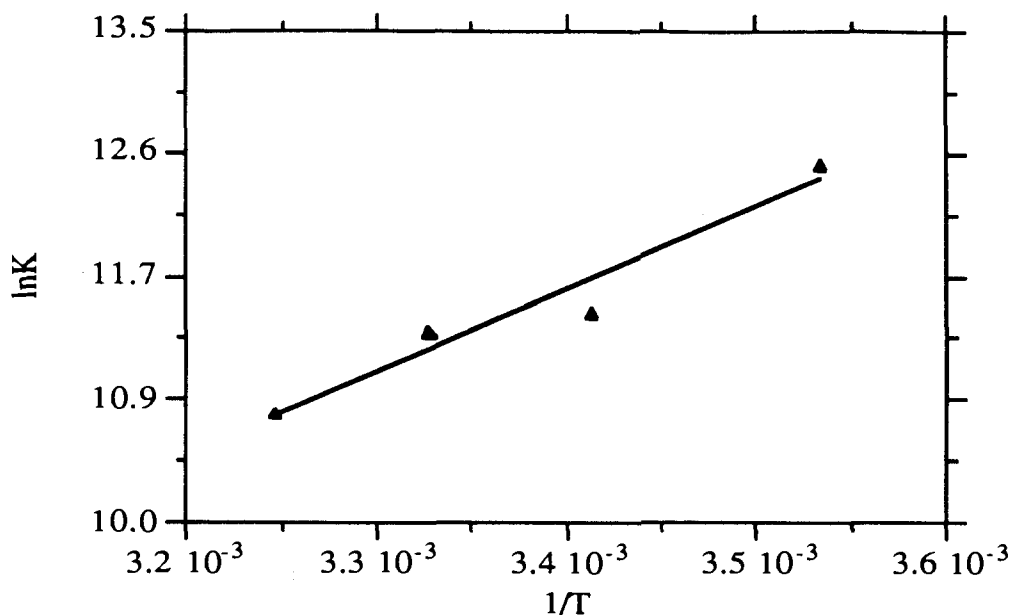
Figure 5.2.6. Plot of lnK versus 1/T.

The same method was applied to the ligand 24Se6. In this case the concentration of 24Se6 was fixed, but the concentration of Pd^{2+} was varied forming a series of solutions with Pd^{2+}/24Se6 ratios of 0.2, 0.4, 0.8, 1.2, 2.7, 5.3 and 15. The absorbance of Pd(II) at the same concentration was subtracted from that of the mixed solution at 314 nm to correct the absorption due to Pd(II) ions. The absorbance at 314 nm dropped to 0.08 at the Pd^{2+}/24Se6 ratio of 5.3. The experiment when repeated gave rise to the same result. Inspection of the volumetric flask containing the solution showed yellow precipitates at the bottom of the flask. Thus, the reduction of the absorbance at this ratio resulted from the precipitation of the complex. However, the reason for the precipitation at this particular ratio is unknown. The resultant absorbance was plotted versus the ratios of Pd^{2+}/24Se6 (Figure 5.2.7), ignoring the point from the solution with precipitation. The plot showed that as the ratio of Pd^{2+}/24Se6 increased the absorbance corresponding to the complex also increased. After the turning point P, the absorbance increment was less significant and eventually reached a maximum; hence, the complexation was considered to be complete.

The ratio in the complex of Pd^{2+} and 24Se6 was found to be 2 by drawing a straight line vertically to the abscissa.
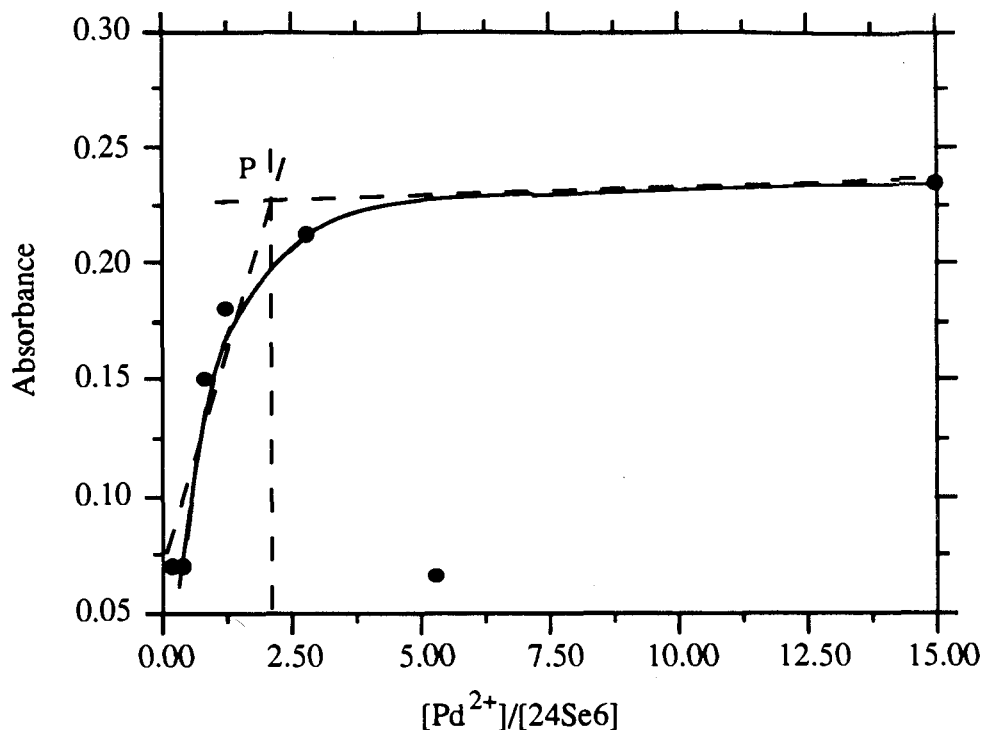
Figure 5.2.7. **Plot of the absorbance maximum (314 nm) versus $[Pd^{2+}]/[24Se6]$ ratio.**

In another experiment, the concentration of Pd^{2+} was fixed, and the concentration of 24Se6 was varied to give a series with $24Se6/Pd^{2+}$ ratios of 0.2, 0.3, 0.4, 0.5, 0.8, 1.0 and 5. The turning point was found at the $24Se6/Pd^{2+}$ ratio of 0.5 on the plot of the absorbance versus $24Se6/Pd^{2+}$, which also indicated that ratio of $24Se6/Pd^{2+}$ was 1:2.

5.2.1.3. Configurations of [Pd(16Se4)]$^{2+}$ Ion in Aqueous Solution

The ^{13}C NMR chemical shifts of the complex [Pd(16Se4)]$^{2+}$ are listed in Table 5.2.5. The ^{13}C NMR spectra of the complex at various temperatures are shown in Figure 5.2.8. At ambient temperature, there are 6 major ^{13}C NMR resonances in addition to some peaks of lower intensity. At higher temperatures the resonance broadened. When the temperature was raised to 389 K, the peaks at 29.96, 29.79 and 29.99 ppm coalesced to one peak at 30.73 ppm; the peaks at 33.65 and 33.70 coalesced to one peak at 34.41 ppm. However, the original spectrum was obtained as the temperature was cooled back to ambient temperature. A similar observation was also made in the ^{1}H NMR spectra at various temperatures (Figure 5.2.9). The ^{77}Se NMR spectrum (at ambient temperature) of the complex [Pd(16Se4)]$^{2+}$ showed two resonances in an approximate 1:1 ratio. Figure 5.2.10 shows the inverse ^{1}H-^{13}C correlated 2D NMR spectrum of [Pd(16Se4)][BF$_4$]$_2$ in D$_2$O at ambient temperature. From the spectrum the correlation between the chemical environments of protons and their connected carbons were shown. For example, the ^{13}C NMR signal at the highest field (26.7 ppm) indicated that this carbon was connected to two protons which were in the same chemical environment because the protons only gave one kind of chemical shift on the ^{1}H axis, but the second and third carbons (from high to low field) had protons which were in different chemical environments because both of them gave two different chemical shifts on the ^{1}H axis.
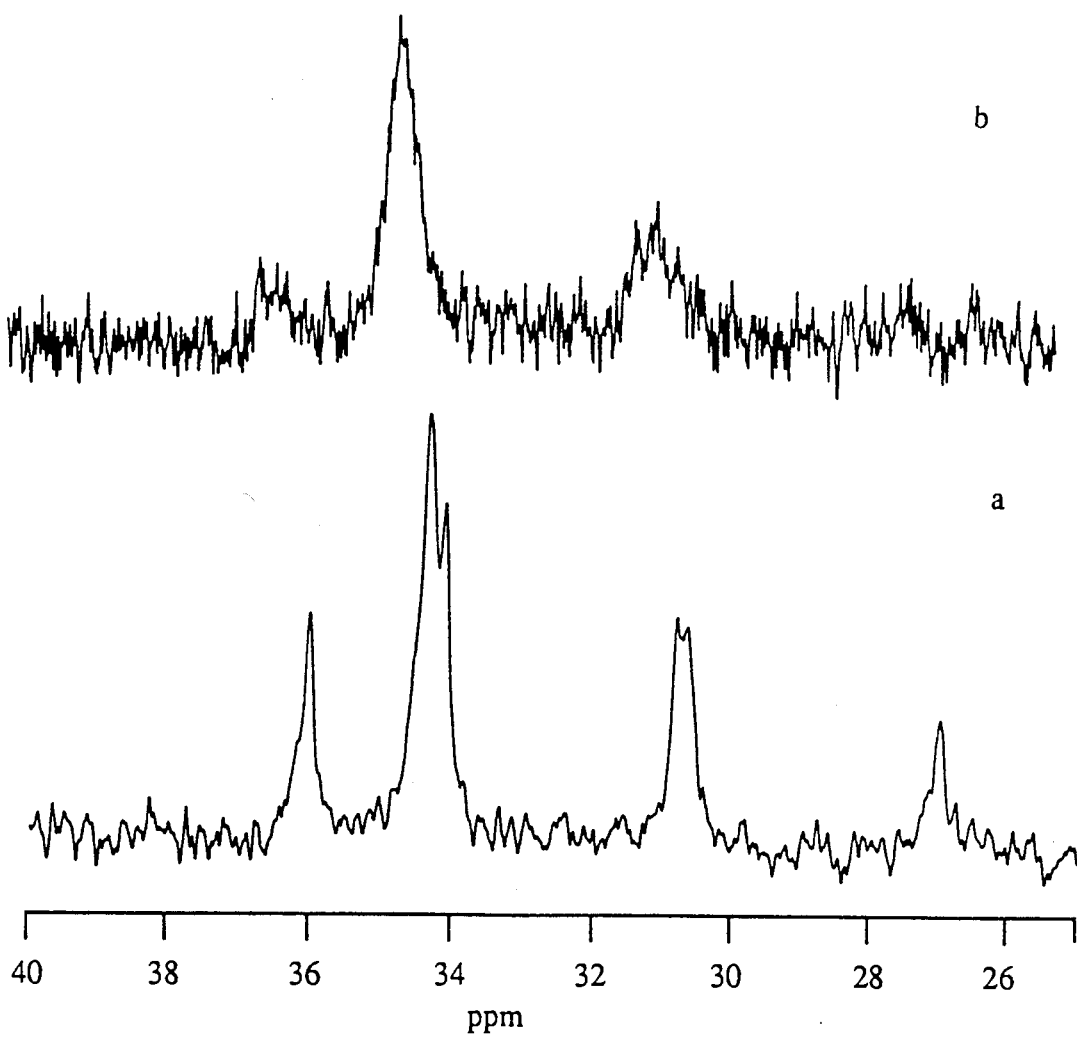
Figure 5.2.8. ^{13}C NMR spectra of [Pd(16Se4)]$^{2+}$ at temperatures: a) 354 K; b) 389 K.
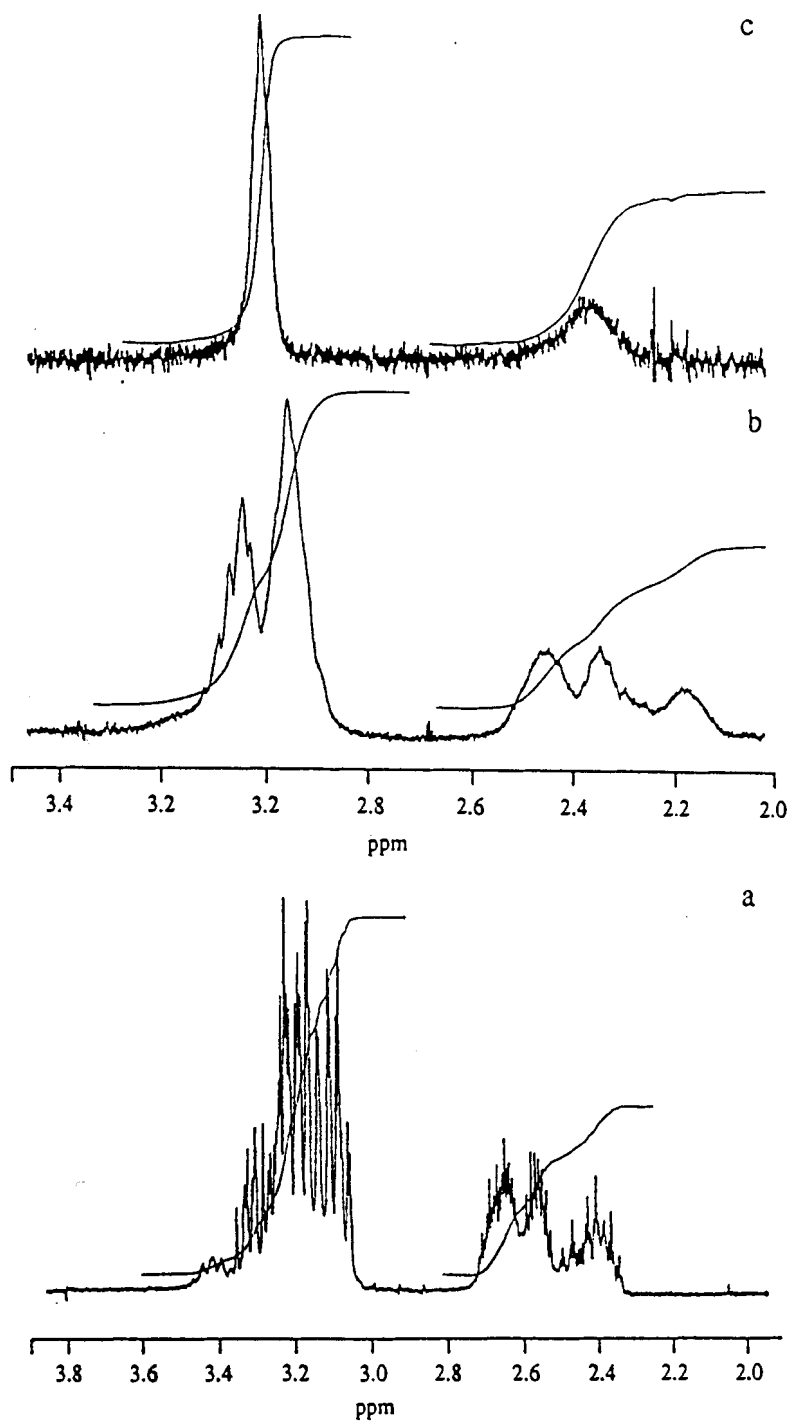
Figure 5.2.9. ^{1}H NMR spectra of [Pd(16Se4)]$^{2+}$ recorded at temperatures: a) room temperature. b) 354 K. c) 389 K.

156
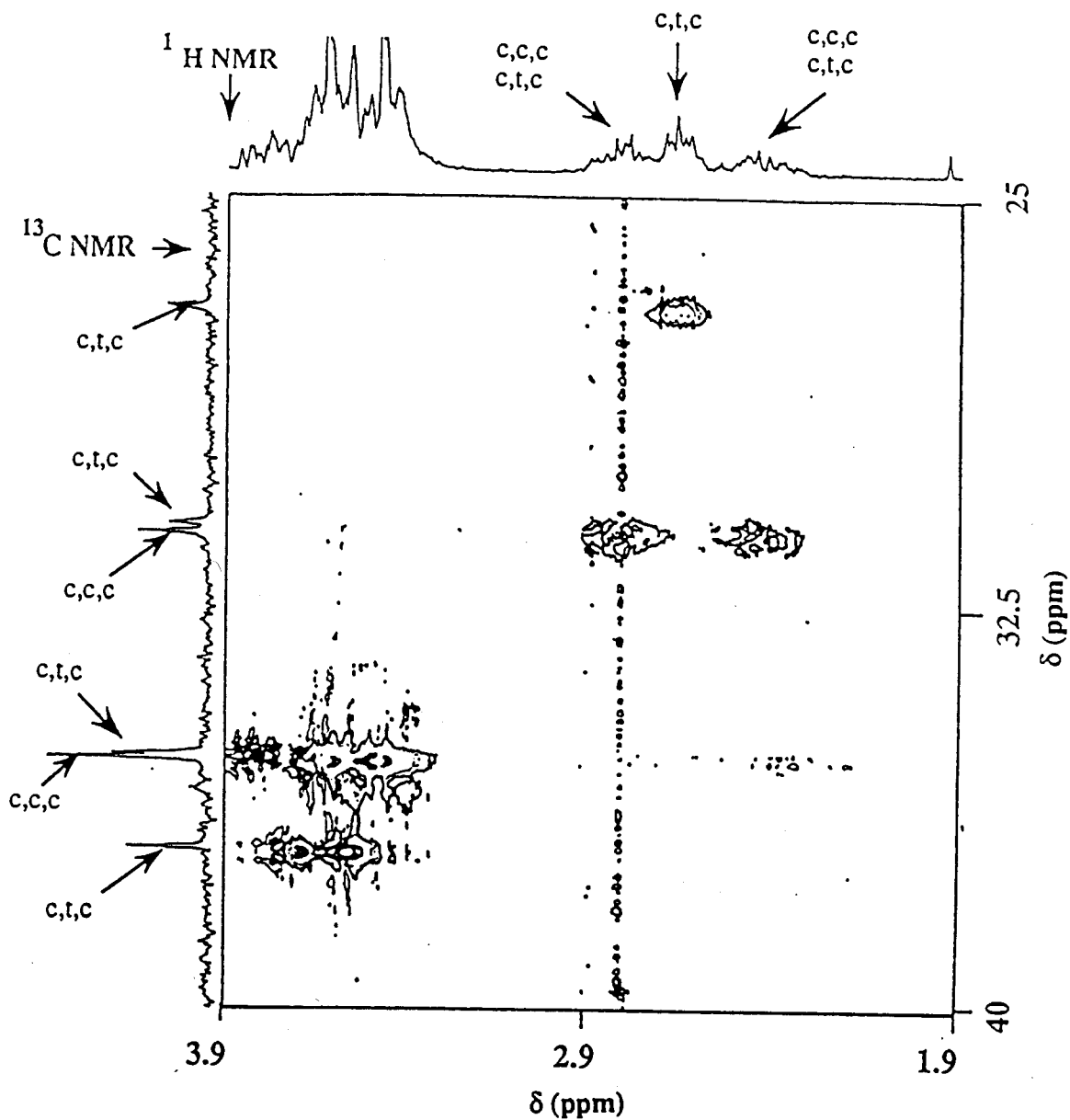
Figure 5.2.10. The inverse ^{1}H-^{13}C correlated 2D NMR spectrum of $[Pd(16Se4)]^{2+}$ recorded at ambient temperature.

157

Table 5.2.5. ^{13}C NMR Chemical Shifts of $[Pd(16Se4)]^{2+}$ at Different Temperatures in D_2O

No.	δ (rel int) Ambient temp	δ (rel int) 353 K	δ (rel int) 389 K
1	26.96(0.5)	26.97	
2	29.79(0.5)	30.56	
3	29.99(1)	30.78	30.73(1)
4	30.22(*)[a]		
5	33.65(1)	34.09	
6	33.70(2)	34.32	
7	34.19(*)[a]		34.41(2)
8	36.14(1)	35.99	36.5(<1)

a. The peak is a minor peak.

5.2.1.4. Cyclic Voltammetry of Pd(II) Complexes of Selenium Coronands

$[Pd(16Se4)](BF_4)_2$ (**34**). A cyclic voltammogram of **34** is shown in Figure 5.2.11, which was recorded on a platinum electrode in CH_3CN (0.1 M Bu_4NClO_4). Cyclic voltammetry on a carbon electrode gave rise to the same cyclic voltammogram. The electron transfer between **34** and the electrodes was irreversible because only one reduction peak current was observed. At a scan rate of 20 mV/s, there was a cathodic peak at -0.562 V vs SCE, corresponding to the redox pair of Pd^{II}/Pd^{I}. There were no anodic peaks observed on the reverse scan. A plot of the cathodic peak current versus the square root of the scan rate was a straight line, indicating that the electrode process was a diffusion controlled process. When the potential was swept further in the cathodic direction, a broad cathodic peak (not shown in Figure 5.2.11) appeared at -1.06 V vs SCE, which was attributed to the redox pair of Pd^{I}/Pd.

$[Pd(16Se4)]ClBF_4$ (**35**). The cyclic voltammogram of **35** is similar to that of **34**. A cathodic peak appeared at -0.47 at a scan rate 50 mV/s in the cathodic direction. The

potential peak at -0.47 V corresponds to the redox pair of Pd^{II}/Pd^{I}. When the potential was scanned further in the cathodic direction, a second cathodic current peak appeared at -0.75 V, which was attributed to the redox pair of Pd^{I}/Pd. There was a broad peak at -0.41 V on the reverse scan, the position of which was not dependent on the scan rates although the cathodic current peak at 0.47 V moved to the more cathodic direction as the scan rates increased; therefore, the broad peak on the reverse scan was probably caused by species adsorbed on the electrode surface.

$[Pd_2(24Se6)Cl_2](BF_4)_2$ (36). A cyclic voltammogram of **36** is shown in Figure 5.2.12, which was recorded on a carbon electrode in CH_3CN (0.1 M Bu_4NClO_4). The cyclic voltammetry on a Pt electrode gave rise to the same cyclic voltammogram. The cyclic voltammogram of $[Pd_2(24Se6)Cl_2][BF_4]_2$ showed the electron transfer was irreversible. At a scan rate of 50 mV/s, the cathodic potential peak that corresponds to the redox pair Pd(II)/Pd(I) appeared at -0.58 V vs SCE. The reduction was a one electron-transfer process for each Pd(II) ion, which has been confirmed by a coulometric study. When the potential was scanned further in the cathodic direction, a second cathodic potential peak was observed, which corresponds to the redox pair Pd(I)/Pd as manifested by the black Pd metal deposited on the Pt electrode surface. There were no anodic peaks observed on the reverse scan. A straight line was obtained from a plot of the cathodic peak currents versus the square root of the scan rates. This indicates that the electrode process is a diffusion-controlled process.
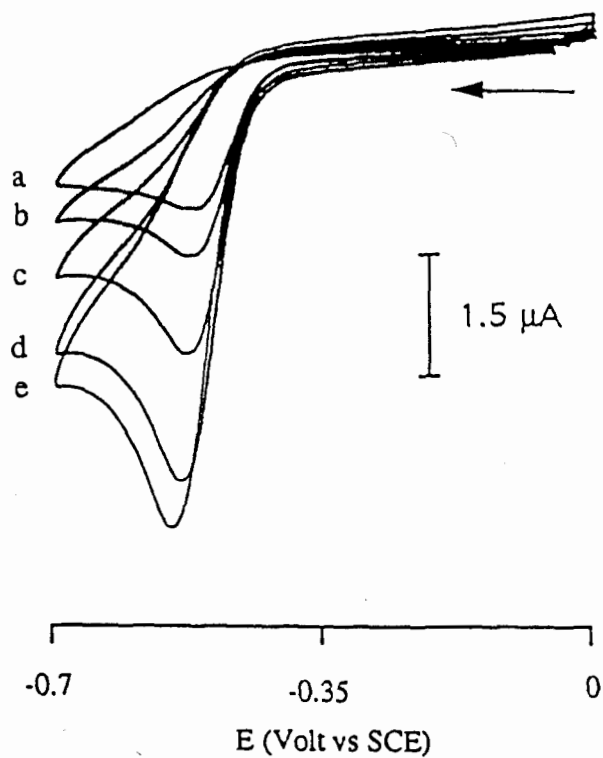
Figure 5.2.11. Cyclic voltammograms of $[Pd(16Se4)](BF_4)_2$ in CH_3CN recorded on a platinum electrode at various scan rates: a) 10 mV/s; b) 20 mV/s; c) 50 mV/s; d) 100 mV/s; e) 200 mV/s. Potential is referenced to SCE.
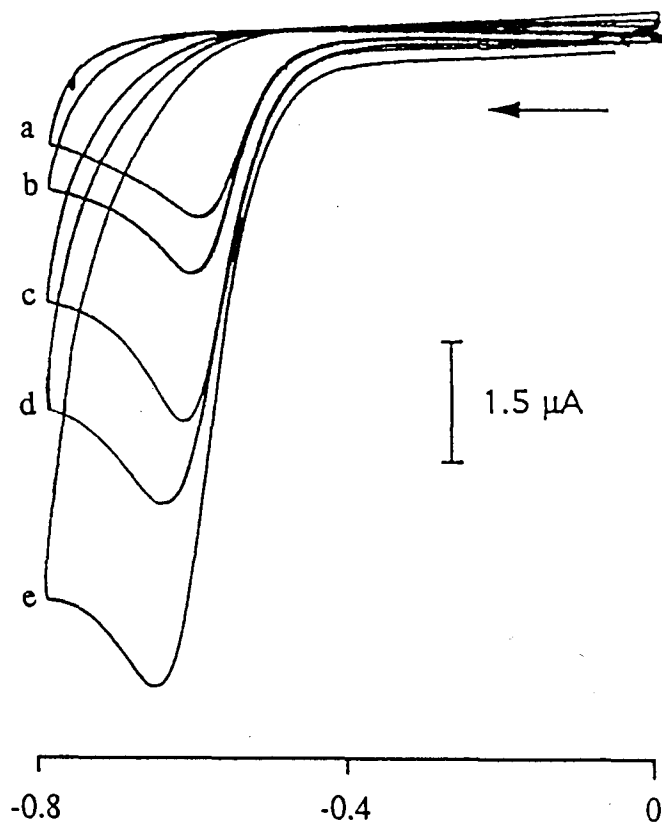
Figure 5.2.12. Cyclic voltammograms of [Pd$_2$(24Se4)][Cl(BF$_4$)]$_2$ in CH$_3$CNrecorded on a carbon electrode at various scan rates: a) 10 mV/s; b) 20 mV/s; c) 50 mV/s; d) 100 mV/s; e) 200 mV/s. Potential is referenced to SCE.

5.2.1.5. Controlled Potential Electrolysis

The electrolysis of Pd(II) selenium coronands was carried out on Pt electrodes in a two-compartment cell as described in Chapter 4. Coulometry of the complex [Pd(16Se4)][BF$_4$]$_2$ (35) was carried out in CH$_3$CN with 0.1 M TEAP as electrolyte. At an applied potential -0.8 V vs SCE, first there appeared a greenish tinge in the originally yellow solution, then the solution turned orange. The total electric charge passed through the solution corresponded to a one-electron transfer process. When the electrolysis ended there was a grayish precipitate at the bottom of the cell. [Pd$_2$(24Se6)Cl$_2$][BF$_4$]$_2$ (36) was electrolyzed at an applied potential -0.8 V vs SCE. The yellow solution turned orange. The total electric charge passed through the solution corresponded to a two-electron transfer process. Because 36 has two Pd(II) ions each Pd ion accepted one electron from the electrode.

5.2.2. Discussion

5.2.2.1. The Structure of Pd(II) Complexes

The only previously reported monomeric transition metal-coronand complex of a cyclic polyselenaether is [Cu(16Se4)][SO$_3$CF$_3$]$_2$ (21)[60] in which the coronand coordinates the metal pseudo-tetragonally but in the so-called c,t,c configuration (i.e. the non-bonding electron pairs of the Se atoms are *cis*, *trans* and *cis* to each other), with weakly bound axial SO$_3$CF$_3^-$ ions.

The Pd-Se bond distances are comparable with previous values (*c.f.* Pd-Se, 2.429(1),2.424(7) and 2.40(1) Å in Pd(II) complexes of dialkylseleno ethers)[169-171]. In (35) there is a small but significant asymmetry in the Pd-Se bond lengths for pairs of trans-related Pd-Se bonds and also in the Se-Pd-Se angles. It is not possible to say whether this asymmetry derives from packing effects and the low crystallographic symmetry or whether

it represents a minimum energy state of the free complex; however, such asymmetry in chemically equivalent bonds is noteworthy.

The tetradentate ligand 16Se4 in the complex $[Pd(16Se4)](BF_4)_2$ can have, in principle, at least four different configurations in solution, in which the Pd(II) ion is square planar. Based on the positions of lone-pair electrons of one selenium atom relative to that of its adjacent selenium atoms and Se-C bonds, these configurations are characterized as c,c,c; c,t,c; t,t,t; and c,t,t[165,172], as illustrated in Figure 5.2.13.

Among these configurations, c,c,c and c,t,c configurations are the most commonly observed configurations in 16Se4 metal complexes. We have observed the c,c,c configuration in the solid-state structure of $[Pd(16Se4)]^{2+}$ and the c,t,c configuration in the solid-state structure of $[Cu(16Se4)][SO_3CF_3]_2$[60] (21). These configurations are also observed in complexes of the sulfur congeners, for example, 16S4 appears as the c, c, c configuration[106] in $[MoO(SH)(16S4)]^+$, $[Pd(16S4)]^{2+}$[1] whereas the c,t,c (uudd) configuration[106] is observed, in $[Fe(16S4)I_2]$, $[Ni(16S4)]^{2+}$[22], $[Rh(16S4)Cl_2]$[24], $[Cd(16S4)]^{2+}$[78] and $[Cu(16S4)]^{2+}$[33]. The c,t,c configuration is observed in $[Hg(16S4)][ClO_4]_2$[106]. The molecular orbital (MO) calculation results[106] on the energy required to transform 16S4 from its free conformation to the conformations in the metal complexes indicate that the c,c,t conformation is the least stable configuration among c,c,c, c,t,c and t,t,t. However, to the best of our knowledge, the c,c,t configuration has not been observed in metal complexes of chalcogen macrocyclic ethers (of either 16Se4 or its sulfur analog) in which the electronic configuration of the metal ions requires square planar or octahedral geometry.

The symmetry of the c,c,t configuration belongs to an m point group, and it would produce three selenium, six carbon and 12 proton resonances in the respective NMR spectra. However, the ^{77}Se NMR spectrum of $[Pd(16Se4)][BF_4]_2$ in D_2O shows only two resonances in a 1:1 ratio. Considering the broad range of ^{77}Se chemical shifts (2000 ppm) and its sensitivity to the chemical environment (six times larger than ^{13}C)[173], it is

unlikely that two of the three selenium NMR absorption lines are overlapping. Furthermore, the relative peak areas in the ^{13}C NMR spectrum of the complex are not consistent with a unique c,c,t configuration in solution. We have ruled out the presence of the uuud configuration of $[Pd(16Se4)]^{2+}$ in solution. Therefore, the two ^{77}Se NMR absorption peaks are attributed to two different configurations of the complex $[Pd(16Se4)][BF_4]_2$ in D_2O; each configuration shows only one ^{77}Se NMR signal because of the symmetry. Table 5.2.6 lists the relationship between the symmetry of the ligand configuration and the number of NMR resonances.

Table 5.2.6. The Relationship between Symmetry of the Ligand Configuration with the Number of Uncoupled NMR Absorption Lines.

Configuration	Symmetry	^{77}Se NMR (area ratio)	^{13}C NMR (area ratio)	^1H NMR (area ratio)
c,c,c	C_{2v}	1	2 (2:1)	4 (2:2:1:1)
c,t,c	C_{2h}	1	4 (2:2:1:1)	7 (2:2:2:2:1:1)
t,t,t	D_{2d}	2 (1:1)	2 (2:1)	3 (1:1:1)
c,c,t	C_s	3 (1:2:1)	6 (1:1:1:1:1:1)	12 2×(1:1:1:1:1:1)
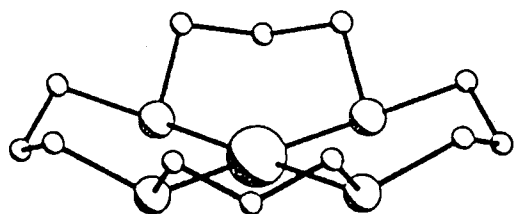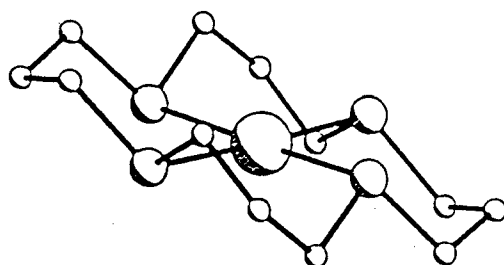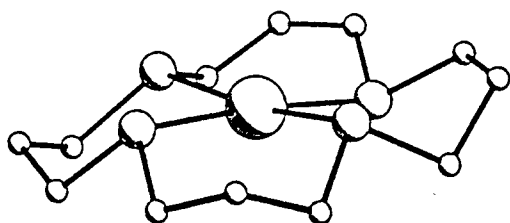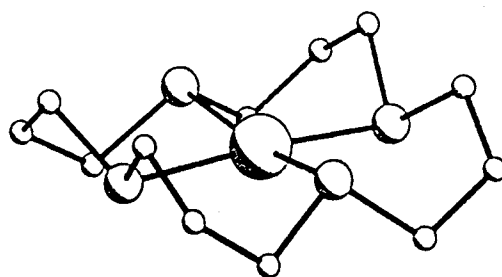
Figure 5.2.13.   Four possible configurations of 16Se4 (8) in the [Pd(16Se4)]$^{2+}$ cation.

Since the c,c,c configuration is the unique isomer in the solid state structure of $[Pd(16Se4)]^{2+}$, this configuration likely also exists in solution. The other configuration in solution will be either c,t,c or t,t,t.

The heteronuclear two-dimensional ^{1}H-$^{13}C\{^{1}H\}$ NMR spectrum shows that $[Pd(16Se4)]^{2+}$ has six ^{13}C NMR signals. The c,c,c isomer will account for two of them. Hence, from the number of ^{13}C NMR signals, the configuration that fits the data is c,t,c. Comparison of the relative intensities of these peaks also corroborates the assignment. The data in Table 5.2.6 indicate that the c,c,c isomer should show two ^{13}C peaks with a 2:1 ratio in which the more intense peak corresponds to the CH_2 group α to the Se atom because every trimethylene unit has two such CH_2 groups and the less intense peak is the CH_2 group β to the Se atom. The c,t,c isomer would have 4 resonances in a ratio of 1:1:0.5:0.5, in which the two more intense peaks are the α-CH_2s and the two less intense peaks are β-CH_2s. (Here, we normalize the intensity ratio based on the c,c,c isomer.) In reality, we observe the intensity ratio (1:1.6:1:0.8:0.5:0.5) that is consistent with the presence of two configurations c,c,c and c,t,c in approximately equal ratio, in D_2O solution.

The c,t,c configuration has a mirror plane that bisects the β-CH_2 of two trimethylene groups that are on the opposite sides of the square plane and a C_2 axis that is perpendicular to the mirror plane and bisects the β-CH_2 in the two other trimethylene groups that are on the two opposite sides of the square plane. Thus, the two protons on the β-CH_2 in the mirror plane could have different chemical shifts because of their different chemical environments whereas the two protons on the β-CH_2 in the C_2 axis plane should have the same chemical shifts because they are symmetry related. In the 2-D NMR spectrum, we do find two kinds of proton signals with exact chemical shift patterns that correlate with the β-CH_2 carbons. The c,c,c configuration has no C_2 symmetry; therefore, all protons on the β-CH_2 carbons are chemically different and show different chemical

shifts, which overlap with one of the β-CH_2 resonances from the c,t,c isomer. Thus, we conclude that there are two major isomers in solution and they have the c,c,c and c,t,c configurations. These two configurational isomers are interconvertible, and the exchange rates become fast at higher temperatures. We speculate that the conversion may go through a well documented process, pyramidal inversion[72,78], although the dissociation-recombination pathway cannot be ruled out.

5.2.2.2. *Irreversibility in Cyclic Voltammetry*

A Pd(II) ion has a d^8 electronic configuration. One-electron transfer reduction of a Pd(II) Se coronand complex yields a Pd(I) coronand complex which has an unpaired electron. The irreversible reduction of the complex $[Pd(16Se4)](BF_4)_2$ may be attributed to the coupling reaction of Pd(I) complexes, forming Pd(I)/Pd(I) metal-metal bonded dimers, which was proposed by Schröder and co-workers[1].

5.2.2.3. *Abnormality of Absorbance at Low Concentration of Ligands*

A plot of the absorbance of $[Pd(16Se4)][BF_4]_2$ (**34**) versus the molar ratio shows a sigmoidal shape. It seems that when the concentration of 16Se4 is lower than that of Pd(II) the absorbance of the complex is also lower than it is supposed to be as indicated by the dotted line (Figure 5.2.5). The explanation is that at low concentration of 16Se4, one 16Se4 ligand may bind more than one Pd(II) ion. Comparison of the conformations of 16Se4 before and after the complexation with Pd(II) ion indicates that there is a significant change. The conformation of 16Se4 before the complexation is a [3535] quadrangle with two Se atoms at the corners. However the conformation after complexation has a mm2 symmetry. Thus, 16Se4 has to go through structural reorganization due to its exodentate conformation[75]. A similar conformation was also observed for free thia macrocycles[76,77,174-176]. In order for a coronand to encapsulate the metal ion, the macrocyclic ring has to change its conformation and reorient the chalcogen lone pairs.

167

Therefore, the complexion of metal ions by a thia macrocycle (the sulfur analog of the selenium coronands) is proposed as a stepwise process, the second step being the rate determining step[80]. This is likely to be the case for selenium coronands to encapsulate the metal ions.

When the concentration of Pd(II) is in excess, one 16Se4 molecule may bind more than one Pd(II) atom because the exodentate Se atoms are easier to access. Consequently, the extra Pd(II) ion hinders the conformational reorientation of the coronand to encapsulate the Pd(II). Hence, the absorbance of the complex is smaller than it is supposed to be at [16Se4]/[Pd(II)] lower than 0.5 and the absorbance versus 16Se4/[Pd(II)] ratio displays a non-cooperative binding feature[168].

5.3. Complexes of Cu Ions and Selenium Coronands

5.3.1. Results

5.3.1.1. Preparation, Characterization and Redox Reaction of Cu(II) Complexes

5.3.1.1.1. Cu(II) Complex of 16Se4 (8)

The copper (II) complex of 16Se4 was prepared by the previously reported method[60]. Addition of 8 in CH_2Cl_2 to $Cu(SO_3CF_3)_2$ (1:1 ratio of 8 and $Cu(SO_3CF_3)_2$) in acetone under nitrogen at 0 °C afforded a dark brown solution, from which brown crystals were isolated and were recrystallized in CH_3NO_2 with the diffusion of diethyl ether vapor into the solution. The resulting complex was characterized as $[Cu(16Se4)][SO_3CF_3]_2$ (21) by microanalysis, UV-visible and ESR spectroscopy, and x-ray crystallography[60].

The x-ray structure (Figure 5.3.1) showed that **21** has a tetragonally distorted octahedral configuration at the Cu atom. Four Se atoms bonded with the Cu atom, forming a square plane: Se-Cu = 2.4554 and 2.4593 Å. Oxygens from anions $CF_3SO_3^-$ bonded with Cu at two apical positions: Cu-O = 2.464 Å. The configuration of **21** can be described as c,t,c[165,172], i.e., the non-bonding electron pairs on the Se atoms are cis, trans and cis with respect to one another.

When **21** was dissolved in CH_2Cl_2, it gave rise to a brown solution. The uv-visible spectrum of the solution showed three absorption bands above 250 nm; λ_{max}(nm(ϵ)): 560 (2957), 464 (11920), 310 (1267) (Figure 5.3.3). There was another peak below 250 nm, which resulted from the selenium coronand and was observed for all Cu(II) complexes of selenium coronands. This band will be left out from the description in future.

The room temperature ESR spectrum (Figure 5.3.4) of **21** in CH_3NO_2 solution gave an isotropic g value of 2.053. ^{63}Cu and ^{65}Cu are nuclei of I = 3/2, and ^{77}Se of I = 1/2; therefore, there were four transition lines due to the Cu nucleus coupling plus satellites due to the Se nucleus coupling observed on the spectrum, with hyperfine constant A_{iso}^{Cu} = 75 G, and A_{iso}^{Se} = 42.5 G. The low temperature ESR spectrum of **21** (Figure 5.3.5) was measured at -148 °C (in CH_3NO_2 and toluene (1:1, v/v)). Under the assumption that the complex was an elongated octahedral and the ESR lines did not have any overlap, as in the model proposed by Sand and his co-workers[177,178], the ESR parameters were determined: $g_{//}$ = 2.085. $A_{//}$ = 0.0150 cm^{-1} ; $g_{\perp}$ = 2.049, $A_{\perp}$ = 0.00428 cm^{-1}. Because of the lack of simulation programs, we could not generate a calculated spectrum from these parameters and compare it with the experimental spectrum.

Redox Behavior

The complex **21** was not stable in CH_3NO_2, THF, and particularly in CH_3CN; the addition of a small amount of CH_3CN into **21** in CH_2Cl_2 immediately caused reduction,

manifested by the brown color fading to light yellow color. During the recrystallization (CH_3NO_2/Et_2O), the copper(II) complex was spontaneously reduced to a copper (I) complex that was isolated and identified[60,61] as the polymerized species $[(Cu(16Se4))_\infty]^{\infty+}([SO_3CF_3]^-)_\infty$ (23). From the solution another yellow crystal was isolated through selective crystallization and was identified as the dication[60] of 16Se4 (8).

UV-visible spectroscopy was used to monitor the change of 21 in solutions by following the characteristic peak at 464 nm. In THF, the absorbance at 464 nm was continuously decreasing with time. In CH_2Cl_2 solution the complex was stable; however, addition of free ligand 8 into the solution caused the reduction of the intensity of the peak at 464 nm (Figure 5.3.6) and the generation of a new peak at 320 nm. The peak at 320 nm was due to the radical cation as it had been already established independently by the oxidation of 8 with $NOBF_4$ and by spectroelectrochemistry (see Chapter 4). The room temperature ESR spectrum of 21 (in CH_3NO_2) in the presence of 8 also revealed that the introduction of 8 to the solution resulted in the ESR signal of 21 decreasing, and concurrently new signals appeared. Therefore, complex 21 undergoes a redox reaction as follows,

$$[Cu(16Se4)]^{2+} + 16Se4 \longrightarrow [Cu(16Se4)]^+ + 16Se4^{2+}$$
$$\quad 21 \qquad\qquad 8 \qquad\qquad\qquad\qquad 23 \qquad\qquad 32$$

in which ligand 8 is the reductant that is oxidized by 21 to the radical cation and dication, since the electrochemical study of 8 revealed that the disproportionation of $8^{+\cdot}$ is impossible (see Chapter 4).
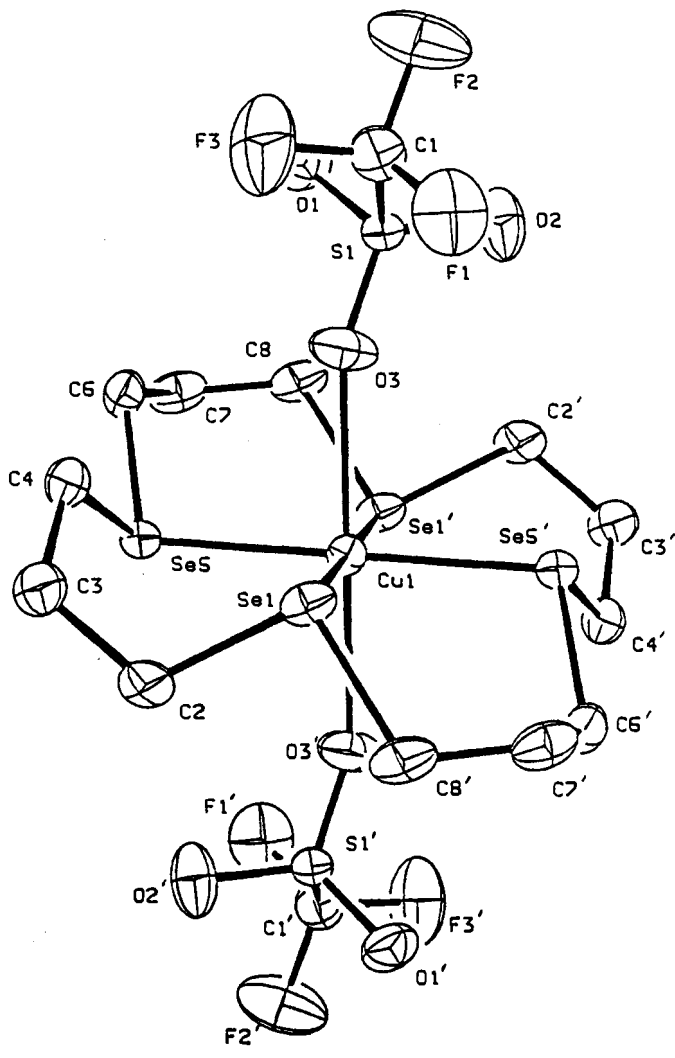
Figure 5.3.1. Structure of [Cu(16Se4)][SO$_3$CF$_3$]$_2$ (21) from X-ray crystallography.
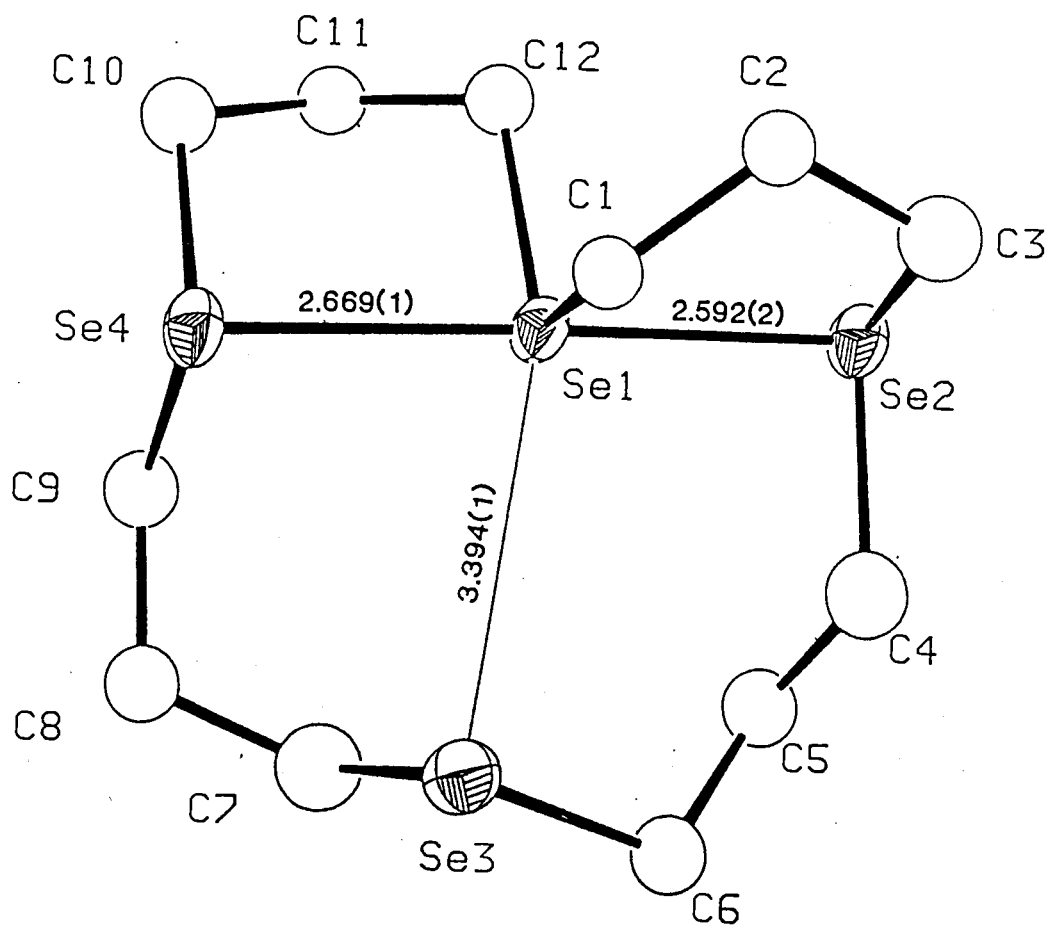
Figure 5.3.2. Structure of [16Se4][SO$_3$CF$_3$]$_2$ (32) from X-ray crystallography.
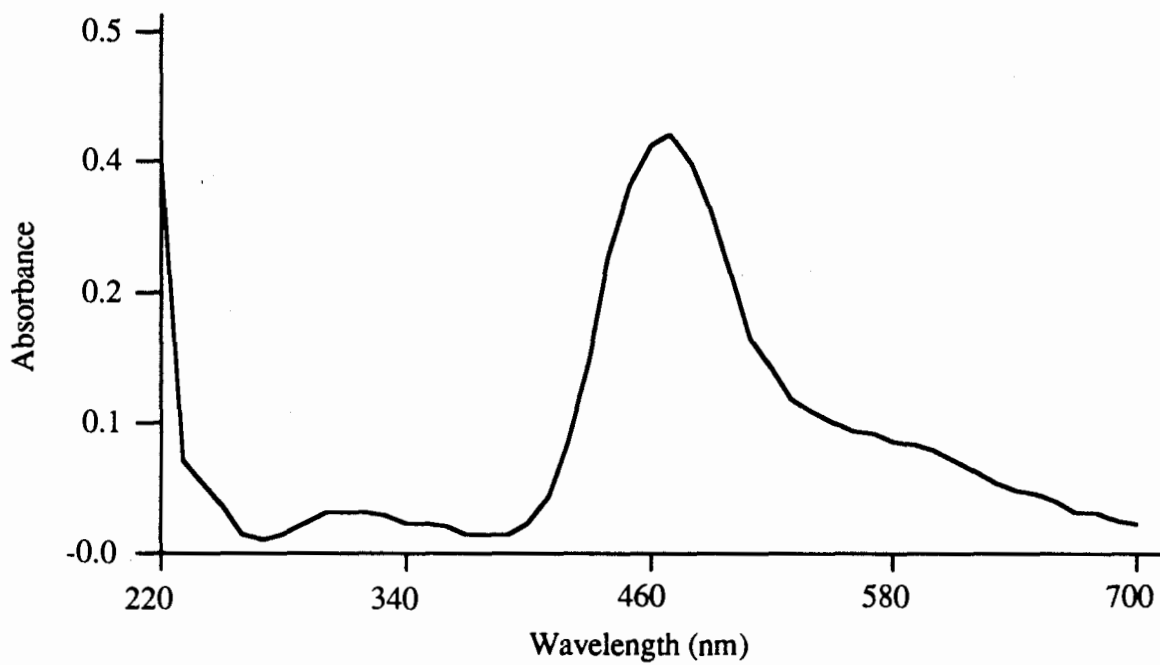
Figure 5.3.3. UV-visible spectrum of $[Cu(16Se4)][SO_3CF_3]_2$ (21) (3.45×10^{-5} M) in CH_2Cl_2.
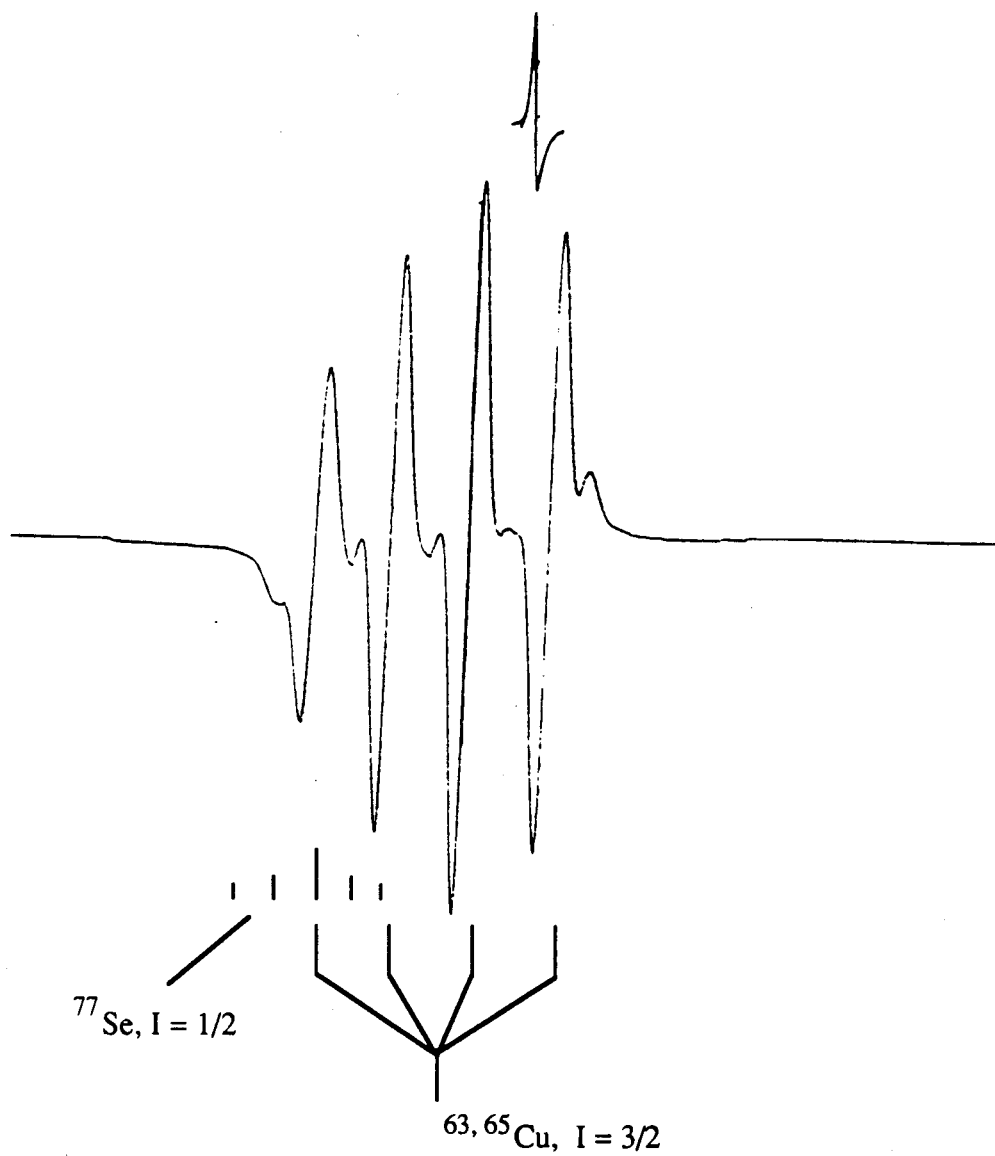
Figure 5.3.4. ESR spectrum of $[Cu(16Se4)][SO_3CF_3]_2$ (21) $(1 \times 10^{-2}$ M) in CH_3NO_2 at room temperature.
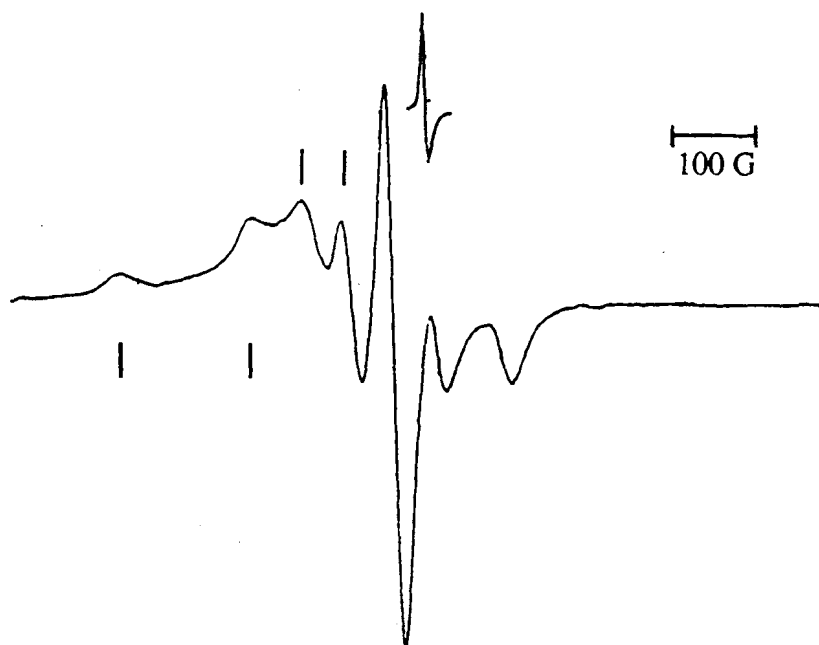
Figure 5.3.5. ESR spectrum of $[Cu(16Se4)][SO_3CF_3]_2$ (21) $(1 \times 10^{-2}$ M) in $CH_3NO_2/CH_3C_6H_5$ (1:1, v/v) at low temperature (125 K).
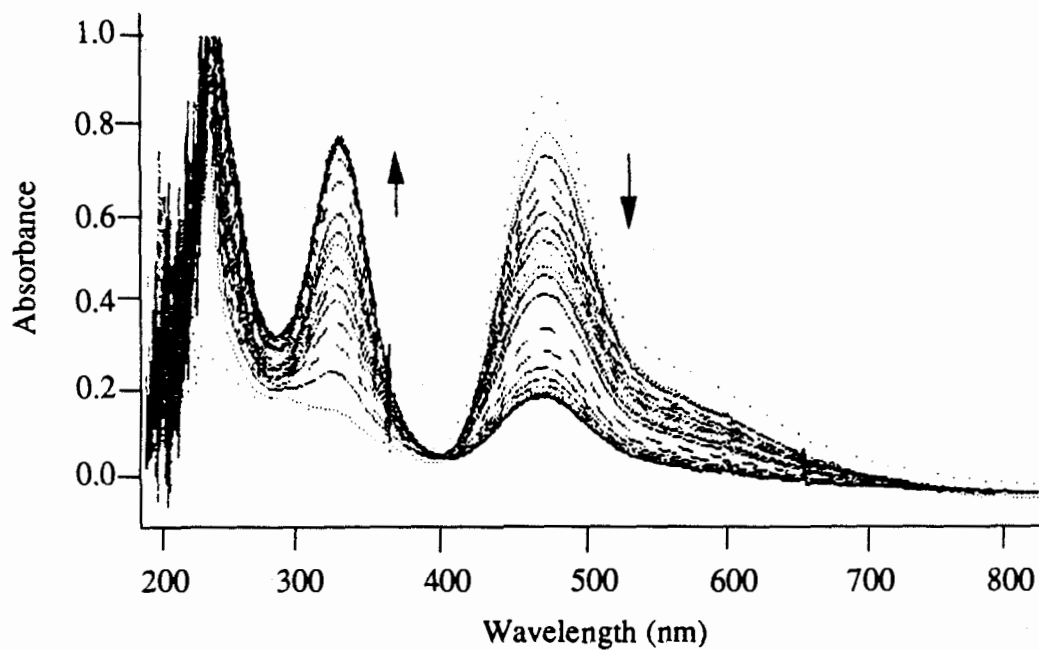
Figure 5.3.6. UV-visible spectra of $[Cu(16Se4)][SO_3CF_3]_2$ (21) $(7.8 \times 10^{-5}$ M) in CH_2Cl_2 in the presence 16Se4 (8) $(1.78 \times 10^{-5}$ M). Dotted line is the original spectrum of $[Cu(16Se4)][SO_3CF_3]_2$. The spectra were taken at an interval of 60 seconds.
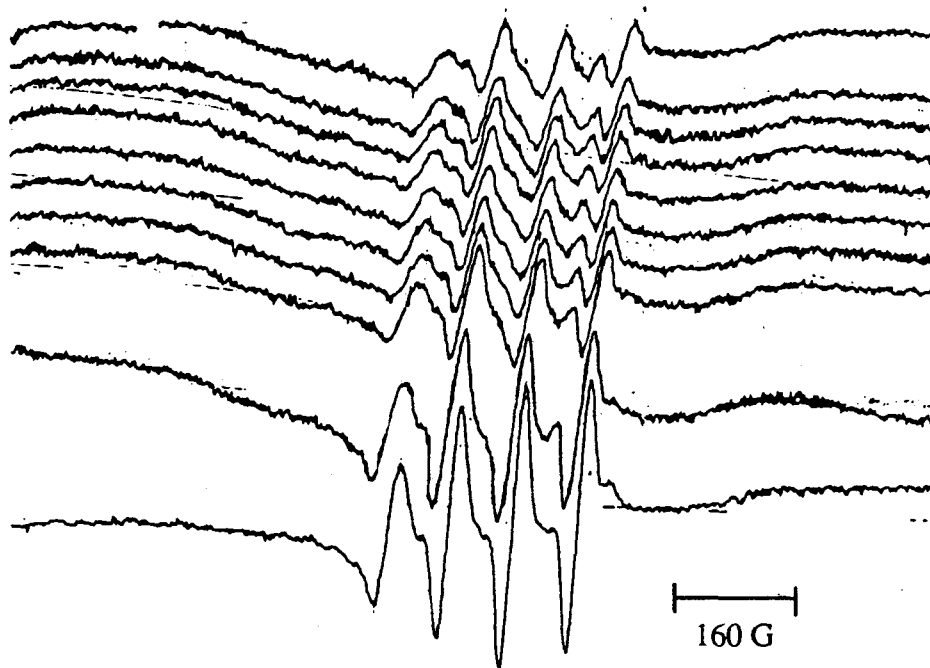
Figure 5.3.7.   ESR spectra of [Cu(16Se4)][SO$_3$CF$_3$]$_2$ (1 × 10^{-2} M) in
CH$_3$NO$_2$ in the presence of 16Se4 (8) (1 × 10^{-2} M) at room
temperature.   The original spectrum is shown in the bottom trace and
subsequent spectra were obtained with an interval of 2 minutes.

177

5.3.1.1.2. Cu(II) Complex of 16Se4(OH)₂ (9)

Addition of **9** in CH_2Cl_2 to $Cu(SO_3CF_3)_2$ (1:1 ratio for **9** and $Cu(SO_3CF_3)_2$) in acetone under nitrogen at temperature 0 °C afforded a dark brown solution from which brown crystals were isolated and recrystallized in CH_3NO_2 with diethyl ether vapor diffusion into the solution. The resulting complex was characterized as $[Cu(16Se4(OH)_2)][SO_3CF_3]_2$ (**39**) by microanalysis, UV-visible, ESR spectroscopy and x-ray crystallography.

Although the crystal structure was severely disordered, the connectivity and stereochemistry of the molecule was clearly revealed. The x-ray structure of **39** (Figure 5.3.8) showed that the complex was in a tetragonally distorted octahedral arrangement at the Cu atom with four selenium atoms coordinating the central copper (II) ion on the square plane; oxygen atoms from one of the hydroxyl groups and from one of the anions ($CF_3SO_3^-$) coordinating the copper (II) ion along the axial axis (Se-Cu = 2.421(2), 2.442(3), 2.445(2) and 2.488(3) Å, Cu-O = 2.445 and 2.58 Å, $\angle$Se-Cu-Se = 85.4(1), 91.6(1), and 176.4(1)). Only one of the hydroxyl groups is involved in the coordination because the arrangement of the two hydroxyl groups in the macrocyclic ring is *cis*. Another anion group, $CF_3SO_3^-$, formed a hydrogen bond with the unbound hydroxyl group on the macrocyclic ring. The configuration of 16Se4(OH)₂ (**9**) in the complex can be described as c,t,c.

When **39** was dissolved in CH_2Cl_2 it gave rise to a brown solution. The uv-visible spectrum (Figure 5.3.9) of the solution showed two absorption bands above 250 nm; λ_{max}(nm(ε)): 448 nm (ε = 6811) with a shoulder at 550 nm (ε = 2000) and 328 nm (ε = 1658).
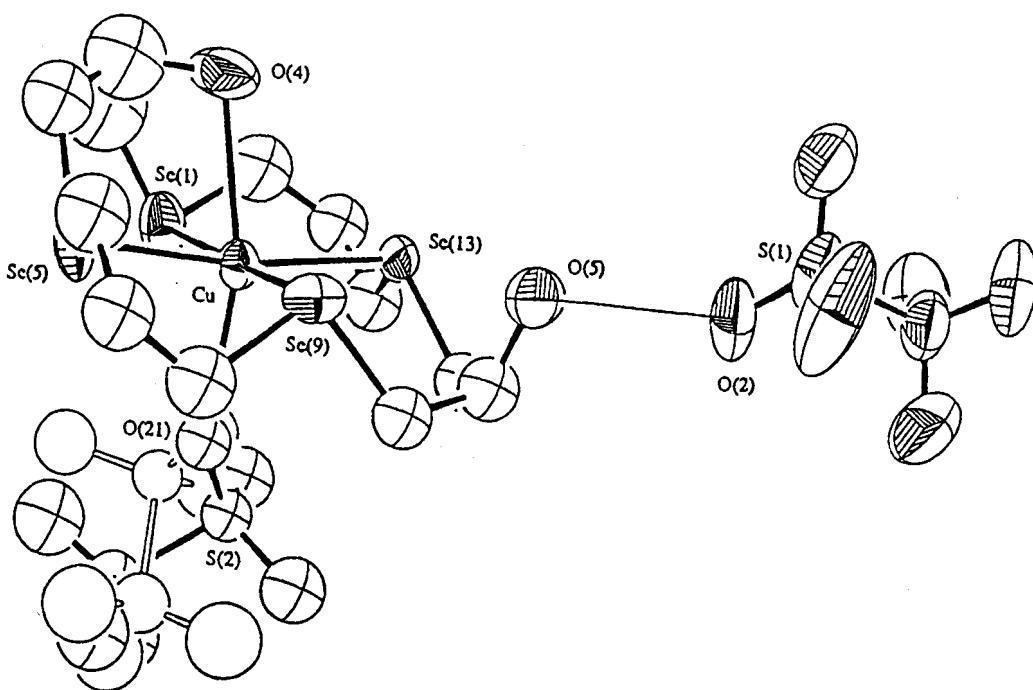
Figure 5.3.8.   Structure of [Cu(16Se4(OH)₂)][SO₃CF₃]₂ (39).
50%-enclosure ellipsoids or sphere, shown, represent a degree of
unmodelled disorder.   For clarity of presentation, one (44.9(6)%
occupancy) of the two disordered orientations of the coordinated
SO₃CF₃ group (partially obscured) is depicted by small spheres and
line bonds. The oxygen atoms involved in the interionic hydrogen
bond are connected with a line.
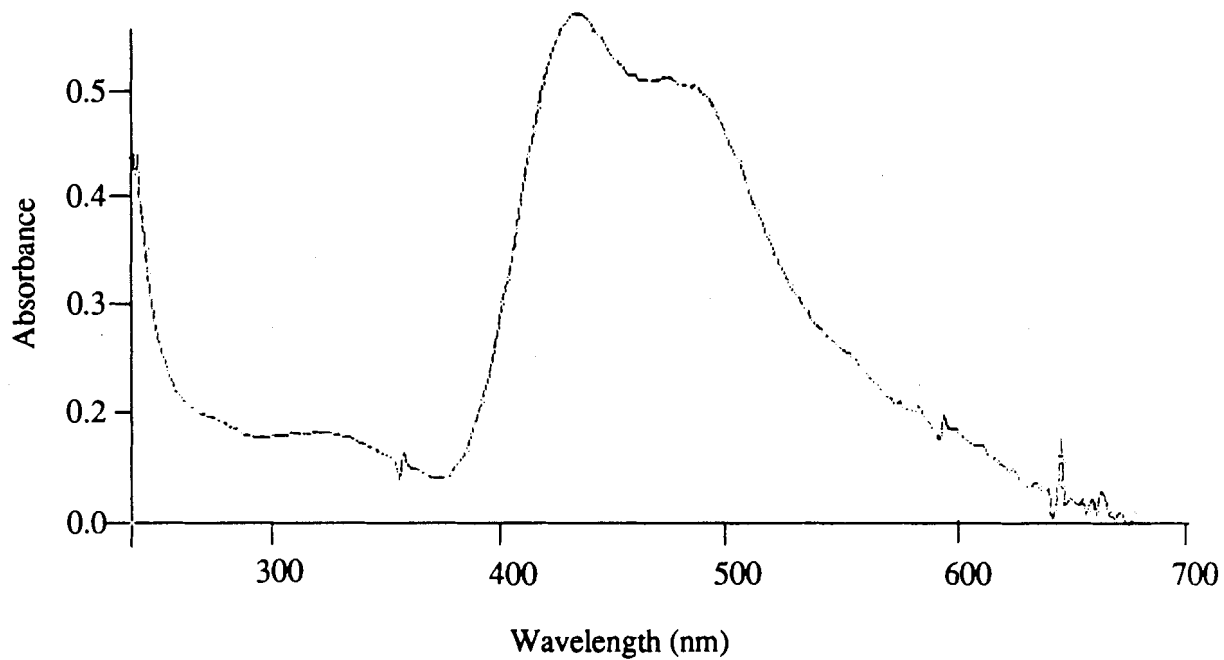
Figure 5.3.9. UV-visible spectrum of $[Cu(16Se4(OH)_2)][SO_3CF_3]_2$ (39) $(1.0 \times 10^{-4}$ M) in CH_2Cl_2.
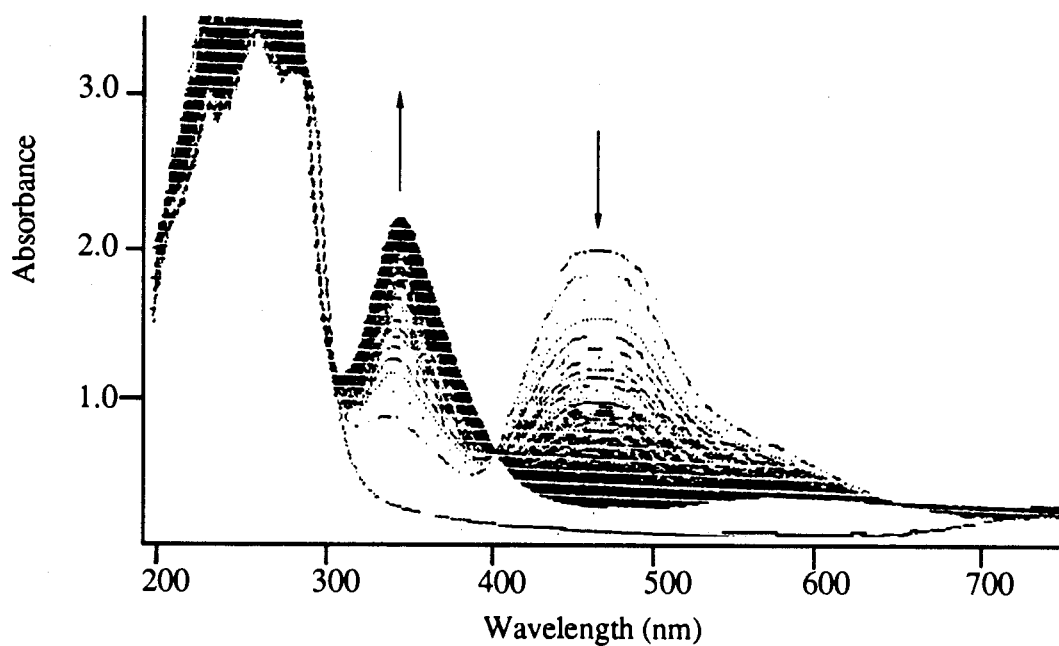
Figure 5.3.10. UV-visible spectra of $[Cu(16Se4(OH)_2)][SO_3CF_3]_2$ (39) in EtOH solution with $[Cu(SO_3CF_3)_2] = 6.65 \times 10^{-3}$ M; $[16Se4(OH)_2] = 2.1 \times 10^{-4}$ M. The spectra were taken at an interval of 2 seconds.
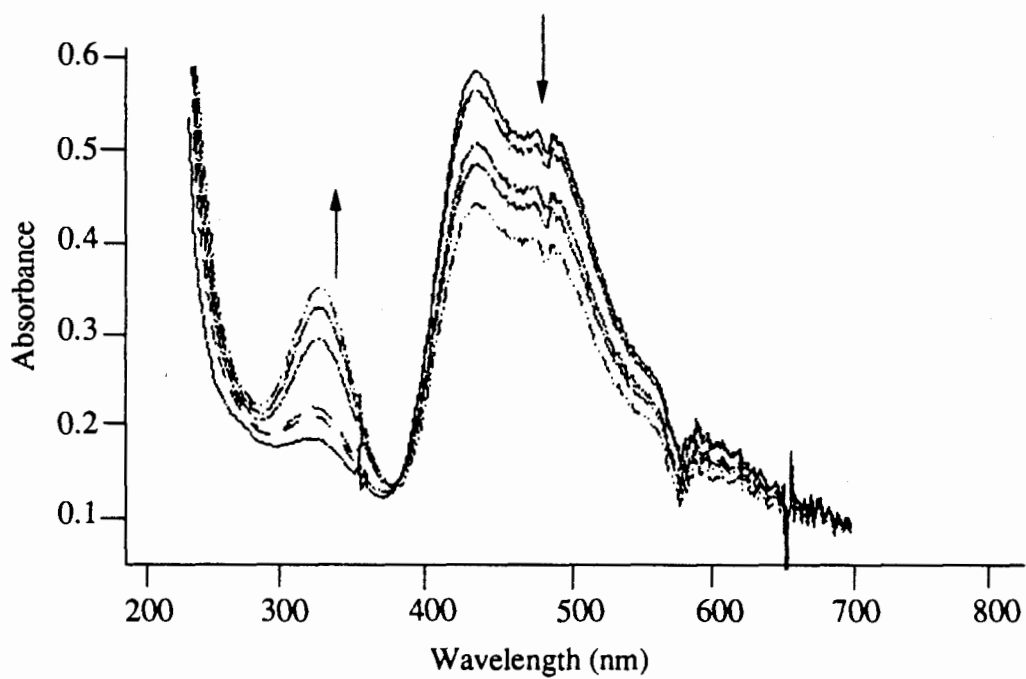
Figure 5.3.11. UV-visible spectra of $[Cu(16Se4(OH)_2)][SO_3CF_3]_2$ $(8.21 \times 10^{-5}$ M) in CH_2Cl_2 in the presence of $16Se4(OH)_2$ (9) $(4.14 \times 10^{-5}$ M). The spectra were taken at an interval of 60 seconds.
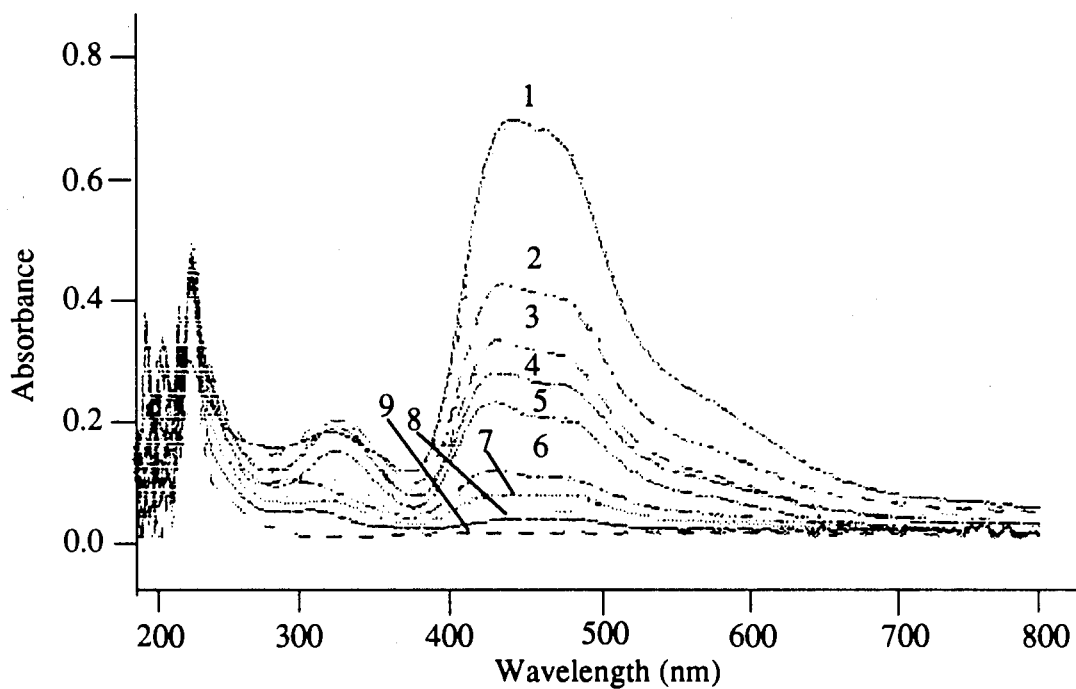
Figure 5.3.12. UV-visible spectra of [Cu(16Se4(OH)₂][SO₃CF₃]₂ (39) in CH₂Cl₂ with the presence of 16Se4(OH)₂ (9). The fractional concentration of 39: 1) 1; 2) 0.8; 3) 0.7; 4) 0.6; 5) 0.5; 6) 0.5; 7) 0.3; 8) 0.2; 9) 0.1.

A room temperature ESR spectrum of **39** (in CH_3NO_2 solution) was recorded, which gave an isotropic g value of 2.050 and hyperfine constants A_{iso}^{Cu} = 77.5 G, A_{iso}^{Se} = 40 G.

Compound **39** was not stable in EtOH. Continuous uv-visible absorption spectra (Figure 5.3.10) at an interval of 2 seconds were recorded on a solution formed by adding **9** (2.1×10^{-4} M) to $Cu(SO_3CF_3)_2$ (6.65×10^{-3} M) both in EtOH. At the beginning, the same spectrum was observed as that from **39** in CH_2Cl_2, and the absorption intensities (448 nm and 328 nm) reached the maximum in about 8 seconds after the mixing. Then, the intensity of the peak at 464 nm started decreasing and virtually disappeared, while the peak at 328 nm was increasing. The isosbestic point at 400 nm indicated that the peak at 328 nm was a species derived from that with λ_{max} 464 nm. In addition, a new band (λ_{max} = 600 nm) also appeared, which was tentatively assigned to a d-d transition band. The peak at 328 nm is unlikely to be from the absorption of the radical cation, $16Se4(OH)_2^{+\cdot}$ ($9^{+\cdot}$), because mixing $16Se4(OH)_2$ (**9**) and $NOBF_4$ in CH_3CN produced a peak around 332 nm whose intensity decreased with time. Thus, the intensity decrease of the peak at 464 nm is attributed to the dissociation of the complex and to the formation of a new Cu(II) complex species that has an absorption peak at 328 nm.

Addition of **9** to **39** ([9]/[39], 1/2) in CH_2Cl_2 also caused the absorption at 448 nm to decrease and the peak at 328 nm to increase (Figure 5.3.11). However, the changing of both absorption intensities stopped within 220 seconds after the addition of **9**. The absorption measurements were continued for 600 seconds; the total reduction of the peak at 448 nm was about 30%.

In another experiment, uv-visible absorption spectra were measured for a series of solutions that were prepared by mixing the stock solutions of **39** and **8** (same concentrations) in various ratios in 10-ml flasks. The spectra are shown in Figure 5.3.12. In comparison with the spectrum of **39** in the absence of **9**, one can observe that as the fractional concentrations of **39** gradually decreased (that of **9** increased) the intensity of the

absorption (448 nm) decreased, but the peak at 330 nm first increased for the fractional concentration of **39** of 0.8, 0.7, 0.6, then shifted to 302 nm and back to 330 nm for the fractional concentration of **39** of 0.4 and 0.3, respectively. When the fractional concentration of **39** became 0.1 the peak at 330 nm shifted to 302 nm again. These observations suggested that the changing of peak position was due to the association-dissociation process.

5.3.1.1.3. *Cu(II) complexes of 8Se2 (16) and 8Se2OH (17)*

Attempts to generate a Cu(II) complex of 8Se2 (**16**) were unsuccessful because of a facile redox reaction. For example, addition of 8Se2 (**16**) in CH_3CN to $Cu(SO_3CF_3)_2$ in the same solvent afforded a transient orange colored solution that turned to a yellow solution, which yielded colorless crystals. The crystals were recrystallized in CH_3CN, and characterized as $8Se2(SO_3CF_3)_2$ (**33**), a dication of 8Se2 (**16**), by ^{1}H, ^{13}C NMR[91] and microanalysis. The uv-visible spectrum of **33** in CH_3CN solution showed an absorbance maximum at 248 nm.

Addition of 8Se2OH (**17**) in CH_2Cl_2 to $Cu(SO_3CF_3)_2$ (2:1 ratio for **17** and $Cu(SO_3CF_3)_2$) in acetone under nitrogen at temperature 0 °C afforded a dark brown solution from which brown crystals were isolated and recrystallized in CH_3NO_2 with diethyl ether vapor diffusion into the solution. The resulting complex was characterized as $[Cu(8Se2OH)_2][CF_3SO_3]_2$ (**41**) by microanalysis, UV-visible and ESR spectroscopy and x-ray crystallography.

The x-ray structure of **41** showed that the Cu atom is on a crystallographic inversion centre (Figure 5.3.13). Each ligand (8Se2OH, **17**) chelated the Cu atom forming a square plane and the oxygens of the OH groups occupied the apical positions. The complex is of a typical tetragonally distorted octahedral symmetry: Se-Cu = 2.4655 (4) and 2.4582 (4) Å, Cu-O = 2.358(3) Å. Anion groups (SO_3CF_3) attached to the hydrogen of hydroxyl groups through hydrogen bonds. The conformation of the eight-membered rings

was predominantly chair-chair (87%). There was 13% disorder from the chair-boat conformation (outlined bonds in Figure 5.3.13).

When **41** was dissolved in CH_2Cl_2 it gave rise to a purple solution. The uv-visible spectrum of the solution showed three absorption bands above 250 nm; λ_{max}(nm(ε)): 571 (8116) , 510 (7050), 386 (7905) (Figure 5.3.14).

A room temperature ESR spectrum of **41** (Figure 5.3.15 a) (in CH_3NO_2 solution) was recorded, which gave an isotropic g value of 2.048 and hyperfine constants A_{iso}^{Cu} = 77.5 G, A_{iso}^{Se} = 30.5 G. A low temperature ESR spectrum of **41** measured at -148 °C in CH_3NO_2 and toluene (1:1, v/v) has the features of a glass. Under the assumption that the complex was an elongated octahedral and the ESR lines did not have any overlap, as the model proposed by Sand and co-workers[177,178], the ESR parameters were determined: $g_{//}$ = 2.085. $A_{//}$ = 0.0155 cm^{-1} ; $g_{\perp}$ = 2.049, $A_{\perp}$ = 0.00335 cm^{-1}. Because of the lack of simulation programs, we could not generate a calculated spectrum from these parameters and compare it with the experimental spectrum.

When CH_3CN was added to the CH_2Cl_2 solution of **41** the purple colour would fade away. However, the purple colour could be restored by adding CH_2Cl_2 into the former solution, which was in contrast to the case of $[Cu(16Se4)][CF_3SO_3]_2$ (**21**). This suggests that the redox reactivity of **41** is different from that of **21**.

Addition of 8Se2OH (**17**) to $[Cu(8Se2OH)_2](CF_3SO_3)_2$ (**41**) (in a ratio of 10 for **17/41**) in CH_2Cl_2 solution caused absorption peaks (571 and 386 nm) to decrease, but the reduction of the peaks stopped when 70% of original intensity (571 nm) had disappeared. In another experiment, uv-visible absorption spectra were measured for a series of solutions that were prepared by mixing stock solutions of **41** and **17** (in the same concentrations) in various ratios. The spectra are shown in Figure 5.3.16. In comparison with the spectrum of **41** in the absence of **17**, the intensity of the spectra decreased as the fractional concentration of **41** gradually decreased (that of **8** increased). However, at the fractional concentration of **41** = 0.2, the absorption peaks (571 nm and 386 nm)

disappeared and a new peak (around 360 nm) appeared. This indicates that a dissociation-association process is involved.

Addition of 8Se2OH (**17**, 7.2×10^{-3} M) to a CH_3NO_2 solution of **41** (1.0×10^{-2}) caused the former dark brown solution to turn into a light brown solution. The ESR spectrum (Figure 5.3.15 b) of the mixture showed new signals with no hyperfine structure at the lower magnetic field in addition to the signals due to **41**.
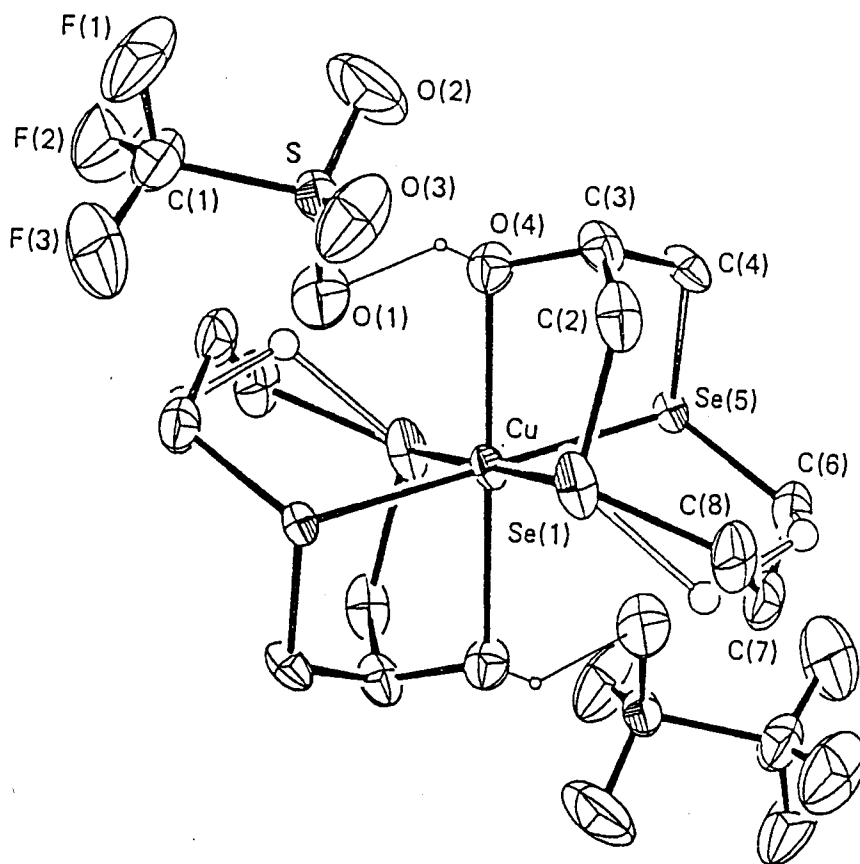
Figure 5.3.13. Structure of $[Cu(8Se2OH)_2][SO_3CF_3]_2$ (41). Boundary ellipses and single line bonds only are shown for the 12.9(6)% conformation of the disordered propylene segment. 50%-enclosure ellipsoids for the non-hydrogen atoms and a sphere of arbitrary radius for the hydroxyl hydrogen atom are depicted. Lines denote the O(4) - H bond and the hydrogen bond to O(1).
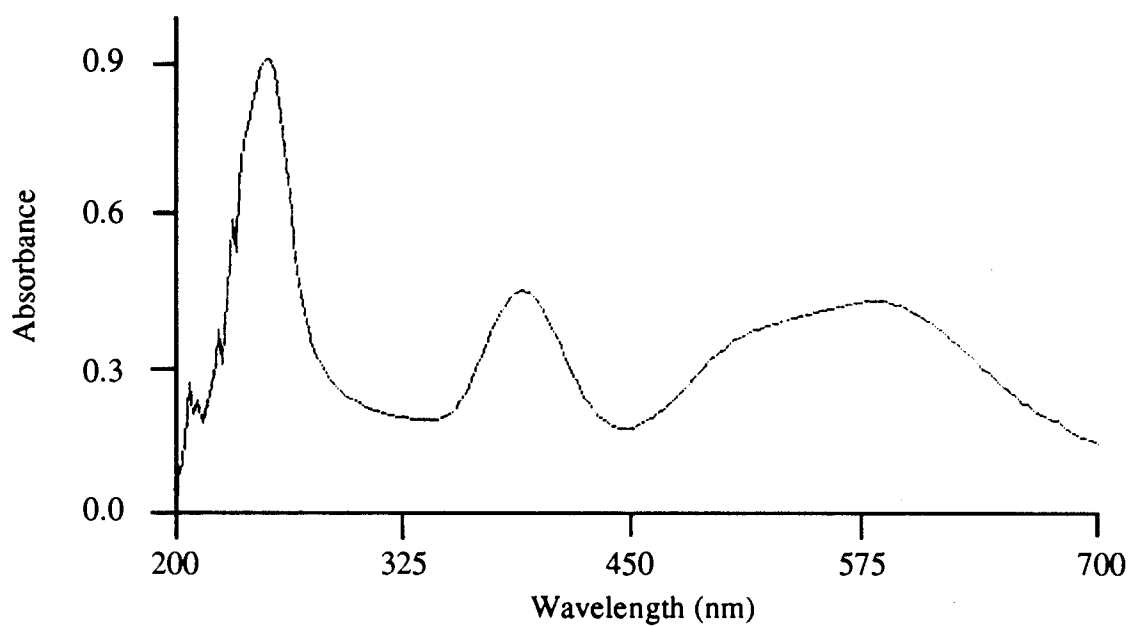
Figure 5.3.14. UV-visible spectrum of $[Cu(8Se2OH)_2][SO_3CF_3]_2$ **(41)** $(9.5 \times 10^{-5}$ M) in CH_2Cl_2 at 25 °C.

189
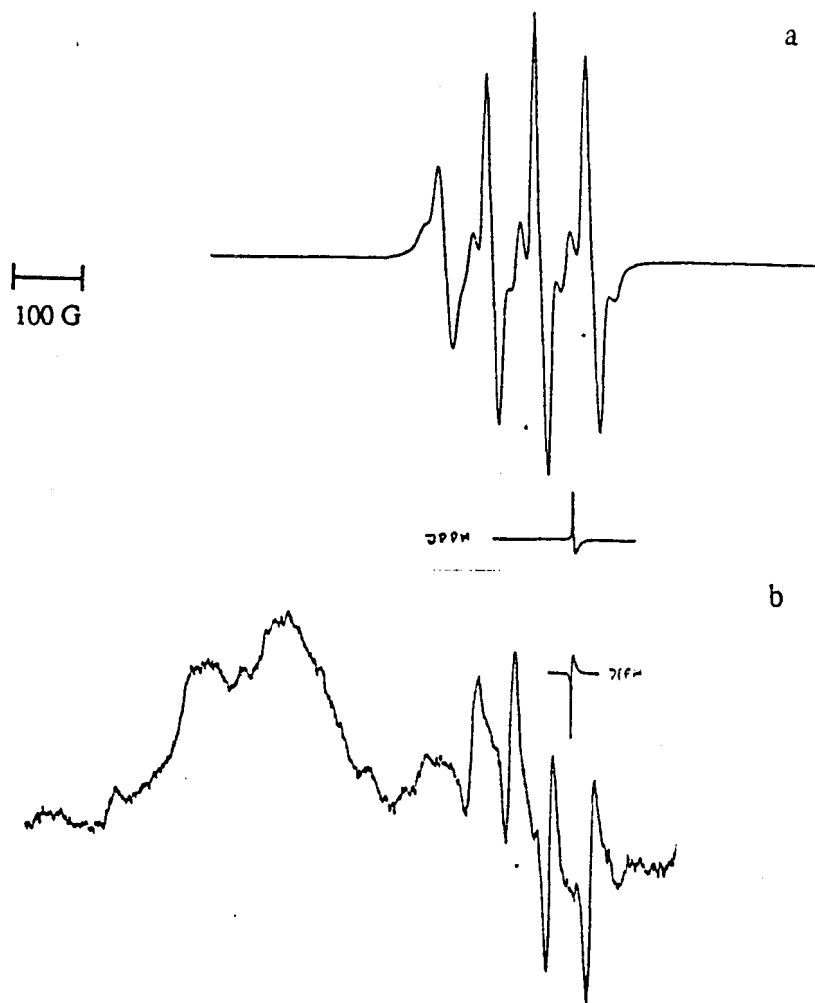
Figure 5.3.15. ESR spectra of [Cu(8Se2OH)$_2$][SO$_3$CF$_3$]$_2$ (41) in CH$_3$NO$_2$ at room temperature. a) [Cu(8Se2OH)$_2$][SO$_3$CF$_3$]$_2$ (41)(1.0 × 10^{-2} M); b) in the presence of 8Se2OH (17)(7.2 × 10^{-3} M), modulation amplitude 2.5 G, microwave power 20 mW.
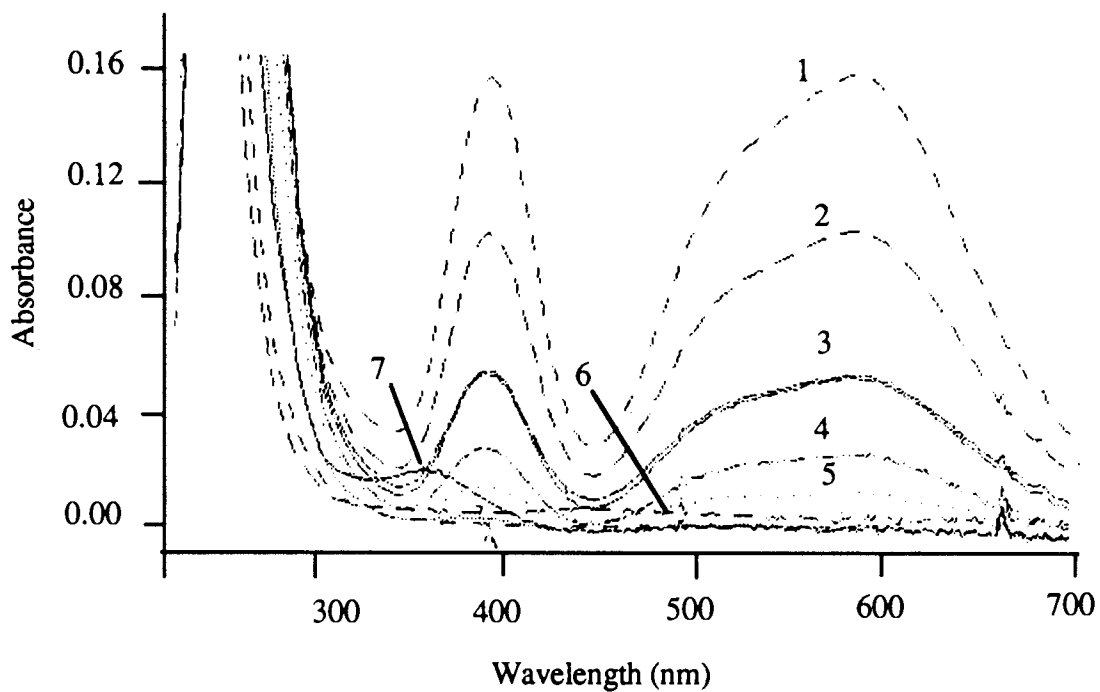
Figure 5.3.16. UV-visible spectra of $[Cu(8Se2OH)_2][SO_3CF_3]_2$ (41) in CH_2Cl_2 in the presence of 8Se2OH (17). [41]/[17] 1) 0.8; 2) 0.7; 3) 0.6; 4) 0.5; 5) 0.4; 6) , 7) 0.2.

5.3.1.1.4. Cu Complexes of 16Se4OH (10)

During the recrystallization of the Cu(II) complex of 16SeOH (**10**) ([Cu(16Se4OH)][SO$_3$CF$_3$]$_2$, **40**), the complex was found to be unstable in CH$_3$NO$_2$ solution with the diffusion of ether vapor into the solution and yield a mixture of the Cu(II) complex, **40** (brown crystals), and Cu(I) complex (white crystals), [Cu(16Se4OH)][SO$_3$CF$_3$][179] (**45**). Both complexes were characterized by microanalysis and the latter by x-ray crystallography.

The structure of **45** contains disordered ion pairs. The predominant combination is shown in Figure 5.3.17. The coordination at Cu is tetrahedral. Bond distances and angles at Cu along with selected bond torsion angles for the cationic complex are listed in Table 5.3.5. The site of hydroxyl substitution in the crystal structure varies between O(7) (56.6(13) %; shown in Figure 5.3.17, the alternate position on the same carbon atom (22.3(12) %), denoted as O(107), and two reasonably situated lesser contributors -- O(15) (11.9(12) %) and O(11) (9.3(11) %), bonded to C(15) and C(11) respectively. O(7), O(11) and O(15) are all in pseudo-equatorial positions (directed away from Cu when viewed as in Figure 5.3.17) and are located such that each would form a hydrogen bond with an oxygen atom from an adjacent anion. In contrast, O(107) is in the pseudo-axial position on C(7) and displays a weaker hydrogen-bonded interaction. The two propylene arrangements represent alternate 'half-boat' conformations of the associated CuSeC$_3$Se six-membered ring. If anions and the ring substituents are ignored the skeletal Cu(16Se4) complex still displays only *1* (*C$_1$*) point-symmetry for either conformation; however, the two conformations are approximately related by a 180° rotation of the complex about the axis passing through Cu and C(3). Thus the forms with oxygen at O(7) or O(15) could merely represent different orientations of the cation, while the O(7)- and O(107)-substituted forms differ from one another in conformation (and orientation). On the other hand,

substitution at O(11) produces a form enantiomeric to, and also differing in conformation

(and orientation) from, the others.
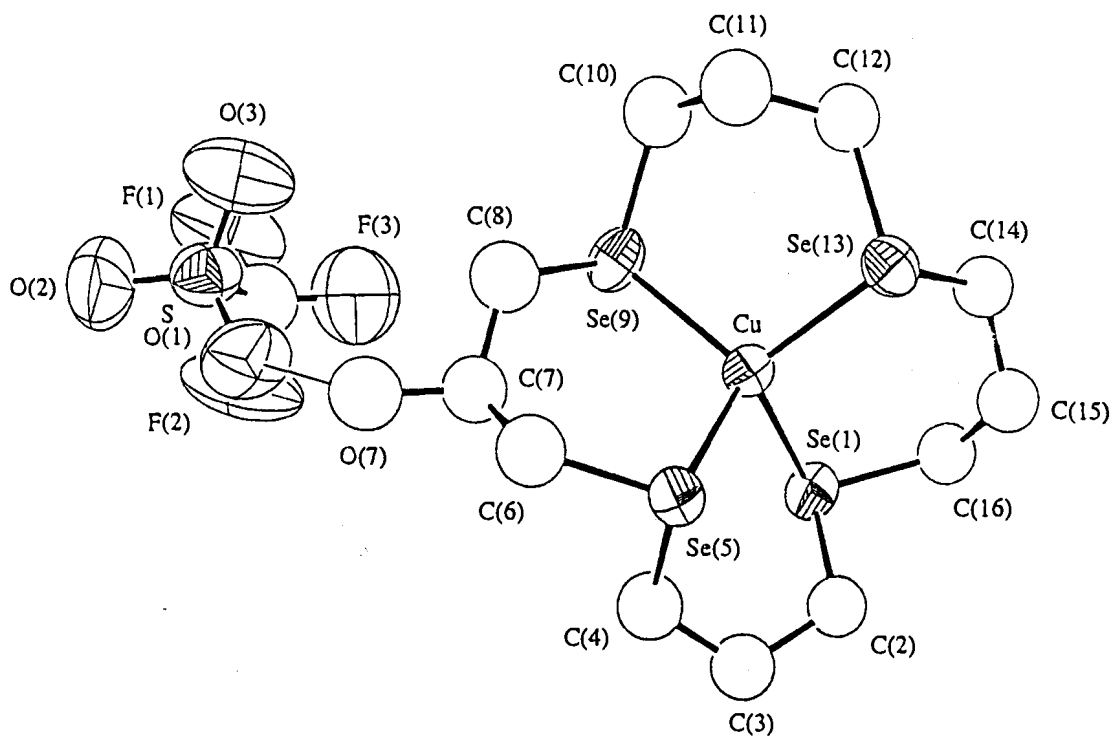
Figure 5.3.17. Structure of [Cu(16SeOH)][SO₃CF₃] (45) from X-ray crystallography. 50% enclosure ellipsoids or spheres for non-hydrogen atoms are depicted. A single line represents the hydrogen bond from O(7) to O(1).

194

5.3.1.1.5. Cu complexes of 16S2Se2 (11)

Addition of 16S2Se2 (**11**) in CH_2Cl_2 to $Cu(SO_3CF_3)_2$ (1:1 ratio for **11** and $Cu(SO_3CF_3)_2$) in acetone under nitrogen at 0 °C afforded a dark brown solution from which brown crystals were isolated and recrystallized in CH_3NO_2 with diethyl ether vapor diffusion into the solution.   The resulted complex was characterized as $[Cu(16S2Se2)][CF_3SO_3]_2$ (**42**) by microanalysis, UV-visible and ESR spectroscopy and x-ray crystallography.

The x-ray structure (at 205 K) of **42** (Figure 5.3.18) shows that the complex is similar to $[Cu(16Se4)](SO_3CF_3)_2$[60] (**21**) and the thia ether complex $[Cu(16S4)](ClO_4)_2$[33]. The complex **42** displayed a tetragonally distorted octahedral arrangement at Cu atom: Two S atoms and two Se atoms occupied the central position on the sides of the square plane; each anion coordinated with Cu weakly via one of the oxygen atoms along the pseudotetragonal axis of the complex. The configuration of 16S2Se2 (**11**) in the complex is described as c,t,c and the conformation of the ligand, 16S2Se2, is described as [4444]. Because there was an unresolved disorder from partial occupancy of each chalcogen site by selenium or sulfur only weighted mean distances were obtained: Cu-S/Se = 2.4095(7), 2.4136(6) Å.   These are intermediate between the Cu-Se bond lengths in $[Cu(16Se4)][SO_3CF_3]_2$ (**21**) (2.4593(6) and 2.4554(6) Å)[60] and the Cu-S bond lengths in $[Cu(16S4)][SO_3CF_3]_2$ (2.3314(13) and 2.3874(17) Å)[33]. The mean Cu-O bond length in **42** (2.46 Å) is indistinguishable from that in **21** (2.464(5) Å).   The weighted-mean chalcogen atom site to carbon atom site 'bond distances' range from S/Se(1)-C(2) 1.897(4) Å to S/Se(1)-C(8) 1.911(4) Å. The C-C bond distances in **42** range from 1.506(6) Å to 1.523(6) Å. The C-S/Se-C bond angles are 95.6(2)° and 94.6(2)°; the C-C-S/Se angles range from 110.6(3)° to 113.7(3)°; the C-C-C angles are 114.4(4)° and 114.5(3)°.

195

A room temperature ESR spectrum of **42** (in CH_3NO_2 solution) was recorded, which gave an isotropic g value of 2.055 and hyperfine constants A_{iso}^{Cu} = 74 G. The satellite lines due to the coupling of ^{77}Se were not resolved.

Redox Behavior

Spontaneous reduction of **42** in organic solvents was observed during recrystallization. In order to obtain crystals for x-ray crystallography, several solvent systems were tried in the recrystallization of **42**. From CH_3NO_2/CH_2Cl_2 (2:1, v/v) with ether vapor diffusion, crystals of **42** with reasonable quality for x-ray crystallography were isolated. However, from the acetone solution with ether vapor diffusion, white crystals were formed and isolated. The white crystal was identified as [Cu(16S2Se2)][CF_3SO_3] (**43**) by microanalysis and x-ray crystallography.

The structure of the predominant (71.9(9) %) conformation of the complex cation of **43** is shown in Figure 5.3.20. The complex cation of **43** has a tetrahedral configuration at the Cu atom that is typical for a d^{10} Cu(I) ion. Because there was an unresolved disorder from partial occupancy of each chalcogen site by Se or S atoms, only weighted mean distances between Cu and chalcogen atoms in Cu(II) complexes were obtained: Cu-Ch 2.335(14), 2.3371(11), 2.3477(11), 2.3511(12) Å (Table 5.3.5). As expected, the Cu-to-chalcogen-atom distances were intermediate between the Cu-Se bond lengths in [Cu(16Se4OH)]$^+$ and typical Cu(I)-S bond lengths (2.243 - 2.338 Å[35,176,180]). Other bond lengths and angles do not deviate significantly from expected values.

Ignoring the variable S/Se site substitution, this conformation displays approximate two-fold rotational symmetry about an axis which intersects the midpoint of the S/Se(1) to S/Se(9) vector and Cu (*i.e.* normal to the projection shown). The alternate conformation (28.7(9) %) replaces C(14)-C(15)-C(16) with C(140)-C(150)-C(160) and is asymmetric.

The redox process that produced **43** was also observed by uv-visible spectroscopy. When **42** was dissolved in CH_2Cl_2, it gave rise to a brown solution. The uv-visible spectrum of the solution showed two absorption bands above 250 nm; λ_{max}(nm(ε)): 456

196

(6872) with a shoulder 570 (900) and 280 (451). Addition of **11** to **42** in CH_2Cl_2 caused the absorption peak at 464 nm to decrease and a new peak at 310 nm to increase (Figure 5.3.21). The peak at 310 nm was due to the absorption of the radical cation of **11**, which was confirmed by reacting $NOBF_4$ with **11** in CH_3CN. The formation of **43** may be represented by the following redox reaction.

$$[Cu(16S2Se2)]^{2+} + 16S2Se2 \longrightarrow [Cu(16S2Se2)]^+ + 16S2Se2^+$$
$$\textbf{42} \qquad\qquad \textbf{11} \qquad\qquad\qquad\qquad \textbf{43} \qquad\qquad \textbf{11}^+\cdot$$
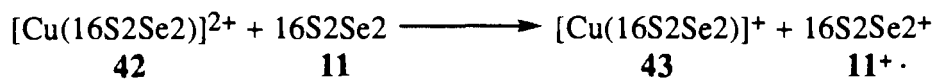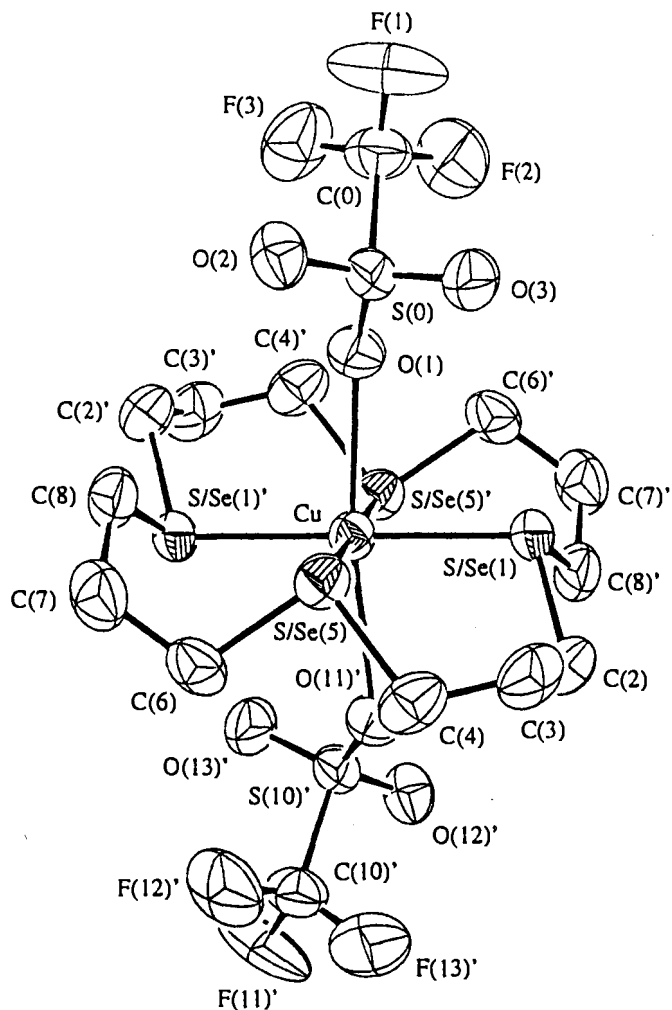
Figure 5.3.18. Structure of [Cu(16S2Se2)](SO₃CF₃)₂ (42). 50% enclosure ellipsoids are shown for the non-hydrogen atoms. For the clarity of presentation, the two disordered orientations of the SO₃CF₃ group are depicted exclusively on opposing sides of the molecule.
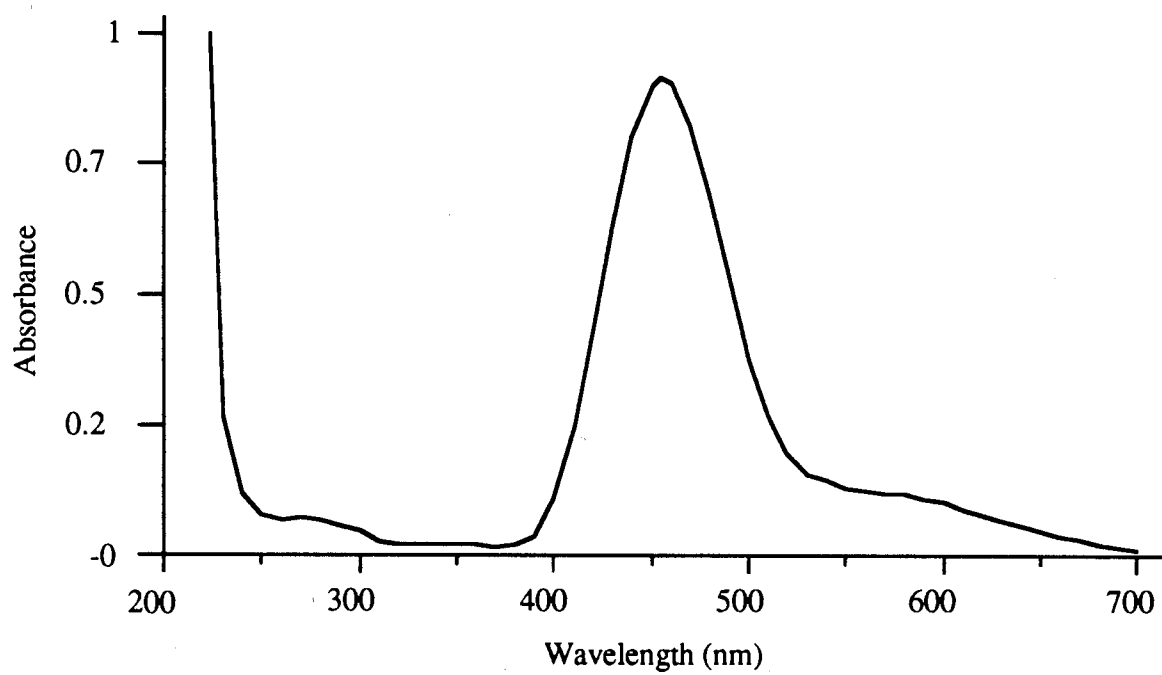
Figure 5.3.19. UV-visible spectrum of $[Cu(16S2Se2)][SO_3CF_3]_2$ (42)(2.66 $\times$ 10^{-4} M)in CH_2Cl_2.
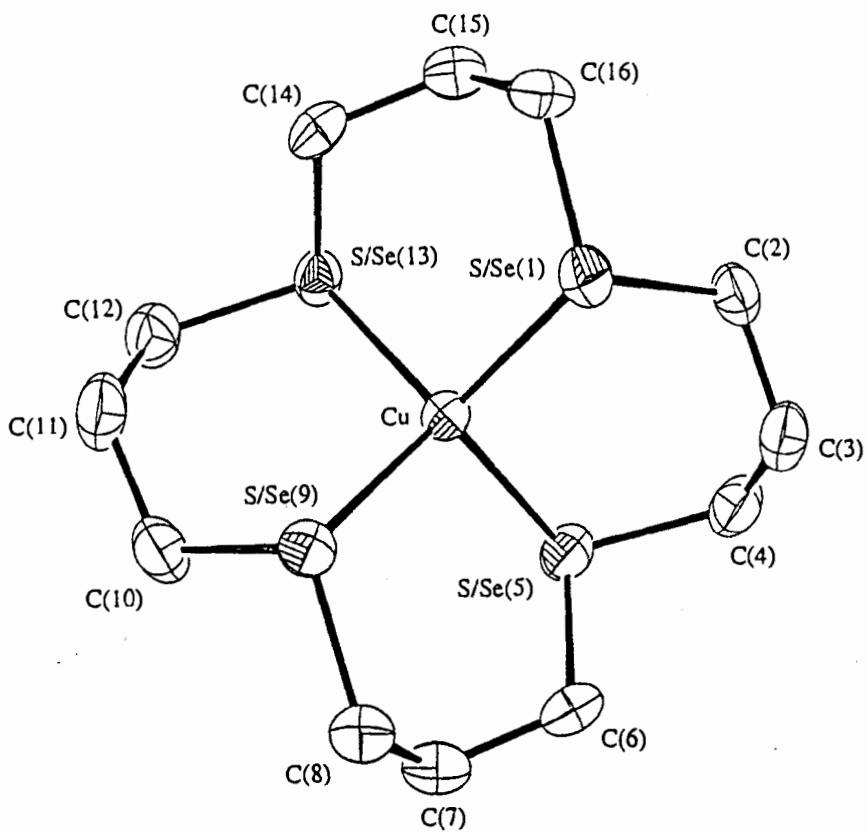
Figure 5.3.20. Structure of [Cu(16S2Se2)]⁺ (43) from X-ray crystallography. 50% enclosure ellipsoids are shown for non-hydrogen atoms.
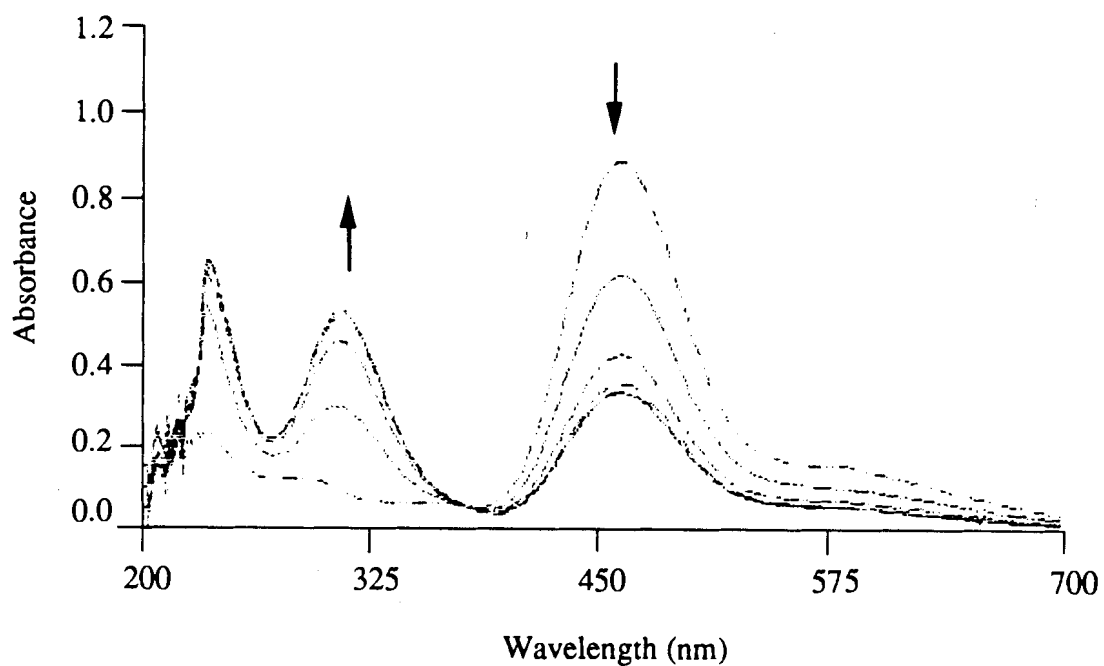
Figure 5.3.21. UV-visible spectra of $[Cu(16S2Se2)][SO_3CF_3]_2$ (42) $(5.33 \times 10^{-5}$ M) in CH_2Cl_2 in the presence 16S2Se2 (11) $(2.62 \times 10^{-5}$ M) at room temperature. The spectra were taken at an interval of 60 seconds.

5.3.1.1.6. Cu(II) Complex of 14Se4 (13)

Addition of **13** in CH_2Cl_2 to $Cu(SO_3CF_3)_2$ (1:1 ratio for **13** and $Cu(SO_3CF_3)_2$) in acetone under nitrogen at temperature 0 °C afforded a dark brown solution from which a brown precipitate was isolated and recrystallized in CH_3NO_2 with diethyl ether vapor diffusion into the solution.   The resulting complex was characterized as $[Cu(14Se4)][CF_3SO_3]_2$ (**44**) by microanalysis, UV-visible and ESR spectroscopy. Unfortunately, a crystal of x-ray crystallographic quality could not be obtained.

When **44** was dissolved in CH_2Cl_2 it gave rise to a brown solution. The uv-visible spectrum (Figure 5.3.21) of the solution showed two absorption bands above 250 nm; λ_{max}(nm(ε)): 418(5241) with a shoulder at 554 (1362) and 280 (1360) nm.

A room temperature ESR spectrum of **44** (in CH_3NO_2 solution) was recorded, which gave an isotropic g value of 2.048 and hyperfine constants A_{iso}^{Cu} = 82.5 G, A_{iso}^{Se} = 32 G. A low temperature ESR spectrum of **44** was measured at -148 °C in CH_3NO_2 and toluene (1:1, v/v). Under the assumption that the complex was an elongated octahedral and the ESR lines did not have any overlap, as the model proposed by Sand and co-workers[177,178], the ESR parameters were determined: $g_{//}$ = 2.075. $A_{/}$ = 0.0155 cm^{-1} ; $g_{\perp}$ = 2.049, $A_{\perp}$ = 0.00335 cm^{-1}. Because of the lack of simulation programs, we could not generate a calculated spectrum from these parameters and compare it with the experimental spectrum.

Addition of **13** caused little change in the uv-visible spectrum, as shown in Figure 5.3.22.
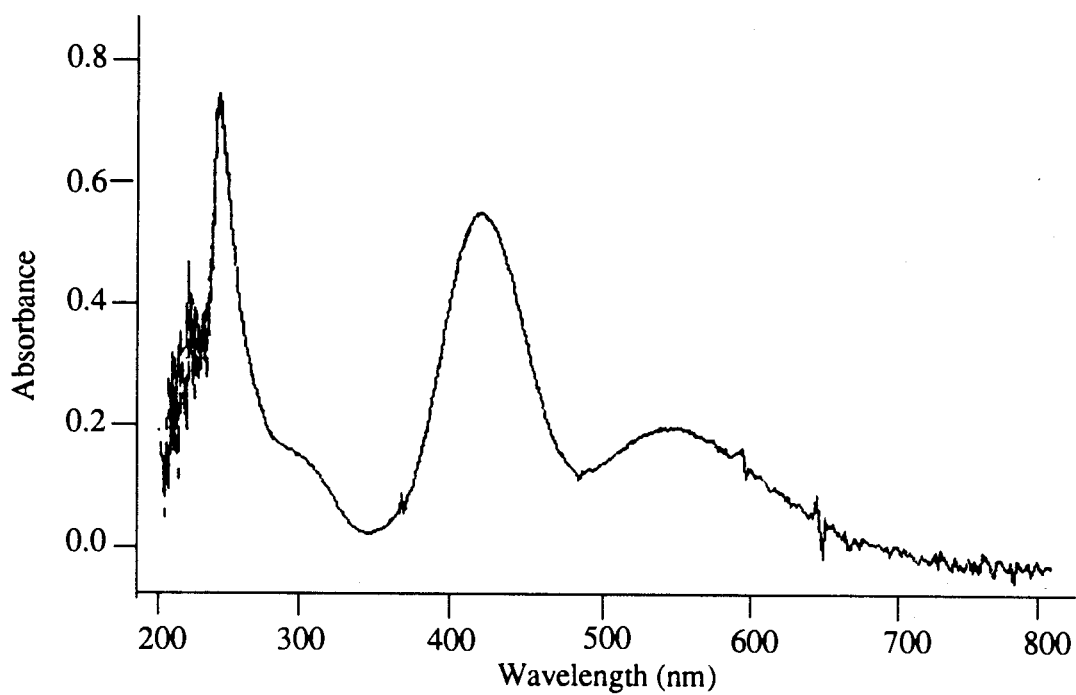
Figure 5.3.22. UV-visible spectrum of $[Cu(14Se4)][SO_3CF_3]_2$ (44) $(1.47 \times 10^{-4}$ M) in CH_2Cl_2.
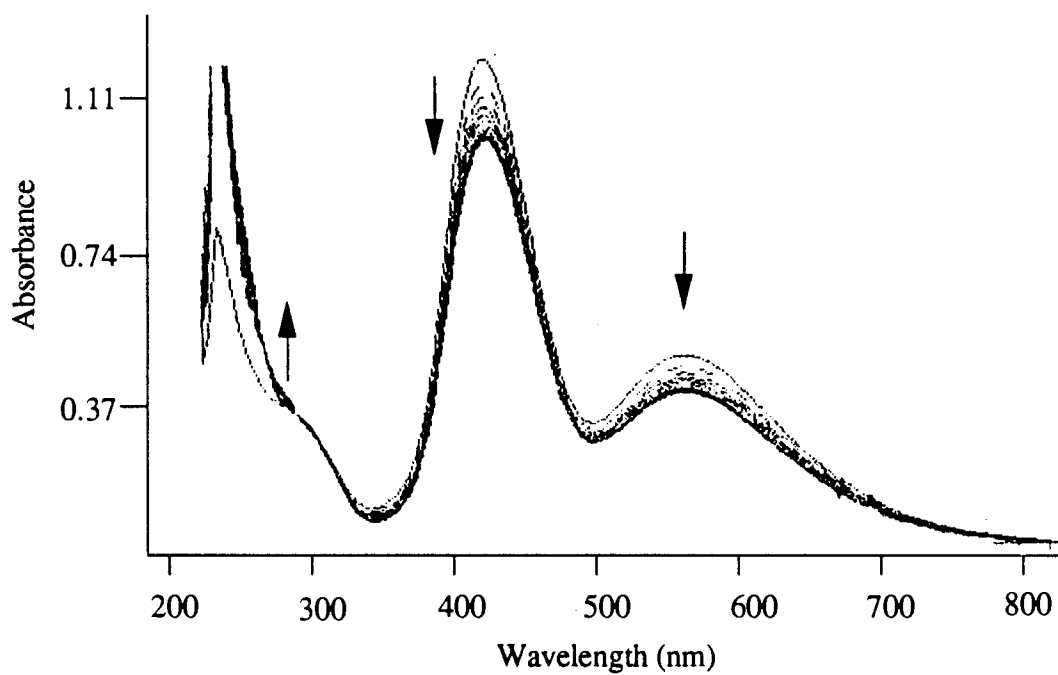
Figure 5.3.23. UV-visible spectra of $[Cu(14Se4)][SO_3CF_3]_2$ (44) $(1.47 \times 10^{-4}$ M) in CH_2Cl_2 in the presence of 14Se4 (13) $(8.77 \times 10^{-5}$ M)

5.3.1.1.7. Cu(I) Complex of 12Se4 (12)

Addition of 12Se4 (12) in CH_2Cl_2, to $Cu(SO_3CF_3)_2$ (in a 1:1 ratio) in acetone afforded a brown solution, then quickly the solution turned into a yellow solution from which a white precipitate was formed. The microanalysis of the white precipitate revealed that it had the empirical formula, [Cu(12Se4)]SO_3CF_3 (46), indicating that 46 was a Cu(I) complex. The compound was not soluble in THF, CH_2Cl_2 or CH_3CN.

5.3.1.1.8. Cu (II) Complex of Dibenzo-14Se4 (14)

The preparation of this complex was not successful. On mixing dibenzo-14Se4, 14, with $Cu(SO_3CF_3)_2$ in acetone solutions, a dark brown solution was immediately formed, but the solution discolored to a greenish solution upon standing. With ether solvent diffusion into the above solution colorless crystals precipitated, which were identified as the starting material 14 by TLC.

Table 5.3.1.   UV-visible Spectroscopic Data of Cu(II) and Pd(II) Complexes of Selenium Coronands

Complexes	λ (nm)(ε)
[Cu(16Se4)][SO_3CF_3]$_2$ (21)	560(2957), 464(11920),310(1267)[a]
[Cu(14Se4)][SO_3CF_3]$_2$ (44)	554(1362), 418(5241), 280(1360)[a]
[Cu(8Se2OH)$_2$][SO_3CF_3]$_2$ (41)	571(8116), 386(7905)[a]
[Cu(16Se4(OH)$_2$)][SO_3CF_3]$_2$ (39)	600(2000), 464(7670), 328(1658)[a]
[Cu(16S2Se2)][SO_3CF_3]$_2$ (43)	570(900), 456(6872), 280(451)[a]
[Pd16Se4](BF_4)$_2$ (34)	314(26758), 210(8409)[b]
[Pd16Se4](BF_4)Cl (35)	314(19949), 210(6548)[b]
[Pd$_2$(24Se6)](BF_4)$_2$Cl$_2$ (36)	366(4837), 294(24838), 216(13145)[b]

a. In CH_2Cl_2.

b. In CH_3CN.

Table 5.3.2. Selected Bond Distances (Å), Bond Angles and Torsion Angles (°) for [Cu(16Se4(OH)₂)][CF₃SO₃]₂ (39) at 190 K.

Table 5.3.2. Selected Bond Distances (Å) , Bond Angles and Torsion Angles (°) for [Cu(16Se4(OH)$_2$)][CF$_3$SO$_3$]$_2$ (39) at 190 K.

Bond Distances (Å)

Cu(1)	Se(1)	2.488		O(4)	C(3)	1.42
Cu(1)	Se(5)	2.445		O(5)	C(11)	1.41
Cu(1)	Se(9)	2.442		C(2)	C(3)	1.49
Cu(1)	Se(13)	2.421		C(3)	C(4)	1.48
Cu(1)	O(21)	2.446		C(6)	C(7)	1.49
Cu(1)	O(201)	2.334		C(7)	C(8)	1.49
Cu(1)	O(4)	2.580		C(10)	C(11)	1.50
Se(1)	C(2)	1.944		C(11)	C(12)	1.49
Se(1)	C(16)	1.929		C(14)	C(15)	1.49
Se(5)	C(4)	1.934		C(15)	C(16)	1.47
Se(5)	C(6)	1.948		Se(9)	C(8)	1.947
Se(9)	C(10)	1.952		Se(13)	C(12)	1.952
Se(13)	C(14)	1.948				

Bond Angles (°)

Se(1)	Cu(1)	Se(5)	85.40	Cu(1)	O(21)	S(2)	136.5
Se(1)	Cu(1)	Se(9)	176.43	Cu(1)	O(201)	S(20)	131.8
Se(1)	Cu(1)	Se(13)	93.25	Cu(1)	O(4)	C(3)	103.6
Se(1)	Cu(1)	O(21)	93.9	Se(1)	C(2)	C(3)	116.4
Se(1)	Cu(1)	O(201)	89.2	O(4)	C(3)	C(2)	112.5
Se(1)	Cu(1)	O(4)	74.5	O(4)	C(3)	C(4)	111.4
Se(5)	Cu(1)	Se(9)	91.62	C(2)	C(3)	C(4)	107.3
Se(5)	Cu(1)	Se(13)	170.92	Se(5)	C(4)	C(3)	115.3
Se(5)	Cu(1)	O(21)	88.2	Se(5)	C(6)	C(7)	112.0
Se(5)	Cu(1)	O(201)	92.3	C(6)	C(7)	C(8)	117.1
Se(5)	Cu(1)	O(4)	79.1	Se(9)	C(8)	C(7)	111.8
Se(9)	Cu(1)	Se(13)	89.39	Se(9)	C(10)	C(11)	112.9
Se(9)	Cu(1)	O(21)	88.0	O(5)	C(11)	C(10)	110.4
Se(9)	Cu(1)	O(201)	92.9	O(5)	C(11)	C(12)	112.0

continuation of:

Table 5.3.2. Selected Bond Distances (Å), Bond Angles and Torsion Angles (°) for [Cu(16Se4(OH)$_2$)][CF$_3$SO$_3$]$_2$ (39) at 190 K.

Bond Angels (Å)

Se(9)	Cu(1)	O(4)	103.0	C(10)	C(11)	C(12)	114.0
Se(13)	Cu(1)	O(21)	100.9	Se(13)	C(12)	C(11)	111.8
Se(13)	Cu(1)	O(201)	96.7	Se(13)	C(14)	C(15)	112.7
Se(13)	Cu(1)	O(4)	91.9	C(14)	C(15)	C(16)	119.0
O(21	Cu(1)	O(4)	163.3	Se(1)	C(16)	C(15)	118.4
O(201)	Cu(1)	O(4)	162.0	Cu(1)	Se(1)	C(2)	99.3
Cu(1)	Se(1)	C(16)	105.2	C(2)	Se(1)	C(16)	94.6
Cu(1)	Se(5)	C(4)	100.0	Cu(1)	Se(5)	C(6)	104.1
C(4)	Se(5)	C(6)	90.4	Cu(1)	Se(9)	C(8)	99.1
Cu(1)	Se(9)	C(10)	103.6	C(8)	Se(9)	C(10)	95.1
Cu(1)	Se(13)	C(12)	105.6	Cu(1)	Se(13)	C(14)	102.0
C(12)	Se(13)	C(14)	93.9				

Torsion Angles (°)

C(16)	Se(1)	C(2)	C(3)	-96.2	C(8)	Se(9)	C(10)	C(11)	170.7
Se(1)	C(2)	C(3)	C(4)	-87.7	Se(9)	C(10)	C(11)	C(12)	-81.5
C(2)	C(3)	C(4)	Se(5)	67.1	C(10)	C(11)	C(12)	Se(13)	79.4
C(6)	Se(5)	C(4)	C(3)	122.7	C(14)	Se(13)	C(12)	C(11)	-172.4
C(4)	Se(5)	C(6)	C(7)	-176.1	C(12)	Se(13)	C(14)	C(15)	-171.0
Se(5)	C(6)	C(7)	C(8)	48.3	Se(13)	C(14)	C(15)	C(16)	-51.2
C(6)	C(7)	C(8)	Se(9)	40.1	C(14)	C(15)	C(16)	Se(1)	-32.6
C(10)	Se(9)	C(8)	C(7)	169.6	C(2)	Se(1)	C(16)	C(15)	167.9
Cu	Se(1)	C(2)	C(3)	10.1	Cu	Se(9)	C(10)	C(11)	70.1
Se(5)	Cu	Se(1)	C(2)	52.5	Se(13)	Cu	Se(9)	C(10)	-53.0
Se(1)	Cu	Se(5)	C(4)	-66.4	Se(9)	Cu	Se(13)	C(12)	53.3
Cu	Se(5)	C(4)	C(3)	18.2	Cu	Se(13)	C(12)	C(11)	-68.7
Cu	Se(5)	C(6)	C(7)	-75.7	Cu	Se(13)	C(14)	C(15)	82.2
Se(9)	Cu	Se(5)	C(6)	18.7	Se(1)	Cu	Se(13)	C(14)	-31.5

continuation of:

Table 5.3.2. Selected Bond Distances (Å) , Bond Angles and Torsion Angles (°) for [Cu(16Se4(OH)$_2$)][CF$_3$SO$_3$]$_2$ (39) at 190 K.

Torsion Angles (Å)

Se(5)	Cu	Se(9)	C(8)	38.5	Se(13)	Cu	Se(1)	C(16)	-21.2
Cu	Se(9)	C(8)	C(7)	-85.7	Cu	Se(1)	C(16)	C(15)	66.9
Se(13)	Cu	Se(1)	C(2)	-118.5	Se(5)	Cu	Se(9)	C(10)	136.0
Se(9)	Cu	Se(5)	C(4)	111.7	Se(1)	Cu	Se(13)	C(12)	-129.1
Se(1)	Cu	Se(5)	C(6)	-159.4	Se(9)	Cu	Se(13)	C(14)	150.9
Se(13)	Cu	Se(9)	C(8)	-150.6	Se(5)	Cu	Se(1)	C(16)	149.8
O(4)	Cu	Se(1)	C(16)	69.9	O(4)	Cu	Se(1)	C(2)	-27.5
O(4)	Cu	Se(5)	C(4)	8.7	O(4)	Cu	Se(5)	C(6)	-84.3
O(4)	Cu	Se(9)	C(8)	117.7	O(4)	Cu	Se(9)	C(10)	-144.8
O(4)	Cu	Se(13)	C(12)	156.3	O(4)	Cu	Se(13)	C(14)	-106.1
Se(1)	Cu	O(4)	C(3)	51.2	Se(5)	Cu	O(4)	C(3)	-37.0
Se(9)	Cu	O(4)	C(3)	-126.1	Se(13)	Cu	O(4)	C(3)	144.0
Cu	O(4)	C(3)	C(4)	60.2	Cu	O(4)	C(3)	C(2)	-60.4
Se(1)	C(2)	C(3)	O(4)	35.1	O(4)	C(3)	C(4)	Se(5)	-56.5
Se(9)	C(10)	C(11)	O(5)	45.6	O(5)	C(11)	C(12)	Se(13)	-46.8
O(21)	Cu	Se(1)	C(2)	140.3	O(201)	Cu	Se(1)	C(2)	144.8
O(21)	Cu	Se(1)	C(16)	-122.3	O(201)	Cu	Se(1)	C(16)	-117.8
O(21)	Cu	Se(5)	C(4)	-160.4	O(201)	Cu	Se(5)	C(4)	-155.4
O(21)	Cu	Se(5)	C(6)	106.6	O(201)	Cu	Se(5)	C(6)	111.6
O(21)	Cu	Se(9)	C(8)	-49.7	O(201)	Cu	Se(9)	C(8)	-53.9
O(21)	Cu	Se(9)	C(10)	47.9	O(201)	Cu	Se(9)	C(10)	43.7
O(21)	Cu	Se(13)	C(12)	-34.5	O(201)	Cu	Se(13)	C(12)	-39.5
O(21)	Cu	Se(13)	C(14)	63.1	O(201)	Cu	Se(13)	C(14)	58.1
Se(1)	Cu	O(21)	S(2)	58.6	Se(1)	Cu	O(201)	S(20)	-9.4
Se(5)	Cu	O(21)	S(2)	143.8	Se(5)	Cu	O(201)	S(20)	76.0
Se(9)	Cu	O(21)	S(2)	-124.5	Se(9)	Cu	O(201)	S(20)	167.7
Se(13)	Cu	O(21)	S(2)	-35.5	Se(13)	Cu	O(201)	S(20)	-102.6
C(20)	S(2)	O(21)	Cu	-137.3	C(200)	S(20)	O(201)	Cu	-162.2

a No e.s.d.s are given for these derived parameters because the disorder of this structure was not fully modeled.

Table 5.3.3. Selected Bond Distances (Å), Bond Angles and Torsion Angles (^{o}) for [Cu(8Se2OH)$_2$][CF$_3$SO$_3$]$_2$(41) at 195 K

Bond Distances (Å)

Se(1)	Cu	2.4655(4) {2.473}[a]		Se(1)	C(2)	1.953(5)
Se(5)	Cu	2.4582(4) {2.461}		Se(1)	C(8)	1.974[b]
Cu	O(4)	2.358(3)		Se(1)	C(18)	1.97
C(2)	C(3)	1.516(6)		Se(5)	C(4)	1.958(4)
C(3)	C(4)	1.512(5)		Se(5)	C(6)	1.958(4)
C(6)	C(7)	1.502		O(4)	C(3)	1.425(4)
C(6)-C(17)		1.52		O(4)	O(1)	2.851(4)
C(7)	C(8)	1.502		O(4)	H(4)	0.79(6)
C(17)	C(18)	1.51		O(1)	H(4)	2.17(6)

Bond Angles (^{o})

C(2)	Se(1)	Cu	96.3(1)	C(4)	Se(5)	Cu	95.6(1)
C(8)	Se(1)	Cu	110.8	C(6)	Se(5)	Cu	110.4(1)
C(8)	Se(1)	C(2)	99.5	C(6)	Se(5)	C(4)	103.1(2)
C(18)	Se(1)	Cu	101.0	Se(5)	Cu	Se(1)	90.90(1)
C(18)	Se(1)	C(2)	116.7	O(4)	Cu	Se(1)	81.60(7)
C(3)	O(4)	Cu	104.8(2)	O(4)	Cu	Se(5)	79.95(7)
H(4)	O(4)	Cu	116(4)	C(7)	C(6)	Se(5)	117.4
H(4)	O(4)	C(3)	110(4)	C(17)	C(6)	Se(5)	119.6
C(3)	C(2)	Se(1)	114.2(2)	C(8)	C(7)	C(6)	116.3
C(2)	C(3)	O(4)	112.1(3)	C(18)	C(17)	C(6)	118.1
C(4)	C(3)	O(4)	107.3(3)	C(7)	C(8)	Se(1)	115.9
C(4)	C(3)	C(2)	116.5(4)	C(17)	C(18)	Se(1)	111.4
C(3)	C(4)	Se(5)	115.2(2)				

continuation of:

Table 5.3.3. Selected Bond Distances (Å), Bond Angles and Torsion Angles (°) for [Cu(8Se2OH)₂][CF₃SO₃]₂(41) at 195 K

Torsion Angles (°)

C(8)	Se(1)	C(2)	C(3)	103.6	C(2)	Se(1)	C(18)	C(17)	23.5
Se(1)	C(2)	C(3)	C(4)	-75.5(3)	C(4)	Se(5)	C(6)	C(17)	55.8
C(2)	C(3)	C(4)	Se(5)	76.2(3)	Se(5)	C(6)	C(17)	C(18)	59.9
C(6)	Se(5)	C(4)	C(3)	-104.1(3)	C(6)	C(17)	C(18)	Se(1)	-80.2
C(4)	Se(5)	C(6)	C(7)	99.3	C(18)	Se(1)	C(2)	C(3)	96.9
Se(5)	C(6)	C(7)	C(8)	-70.1	Se(1)	C(2)	C(3)	O(4)	48.6(2)
C(6)	C(7)	C(8)	Se(1)	75.7	O(4)	C(3)	C(4)	Se(5)	-50.3(2)
C(2)	Se(1)	C(8)	C(7)	-108.2(3)					

a The values in { } are distances corrected for rigid body thermal motion.

b Values with no e.s.d.s involve disordered atom sites and were affected by restraints.

Table 5.3.4. Selected Bond Distances (Å), Bond Angles and Torsion Angles (°) for [Cu(16S2Se2)][CF₃SO₃]₂(42)

Bond Distances (Å)

S/Se(1)	Cu	2.4095(7)		S/Se(5)	C(4)	1.900(4)
S/Se(5)	Cu	2.4136(6)		S/Se(5)	C(6)	1.909(4)
Cu	O(1)	2.44^a		C(2)	C(3)	1.523(6)
Cu	O(11)	2.48		C(3)	C(4)	1.510(6)
S/Se(1)	C(2)	1.897(4)		C(6)	C(7)	1.510(6)
S/Se(1)	C(8)	1.911(4)		C(7)	C(8)	1.506(6)

Bond Angles (°)

S/Se(1)	Cu	S/Se(1)	180	C(2)	S/Se(1)	Cu	107.0(1)
S/Se(5)	Cu	S/Se(1)	89.28(2)	C(8)	S/Se(1)	Cu	101.8(1)
S/Se(5)	Cu	S/Se(1)	90.72(2)	C(8)	S/Se(1)	C(2)	95.6(2)
S/Se(5)	Cu	S/Se(5)	180	C(4)	S/Se(5)	Cu	107.5(1)
O(1)	Cu	S/Se(1)	86.7(3)	C(6)	S/Se(5)	Cu	101.5(1)
O(1)	Cu	S/Se(1)	93.3(3)	C(6)	S/Se(5)	C(4)	94.6(2)
O(1)	Cu	S/Se(5)	91.7(4)	S(0)	O(1)	Cu	140.3(6)
O(1)	Cu	S/Se(5)	88.3(4)	S(10)	O(11)	Cu	131.1(5)
O(11)	Cu	S/Se(1)	93.5(3)	C(3)	C(2)	S/Se(1)	111.9(3)
O(11)	Cu	S/Se(1)	86.5(3)	C(4)	C(3)	C(2)	114.4(4)
O(11)	Cu	S/Se(5)	87.4(4)	C(3)	C(4)	S/Se(5)	113.7(3)
O(11)	Cu	S/Se(5)	92.6(4)	C(7)	C(6)	S/Se(5)	110.7(3)
O(1)	Cu	O(1)	180	C(8)	C(7)	C(6)	114.5(3)
O(11)	Cu	O(1)	171.9(7)	C(7)	C(8)	S/Se(1)	110.6(3)
O(11)	Cu	O(11)	180				

Continuation of:

Table 5.3.4. Selected Bond Distances (Å) , Bond Angles and Torsion Angles (°) for [Cu(16S2Se2)][CF₃SO₃]₂(42)

Torsion Angles (°)

C(8)'	S/Se(1)	C(2)	C(3)	-173.2(3)	C(4)	S/Se(5)	C(6)	C(7)	166.9(3)
S/Se(1)	C(2)	C(3)	C(4)	78.7(3)	C(6)	C(7)	C(8)	S/Se(1)'	47.1(2)
C(2)	C(3)	C(4)	S/Se(5)	-77.1(3)	S/Se(5)	C(6)	C(7)	C(8)	43.5(2)
C(6)	S/Se(5)	C(4)	C(3)	169.2(3)	C(2)	S/Se(1)	C(8)'	C(7)'	-167.2(3)
Cu	S/Se(1)	C(2)	C(3)	-69.0(2)	Cu	S/Se(5)	C(4)	C(3)	65.6(2)
Cu	S/Se(1)	C(8)'	C(7)'	84.1(2)	Cu	S/Se(5)	C(6)	C(7)	-84.2(2)
C(2)	S/Se(1)	Cu	S/Se(5)	51.6(1)	C(2)	S/Se(1)	Cu	O(1)	143.4(3)
C(2)	S/Se(1)	Cu	S/Se(5)'	-128.4(1)	C(2)	S/Se(1)	Cu	O(1)'	-36.6(3)
C(8)'	S/Se(1)	Cu	S/Se(5)'	151.3(1)	C(8)'	S/Se(1)	Cu	O(1)	-116.9(3)
C(8)'	S/Se(1)	Cu	S/Se(5)'	-28.7(1)	C(8)'	S/Se(1)	Cu	O(1)'	63.1(3)
C(4)	S/Se(5)	Cu	S/Se(1)	-49.9(1)	C(4)	S/Se(5)	Cu	O(1)	-136.5(3)
C(4)	S/Se(5)	Cu	S/Se(1)'	130.1(1)	C(4)	S/Se(5)	Cu	O(1)'	43.5(3)
C(6)	S/Se(5)	Cu	S/Se(1)	-148.5(1)	C(6)	S/Se(5)	Cu	O(1)	124.9(3)
C(6)	S/Se(5)	Cu	S/Se(1)'	31.5(1)	C(6)	S/Se(5)	Cu	O(1)'	-55.1(3)

' indicates 2-x, 1-y, -z.

[a] Parameters for which no e.s.d.s are given were either constrained or restrained.

Table 5.3.5. Selected Bond Distances (Å), Bond Angles and Torsion Angles (°) for [Cu(16Se4OH)][SO$_3$CF$_3$] (45) at 297 K, and [Cu(16Se2S2)][SO$_3$CF$_3$] (43) at 205K.

45	43[a]

Bond Distances (Å)

Cu-Se(1) 2.4289(14)	Cu-S/Se(1) 2.3511(12)
Cu-Se(9) 2.3695(14)	Cu-S/Se(9) 2.3236(14)
Cu-Se(5) 2.4182(15)	Cu-S/Se(5) 2.3371(11)
Cu-Se(13) 2.3726(15)	Cu-S/Se(13) 2.3477(11)

Bond Angles (°)

Se(1)-Cu-Se(5) 100.08(5)	S/Se(5)-Cu-S/Se(1) 109.57(4)
Se(5)-Cu-Se(9) 108.23(5)	S/Se(9)-Cu-S/Se(5) 108.20(4)
Se(1)-Cu-Se(9) 116.95(6)	S/Se(9)-Cu-S/Se(1) 110.31(4)
Se(5)-Cu-Se(13) 112.84(5)	S/Se(13)-Cu-S/Se(5) 116.37(4)
Se(1)-Cu-Se(13) 108.13(5)	S/Se(13)-Cu-S/Se(1) 105.47(4)
Se(9)-Cu-Se(13) 110.34(6)	S/Se(13)-Cu-S/Se(9) 106.83(4)

Torsion Angles (°)

C(16)-Se(1)-C(2)-C(3)	-174.8(8)	C(16)-S/Se(1)-C(2)-C(3)	-177.4(3)
Se(1)-C(2)-C(3)-C(4)	-45.0(5)	S/Se(1)-C(2)-C(3)-C(4)	98.7(3)
C(2)-C(3)-C(4)-Se(5)	-48.5(5)	C(2)-C(3)-C(4)-S/Se(5)	-71.2(3)
C(6)-Se(5)-C(4)-C(3)	-171.6(8)	C(6)-S/Se(5)-C(4)-C(3)	-79.2(3)
C(4)-Se(5)-C(6)-C(7)	-72.3(6)	C(4)-S/Se(5)-C(6)-C(7)	173.2(3)
Se(5)-C(6)-C(7)-C(8)	-70.8(7)	S/Se(5)-C(6)-C(7)-C(8)	-95.1(3)
C(6)-C(7)-C(8)-Se(9)	88.1(8)	C(6)-C(7)-C(8)-S/Se(9)	69.0(3)
C(10)-Se(9)-C(8)-C(7)	-161.4(9)	C(10)-S/Se(9)-C(8)-C(7)	78.9(3)
C(8)-Se(9)-C(10)-C(11)	82.6(9)	C(8)-S/Se(9)-C(10)-C(11)	-178.8(3)
Se(9)-C(10)-C(11)-C(12)	78.1(10)	S/Se(9)-C(10)-C(11)-C(12)	95.6(3)
C(10)-C(11)-C(12)-Se(13)	-96.8(11)	C(10)-C(11)-C(12)-S/Se(13)	-68.6(3)
C(14)-Se(13)-C(12)-C(11)	153.4(11)	C(14)-S/Se(13)-C(12)-C(11)	-77.8(3)

continued......

Continuation of:

Table 5.3.5. Selected Bond Distances (Å), Bond Angles and Torsion Angles (°) for [Cu(16Se4OH)][SO₃CF₃] (45) at 297 K, and [Cu(*16Se2S2*)][SO₃CF₃] (43) at 205K.

$$[Cu(16Se4OH)][SO_3CF_3]$$

45   **43**[a]

Torsion Angles (°)

45		43	
C(12)-Se(13)-C(14)-C(15)	-163.8(8)	C(12)-S/Se(13)-C(14)-C(15)	178.9(6)
Se(13)-C(14)-C(15)-C(16)	97.6(8)	S/Se(13)-C(14)-C(15)-C(16)	-101.8(6)
C(14)-C(15)-C(16)-Se(1)	-74.1(7)	C(14)-C(15)-C(16)-S/Se(1)	66.1(4)
C(2)-Se(1)-C(16)-C(15)	-72.1(6)	C(2)-S/Se(1)-C(16)-C(15)	87.0(4)
C(110)-Se(9)-C(8)-C(7)	-151.4(11)	C(160)-S/Se(1)-C(2)-C(3)	-156.5(5)
C(8)-Se(9)-C(110)-C(111)	158.1(21)	C(140)-S/Se(13)-C(12)-C(11)	-64.7(7)
Se(9)-C(110)-C(111)-C(112)	-101.4(23)	C(12)-S/Se(13)-C(140)-C(150)	-164.3(17)
C(110)-C(111)-C(112)-Se(13)	77.0(19)	S/Se(13)-C(140)-C(150)-C(160)	-51.0(11)
C(14)-Se(13)-C(112)-C(111)	82.8(16)	C(140)-C(150)-C(160)-S/Se(1)	-39.9(11)
C(112)-Se(13)-C(14)-C(15)	-174.0(10)	C(2)-S/Se(1)-C(160)-C(150)	166.9(13)

[a] The parameters for **43** are calculated using refined weighted-mean atomic positions for the disordered chalcogen atom sites.

5.3.1.2. Cyclic Voltammetry of Copper(II) Complexes of Selenium Coronands

Cu(SO$_3$CF$_3$)$_2$. Cyclic voltammetry of Cu(CF$_3$SO$_3$)$_2$ was carried out in CH$_3$CN (0.1 M tetraethylammonium perchlorate (TEAP) as the supporting electrolyte), with a three-electrode cell: a Pt working electrode, a Pt wire counter electrode and a saturated calomel electrode (SCE) reference electrode. The potential scan was started from 1.6 V, where the current was zero, to 0 V and back to 1.6 V. The cyclic voltammogram of Cu(SO$_3$CF$_3$)$_2$ showed a quasi-reversible electrode reaction with E$_{1/2}$ (calculated by $\frac{(E_{pa} + E_{pc})}{2}$) at 1.10 V vs SCE; scan rate = 10 mV/s, ΔE$_p$ = 0.14 V. Plots of both the cathodic and anodic current peaks versus the square root of scan rates gave straight lines, indicating that the electrode processes were diffusion controlled. The compound was further reduced as the potential was swept to the more cathodic direction; at a scan rate of 20 mV/s, a second cathodic peak appeared at -0.29 V. This cathodic peak had stripped features indicating the deposition of Cu on the electrode. It corresponded to the Cu(I)/Cu redox couple.

Table 5.3.6. Cyclic Voltammetric Data of Cu(SO$_3$CF$_3$)$_2$ Over a Scan Range 1.0-0.3 V.

υ (mV/s)	E$_{pc}$[a]	E$_{pa}$[a]	ΔE$_p$[a]	i$_c$[b]	i$_a$[b]	i$_a$/i$_c$
10	1.03	1.17	0.14	4.22	3.59	0.852
20	1.01	1.17	0.16	6.25	5.78	0.925
50	1.00	1.19	0.19	9.63	7.66	0.848
100	0.99	1.21	0.22	12.5	11.3	0.900
200	0.99	1.21	0.22	13.1	10.5	0.797

a. E$_{pc}$ and E$_{pa}$ are cathodic and anodic peak potentials, respectively in volts versus SCE.

b. i$_a$ and i$_c$ are anodic and cathodic peak currents, respectively in μA.

[Cu(16Se4)][SO$_3$CF$_3$]$_2$ (21). Cyclic voltammetry of 21 was studied in CH$_2$Cl$_2$ (0.05 M TEAP as electrolyte) on a Pt electrode. Figure 5.3.24 shows the single scanned cyclic voltammogram of 21, which was recorded over the potential range 1.0-0.3 V with several different scan rates. One pair of cathodic and anodic waves was shown, which related the one-electron transfer redox pair of Cu(II)L/Cu(I)L (L designates the selenium coronands); ΔE_p = 0.192 V, $E_{1/2}$ = 0.673 V vs SCE at a scan rate 20 mV/s . ($E_{1/2}$ was calculated by (E_{pa} + E_{pc})/2 and corrected by subtraction of 0.062 V that was obtained from the calibration of the SCE.) The electrode process was quasi-reversible because the cathodic-anodic peak separation ΔE_p increased when the scan rates increased. Moreover, on increasing the scan rate from 20 mV/s to 200 mV/s, the ratio of anodic current to cathodic current decreased from 0.69 to 0.50.

As the potential was swept to the more negative direction until -1.0 V, two more irreversible reduction peaks were seen at 0.087 V and -0.65 V. These peaks were attributed to Cu(I)L/Cu redox couples, possibly due to the reduction of mono-Cu(I) 21 and polymerized Cu(I) 21 complexes[61]. The latter, in which 16Se4 has less ring strain was more stable and was reduced at a lower potential.

A cyclic voltammogram of 21 with a scan range over 1.6 to 0.3 V showed an additional redox wave with $E_{1/2}$ = 1.06 V (20 mV/s) (Figure 5.3.25). The current at the initial scan potential (1.6 V) was not zero, indicating that there was an oxidation reaction at the electrode before the potential sweeping. This reaction is presumably attributed to the oxidation of Cu(II)L to Cu(II)L$^+$·. As the potential was swept (50 mV/s) in the cathodic direction the oxidized 21 was reduced and gave a first wave (E_{pc1} = 1.01 V) corresponding to the Cu(II)L$^+$·/Cu(II)L redox couple and the second wave (E_{pc2} 0.631 V) corresponding to the CuL(II)/Cu(I)L redox couple. The potential scan was reversed at 0.3 V and the pertinent anodic peaks were observed at 0.850 and 1.33 V, respectively on the reverse scan. The reduction of Cu(II)L is a diffusion controlled process because a plot of the first cathodic peak currents versus the square root of the scan rates gave a straight line. Because

of the difficulty in determining the current base lines, similar plots for other peak currents could not be obtained. The cyclic voltammograms of **21** were not dependent on the initial potentials; a potential sweeping loop from 0.3 V to 1.6 V then back to 0.3 gave rise to the same cyclic voltammograms at various scan rates as that from the initial potential 1.6 V, which indicates that the redox reaction of **21** is a chemically reversible reaction. At the initial potential of 0.3 V, **21** was reduced to Cu(I)16Se4 at the Pt electrode. The redox reactions on the electrode may expressed as

$$Cu(II)16Se4^{2+} + e \rightleftharpoons Cu(I)16Se4^{+} \qquad (5.3.1)$$

$$Cu(II)16Se4^{3+} + e \rightleftharpoons Cu(I)16Se4^{2+} \qquad (5.3.2)$$
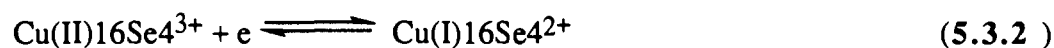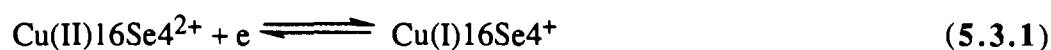
Table 5.3.7.   Cyclic voltammetric Data of [Cu(16Se4)][SO$_3$CF$_3$]$_2$ (21).

υ (mV/s)	E_{pc}^a	E_{pa}^a	ΔE_p^a	i_c^b	i_a^b	i_a/i_c
Potential scan range over 1.0 - 0.3 V
20	0.639	0.831	0.192	8.45	5.00	0.69
50	0.597	0.834	0.237	11.1	7.50	0.68
100	0.516	0.856	0.340	15.0	8.75	0.58
200	0.482	0.900	0.418	18.8	9.38	0.50

Potential scan range over 1.0 - 0.3 V

υ (mV/s)	E_{pc1}^a	E_{pa1}^a	ΔE_p^a	E_{pc2}^a	E_{pa2}^a	ΔE_p^a	i_{c1}^b
20	1.02	1.23	0.210	0.632	0.788	0.156	9.38
50	1.01	1.33	0.320	0.631	0.850	0.219	14.06
100	0.948	1.33	0.382	0.569	0.850	0.281	16.6
200	0.928	1.35	0.422	0.538	0.928	0.390	20.6

Potential scan range over 1.6 - 0.3 V

a. E_{pc} and E_{pa} are cathodic and anodic peak potentials, respectively in volts versus SCE.

b. i_a and i_c are anodic and cathodic peak currents, respectively in μA.
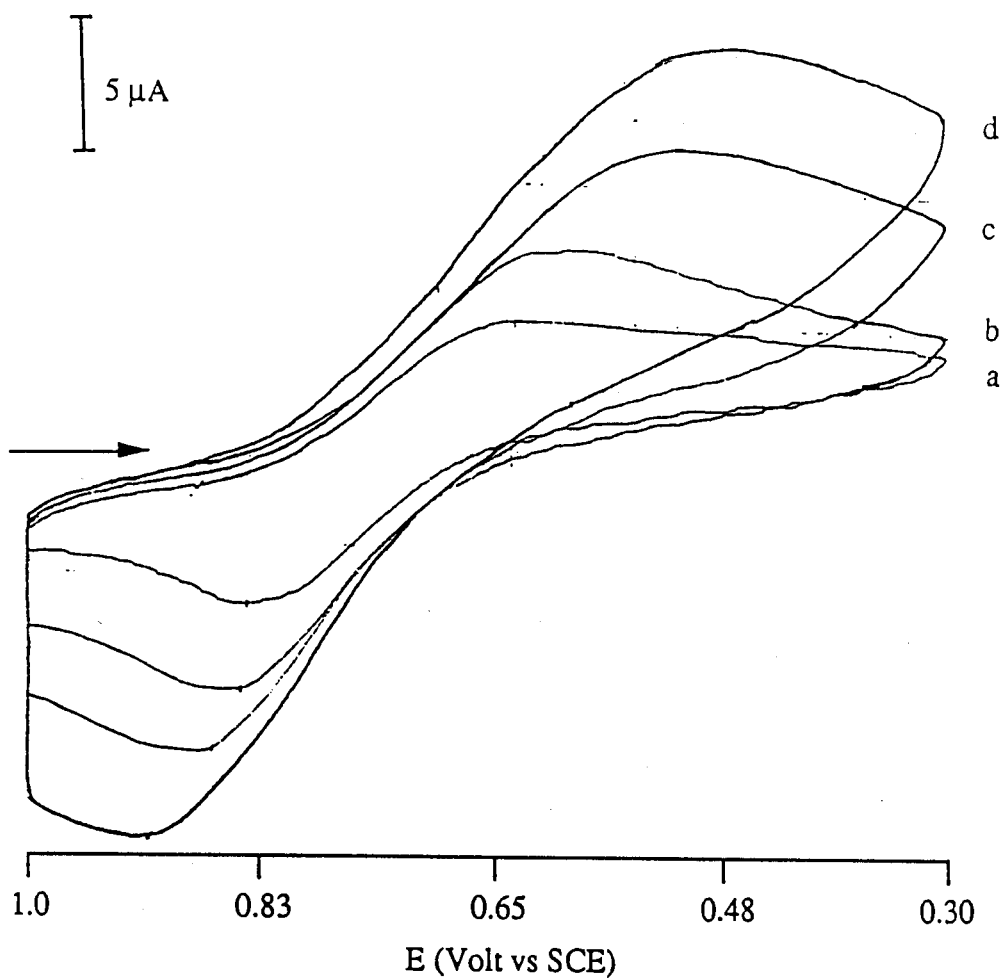
Figure 5.3.24. Cyclic voltammograms of [Cu(16Se4)]-
[SO$_3$CF$_3$]$_2$ (21) (1× 10^{-3} M, in CH$_2$Cl$_2$) recorded at scan
rates: a) 20 mV/s; b) 50 mV/s; c) 100 mV/s; d) 200 mV/s.
Working electrode: Pt. Reference electrode: SCE.
Electrolyte: 0.05 M tetraethylammonium perchlorate
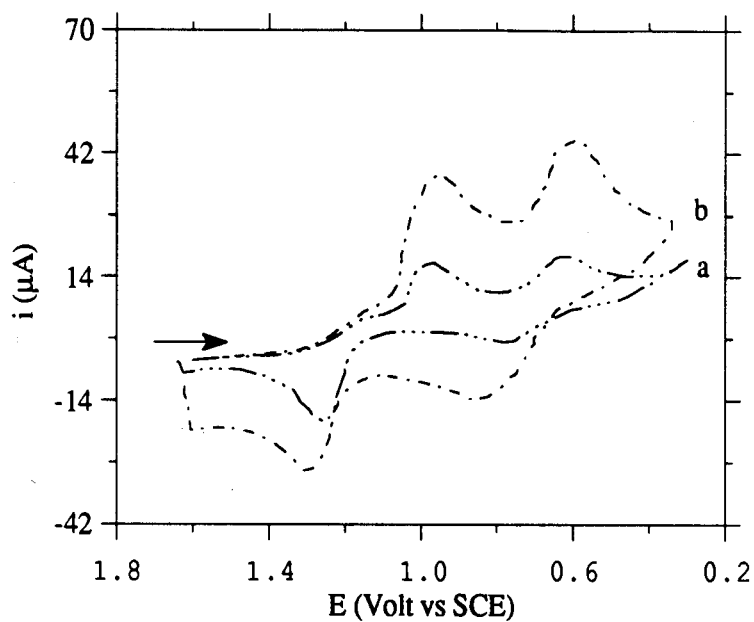
Figure 5.3.25. Cyclic voltammogram of $[Cu(16Se4)][SO_3CF_3]_2$ (21) (1×10^{-3} M, CH_2Cl_2) recorded at scan rates: a) 50 mV/s; b) 200 mV/s. Working electrode: Pt. Reference electrode: SCE. Electrolyte: 0.05 M tetraethylammonium perchlorate

[Cu(14Se4)][CF$_3$SO$_3$]$_2$ (**44**).   Cyclic voltammetry of **44** was carried out in CH$_2$Cl$_2$ (0.05 M TEAP as supporting electrolyte) with a previously described three-electrode cell, except that the working electrode was a carbon electrode because it was more sensitive for **44**.

The cyclic voltammograms of **44** (Figure 5.3.26) showed a pair of quasi-reversible redox waves: E$_{1/2}$ = 0.641 V vs SCE, ΔE$_p$ = 0.444 V and i$_{pa}$/i$_{pc}$ = 0.876, at a scan rate of 20 mV/s. These waves related to the redox couple Cu(II)L/Cu(I)L. As the scan rates increased the ΔE$_p$ also increased.

Table 5.3.8.   Cyclic Voltammetric Data of [Cu(14Se4)][CF$_3$SO$_3$]$_2$(44).

Potential scan range over 1.0 - 0.3 V					
υ (mV/s)	E$_{pc}$[a]	E$_{pa}$[a]	ΔE$_p$[a]	i$_c$[b]	i$_a$[b]	i$_a$/i$_c$
20	0.481	0.925	0.444	4.38	5.00	0.876
50	0.431	0.956	0.525	7.50	6.88	1.07
200	0.363	1.00	0.637	10.0	12.5	0.800
300	0.347	1.02	0.673	13.8	16.9	0.810
500	0.322	1.07	0.748	18.1	21.9	0.829

a. E$_{pc}$ and E$_{pa}$ are cathodic and anodic peak potentials, respectively in volts versus SCE.
b. i$_a$ and i$_c$ are anodic and cathodic peak currents, respectively in μA.

Figure 5.3.27 (a) shows the voltammogram obtained by a potential scan loop from 1.6 V to -0.4 V and back to 1.6 V at a scan rate 200 mV/s. Three cathodic peaks were shown at 0.959, 0.649, and 0.381 V respectively in the forward scan and two anodic peaks were shown at 0.944 and 1.29 V in the backward scan at a scan rate 200 mV/s. The same cyclic voltammogram (Figure 5.3.27 b) resulted with a scan loop from -0.5 V to 1.5 V and back to -0.5 V. The redox waves of 0.381 V (reduction peak potential) and 0.959 V (oxidation peak potential) were assigned to the redox couple Cu(II)L/Cu(I)L. The anodic peak at 1.29 V was tentatively attributed to the Cu(II)L$^{+\cdot}$ species. The cathodic current peak at 0.649 V was due to an unknown species adsorbed on the electrode. This peak

increased in the second potential sweep cycle but other current peaks remained at the same heights.

[Cu((8Se2OH)₂)][CF₃SO₃]₂ (**41**). Cyclic voltammetry of **41** was studied in CH_3NO_2 (0.1 M TEAP as the supporting electrolyte), because its solubility was low in CH_2Cl_2. The working electrode was a carbon electrode; on a Pt working electrode the reaction was sluggish. At a scan rate of 20 mV/s, with a potential sweep loop from 0.8 V to -0.4 V then to 1.2 V, a quasi-reversible cyclic voltammogram was observed, which showed an anodic peak at 0.393 V and a broad cathodic peak centred at 0.675 V ; ΔE_p = 0.282 V I_a/I_c = 0.737. The redox waves corresponded to the single electron transfer redox couple Cu(II)L/Cu(I)L; $E_{1/2}$ = 0.534 V. The anodic to cathodic peak current ratio increases as the scan rates increase. The same cyclic voltammogram was obtained with a scan loop from 0 V to 1.4 V then back to 0 V. Furthermore, scanning the potential up to 1.6 V resulted in no second oxidation peak as observed for the previous Cu(II) complexes of selenium coronands. Table 5.3.9 lists the cyclic voltammetric data of **41**, and Figure 5.3.28 shows the cyclic voltammograms of **41** at various scan rates.

Table 5.3.9. Cyclic Voltammetric Data of [Cu(8Se2OH)₂][CF₃SO₃]₂(41).

υ (mV/s)	E_{pc}[a]	E_{pa}[a]	ΔE_p[a]	i_c[b]	i_a[b]	i_a/i_c
Potential scan range over 0.8 - -0.4 - 1.4 V
20	0.393	0.675	0.282	21.8	15.6	0.737
50	0.363	0.706	0.343	30.6	18.8	0.613
100	0.331	0.731	0.400	36.9	28.1	0.763
200	0.300	0.763	0.463	53.1	43.8	0.823
300	0.284	0.800	0.516	57.5	56.3	0.978

a. E_{pc} and E_{pa} are cathodic and anodic peak potentials, respectively in volts versus SCE. E_{pa} values are read from the centre of the broad anodic peaks.

b. i_a and i_c are anodic and cathodic peak currents, respectively in µA.
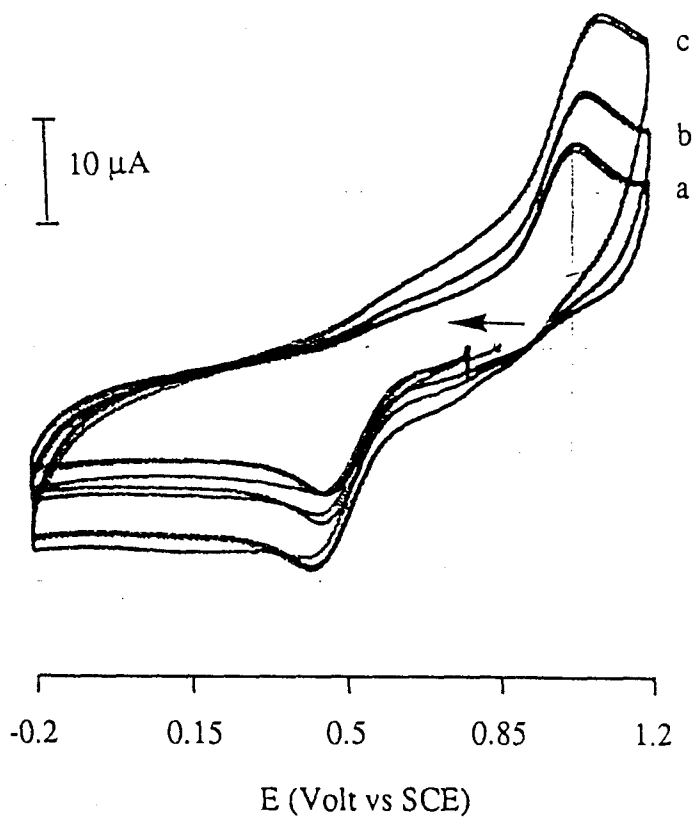
Figure 5.3.26. Cyclic voltammograms of $[Cu(14Se4)][SO_3CF_3]_2$ (44) (1×10^{-3} M, in CH_2Cl_2) recorded at scan rates: a) 200 mV/s; b) 300 mV/s; c) 500 mV/s. Working electrode: Pt. Reference electrode: SCE. Electrolyte: 0.05 M tetraethylammonium perchlorate.
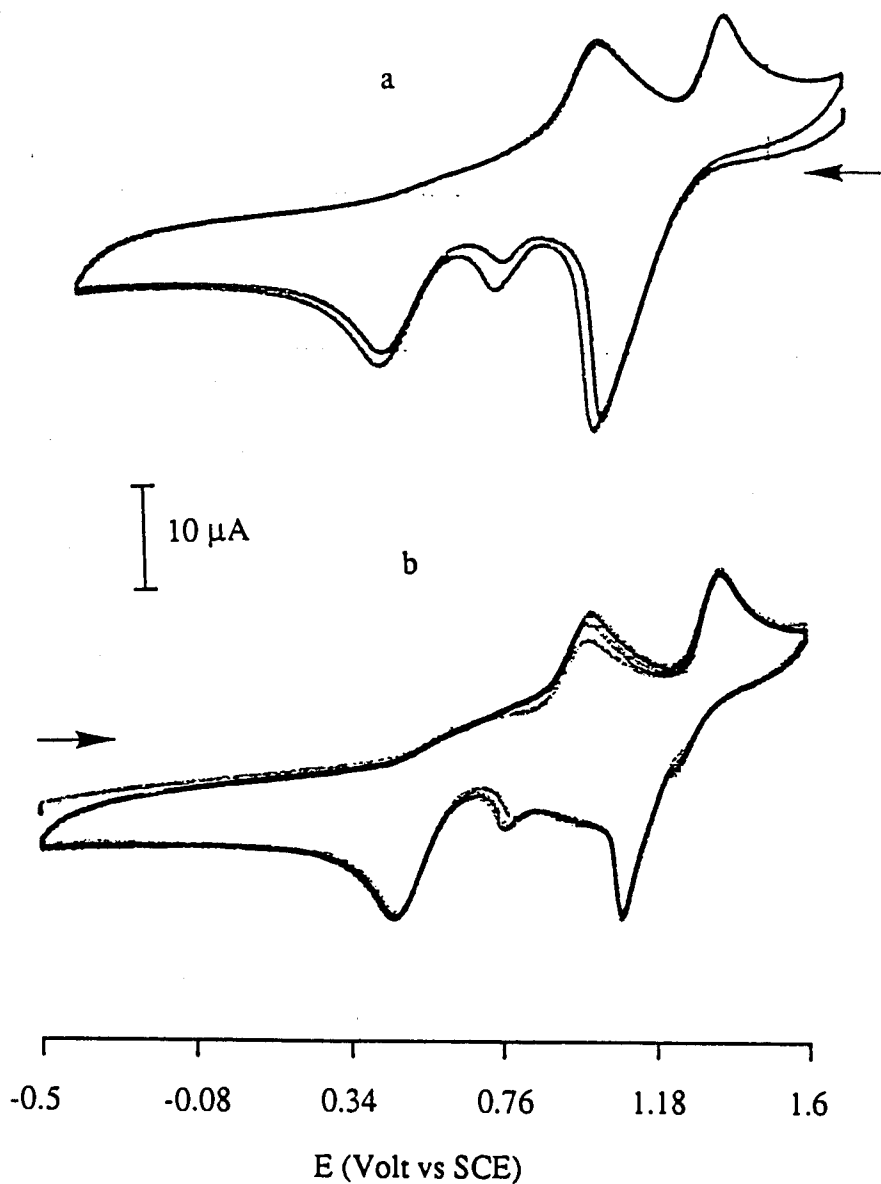
Figure 5.3.27. Cyclic voltammograms of [Cu(14Se4)][SO$_3$CF$_3$]$_2$
(44) (1 × 10^{-3} M, in CH$_2$Cl$_2$) recorded at a scan rate of 200 mV/s
with different initial potentials: a) 1.6 to -0.4 V; b) -0.5 to 1.5 V.
Working electrode: Pt. Reference electrode: SCE. Electrolyte: 0.05
M tetraethylammonium perchlorate.
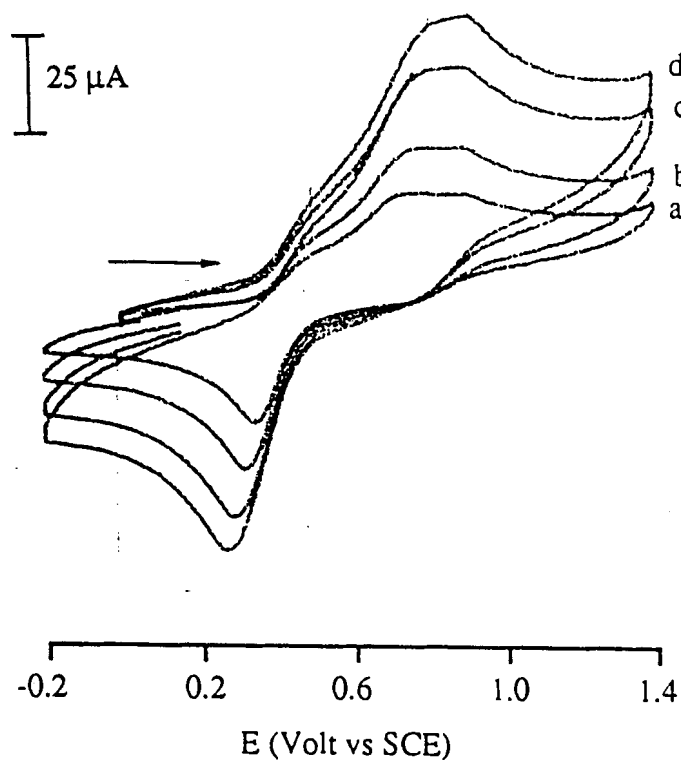
Figure 5.3.28. Cyclic voltammograms of $[Cu(8Se2OH)_2][CF_3SO_3]_2$ **(41)** (1×10^{-3} M in CH_3NO_2) recorded at scan rates: a) 20 mV/s; b) 50 mV/s; c) 100 mV/s; d) 200 mV/s. Working electrode: Carbon. Reference electrode: SCE. Electrolyte: 0.1 M tetraethylammonium perchlorate.

[Cu(16Se4(OH)$_2$)][SO$_3$CF$_3$]$_2$(**39**). Cyclic voltammetry of **39** was studied in nitromethane (0.1 M TEAP as supporting electrolyte) because the solubility of **39** was low in CH$_2$Cl$_2$. The cyclic voltammogram recorded with a scan loop from -0.4 V to 1.0 V and back to 0.4 V at a scan rate of 20 mV/s shows a broad anodic peak at 0.694 V and a cathodic current peak at 0.429 V; E$_{1/2}$ = 0.524 V, ΔEp = 154 mV and i$_a$/i$_c$ = 0.46. These redox waves related to a quasi-reversible one-electron electrode reaction of the Cu(II)L/Cu(I)L pair. As the scan rates increased, the peak separation ΔE$_p$ increased, but the anodic to cathodic current ratios decreased.

At a scan rate of 50 mV/s, the broad anodic current peak seemed to be comprised of two peaks with maxima at 0.647 and 0.772 V (Figure 5.3.29). The latter became stronger as the scan rate increased and eventually two peaks merged to one peak (0.803 V) at scan rate of 200 mV/s. This indicated the presence of different isomers of **39**, which were reduced at different potentials. Moreover, there appeared a small bump at 0.256 V in the anodic scan (forward scan) at scan rates over 100 mV/s. When the anodic potential exceeded 1.4 V, **39** was further oxidized and a second oxidation peak was seen (Figure 5.3.30).

Table 5.3.10. **Cyclic Voltammetric Data of [Cu(16Se4(OH)$_2$)]-[CF$_3$SO$_3$]$_2$ (39).**

Potential scan range over -0.4 - 1.0 V						
υ (mV/s)	E$_{pc}$[a]	E$_{pa}$[a]	ΔE$_p$[a]	i$_c$[b]	i$_a$[b]	i$_a$/i$_c$
20	0.509	0.663	0.154	6.88	3.13	0.455
50	0.506	0.772[c]	0.266	11.9	4.00	0.337
100	0.478	0.788[c]	0.310	17.5	7.50	0.250
200	0.459	0.803	0.344	25.2	8.66	0.270
500	0.413	0.819	0.406	46.3	12.5	0.270

continued......

Continuation of

Table 5.3.10. Cyclic Voltammetric Data of [Cu(16Se4(OH)$_2$)]-

[CF$_3$SO$_3$]$_2$ (39)

	Potential scan range over -0.4 - 1.6 V						
υ (mV/s)	$E_{pc1}{}^a$	$E_{pa1}{}^a$	$\Delta E_p{}^a$	$E_{pc2}{}^a$	$E_{pa2}{}^a$	$\Delta E_p{}^a$	$i_{c1}{}^b$
20	\	0.631	0.210	0.350	1.21	0.156	9.38
50	0.1	0.694^c	0.320	0.413	1.21	0.219	14.06
100	0.1	0.718^c	0.382	0.438	1.21	0.281	16.6
200	0.1	0.706^c	0.422	0.413	1.23	0.390	20.6

a. E_{pc} and E_{pa} are cathodic and anodic peak potentials, respectively in volts versus SCE.

b. i_a and i_c are anodic and cathodic peak currents, respectively in μA.

c. Values are the centre of the anodic potential peak.

[Cu(16S2Se2)][CF$_3$SO$_3$]$_2$ (42). Cyclic voltammetry of **42** was carried out in CH$_2$Cl$_2$ (0.05 M TEAP as supporting electrolyte) at a Pt working electrode. Over a scan loop from 1.2 V to 0 V then back to 1.2 V, a pair of quasi-reversible redox waves was observed: $E_{1/2}$ was 0.716 V, ΔE_p was 0.269 V, half potential peak width (E_p - $E_{p/2}$) was 0.106 V and i_a/i_c was 0.94 at a scan rate 20 mV/s (Figure 5.3.31). Increasing the scan rates resulted in increasing the potential peak separation (ΔE_p) between anodic peak and cathodic peak, which suggests that the electrode process is a quasireversible one-electron transfer redox reaction that is attributed to the redox couple Cu(II)L/Cu(I)L.

In another experiment with the potential scanning loop from 0 V to 1.2 V then back to 0 V, at a scan rate of 20 mV/s a pair of quasireversible redox waves was observed: $E_{1/2}$ = 0.771 V vs SCE; ΔE_p = 0.117 V, E_p - $E_{p/2}$ = 0.087 V. The ratio of i_c/i_a was 0.778 (Figure 5.3.32). These parameters suggested a faster electrode reaction when the initial potential started at 0 V, at which **42** was reduced to [Cu(16S2Se2)][SO$_3$CF$_3$] (**43**) in the vicinity of the Pt electrode.

226

When the potential was scanned (50 mV/s) from 1.0 V towards 1.8 V, **42** was further oxidized resulting in an anodic peak at 1.43 V, but no cathodic peak appeared on the reverse scan. When the scan rate was increased to 500 mV/s, the cathodic peak on the reverse scan was observed at 1.22 V with an i_c/i_a ratio of 0.14 (Figure 5.3.33), implying that there are complications of homogeneous chemical reactions that consumed the oxidized Cu(II)L species and competed with the electrode reaction. When the scan rate was 20 mV/s the anodic current did not form a peak but a plateau.

Table 5.3.11. Cyclic Voltammetric Data of [Cu(16S2Se2)][CF$_3$SO$_3$]$_2$ (42).

Potential scan range over 1.2 - 0.0 V						
υ (mV/s)	$E_{pc}{}^a$	$E_{pa}{}^a$	$\Delta E_p{}^a$	$i_c{}^b$	$i_a{}^b$	i_a/i_c
10	0.556	/	/	1.00	/	/
20	0.581	0.850	0.269	1.30	1.38	0.942
50	0.525	0.900	0.375	1.63	1.94	0.840
100	0.523	0.930	0.407	1.88	2.56	0.734
200	0.500	0.963	0.463	2.63	3.63	0.725
500	0.456	1.01	0.554	3.63	5.68	0.675

Potential scan range over 0.0 - 1.2 V						
υ (mV/s)	$E_{pc}{}^a$	$E_{pa}{}^a$	$\Delta E_p{}^a$	$i_c{}^b$	$i_a{}^b$	i_c/i_a
10	0.828	0.725	0.103	1.44	1.75	0.821
20	0.829	0.712	0.116	1.75	2.25	0.778
50	0.837	0.701	0.136	2.63	3.19	0.824
100	0.850	.700	0.150	3.38	4.63	0.730
200	0.888	0.662	0.225	3.88	5.63	0.689
500	0.919	0.638	0.281	4.88	8.65	0.564

Continuation of

Table 5.3.11. Cyclic Voltammetric Data of [Cu(16S2Se2)][CF$_3$SO$_3$]$_2$(42)

	Potential scan range over 1.0 - 1.8 V					
υ (mV/s)	$E_{pc2}{}^a$	$E_{pa2}{}^a$	$\Delta E_p{}^a$	$i_{a2}{}^a$	$i_{c2}{}^b$	i_{c2}/i_{a2}
20	$/^c$	/	/	/	/	/
50	/	1.43	/	1.44	/	/
100	/	1.44	/	2.25	/	/
200	/	1.46	/	3.56	/	/
500	1.22	1.36	0.360	7.25	1	0.14

a. E_{pc} and E_{pa} are cathodic and anodic peak potentials, respectively in volts versus SCE.

b. i_a and i_c are anodic and cathodic peak currents, respectively in μA.

c. Data not available.

5.3.1.3. Controlled Potential Electrolysis of Selected Cu(II) Complexes

Controlled potential electrolysis experiments were performed on the representative compounds [Cu(16S2Se2)][CF$_3$SO$_3$]$_2$ (**42**), [Cu(16Se4)][SO$_3$CF$_3$]$_2$ (**21**) and [Cu(16Se4(OH)$_2$)][CF$_3$SO$_3$]$_2$ (**39**) (0.05 M in CH$_2$Cl$_2$ with TEAP as supporting electrolyte) in a two-compartment cell on a Pt electrode. At the applied potential of 0 V vs SCE the electrolysis occurred, as manifested by a change in the brown solution to a light yellow solution. The total electric charge passed through the solution was recorded on a coulometer. The results revealed that the reduction was a one-electron process for each complex.
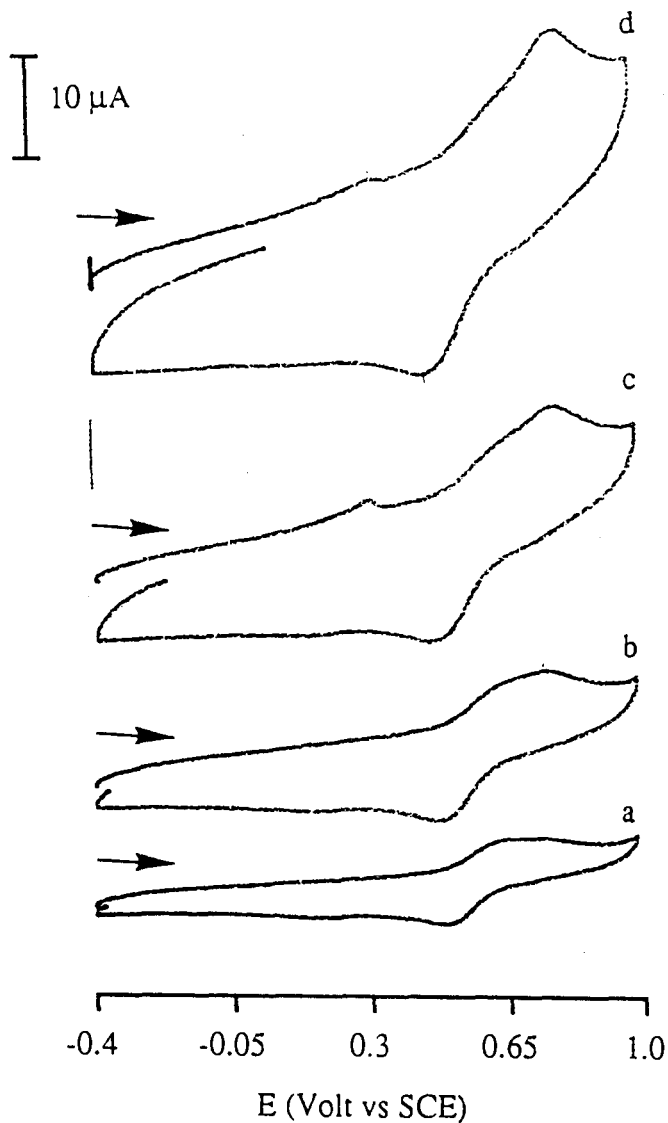
Figure 5.3.29. Cyclic voltammograms (scan range -0.4 - 1.0 V) of [Cu(16Se4(OH)$_2$)][CF$_3$SO$_3$]$_2$ (39) (1 × 10^{-3} M, in CH$_3$NO$_2$) recorded at scan rates: a) 20 mV/s; b) 50 mV/s; c) 100 mV/s; d) 200 mV/s. Working electrode: Carbon. Reference electrode: SCE. Electrolyte: 0.1 M tetraethylammonium perchlorate.
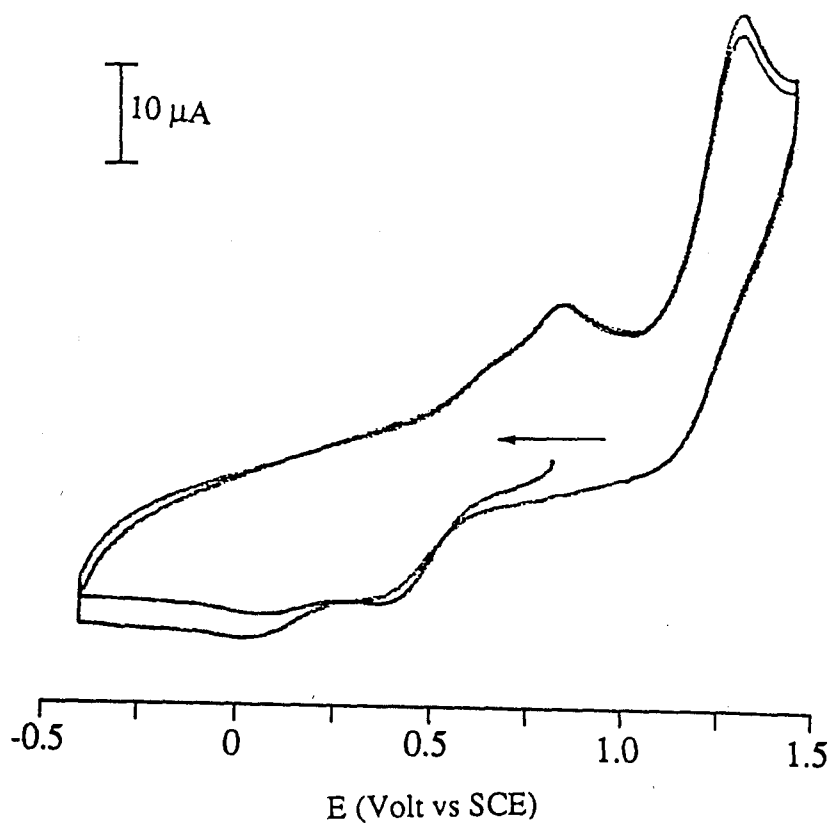
Figure 5.3.30. The cyclic voltammograms (scan range -0.4 - 1.0 V) of [Cu(16Se4(OH)$_2$)][CF$_3$SO$_3$]$_2$ (39) (1 × 10^{-3} M) in CH$_3$NO$_2$ with a scan rate of 200 mV/s. Working electrode: Carbon. Reference electrode: SCE. Electrolyte: 0.1 M tetraethylammonium perchlorate.
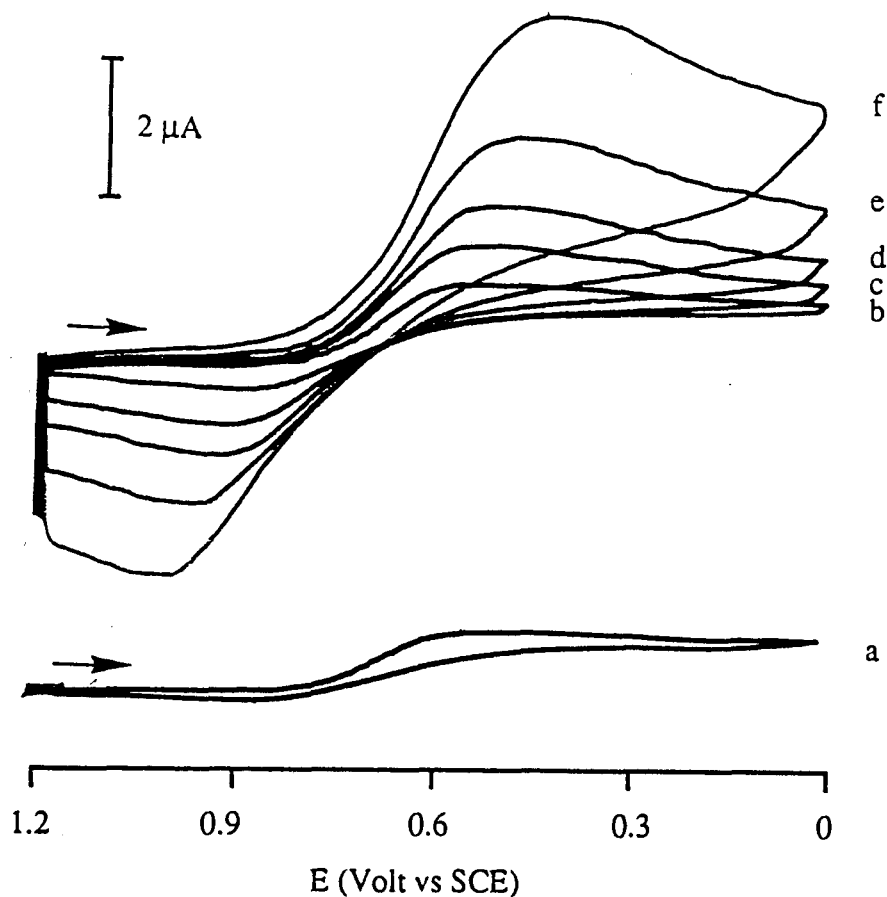
Figure 5.3.31. The cyclic voltammograms (scan range 1.2-0 V) of [Cu(16S2Se2)][CF$_3$SO$_3$]$_2$ (42) (1 × 10^{-3} M, in CH$_2$Cl$_2$) recorded at scan rates: a) 10 mV/s; b) 20 mV/s; c) 50 mV/s; d) 100 mV/s; e) 200 mV/s.; f) 500 mV/s. Working electrode: Pt. Reference electrode: SCE. Electrolyte: 0.05 M tetraethylammonium perchlorate.
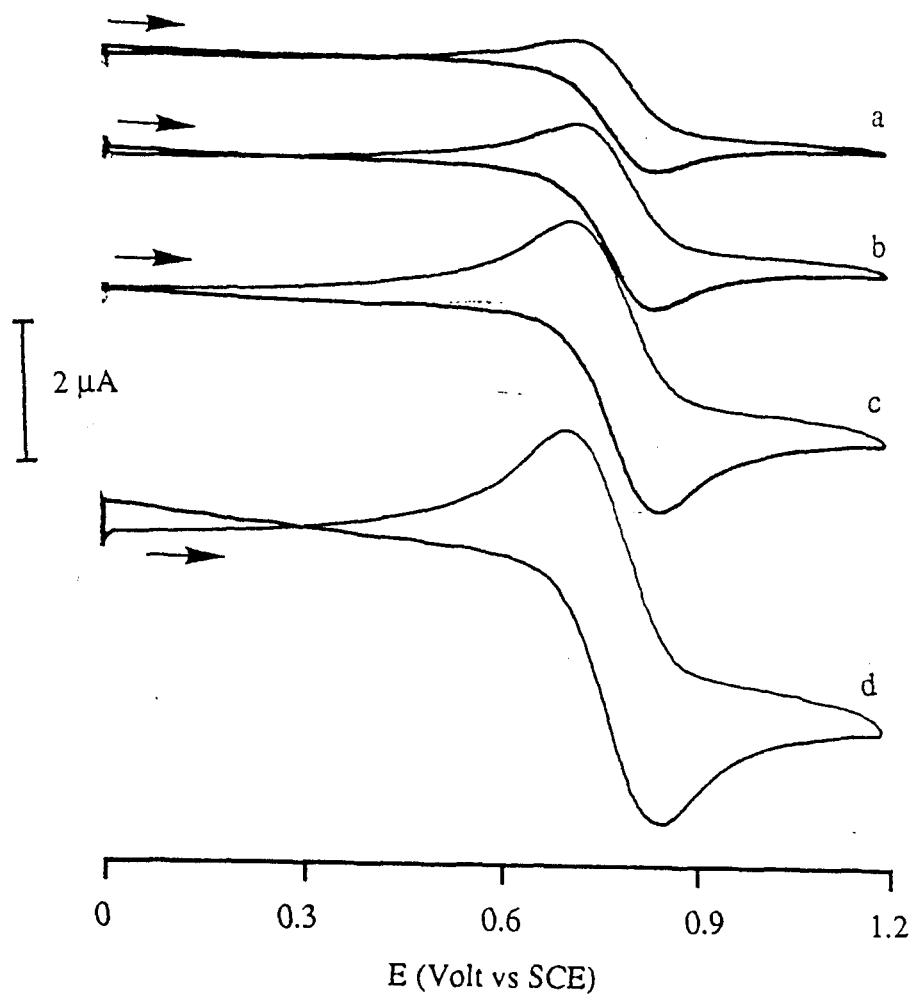
Figure 5.3.32. Cyclic voltammograms (scan range 0-1.2 V) of [Cu(16S2Se2)][CF$_3$SO$_3$]$_2$ (42) (1 × 10^{-3} M, in CH$_2$Cl$_2$) recorded at scan rates: a) 20 mV/s; b) 50 mV/s; c) 100 mV/s; d) 200 mV/s. Working electrode: Pt. Reference electrode: SCE. Electrolyte: 0.05 M tetraethylammonium perchlorate.

2 µA

1.2   1.35   1.5   1.65   1.8

E (Volt vs SCE)
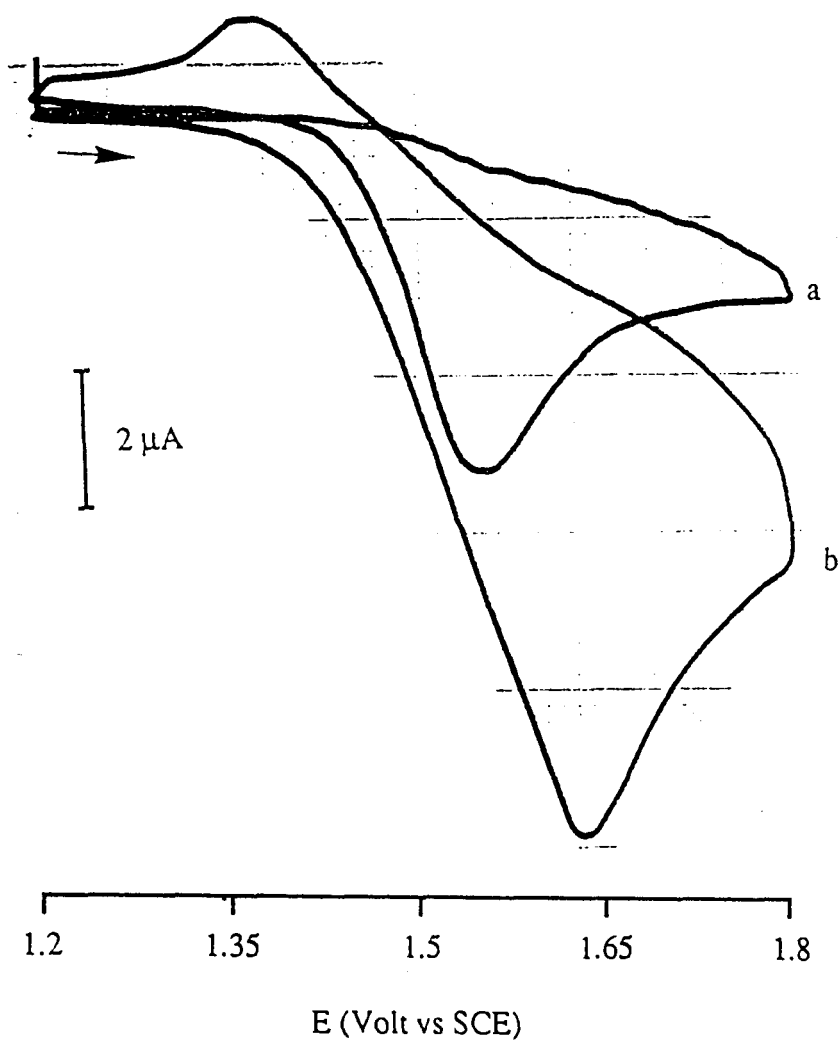
Figure 5.3.33.   Cyclic voltammograms (scan range 1.2-1.6 V) of [Cu(16S2Se2)][CF$_3$SO$_3$]$_2$ (42) (1 × 10^{-3} M, in CH$_2$Cl$_2$) at scan rates : a) 200 mV/s; b) 500 mV/s. Working electrode: Pt. Reference electrode: SCE. Electrolyte: 0.05 M tetraethylammonium perchlorate.

5.3.1.4. *Kinetic Study of the Redox Reaction of [Cu(16Se4)] [SO₃CF₃]₂ (21)*

5.3.1.4.1.   Determination of the Rate Law

In section 5.3.1 we have described the redox reaction between [Cu(16Se4)][SO₃CF₃]₂ (**21**) and 16Se4 (**8**), which resulted in the formation of [Cu(16Se4)][SO₃CF₃] and the dication of 16Se4. In this section we would like to probe the mechanism of this reaction. Thus, the rate law of the reaction must be determined. Based on the reaction products, the overall redox reaction may be depicted by the following equation (5.3.9) :

$$[Cu(16Se4)]^{2+} + 16Se4 \longrightarrow [Cu(16Se4)]^{+} + 16Se4^{2+} \qquad (5.3.9)$$
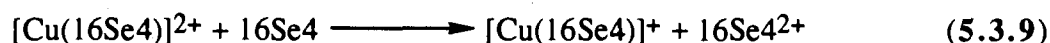
The rate of the reaction (5.3.9) may be expressed by Eq(5.3.10)

$$-d[Cu(II)L]/dt = k[Cu(II)L]^{\alpha}[L]^{\beta} \qquad (5.3.10)$$

Here L represents 16Se4 (**8**), α and β are the orders of the reaction with respect to the concentration of each reactant. The values of α and β can be determined by the initial-rate method[181]. In this method, the initial reaction rates are measured under the condition in which the concentration of each reagent is alternatively chosen to remain constant during the measurements. Then the logarithm of reaction rate (at time zero) is plotted versus that of the initial concentration of each reagent; α and β are determined from the slopes of the plots. The initial reaction rates are used so that the complication of the involvement of products can be avoided.

Experimentally, the reaction was carried out under pseudo first-order reaction conditions in CH₂Cl₂ solutions. Two conditions were used

234

1. [Cu(II)L] << [L]; [L] was set constant, but [Cu(II)L] was varied; thus,

$$\frac{-d[Cu(II)L]}{dt} = k[Cu(II)L]^{\alpha}[L]^{\beta} = k_{obs}[Cu(II)L]^{\alpha} \qquad (5.3.11)$$

$$\ln[-d[Cu(II)L]/dt] = \alpha \ln[Cu(II)L] + \ln k_{obs} \qquad (5.3.12)$$

2. [Cu(II)L] << [L]; [Cu(II)L] was set constant, but [L] was varied; thus,

$$\ln[-d[Cu(II)L]/dt] = \beta \ln[L] + \ln k + \ln[Cu(II)L]^{\alpha} \qquad (5.3.13)$$

Here [L] and [Cu(II)L] are the initial concentrations of 16Se4 (8) and [Cu(16Se4)]-[SO$_3$CF$_3$]$_2$ (21). In both situations the concentration of 8 was in excess because the solubility of 21 in CH$_2$Cl$_2$ was low; it was impossible to prepare a high concentration solution of 21. This problem was solved by condition 2. For a set of kinetic runs in which the initial concentration of 21 was the same for each run, but the concentration of 8 was varied, the initial reaction rate became a function of [8]. Hence, α and β could be determined from the plots of $\ln[-d[Cu(II)L]/dt]$ versus $\ln[Cu(II)L]$ or $\ln[L]$.

The reaction was initiated by introducing the 16Se4 solution into an uv cuvette with a syringe. By monitoring the absorption peak at 464 nm, the reaction was followed. A typical plot of absorbance as a function of time is shown in Figure 5.3.34: The absorption peak (464 nm) of 21 decreased while a new absorbance at 322 nm grew as a function of time. The peak at 332 nm had been identified as the radical cation of 16Se4. The first order kinetic equation gave the best fit for the absorbance function (at 466 nm) with time, as expressed in Eq (5.3.14). The growth of the peak at 322 nm also obeyed the first order rate law in the first 200 seconds. This peak (322 nm) started decreasing after 200 seconds.

$$A_{obs} = P_3 + P_2 \exp(-k_{obs}t) \qquad (5.3.14)$$

In Eq. (5.3.14), P_2 and P_3 are the fitting constants which can be rewritten as

$$A_{obs} = (A_0 - A_\infty) \exp(-k_{obs}t) + A_\infty$$

$$\approx \varepsilon C_0 \exp(-k_{obs}t) + A_\infty \qquad\qquad (5.3.15)$$

In Eq (5.3.15), ε is the molar extinction coefficient of **21**, A_∞, is the absorbance of **21** at infinite time t_∞, A_{obs} is the absorbance at time t, and C_0 is the initial concentration of **21**. Because A_∞ was negligible, the apparent molar extinction coefficient of **21** can be found by plotting P_2 vs C_0. The ε value was comparable to that determined from the CH_2Cl_2 solution of **21**.
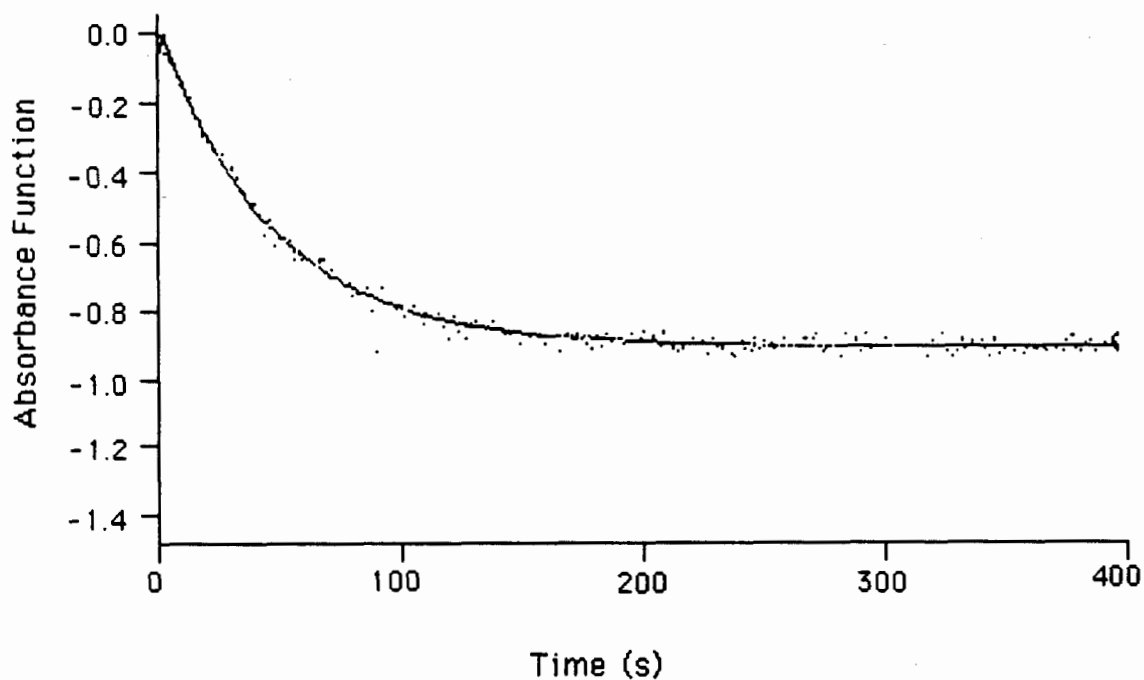
Figure 5.3.34. **Typical trace of the absorbance function (466 nm) of [Cu(16Se4)][SO$_3$CF$_3$]$_2$ with time. [[Cu(16Se4)][SO$_3$CF$_3$]$_2$] = 6.0 × 10^{-5} M, [16Se4] = 1.5 × 10^{-3} M. Dotted line is experimental data; solid line is the simulation.**

236

The initial reaction rate $\frac{dA}{dt}$ was determined by taking the first derivative of Eq (5.3.14) at $t = 0$. Then plotting $\ln(dA/dt)$ vs $\ln[8]$ and $\ln[21]$ the slopes obtained are 1.07 and 0.83 with respect to the concentrations of **21** and **8** (Figure 5.3.35 and Figure 5.3.36). Therefore, initially the redox reaction is first order with respect to [21] and [8], and the redox reaction rate can be expressed as,

$$- \frac{d[[Cu(16Se4)][SO_3CF_3]_2]}{dt} = k[[Cu(16Se4)][SO_3CF_3]_2][16Se4] \qquad (5.3.17)$$

The initial reaction rates and observed rate constants of the reaction (5.3.9) are listed in Table 5.3.12.

Table 5.3.12. Kinetic Data for Rate Law Determination

[21](M)	[8](M)	$dA/dt\vert_{t=0}$ (466 nm)	ε (cm^{-1}M^{-1})	k_{obs} (min^{-1})
4.9×10^{-5}	1.2×10^{-3}	0.688 ± 0.10	11920 ± 360	1.58 ± 0.04
6.0×10^{-5}	1.2×10^{-3}	0.906 ± 0.14	11920 ± 360	1.24 ± 0.02
6.9×10^{-5}	1.2×10^{-3}	0.944 ± 0.14	11920 ± 360	1.18 ± 0.04
7.9×10^{-5}	1.2×10^{-3}	1.19 ± 0.06	11920 ± 360	1.25 ± 0.03
6.0×10^{-5}	6.0×10^{-4}	0.54 ± 0.05	11920 ± 360	0.817 ± 0.05
6.0×10^{-5}	9.0×10^{-4}	0.74 ± 0.02	11920 ± 360	1.139 ± 0.03
6.0×10^{-5}	1.2×10^{-3}	0.95 ± 0.03	11920 ± 360	1.567 ± 0.05
6.0×10^{-5}	1.5×10^{-3}	1.20 ± 0.08	11920 ± 360	1.987 ± 0.11
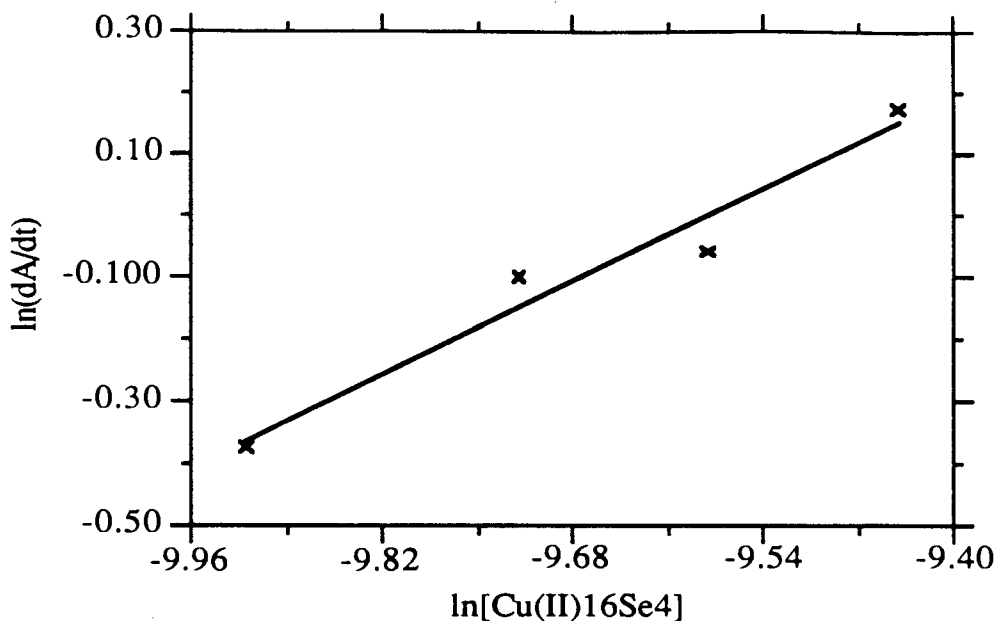
Figure 5.3.35. Plot of ln(dA/dt) vs ln[[Cu(16Se4)][SO$_3$CF$_3$]$_2$]. [[Cu(16Se4)][SO$_3$CF$_3$]$_2$] = 4.9-7.9 × 10^{-5} M, [16Se4] = 1.2 × 10^{-3} M.
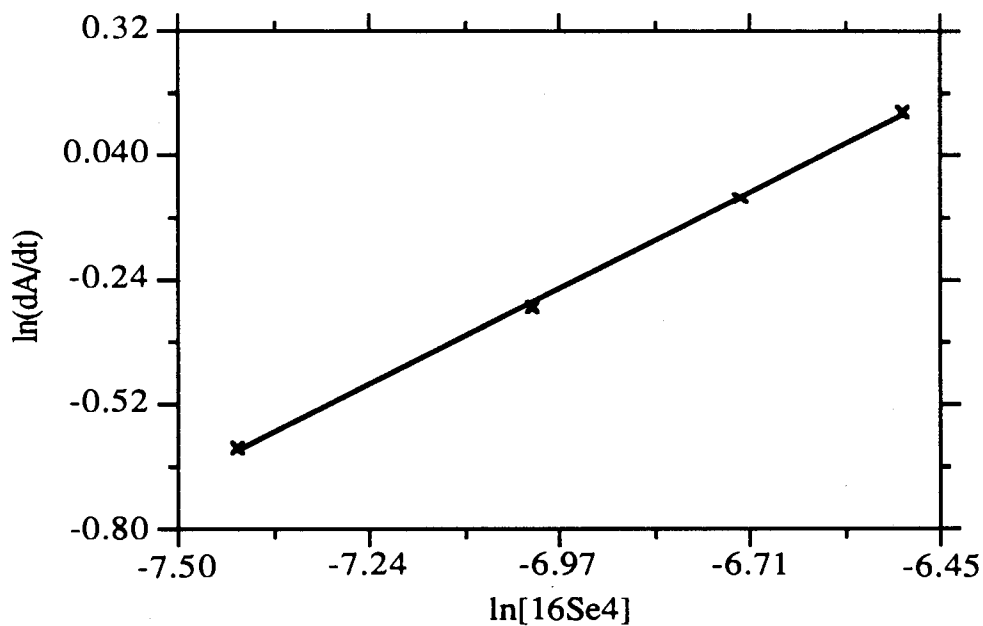
Figure 5.3.36. Plot of ln(dA/dt) vs ln[16Se4]. [16Se4] = 6.0-15 × 10^{-4} M, [[Cu(16Se4)][SO$_3$CF$_3$]$_2$] = 6.0 × 10^{-5}M.

5.3.1.4.2. *Determination of the Stoichiometry of the Reaction*

The reaction was also run with the same initial concentrations of **21** and **8**. Experimental data under these conditions gave the most satisfactory straight lines when treated by the following integrated form of the rate equation Eq(5.3.18).

$$- \frac{d[[Cu(16Se4)]^{2+}}{dt} = k[[Cu(16Se4)]^{2+}[16Se4]$$
$$= k(a-2x)(b-x) \qquad (5.3.18)$$

$$kt = \frac{2}{a-2b} \ln \frac{a-2x}{b-x} + \ln \frac{a}{b} \qquad (5.3.19)$$

where a and b are the initial concentrations of **21** and **8**, respectively, and x is the amount of **21** which has been reduced at time t. This relationship means that the redox reaction proceeds according to the following stoichiometry:

$$2[Cu(16Se4)]^{2+} + 16Se4 \longrightarrow 2[Cu(16Se4)]^{+} + 16Se4^{2+} \qquad (5.3.20)$$
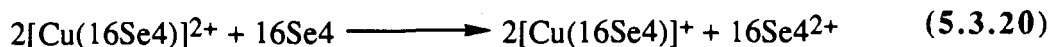
If this stoichiometry is correct then when the initial concentration of **8** is half that of **21**, i.e. b = a/2, the kinetic behavior would become a simple second order reaction which should have the form of Equation 5.3.22.

$$- \frac{d[[Cu(16Se4)][SO_3CF_3]_2]}{dt} = k[[Cu(16Se4)][SO_3CF_3]_2][16Se4]$$
$$= k(a-2x)(b-x) = k(a-2x)(\frac{a}{2} - 2*\frac{x}{2})$$
$$= \frac{k}{2}(a-2x)^2 \qquad (5.3.21)$$

Hence,

$$\frac{kt}{2} = \frac{1}{[[Cu(16Se4)][SO_3CF_3]_2]_o} - \frac{1}{[[Cu(16Se4)][SO_3CF_3]_2]_t}$$
$$(5.3.22)$$

Hence, reactions were carried out under conditions in which the concentration of 16Se4 (**8**) was 0.38, 0.5 and 0.63 times that of [Cu(16Se4)][SO_3CF_3]_2 (**21**) (Table

5.3.13). Figure 5.3.37 and 5.3.38 show plots of 1/[21] and $\ln \frac{a-2x}{b-x}$ versus time. The points shown covered about 62%, 66% and 77% of the 21 that reacted; after that the rate of the reduction slowed down significantly and the plot curved (see Appendix).

Table 5.3.13. Initial Concentrations of 21 and 8 in CH_2Cl_2 at 25 °C and Rate Constants.

[21](M)	[8](M)	k ($M^{-1}s^{-1}$)
7.8×10^{-5}	1.8×10^{-5}	29.67 ± 0.78
7.8×10^{-5}	3.6×10^{-5}	26.21 ± 0.94
7.8×10^{-5}	4.4×10^{-5}	31.26 ± 1.2
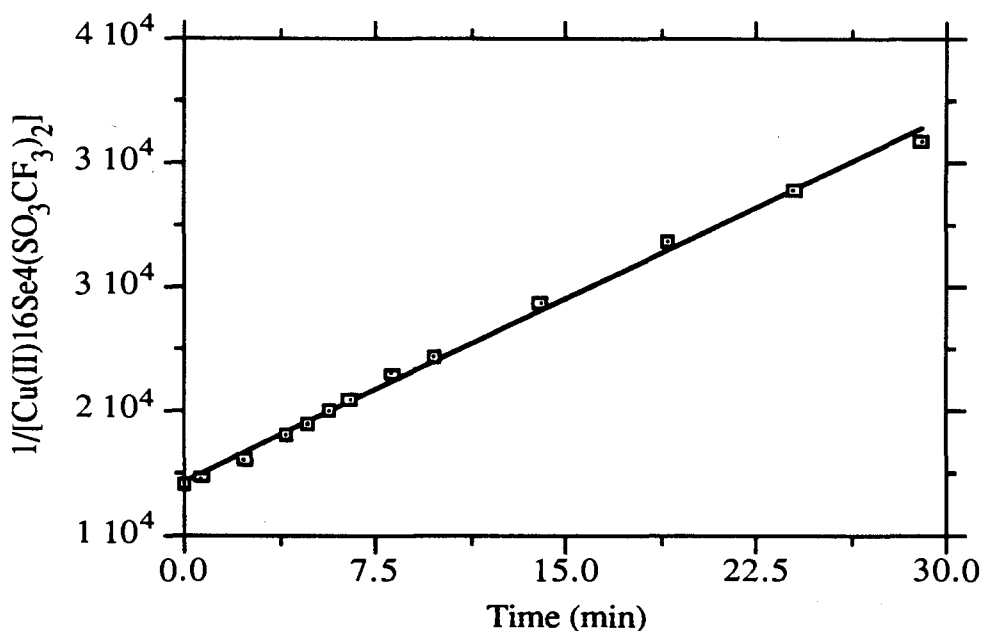
Figure 5.3.37. The quantity $1/[[Cu(16Se4)][SO_3CF_3]_2]$ plotted vs. time in the form of Eq (5.3.22) for the reduction of $[Cu(16Se4)][SO_3CF_3]_2$ with 16Se4 in CH_2Cl_2 at 25 °C. $[[Cu(16Se4)][SO_3CF_3]_2] = 7.8 \times 10^{-5}$ M, $[16Se4] = 3.6 \times 10^{-5}$ M.
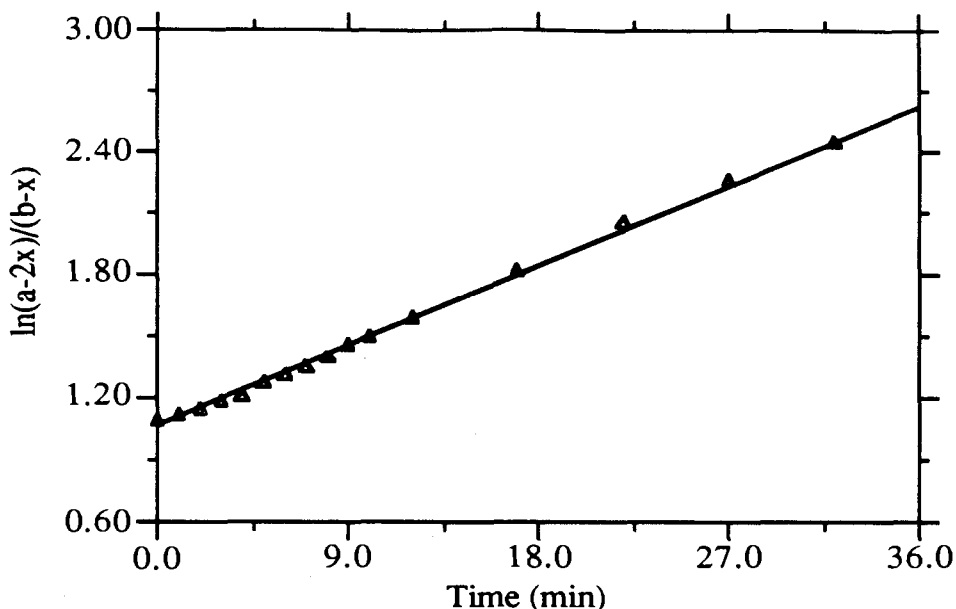
Figure 5.3.38. The quantity ln(a-2x)/b-x) plotted vs time in the form of Eq (5.3.19) for the reduction of $[Cu(16Se4)][SO_3CF_3]_2$ with 16Se4 in CH_2Cl_2 at 25 °C. $[[Cu(16Se4)][SO_3CF_3]_2] = 7.8 \times 10^{-5}$ M, $[16Se4] = 1.8 \times 10^{-5}$ M.

5.3.1.4.3. Reaction at Various Temperatures

The redox reaction was run at 1.0, 10, 15 and 25 °C. The initial concentration of 16Se4 was half that of $[Cu(16Se4)][SO_3CF_3]_2$; thus, data were interpreted in terms of a simple second order reaction (Eq 5.3.21). The results are shown in Figure 5.3.39-40 and Table 5.3.14. According to the Arrehnius Equation and Eyring theories of the reaction rate, the relationship of reaction rate and activation parameters are expressed as follows,

$$k = A*exp(-Ea/RT) \qquad (5.3.23)$$

$$k = \frac{k_B T}{h} exp(-\Delta G^{\neq}/RT) \qquad (5.3.24)$$

$$\Delta G^{\neq} = \Delta H^{\neq} - T\Delta S^{\neq} \qquad (5.3.25)$$

$$\Delta H^{\neq} = E_a - RT \qquad\qquad (5.3.26)$$

$$\Delta S^{\neq} = R(\ln A - \ln\frac{k_B T}{h}) \qquad\qquad (5.3.27)$$

where E_a is the activation energy of the reaction; k is the rate of the reaction; $\Delta G^{\neq}$ is the activation free energy of the reaction; $\Delta H^{\neq}$ is the activation enthalpy of the reaction; $\Delta S^{\neq}$ is the activation entropy of the reaction; k_B is the Boltzmann constant and the rest have their normal meanings. By plotting lnk vs 1/T, E_a was determined as 34.7 ± 2.0 kJ mol^{-1}.

Table 5.3.14. Activation Parameters for the Reduction of $[Cu(16Se4)][SO_3CF_3]_2$ (21).

21 (M)	8 (M)	t (°C)	k(M^{-1}s^1)
7.8×10^{-5}	3.6×10^{-5}	1.0	7.198 ± 0.16
7.8×10^{-5}	3.6×10^{-5}	10	9.965 ± 0.16
7.8×10^{-5}	3.6×10^{-5}	15	15.71 ± 0.46
7.8×10^{-5}	3.6×10^{-5}	25	22.66 ± 0.94

$E_a = 4171.5 \times 8.31 = 34.7 \pm 2.0$ kJmol^{-1}

$\Delta H^{\neq} = (8.29 \times 10^3 - 1.988 \times 298) \times 4.18 = 32.2 \pm 3.6$ kJmol^{-1}

$\Delta S^{\neq} = 1.988 \times (17.07 - \ln\frac{1.38 \times 10^{-23} \times 298}{6.626 \times 10^{-34}}) \times 4.18 = -103 \pm 10$ Jmol^{-1}
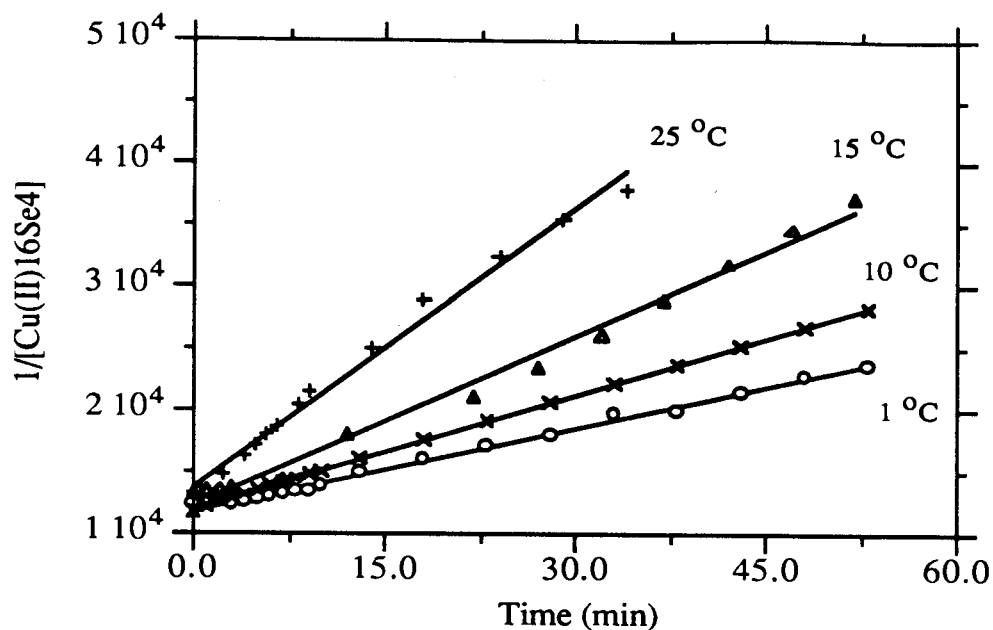
Figure 5.3.39. Plot of $1/[[Cu(16Se4)][SO_3CF_3]_2]$ vs time at various temperatures (data from Table 5.3.14).
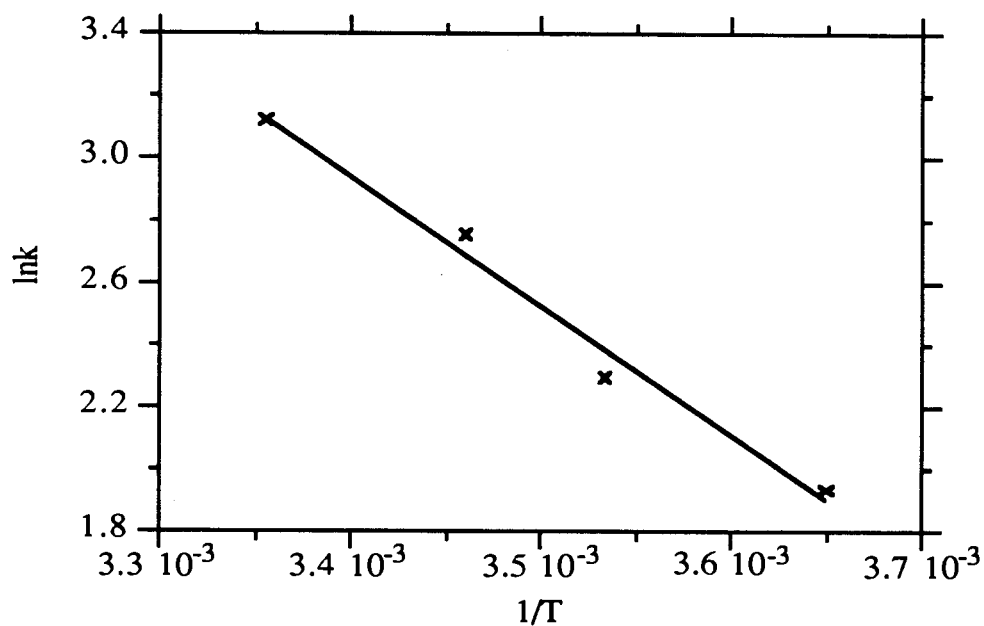
Figure 5.3.40. Plot of lnk vs 1/T. The slope is -4171 ± 472.3 and the intercept is 17.01 ± 1.655.

5.3.1.4.4. Kinetics in the Presence of [Cu(16Se4)][CF₃SO₃] (23)

The study of the kinetics of the redox reaction was carried out in the presence of [Cu(16Se4)][SO₃CF₃] (23). The rate constants were calculated according to Equation 5.3.19 and were compared with those from the kinetics in the absence of [Cu(16Se4)]⁺, as shown in Table 5.3.15.

Table 5.3.15. **Kinetic Data Measured in the Presence and Absence of [Cu(16Se4)][CF₃SO₃] (in CH₂Cl₂).**

$[Cu(16Se4)]^{2+}$ (M)	$[Cu(16Se4)]^{+}$ (M)	[16Se4] (M)	k_{obs} (M^{-1}s^{-1})
7.8×10^{-5}	0	2.05×10^{-5}	21.3
7.8×10^{-5}	7.5×10^{-5}	2.05×10^{-5}	17.5
7.8×10^{-5}	0	2.73×10^{-5}	33.2
7.8×10^{-5}	7.5×10^{-5}	2.73×10^{-5}	17.8

5.3.1.4.5. Kinetics of the Redox Reaction of [Cu(16S2Se2)][CF₃SO₃]₂ (42)

The study of the kinetics of the redox reaction of **31** with 16S2Se2 (**11**) was also performed as described for **21**. Addition of **11** to **31** in CH₂Cl₂ resulted in the characteristic peak of **31** (460 nm) decreasing under the conditions listed in Table 5.3.16. The absorbance at 460 nm was plotted as a function of time with the equations 5.3.19 and 5.3.22 as shown in Figure 5.3.41-42, indicating that **31** reacts with **11** in a similar fashion.

244

Table 5.3.16. **Experimental Conditions of the Reaction between**
[Cu(16S2Se2)][CF$_3$SO$_3$]$_2$ and 16S2Se2 (CH$_2$Cl$_2$).

[[Cu(16S2Se2)][CF$_3$SO$_3$]$_2$] (M)	[16S2Se2] (M)	k (M^{-1}s^{-1})
5.33 × 10^{-5}	2.91 × 10^{-5}	54.5±5.8
5.33 × 10^{-5}	4.65 × 10^{-5}	66.3±5.6
5.33 × 10^{-5}	5.81 × 10^{-5}	55.4±1.8
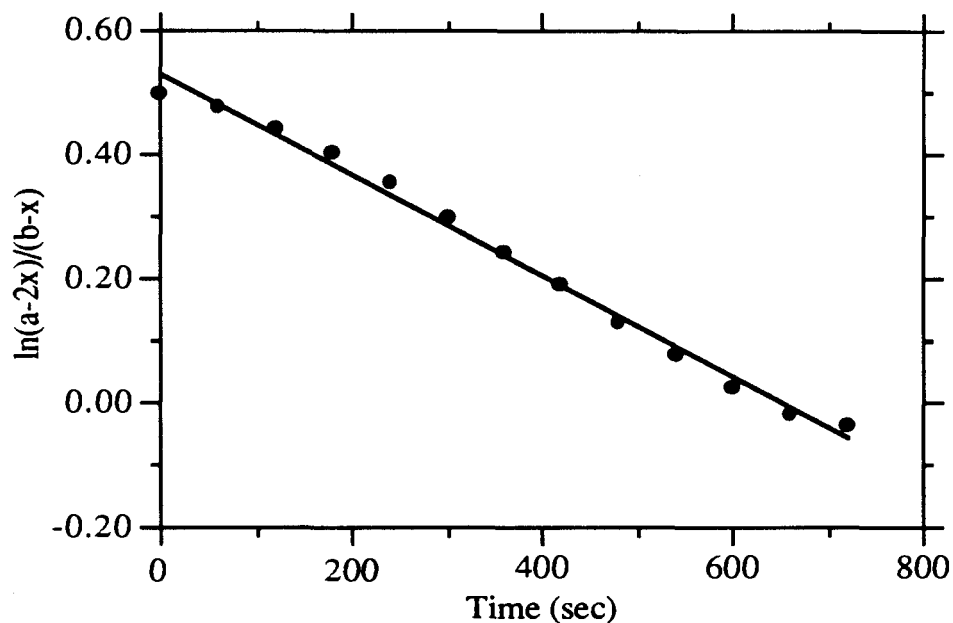
Figure 5.3.41. The quantity of ln(a-2x)/b-x) plotted vs. time in the form of Eq (5.3.21) for the reduction of [Cu(16S2Se2)][SO$_3$CF$_3$]$_2$ with 16S2Se2 in CH$_2$Cl$_2$ at 25 °C. [[Cu(16S2Se2)][SO$_3$CF$_3$]$_2$] = 5.33 × 10^{-5} M, [16S2Se2] = 2.91 × 10^{-5} M.
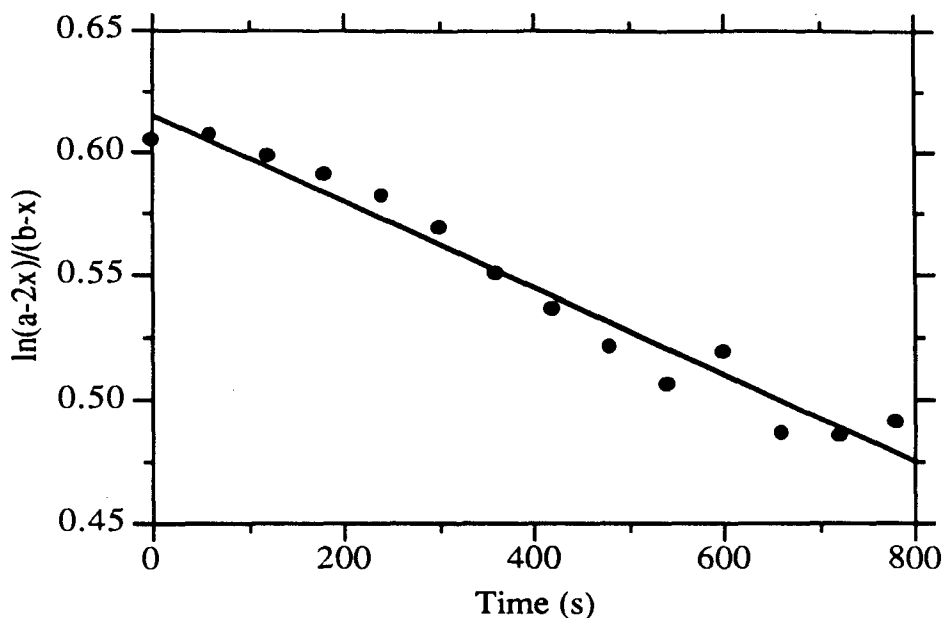
Figure 5.3.42. The quantity of $\ln(a-2x)/(b-x)$ plotted vs time in the form of Eq (5.3.22) for the reduction of $[Cu(16S2Se2)][SO_3CF_3]_2$ with 16S2Se2 in CH_2Cl_2 at 25 °C. $[[Cu(16Se4)][SO_3CF_3]_2] = 5.33 \times 10^{-5}$ M, $[16Se4] = 5.81 \times 10^{-5}$ M.

5.3.2. *Discussion*

5.3.2.1. *The Structures of Cu Complexes of Selenium Coronands*

Copper (II) Complexes

Copper (II) ion adopts a tetragonally distorted octahedral configuration in complexes $[Cu(16Se4(OH)_2)][CF_3SO_3]_2$ **(39)** and $[Cu(16S2Se2)][CF_3SO_3]_2$ **(31)**, similar to that $[Cu(16Se4)][SO_3CF_3]_2$ **(21)**[60] and Cu(II) complexes of thia macrocycles[30,33,35]. The selenium coronands (16Se4 moiety) are in a conformation that can be characterized as c,t,c[165,172], i.e., the non-bonding electron pairs on the Se atoms

246

are alternatively cis, trans and cis. The fused six-membered rings usually have alternative chair and boat conformations, but in $[Cu(16Se4(OH)_2)][CF_3SO_3]_2$ (**39**) the coordinated OH group locks one of the chair rings into the boat conformation. The long Cu-O(4) distance (2.58(1) Å) and the Se-Cu-O(4) angles show this to be a strained arrangement. These Cu(II) selenium coronand complexes have elongated Cu-O bond distances, which is a result of Jahn-Teller distortion at the apical positions[41].

The conformation of the selenium coronands (except 8Se2 and 8Se2OH) in the copper (II) complexes is significantly different from that of the free coronands. In the complexes, the Se atoms in the sixteen-membered ring do not take the corner positions as observed in 16Se4[75] and 16S2Se2.

The copper (II) complex of 8Se2OH (**17**) is also a tetragonally distorted octahedral. The Cu-Se bond distances are not much different from that in the previous complexes, but the Cu-O bond distances are shorter. The structure of the complex cation of **17** is very similar to that of $[Cu(8S2OH)_2][ClO_4]_2$[81](where 8S2OH = 3-hydroxy-1,5-dithiacyclooctane). Both are centrosymmetric and have an approximately tetragonally distorted octahedral coordination of the copper ion with the hydroxyl oxygen atoms occupying the more weakly bound axial positions. The Cu-O bond distance in **17** (2.358(3) Å) is not significantly different from that in $[Cu(8S2OH)_2][ClO_4]_2$ (2.350(2) Å). In **17** the Cu-O(4) bond is tilted 13.3 º from the normal to the $CuSe_4$ plane, while the analogous angle in $[Cu(8S2OH)_2][ClO_4]_2$ was 13.6 º. In both structures the hydroxyl groups form hydrogen bonds of comparable strengths to neighboring anions. A notable difference is that, whereas **17** displays predominantly (77.1(6)%) the chair-chair conformation with a lesser (12.9(6)%) contribution from a boat-chair form for the eight-membered ring, $[Cu(8S2OH)_2][ClO_4]_2$ displayed only the boat-chair conformation as did its 3-methoxy analog[182]. There are no atypical bond distances or bond angles in the structure of **17**.

Copper (I) Complexes

The complexes [Cu(16S2Se2)][CF$_3$SO$_3$] (**43**) and [Cu(16Se4OH)][CF$_3$SO$_3$] (**45**) adopt a tetrahedral configuration, which appears to be the most favored configuration for Cu(I) ions. The conformation of the ligand 16S2Se2 in complex **43** can be characterized as t,t,t (or udud)[106,172,183], i.e., the non-bonding electron pairs on the Se atoms are trans to each other. Both complexes appear as monomers in contrast to the solid state structure of [Cu(16Se4)][SO$_3$CF$_3$] (**23**), which is an oligomer although the tetrahedral configuration is also observed[61]. Compound **23** contained a three-dimensionally polymeric cation in which each copper atom was tetrahedrally coordinated to selenium atoms from four different 16Se4-rings[61], which remained in the free-ligand conformation. In several closely comparable Cu complexes of thia coronands, the Cu(I) ion adopts the tetrahedral configurations, e.g., in the monomer Cu(I) complexes of 15S5[35], 16S6[184] and 18S6[30].

Conformational analysis of selenium coronands in the Cu(I) complexes can be performed through the analysis of torsion angles of two sequences, namely, C-C-C-Se and C-Se-C-C. Thus, the conformation of 16S2Se2 in [Cu(16S2Se2)](SO$_3$CF$_3$) (**43**) can be described as AG$^+$G$^-$G$^-$AG$^-$G$^+$G$^+$AG$^+$G$^-$G$^-$AG$^-$G$^+$G$^+$, staring with the sequence Se(1)-C(2)-C(3)-C(4) (G$^+$) and proceeding clockwise. Here, A represents *anti* and G$^+$ and G$^-$ represent positive and negative *gauche* arrangements. The conformation of 16S2Se2 in [Cu(16Se4OH)](SO$_3$CF$_3$) (**45**) is described as AG$^-$G$^-$AG$^-$G$^-$G$^+$AG$^+$G$^+$G$^-$AAG$^+$G$^-$G$^-$. The sequence of bond torsion angles about the coronand rings in the conformations found for **43** and **45** display similar features. They display a repeating pattern of three *gauche* followed by one *anti* torsional arrangements (Figure 5.3.43), where the first and third always have opposite signs (e.g. G$^+$G$^-$G$^-$A etc.). The chalcogen atoms prefer positions between *gauche* and *anti* torsional arrangements (denoted GA). Moreover, the CH$_2$ β to the chalcogen atoms is between two *gauche* torsion angles with opposite signs. This is strictly obeyed in the predominant conformation of **43** (Figure 5.3.43), but in its alternative

conformation, and in the two observed for **45**, there is an additional *anti* relationship such that one chalcogen atom in each case resides in a position denoted AA. Consequently, the β-CH_2 in the related trimethylene resides in *gauche* arrangements with the same signs (Figure 5.3.43). In these cases the *anti* bond torsion angles show larger deviations from 180 $^{\circ}$.

In the free coronand the chalcogen atoms prefer *gauche* arrangements[36,75]. In coronand complexes such an arrangement does not occur since bonding with a metal ion requires the chalcogen atom to have its non-bonded electron pairs pointing towards the centrally located metal cation. Thus, for square planar coordination of 16Se4 the chalcogen atoms are located in AA sites[60]. Tetrahedral coordination, as described herein, apparently favors positioning of S or Se in GA sites. It would be of interest to compare these conformations and configurations with those for the potentially symmetrical species [Cu(16Se4)]$^+$ or [Cu(16S4)]$^{+}$[163]; however, suitable crystals containing these cations have not been obtained.
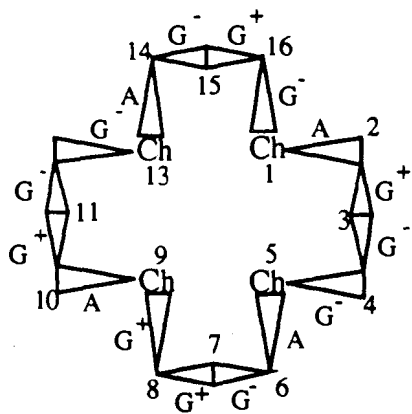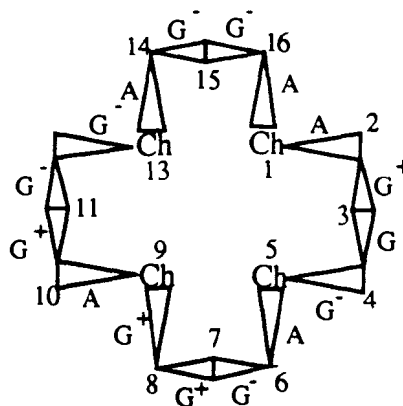
Ch = chalcogen S/Se
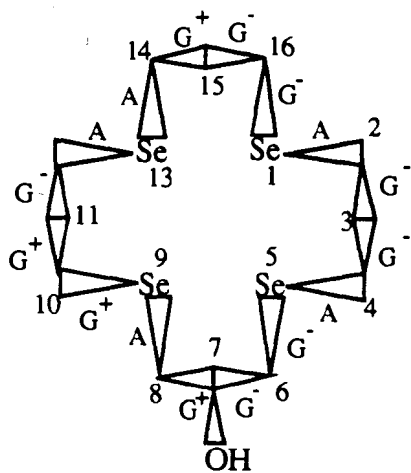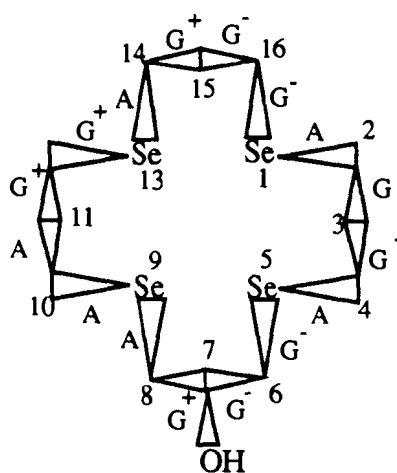
Figure 5.3.43. The conformations of [Cu(16S2Se2)]⁺; a) major, b) minor and the conformations of [Cu(16Se4OH)]⁺; c) major, d) minor.

250

5.3.2.2. Assignment of the Bands in the UV-visible Spectra

Characteristically, the uv-visible spectra of these Cu(II) selenium complexes, except for **41**, consist of three bands: a strong absorption band around 250 nm, an intense absorption band around 450 nm with a shoulder extending to 500-550 nm and a weak absorption band around 280-320 nm. The absorption peak at 250 nm is also observed in the spectra of the uncomplexed selenium coronands; therefore, it is assigned to σ-σ^* transitions of the Se-C bonds.

The assignments of the rest of the absorption bands are made by reference to those of the Cu(II) complexes of thia macrocycles[3,7,12,185,186] because of their similarity in electronic structures (Se and S in the same group in the periodic table). In addition, the appearance of the uv-visible spectra of these Cu(II) complexes is also similar. Hence, the absorption peaks around 450-470 nm are assigned to the charge transfer transition from ligand to metal ion (LMCT), i.e., Se(σ)-Cu(II)($d_{x^2-y^2}$). According to the molecular orbital description of the bonding in complexes, Cu(II) is an ion of $3d^9$ configuration that has 9 electrons in five d orbitals: $d_{x^2-y^2}$, d_{z^2}, d_{xy}, d_{yz} and d_{xz}. For the case of Se atoms, there are two-pairs of non-bonding electrons available for coordination with the Cu atom. Based on the symmetry and the energy criteria, the $d_{x^2-y^2}$ orbital is suitable for the formation of σ bonds with the non-bonding electrons on the Se atoms in the coronands. The σ-bonding orbital contains more contribution of Se and the σ-antibonding orbital has more contribution of $d_{x^2-y^2}$ in Cu(II). The charge transfer transition is from these two orbitals, which is allowed and of large absorbance coefficient ($\varepsilon = \sim 10^4$). Complex Cu(8Se2OH)$_2$(CF$_3$SO$_3$)$_2$ has a very broad absorption band at 571 nm that is assigned to Se(σ)$\rightarrow$Cu(II)($d_{x^2-y^2}$) ligand to metal charge transfer (LMCT) transitions.

The charge transfer transition absorption maxima (λ_{max}) of the Cu(II) complexes of selenium coronands appear at longer wavelengths in comparison with those of the Cu(II) complexes of thia macrocycles (about 400 nm in MeOH)[7,12]. The possible cause that

results in longer wavelength charge transfer absorption band is that selenium coronands are more easily oxidized than thia macrocycles. For a given metal ion, ligand to metal charge transfer energies decrease as the ligand becomes more readily oxidizable[187].

The assignments of the shoulder that is centered at about 570 nm in the uv-visible spectra of Cu(II) selenium coronands are ambiguous. Two proposals were presented in the literature for the interpretation of the similar absorption peak (~600 nm) in the Cu(II) complexes of thioethers. One proposal suggests that the absorption results from the $Se(\pi) \rightarrow Cu(II)(d_{x^2-y^2})$ charge transfer transition[46,47], whereas another suggests that they are d-d transitions with abnormal intensity borrowed from the low-lying σ charge transfer[188].

The absorption band at 330 nm was tentatively assigned to the charge transfer transition of Cu-O bonds between Cu(II) and the oxygen of triflates, because the substitution of hydroxy groups on the coronand (16Se4 moiety) results in the enhancement of the peak intensity at 330 nm. The weak absorption intensity of this band accounts for the elongated Cu-O bonds (sum of covalent Cu-O radii: 2.1 Å). In the Cu(II) complexes of hydroxyl substituted selenium coronands this band is noticeably more intense (Cu-O = 2.445(8) Å in $[Cu(16Se4(OH)_2)][SO_3CF_3]_2$ compared to Cu-O = 2.464(5) Å in $[Cu(16Se4)][SO_3CF_3]_2$).

5.3.2.3. Redox Behavior and Electrochemistry

Cyclic voltammetry of the Cu(II) complexes of selenium coronands has shown that the redox reaction of Cu(II)L/Cu(I)L pair is chemically reversible. This reversibility may result from the stabilization of Cu(I) ions through coordination to the selenium coronands. The usual oxidation states of copper are Cu(II) and Cu(I). In aqueous solution Cu(II) ion is more stable than Cu(I) because Cu(II) has higher heat of hydration, whereas Cu(I) undergoes a disproportionation reaction[189]. Therefore, there is no anodic peak on the

252

reverse scan in the cyclic voltammogram of Cu(II) in aqueous solutions. The pertinent data[7] for the Cu ions in aqueous solution are listed as follows.

$$Cu(II) + e^- \longrightarrow Cu(I) \qquad E^o = 0.153 \text{ V vs NHE}$$

$$Cu(II) + e^- \longrightarrow Cu \qquad E^o = 0.337 \text{ V vs NHE}$$

$$Cu(I) + e^- \longrightarrow Cu \qquad E^o = 0.521 \text{ V vs NHE}$$

$$Cu(I) + Cu(I) \rightleftharpoons Cu(II) + Cu \quad K = 1.7 \times 10^6 \text{ M}^{-1}$$
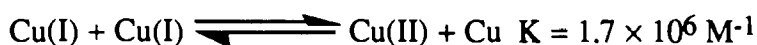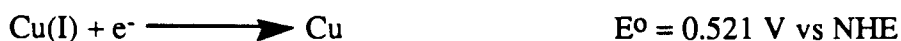
Table 5.3.17. **Redox Potential of Cu(II) Complexes of Selenium Coronands**

Cu(II) selenium coronands	$E_{1/2}^a$ or E_p^a (Volt vs SCE)	Solvent
$[Cu(16Se4)][SO_3CF_3]_2$ (**21**)	0.640	$CH_2Cl_2{}^d$
$[Cu(16S2Se2)][CF_3SO_3]_2$ (**31**)	$0.709^b, 0.801^c$	$CH_2Cl_2{}^d$
$[Cu(14Se4)][CF_3SO_3]_2$ (**44**)	0.602	$CH_2Cl_2{}^d$
$[Cu(16Se4(OH)_2)][CF_3SO_3]_2$ (**39**)	0.428	$CH_3NO_2{}^e$
$[Cu(8Se2OH)_2][CF_3SO_3]_2$ (**41**)	0.485	$CH_3NO_2{}^e$

a. For the first redox pair Cu(II)L/Cu(I)L, $E_{1/2} = (E_{pa} + E_{pc})/2$. At a scan rate of 20 mV/s

b. Initial scanning potential: 1.2 V; final scanning potential: 0 V.

c. Initial scanning potential: 0 V; final scanning potential: 1.2 V.

d. 0.05 M tetraethylammonium perchlorate as supporting electrolyte.

e. 0.1 M tetraethylammonium perchlorate as supporting electrolyte.

Another implication of the stabilization of Cu(I) ion by the coordination environment around the Cu atom is that the redox potential of Cu(II) rises in complexes of selenium coronands; the $E_{1/2}$ values are of the range 0.4-0.8 V vs SCE (Table 5.3.17) in comparison with that of Cu(II) complexes with nitrogen- or oxygen-donor ligands, in

aqueous solution, $E_{1/2}$ values between 0 and -0.7 V[11,30] vs SCE. Similarly, increased redox potentials have also been observed in the Cu(II) complexes of thia macrocycles (~0.7 V vs NHE)[190]. Two factors have been proposed to explain the unusual redox potentials of Cu(II) complexes of thia macrocycles; 1) the Cu(I) is stabilized by stereochemical properties of the ligands, which alter the properties of Cu(II) by constricting and dilating their coordination sphere[2]. Patterson and Holm[11] have shown structural factors which facilitate configuration change (from tetragonal to tetrahedral configurations) of complexes result in high redox potentials, in a series of bis-chelate amine Cu(II) complexes. 2) Electronic properties of thioethers. That is through dπ-dπ interactions between ligand and the Cu atom; the electron density delocalizes from the filled Cu(I) 3d orbitals into empty sulfur 3d orbitals[30], as proposed for the ability of phosphines to stabilize the low valence states of transition metal ions.[191,192,193,194]. Molecular orbital calculations suggest that dπ-dπ interactions (π-acidity) have more contribution to the stabilization of Cu(I)-thioether complexes than to Cu(II)-thioether complexes[193]. A recent calculation indicates that dimethyl selenoether has weak π-acidity[195].

The conformations of the selenium coronands in Cu(II) complexes are quite different from those of the free ligands; therefore, there are constraints imposed on the Cu(II) ion which may result in high redox potentials. The spontaneous reduction of the Cu(II) selenium coronands to Cu(I) selenium coronands is an indication that the selenium coronands preferentially stabilize the Cu(I) ions

It is conceivable that changing the oxidation state of Cu(II) to Cu(I) should be accompanied by configurational changes because of significant differences between the configurations of copper (II) complexes (octahedral or tetragonal configurations[196]) and Cu(I) complexes (tetrahedral configurations). This configurational change may be reflected in the cyclic voltammograms of the Cu(II) selenium coronand complexes. A reversible cyclic voltammogram corresponds to a system in which the electron transfer to the electrode is the rate determining step[182], i.e., the configuration change of the complex must be faster

than the electron transfer. Otherwise, quasi-reversible or even irreversible cyclic voltammograms would be produced. Thus, quasireversible cyclic voltammograms of copper (II) complexes of selenium coronands may indicate that the configuration change is slower than the electron transfer to the electrode. For example, the cyclic voltammogram of $[Cu(14Se4)][SO_3CF_3]_2$ shows the largest peak (Table 5.3.18) separation among the Cu(II) complexes. Probably, this is because the smaller ring of 14Se4 has difficulty in the interconversion of configuration from distorted tetragonal geometry to tetrahedral geometry.

Table 5.3.18. **Peak Potential Separation of the Cu(II) Complexes of Selenium Coronands**

Compounds	υ (mV/s)	ΔEp (V)
$[Cu(16Se4)][SO_3CF_3]_2$ (**21**)	20	0.192
$[Cu(16S2Se2)][CF_3SO_3]_2$ (**31**)	20	0.269
$[Cu(14Se4)][SO_3CF_3]_2$ (**34**)	20	0.444
$[Cu(16Se4(OH)_2)][CF_3SO_3]_2$ (**39**)	20	0.154
$[Cu(8Se2OH)_2][CF_3SO_3]_2$ (**41**)	20	0.282

On the cyclic voltammograms (scanning from -0.4 to 1.0 V vs SCE) of Cu(II) complexes of selenium coronands with hydroxyl substituents one would find that the broad oxidation peak is comprised of more than one peak, e.g., $[Cu(16Se4(OH)_2)][CF_3SO_3]_2$ (**39**) has two oxidation peaks at a scan rate of 20 mV/s (Figure 5.3.29). As the scanning rates increase the peak current at higher potential increases more than the peak current at the lower potential. When the scanning rate reaches 200 mV/s only the higher potential peak appears. This is an indication that two types of Cu(I)L isomers exist in solution (Scheme 5.3.1); one is designated as A that is more stable and is shown at higher potential, and the other is designated B. A and B are in equilibrium. At slow scanning rates, through the

equilibrium, mainly the less stable species (appears at lower potential) is oxidized. When the cyclic voltammetric potential scanning rates exceed the conversion rate of A to B, the oxidation of the more stable isomer becomes important; thus, only one oxidation peak is observed at the higher potential. This also explains the broad oxidation peaks observed in the cyclic voltammograms of [Cu(8Se2OH)$_2$][SO$_3$CF$_3$]$_2$.

Scheme   5.3.1

Cu(I)L (A)

Cu(II)L + e$^-$ k_{BA} $\uparrow\downarrow$ k_{AB}

Cu(I)L (B)
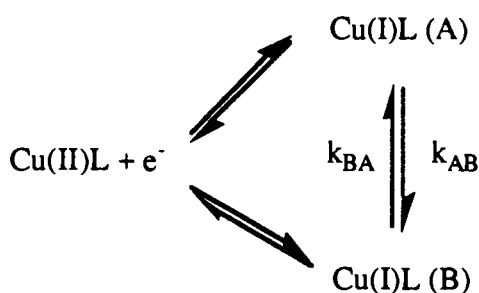
The dependence of cyclic voltammograms of [Cu(16S2Se2)][CF$_3$SO$_3$] (**42**) on the initial scan potentials may also result from the species of different conformations; the E_{pa} values from the cyclic voltammograms of scan range (0-1.2 V) is lower than that from the cyclic voltammograms of scan range (1.2-0 V). At the initial potential of 0 V, [Cu(16S2Se2)][CF$_3$SO$_3$] has time to transform to a more reactive species through a similar equilibrium to that shown in Scheme 5.3.1; hence, the oxidation peak appears at lower potential. On the other hand, at the initial potential of 1.2 V, the reduced species has less time to reach the more reactive species through equilibrium; therefore, the oxidation peak is at higher potential.

It is uncertain what is the cause of the redox wave at 1.1 V vs SCE. Two possibilities can be thought of : 1) it results from the oxidation of the selenium coronands in the complexes; 2) it results from the oxidation of Cu(II) complexes to Cu(III) complexes. In the literature there are reports of a Cu(III) complex of a nitrogen coronand (14N4)[197]

and other nitrogen containing ligands (peptides)[198-204], which are obtained from the oxidation of Cu(II) complexes of the corresponding ligands. The reported Cu(III) species usually have redox potentials around 1 V vs SCE[199,201,202]. The more relevant Cu(II) complex[197] of 14N4 has an absorption peak at 400 nm ($\varepsilon \sim$ 10,000). When the complex was electrolyzed with controlled potential in 10 M $HClO_4$ the peak at 400 nm decreased and a new peak appeared at 250 nm ($\varepsilon \sim$ 4000).

A spectroelectrochemical method has been applied to the study of the $[Cu(16Se4)][SO_3CF_3]_2$ complex. With a Pt electrode made from an Pt wire in a cobweb shape and at a applied potential of 1.6 V vs SCE to the $[Cu(16Se4)][SO_3CF_3]_2$ (21) in CH_2Cl_2, the absorbance at 464 nm does not change but a new peak at 320 nm appears after several minutes. When a Pt thin film electrode is used, if the applied potential is over 1 V vs SCE the instrument is overloaded. The same phenomenon as the previous one is observed. Hence, there is no conclusive evidence to support the existence of Cu(III) complexes. The ideal way to characterize the species may lie in an experiment that incorporates the electrolysis with ESR spectroscopy. If the species is a Cu(II)L$^{+\cdot}$, it should be ESR active; if the species is a Cu(III)L, it is should be ESR inactive (assuming that the d^8 electronic configuration of Cu(III) adopts a low-spin configuration). Unfortunately, we don't have the facility to do this experiment at the present time. Based on the unchanged absorbance at 464 nm and the appearance of the 322 nm peak, we attribute the species to the Cu(II)L$^{+\cdot}$ species.

5.3.2.4. *The Mechanism of the Redox Reaction of $[Cu(16Se4)][SO_3CF_3]_2$*

The products from the spontaneous reduction of $[Cu(II)(16Se4)][SO_3CF_3)]_2$ are the corresponding Cu(I) complex and 16Se4 dication. This indicates that in the redox reaction, 16Se4 is the reductant and the copper complex is the oxidant. Addition of 16Se4 into the Cu(II) complex in CH_2Cl_2 indeed causes the reduction reaction, and the rate of the reaction is first order with respect to both reactants. In the uv-visible spectra, the redox

process is manifested by the absorption peak of the Cu(II) complex decreasing and concurrently a new peak at 322 nm increasing. This new peak is proved to be from the absorption of the radical cation, $16Se4^{+\cdot}$, by studying the redox properties of the selenium coronand by various electrochemical methods (see Chapter 4). Furthermore, the results from the coulometry of 16Se4 revealed that the dication of 16Se4, $16Se4^{2+}$, cannot be formed by the disproportionation of $16Se4^{+\cdot}$, because the reaction is very unfavorable thermodynamically (see Chapter 4). Combining all the information, we propose the following mechanism:

Scheme 5.3.2

$$Cu(II)L^{2+} + L \underset{k_{-1}}{\overset{k_1}{\rightleftharpoons}} L^{+\cdot} + Cu(I)L^+ \qquad (5.3.28)$$

$$Cu(II)L^{2+} + L^{+\cdot} \xrightarrow{k_2} L^{2+} + Cu(I)L^+ \qquad (5.3.29)$$
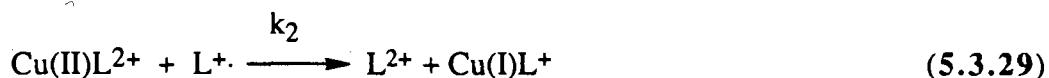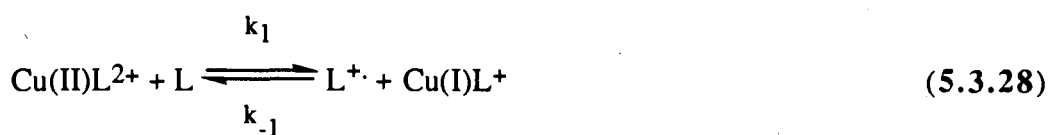
Here, L represents the selenium coronand. When the free ligand, 16Se4, is added into the Cu(II) complex solution, 16Se4 is oxidized to the radical cation and the Cu(II) complex becomes a Cu(I) complex. The radical cation of 16Se4 is further oxidized by another Cu(II) complex to the dication. This second electron transfer step is designated as the rate determining step because this step involves bringing two positively charged species to each other, which has to overcome the extra barrier from the electrostatic repulsion. Applying the steady state approximation to $[L^{+\cdot}]$, the overall reaction rate may be expressed as

$$Rate = \frac{k_1 k_2 [Cu(II)L^{2+}]^2 [L]}{k_{-1}[Cu(I)L^+] + k_2[Cu(II)L^{2+}]} \qquad (5.3.30)$$

When $k_{-1}[Cu(I)L^+] \ll k_2[Cu(II)L^{2+}]$, the rate expression becomes,

$$\text{Rate} = k_1[Cu(II)L^{2+}][L] \qquad\qquad (5.3.31)$$

At the initial stage of the reaction, the concentration of Cu(I)L is negligible and the condition $k_{-1}[Cu(I)L^+] \ll k_2[Cu(II)L^{2+}]$ is satisfied. Therefore, Eq 5.3.30 reduces to a second order reaction (Eq 5.3.31); the kinetic behavior of the electron transfer reaction exhibits a simple second order reaction. As the reaction continues, the reduction product $Cu(I)L^+$ accumulates, and the plot $\ln(a-2x)/(b-x)$ vs time deviates from linearity. Also, in the presence of $[Cu(16Se4)]^+$, k_1 values are smaller than those determined in the absence of $[Cu(16Se4)]^+$ because the term of $[Cu(16Se4)]^+$ is in the denominator. Similar kinetic observations have been reported for the Fe(III) redox system[205] that has the same overall rate expression as Eq. 5.3.30.

A bimolecular electron transfer process may be expressed as[206]

Scheme 5.3.3

$$A^+ + B \underset{}{\overset{}{\rightleftarrows} } [A^+B] \underset{}{\overset{}{\rightleftarrows} } [AB^+] \underset{}{\overset{}{\rightleftarrows} } A + B^+$$
$$\quad i \qquad\qquad\quad p \qquad\qquad\quad s \qquad\qquad\quad f$$
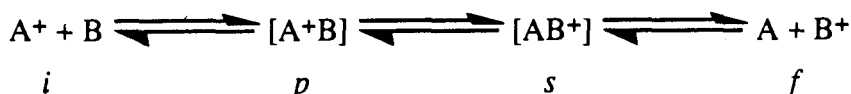
where A and B denote the reactants, and the positive charge sign denotes the oxidant; the states i and f are the initial and final states, with the reactants far apart; states p and s are precursor and successor states. It is assumed that reactions between i and p, and between s and f involve the motion of the A and B with little if any transfer of the electron, while the reactions between p and s involves electron transfer with the A-B distance more or less fixed (Frank-Condon principle[207]). Depending on the rate constants involved, the states p and s may or may not correspond to well defined chemical species. Accordingly, we propose that in order for an electron transfer from 16Se4 to $[Cu(16Se4)]^{2+}$ first, the Cu(II) complex partially dissociates so that another incoming coronand can coordinate with the

Cu(II) ion, then the electron transfers, and then products separate apart (Scheme 5.3.4). In these processes (complexation, electron transfer and product dissociation) any step can be the rate determining step, depending on the particular reactants.

Scheme 5.3.4

S = Solvent
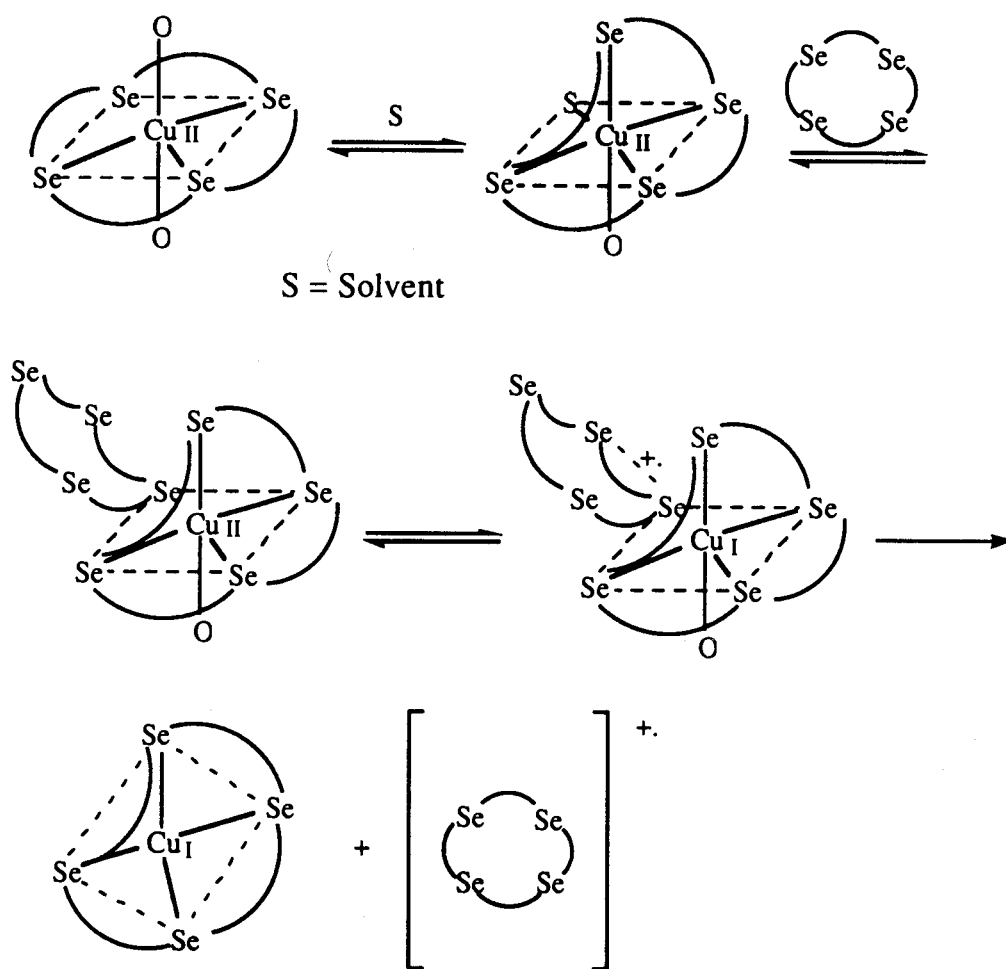
Formation of the coordinate bond between the Cu(II) ion and selenium coronand ligands is important for electron transfer because the redox reactivity of a metal ion is controlled by its immediate coordination environment[11,189,208]. Copper in any oxidation state is known to be influenced by the presence of ligands and the difference in stereochemistry of the Cu(II) and Cu(I) states[209]. The unusually high redox potential of blue copper proteins[10] is attributed to the distorted octahedral ligand coordination environment

imposed by the protein. Recently an x-ray crystallographic structure of azurin suggested that such structural distortion exists[8].

Complexation may play an important role in the oxidation of 16Se4$^{+\cdot}$ to 16Se4^{2+} by [Cu(II)(16Se4)]$^{2+}$. The $E_{1/2}$ of [Cu(16Se4)][SO$_3$CF$_3$]$_2$ is 0.640 V, $E_{1/2}$ of 16Se4 is 0.508 V for first redox cycle and 1.41 V for second redox cycle. Thermodynamically, it is not favorable for [Cu(16Se4)][SO$_3$CF$_3$]$_2$ to oxidize the radical cation of 16Se4. It is also the case for 12Se4 (**12**). This coronand has a E_p of 1.54 V and it is not oxidized by NOBF$_4$ in CH$_3$CN. However, upon mixing **12** with Cu(SO$_3$CF$_3$)$_2$ the Cu(I) complex is obtained. Formation of the complex makes the oxidation feasible. In addition, the dication 16Se4^{2+} and the Cu(I) complex of 12Se4 are almost insoluble in CH$_2$Cl$_2$ and CH$_3$CN, and the precipitation moves the reaction to the product side.

In aqueous solution, the redox potential of Cu^{2+} is 0.153 V vs NHE[7], but in CH$_3$CN it is 1.242 V vs NHE. Acetonitrile forms complexes with copper (II) ions that can be isolated[210]. This explains why the reduction of [Cu(16Se4)][SO$_3$CF$_3$]$_2$ is fast in CH$_3$CN; the CH$_3$CN competes with the coronand in complexation of Cu(II) ion, resulting in the dissociation of 16Se4 which is then oxidized by the remaining [Cu(16Se4)][SO$_3$CF$_3$]$_2$ (**21**) or other Cu(II) species in the solution.

Substitution of hydroxyl groups on the coronands may alter the rate-determining step of the electron transfer reaction. Both 8Se2OH and 16Se4(OH)$_2$ can be oxidized by NOBF$_4$ in CH$_3$CN. More importantly, after the first electron transfer occurs, the radical cation of the 16Se4 moiety that still coordinates to the Cu(I)L can regain an electron from Cu(I)L and go back to the starting material (the chemical reversibility of the Cu(II) complexes of selenium coronands has been confirmed by cyclic voltammetry), or dissociate and be re-oxidized by another Cu(II)L to dication. By using the same argument that Musker[81] used to interpret the different redox reactivity of 8S2 and 8S2OH towards Cu(II) in MeOH solution, we propose that the dissociation of the radical cation from the Cu(I) ion is presumably through a nucleophilic attack by the non-bonding electron pair from another

Se atom interacting with the Se atom bonding with the Cu atom along the direction of the lowest unoccupied orbital (i.e. σ^*). A linear arrangement of Cu-Se···Se may be required in the transition state in order to have the most efficient interaction and charge separation. When there are hydroxyl group substituents on the macrocyclic rings such linear arrangements are impossible because of the affinity of the oxygen atoms. Hence, the reverse reaction in which the electron transfers back to the radical cation becomes predominant. Therefore, the Cu(II) complexes of 8Se2OH and 16Se4(OH)$_2$ do not undergo significant redox reaction with their free ligands. The changes of the uv-visible absorption intensity of the copper complexes in the presence of free coronands result from changing complexation. The ESR spectrum of [Cu(8Se2OH)$_2$][CF$_3$SO$_3$]$_2$ (**41**) in the presence of free 8Se2OH suggests that another Cu(II) species is formed besides the original complex. It is necessary to point out that another Cu(II) complex, namely, [Cu(16Se4OH)][SO$_3$CF$_3$]$_2$ also undergoes redox reaction during the recrystallization. The corresponding Cu(I) complex is isolated, although addition of the free ligand 16Se4OH (1/2 of the complex concentration) into the Cu(II) complex solution (CH$_2$Cl$_2$) only causes one-third reduction of the complex's absorption intensity. This indicates that the hydroxyl substituents in the macrocyclic ring retard the redox reaction but do not completely stop the reaction.

Taking these facts into account, the spontaneous redox reaction of the Cu(II)(16Se4)$^{2+}$ can be expressed as in Scheme 5.3.5.

Scheme 5.3.5

$$\text{Cu(II)16Se4}^{2+} \rightleftharpoons \text{Cu(II)}^{2+} + \text{16Se4} \tag{5.3.32}$$

$$\text{16Se4} + \text{Cu(II)16Se4}^{2+} \rightleftharpoons \text{16Se4}\cdots\text{Cu(II)16Se4}^{2+} \tag{5.3.33}$$

$$\text{16Se4}\cdots\text{Cu(II)16Se4}^{2+} \rightleftharpoons \text{16Se4}^{+\cdot} + \text{Cu(I)16Se4}^{+} \tag{5.3.34}$$

$$16Se4 + 16Se4^{+\cdot} \rightleftharpoons (16Se4)_2^{+\cdot} \qquad (5.3.35)$$

$$Cu(II)16Se4 + 16Se4^{+\cdot} \rightleftharpoons 16Se4^{+\cdot}\cdots Cu(II)16Se4 \qquad (5.3.36)$$

$$16Se4^{+\cdot}\cdots Cu(II)16Se4^{2+} \longrightarrow 16Se4^{2+} + Cu(I)16Se4^{+} \qquad (5.3.37)$$
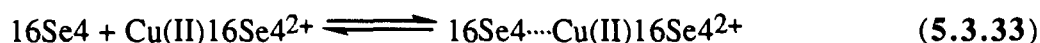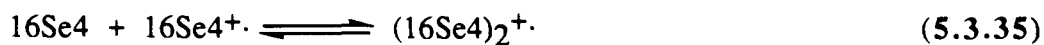
In conclusion, Pd(II) and Cu(II) complexes of selected selenium coronands have been prepared. The configurations of these complexes are determined by electronic requirements of the metal ions and the conformational flexibility of the selenium coronands. Thus, the Pd(II) complexes have a square planar configuration about a Pd atom, the Cu(II) complexes have a tetragonally distorted octahedral configuration about a Cu atom and the Cu(I) complexes have a tetrahedral configuration about a Cu atom. In these complexes the conformation of 16Se4 has shown different forms; all of them differ significantly from the conformation of free 16Se4. This finding may provide guidelines for design of new coronands which can bind the metal ions with more specificity and stability. The Cu(II) complexes have shown a redox reaction with the selenium coronand ligands. This is a unique reaction for the chemistry of selenium coronands and does not appear to occur with the sulfur congeners.

CHAPTER VI
CONCLUSIONS

In summary, we have synthesized selenium coronands either containing functional groups or with an odd-number of donor atoms, with success, through a one-step or stepwise strategy. A mixed sulfur/selenium coronand has also been synthesized. These coronands can be used for further investigation of the effects of donor atoms or substituents, in the inner coordination sphere, on the properties of metal ion complexes in terms of stability and reactivity. Also, the functional groups on the selenium coronands can serve as handles for further modifications or for attachment to polymers for developing new materials[108].

The radical cations of selenium coronands were prepared chemically and electrochemically and identified by uv-visible spectroscopy. Cyclic voltammetry of these selenium coronands was carried out in CH_3CN. Selenium coronands, in general, show a susceptibility towards oxidation. Most of the coronands examined have shown chemically reversible behavior toward oxidation. This reversibility can be attributed to the formation of a two-center three-electron bond within a radical cation (transannular interaction) or between a radical cation and a neutral coronand. 16Se4 (**8**) has been studied in detail by cyclic voltammetry, coulometry, and spectroelectrochemistry. Its two redox pairs (on the cyclic voltammogram) consist of two single electron transfer processes with $E^1_{1/2}$ 0.503 V and $E^2_{1/2}$ 1.41 V respectively. The disproportionation of the radical cation of 16Se4 to form 16Se4^{2+} is not favored.

Pd(II) and Cu(II) complexes of selected selenium coronands have been prepared and characterized by x-ray crystallography. The configurations of these complexes are determined by the electronic requirements of the metal ions and the conformational flexibility of the selenium coronands. In these complexes the conformation of 16Se4 (**8**) has shown different forms, all of which differ significantly from the conformation of the

free ligand **8**. This finding may provide guidelines for the design of new coronands which can bind metal ions with greater specificity and stability. The Cu(II) complexes have shown a redox reaction with the selenium coronands themselves. This is a unique reaction for the chemistry of selenium coronands and does not appear to occur with the sulfur congeners.

CHAPTER VII
EXPERIMENTAL

7.1. General Conditions

Melting points were determined on a Fisher-Johns melting-point apparatus and are uncorrected. ^{1}H NMR spectra were recorded either on Bruker SY-100 at 100 MHz or Bruker AMX-400 NMR spectrometers at 400.13 MHz. ^{13}C NMR and ^{77}Se NMR spectra were recorded on Bruker AMX-400 NMR spectrometer at 100.6 and 76.3 MHz for carbon and selenium respectively. For the ^{1}H NMR and ^{13}C NMR spectra, chemical shifts were obtained in ppm with respect to $SiMe_4$; coupling constants were obtained from a first-order analysis of the spectra.

The ^{1}H-homonuclear chemical-shift correlated (COSY) spectra were acquired with initial data sets of 512×2048 data points which were zero-filled once in the F_1 direction to give a final data set of 1024×1024 real data points.

For the inverse detection experiments a 4-pulse sequence was used for the ^{1}H{^{13}C}-^{13}C correlation[211]; the same sequence, incorporating a BIRD pulse in the preparation period, was used for the ^{1}H-^{13}C correlation[212]. In both cases, time proportional phase increments were used in F_1. The data sets of 512×2048 data points were zero-filled once in both the F_1- and the F_2-directions, to give a final data set of 1024×2048 real data points, with a digital resolution of 10.3 and 1.0 Hz/pt in the F_1- and F_2-directions, respectively.

Solid-state NMR spectra were recorded on an instrument (built inhouse) operating at a field of 1.4 T or 3.5 T. This produces original resonance frequencies of 11.4 or 28.5 and 15.1 or 37.5 MHz for ^{77}Se and ^{13}C, respectively. Spectra were excited by using single-contact Hartmann-Hahn cross polarization. The matched radio frequency field strengths were 40 and 50 kHz for ^{77}Se and ^{13}C, respectively. The same field strength was

used for proton decoupling during data acquisition. Samples were spun at the magic angle at frequencies of 2-3 kHz. The magic angle was correctly set within $\pm 0.1^\circ$ by optimizing the line width on well-crystallized samples of $(t\text{-}Bu_2Sn)_2Se_2$ and $H_2C_2O_4 \cdot 2H_2O$. Chemical shifts were measured relative to long cylindrical samples of aqueous H_2SeO_3 and C_6H_6. These were converted to shifts based on the standard Me_2Se and TMS scales by using literature data[59, 72-74].

ESR spectra were recorded on Varian E-4 EPR Spectrometer equipped with a Varian Temperature Controller. The magnetic field was calibrated with DPPH (g = 2.0036)[213]. For experiments at ambient temperature, nitromethane was used as the solvent; for experiments at low temperature, mixed solvents, nitromethane and toluene (1:1, v/v) were used. The concentration of copper(II) complexes of selenium coronands was about 1×10^{-3} M. Measurements were obtained from a solution sample in a melting point capillary that was placed in a normal ESR tube.

X-Ray crystallography was carried out by Drs. R. J. Batchelor, and F. W. B. Einstein.

Chemical ionization mass spectra were measured on a Hewlett-Packard HP-5899 mass spectrometer with isobutane as the reacting gas.

Analytical TLC was performed on precoated aluminum plates with Merck silica gel 60F-254 as the absorbent. The developed plates were air dried, exposed to uv light and/or sprayed with 10% H_2SO_4 in ethanol, and heated to 100 °C. Flash column chromatography was performed on Kieselgel 60 (230-400) according to a published procedure[214].

Microanalyses were performed by M. K. Yang of the Microanalytical Laboratory of Simon Fraser University.

7.2. Solvents and Chemicals

7.2.1. Solvents

Acetonitrile (Fisher or Caledon, AR or HPLC grade) was refluxed with CaH_2 and distilled under N_2 before use. Dichloromethane (CH_2Cl_2, Aldrich, AR grade) was distilled from P_2O_5 under N_2. Nitromethane (CH_3NO_2, Fisher, certified) was dried over $CaCl_2$, and distilled from P_2O_5 under N_2. Tetrahydrofuran (THF, Aldrich, AR grade) was refluxed with Na and benzophenone until a purple solution was formed, then was distilled under N_2 before use. N,N-Dimethylformamide (DMF, Aldrich, A.C.S. reagent) was dried over molecular sieves and distilled under reduced pressure before use.

7.2.2. Chemicals

Tetraethylammonium perchlorate (Kodak) was dried under vacuum at 70 °C. $NOBF_4$ (Aldrich) was sublimed at 100 °C under vacuum, sealed in a vial and was kept in a freezer (- 20 °C).

7.2.3. Preparation of Selenium Coronands and Metal Ion Complexes

16Se4(OH)$_2$ (9) and 8Se2OH (17). To 2-hydroxy-1,3-propanediselenocyanate ($NCSeCH_2CH(OH)CH_2SeCN$, 1.6 g, 5.97 mmol) in dry THF (50 ml) was added, with stirring, $NaBH_4$ (0.96 g, 0.025 mol) in dry EtOH (20 ml). A yellow homogeneous solution was formed. Then, $Br(CH_2)_3Br$ (2.0 g, 9.90 mmol) in dry THF (20 ml) was added to the above solution. The mixture was stirred overnight at ambient temperature. After removal the solvent under reduced pressure, the mixture was poured into water and extracted with CH_2Cl_2. The extract was washed with water (3 × 25 ml), and dried over $MgSO_4$. After removal of the solvent, purification by silica gel flash chromatography (hexane: ethyl acetate (3:1, v/v) yielded 8Se2OH **17** as a colorless oil (360

mg, 23%) which became white waxy needles upon cooling in a refrigerator and 16Se4(OH)$_2$ **9** as a white solid (362 mg, 12%). Data for 8Se2OH (**17**): mp: 34-35 °C. ^{1}H NMR (400 MHz, CDCl$_3$). δ 2.32-2.48 (2H, dtt, J$_{fg}$ = 13 Hz, J$_{fd}$ 3.75 Hz, J$_{fe}$ = 8.00 Hz, Jge = 4.25 Hz, Jgd = 7.50 Hz, SeCH$_2$C(H$_f$)H$_g$CH$_2$Se), 2.68-2.74 (2H, ddd, J$_{ed}$ = 13.4 Hz, J$_{ef}$ = 8.00 Hz, J$_{eg}$ = 4.25 Hz, SeCH$_2$CH(H)C(H$_d$)H$_e$Se), 2.79-2.86 (2H, ddd, J$_{de}$ = 13.4 Hz, J$_{dg}$ = 7.50 Hz, J$_{df}$ = 3.75 Hz, SeCH$_2$CH(H)HC(H$_d$)H$_e$Se), 2.96-3.03 (2H, dd, J$_{cb}$ = 13.8 Hz, J$_{ca}$ = 7.00 Hz, SeC(H$_c$)H$_b$-CHOHCH$_2$Se), 3.13-3.18 (2H, dd, J$_{bc}$ = 13.8 Hz, J$_{ba}$ = 3.00 Hz, SeC(H$_c$)H$_b$CHOHCH$_2$Se), 3.98 (2H, s(br), SeCH$_2$CHOHCH$_2$Se). ^{13}C NMR (100 MHz, CDCl$_3$). δ 23.9 (α-CH$_2$Se-, rel. int. 2), 30.2 (α-CH(OH)Se-, rel. int. 2), 30.8 (β-CH$_2$, rel. int. 1), 69.4 (β-CHOH, rel. int. 1). IR (Nujol): 3400 (υ-OH), 1290, 1230, 1120 , 1090 (υ=C-O) cm^{-1}. Anal. Calc. for C$_6$H$_{12}$OSe$_2$: C, 27.91; H, 4.651. Found: C, 28.14; H, 4.62.

Data for 16Se4(OH)$_2$ (**9**): mp: 79-80 °C. ^{1}H NMR (400 MHz, CDCl$_3$). δ 2.09 (4H, p, J = 6.4 Hz, SeCH$_2$CH$_2$CH$_2$Se), 2.66-2.90 (18H, m, SeCH$_2$CHOHCH$_2$Se & OH), 3.88 (2H, m, SeCH$_2$CHOHCH$_2$Se). ^{13}C NMR (100 MHz, CDCl$_3$). δ 24.3 (α-CH$_2$Se-, rel. int. 2), 31.3 (α-CH(OH)Se-, rel. int. 2), 31.6 (β-CH$_2$, rel. int. 1), 70.1 (β-CHOH, rel. int. 1). MS: 498 (M$^+$-18). IR (Nujol): 3400 (υ-OH), 1290, 1230, 1120 , 1050 (υ=C-O) cm^{-1}. MS: 498 (M$^+$ - 18). Anal. Calc. for C$_{12}$H$_{24}$O$_2$Se$_4$: C,27.91; H, 4.651. Found: C, 28.07; H, 4.56.

Poly(1,2-diselenobenzene) (26)[94]. Na (2.9 g, .12 mol) in small pieces was added to selenium powder (9.5 g, 0.12 mol) in DMF (60 ml) that was stirred and heated to 100 °C. Reaction occurred upon the addition of Na to give a brown solution, which was kept at 100 °C for 20 min. Subsequently, 1,2-dibromobenzene (7.3 ml, 11.6 g, 0.049 mol) was added dropwise into the above solution. The solution was kept gently boiling for 38 hours. The mixture, after being cooled to ambient temperature, was poured into a water/MeOH solution (500 ml, 1:1, v/v). A bright orange precipitate was formed, filtered

and washed with water/MeOH (2:1, v/v), MeOH and CH_2Cl_2. Compound **39** was obtained as an orange solid (6.2 g 66% yield).

1,2-Bis(3-hydroxy-1-propylseleno)benzene (**27**). To poly(1,2-diselenobezene), **39**, (1.0 g, 0.0042 mol) in dry THF (50 ml) was added $NaBH_4$ (0.65 g, 0.02 mol) in dry EtOH (20 ml). A light yellow clear solution was formed, to which 3-bromo-1-propanol (2.36 g, 0.017 mol) in dry THF (30 ml) was added. The mixture was stirred at ambient temperature for 48 h, then poured into water (150 ml) and extracted with CH_2Cl_2 (3 × 30 ml). The combined extracts were washed with water, dried (Na_2SO_4) and concentrated in vacuo to yield a light yellow oil. Purification by silica gel flash chromatography (hexane:ethyl acetate (1:1)) yielded a yellow oil (1.0 g, 66% yield). ^1H NMR (100 MHz, $CDCl_3$). δ 1.97 (4H, p, J = 6.6 Hz, $SeCH_2C\underline{H}_2CH_2OH$), 2.72 (2H, OH's, m), 3.02 (4H, triplet, J = 6.6 Hz, $SeC\underline{H}_2CH_2CH_2OH$), 3.78 (4H, triplet, J = 6.61 Hz, $SeCH_2CH_2C\underline{H}_2OH$), 7.11-7.46 (4H, m, Ar$\underline{H}$). ^{13}C NMR (100 MHz, $CDCl_3$). δ 24.3 (Se$\underline{C}H_2$'s), 32.3 (β-$\underline{C}H_2$'s), 62.3 (-$\underline{C}H_2OH$), 127.3, 132.0 and 134.9 (benzene ring). IR(pure sample). 3400 (br, ν-OH), 3040 (ν-ArH), 2930, 2850 (s, ν-CH), 1435 (s, δ-CH), 1240, 1050 (s, ν-C-O), 900 cm^{-1}. MS: 352 (M+). Anal. Calc. for $C_{12}H_{18}Se_2O_2$: C, 40.92; H, 5.15. Found: C, 41.08 ; H, 5.20.

1,2-Bis(3-chloro-1-propylseleno)benzene (**28**). To thionyl chloride (10 ml), was added dropwise 1,2-bis(3-hydroxy-1-propylseleno)benzene, **27**, (1.35 g, 0.004 mol) in dry CH_2Cl_2 (5 ml). The mixture was stirred and refluxed for 1.5 h. Then the thionyl chloride was removed in vacuo. The residue was diluted with water (50 ml) and extracted with CH_2Cl_2 (20 ml × 3). The combined extracts were washed with water (20 × 3), dried over Na_2SO_4 and concentrated in vacuo to yield a yellow oil. Purification by silica gel flash chromatography (hexane: ethyl acetate, 20:1) yielded 1,2-bis(3-chloro-1-propylseleno)benzene (420 mg, 31% yield). ^1H NMR (100 MHz, $CDCl_3$). δ 2.15 (4H, p, J = 6.6 Hz, $SeCH_2C\underline{H}_2CH_2Cl$), 3.10 (4H, t, J = 6.9 Hz, $SeC\underline{H}_2CH_2CH_2Cl$), 3.70 (4H, t, J = 6.3 Hz, $SeCH_2CH_2C\underline{H}_2Cl$), 7.17-7.80 (4H, m, ArH). ^{13}C NMR (100 MHz,

CDCl$_3$). δ 24.6 (Se$\underline{C}$H$_2$'s), 32.4 (β-$\underline{C}$H$_2$'s), 44.3 (-$\underline{C}$H$_2$Cl), 127.5, 132.1 and 134.0 (benzene ring). IR (pure sample). 3040 (ν-ArH), 2940 (s, δ-CH), 1550 (s, ν-C=C, Ar) cm^{-1}. MS: 390 (M$^+$ + 1). Anal. Calc. for C$_{12}$H$_{17}$Cl$_2$Se$_2$: H, 4.12; C, 37.11. Found: H, 4.10; C, 37.32.

Dibenzo-14Se4 (14). To poly(1,2-diselenobenzene), **26**, (246 mg, 1.05 mmol) in dry THF (10 ml) was added dropwise NaBH$_4$ (160 mg, 4.21 mmol) in dry EtOH (5 ml) at ambient temperature. Then, 1,2-bis(3-chloro-1-propylseleno)benzene, **28**, (340 mg, 0.874 mmol) in THF (20 ml) was added dropwise to the above solution. The reaction mixture was stirred at ambient temperature for 24 h, then diluted with water (20 ml) and extracted with CH$_2$Cl$_2$ (20 ml $\times$ 3). The combined extracts were washed with water (20 ml $\times$ 3), dried over Na$_2$SO$_4$ and concentrated in vacuo to yield a thick orange oil. Purification by silica gel flash chromatography (hexane : ethyl acetate, 20 : 1, v/v) yielded dibenzo-14Se4 (290 mg, 60% yield) as yellowish crystals which was recrystalized form CH$_2$Cl$_2$/EtOAc. mp.: 171-172 °C. ^{1}H NMR (100 MHz, CDCl$_3$). δ 1.98 (4H, p, J=7.1 Hz, SeCH$_2$C$\underline{H}$$_2CH_2$Se), 3.02 (8H, t, J=7.1 Hz, SeC$\underline{H}$$_2CH_2CH_2$Se), 6.95-7.35 (8H, m, Ar$\underline{H}$). ^{13}C NMR (100 MHz, CDCl$_3$). δ 27.0 (Se$\underline{C}$H$_2$'s), 29.3 (β-$\underline{C}$H$_2$'s), 127.3, 133.7 and 134.1 (benzene ring). IR(KBr salt). 3030 (ν-ArH), 2910 (s, ν-CH), 1550 (ν-C=C), 1210, 1020 cm^{-1}. UV(CH$_2$Cl$_2$). $\lambda(\varepsilon)$: 256 nm (2.2 $\times$ 10^4), 274 nm (2.2 $\times$ 10^4). MS: 552 (M$^+$). Anal. Calc. for C$_{18}$H$_{20}$Se$_4$: H, 3.65; C, 39.15. Found: H, 3.51; C, 39.10.

1,3-Bis(3-mercaptopropylseleno)propane (30). To 1,3-propanediseleno-cyanate (2.0 g, 0.08 mol) in dry THF (30 ml) was added dropwise NaBH$_4$ (1.2 g, 0.032 mol) in dry EtOH (15 ml) at ambient temperature. Then, 3-chloropropanethiol (1.76 g, 0.0159 mol) in THF (20 ml) was added dropwise to the above solution. The reaction mixture was stirred at ambient temperature for 96 h. Subsequently, the solution was concentrated in vacuo, diluted with water (20 ml) and extracted with CH$_2$Cl$_2$ (20 ml $\times$ 3). The combined extracts were washed with water (20 ml $\times$ 3), dried over Na$_2$SO$_4$ and concentrated in vacuo to yield a thick orange oil. Purification by silica gel flash

chromatography (hexane : ethyl acetate, 10 : 1) yield 1,3-bis(3-mercaptopropylseleno)-propane (2.55 g, 60% yield) as a yellowish liquid. ^{1}H NMR (100 MHz, CDCl$_3$). δ 1.53 (2H, p, J = 8.6 Hz, -SeCH$_2$C$\underline{H}_2$CH$_2$Se-), 2.05 (4H, p, J=8.6 Hz, HSCH$_2$C$\underline{H}_2$CH$_2$SeCH$_2$CH$_2$CH$_2$SeCH$_2$C$\underline{H}_2$CH$_2$SH), 2.88 (12H, p, J=8.6 Hz, HSC$\underline{H}_2$-CH$_2$C$\underline{H}_2$SeC$\underline{H}_2$CH$_2$-C$\underline{H}_2$SeC$\underline{H}_2$-C$\underline{H}_2$CH$_2$SH). ^{13}CNMR (100 MHz, CDCl$_3$). δ 22.1 (CH$_2$'s α to Se, showing triplet satellite peak), 23.67 (CH$_2$'s α to Se, shown triplet satellite peak), 24.4 (CH$_2$'s β to SH), 31.1 (CH$_2$'s β to Se), 34.3 (CH$_2$'s α to SH). IR(pure). 2830-2940 (s, ν-CH), 2540 (ν-SH), 1440(δ-CH) cm^{-1}. MS: 350 (M$^+$). Anal. Calc. for C$_9$H$_{18}$Se$_2$S$_2$: H, 5.71; C, 30.86. Found: H, 5.72; C, 30.92.

16S2Se2 (11). To a suspension of Cs$_2$CO$_3$ (2g, 0.00613 mol) in dry DMF (50 ml) heated to 60 °C was added dropwise dibromopropane (1.15 g, 0.00569 mol) in dry DMF (50 ml) and 1,3-bis(3-mercaptopropylseleno)propane, **30** (2 g, 0.00574 mol) in DMF (50 ml) dropwise. The addition process took about 3 hours. The reaction mixture was stirred at 65-70 °C for 6 days. Then, the solution was concentrated in vacuo, diluted with water (30 ml) and extracted with CH$_2$Cl$_2$ (30 ml × 3). The combined extracts were washed with water (20 ml × 3), dried (Na$_2$SO$_4$) and concentrated in vacuo to yield a thick orange oil. Purification by silica gel flash chromatography (hexane : ethyl acetate, 250 : 1.5, v/v) yielded 1,5-diselena-9,13-dithiacyclohexadecane (500 mg, 22% yield) as white crystals. mp: 53-54 °C. ^{1}H NMR (100 MHz, CDCl$_3$). δ 1.97 (8H, overlapped pentets, J = 6.0 Hz, -SCH$_2$C$\underline{H}_2$CH$_2$S- and -SeCH$_2$C$\underline{H}_2$CH$_2$Se-), 2.87 (8H t, J = 6.0 Hz, -C$\underline{H}_2$SeC$\underline{H}_2$CH$_2$CH$_2$SeC$\underline{H}_2$-). 3.05 (8H, t, J = 6.0 Hz, -C$\underline{H}_2$SC$\underline{H}_2$CH$_2$C$\underline{H}_2$SC$\underline{H}_2$-). ^{13}CNMR (100 MHz, CDCl$_3$), δ 22.7 (CH$_2$'s α to Se), 23.8 (CH$_2$'s α to Se), 29.8 (β-CH$_2$'s), 30.8 (β-CH$_2$'s), 31.8, 32.0 (CH$_2$'s α to S). IR(KBr). 2857, 2928 (s, ν−CH), 1451 (s, δ−CH), 1240, 1042 (ν−SeC or ν−SC) cm^{-1}. MS: 390 (M$^+$). Anal. Calc. for C$_{12}$H$_{24}$Se$_2$S$_2$: C, 36.92; H, 6.20. Found: C 37.05; H 6.27.

Cu(CF$_3$SO$_3$)$_2$[215]. CuO (0.64 g, 8.0 × 10^{-3} mol) was added to HSO$_3$CF$_3$ (2.42 g, 0.016 ml) in H$_2$O (2 ml). A clear blue solution was formed upon heating. The solution

was filtered and boiled to evaporate the water. A white solid, $Cu(SO_3CF_3)_2$ (1.72 g, 62 % yield) was obtained and was dried at 70 °C under vacuum for 20 h.

[Cu(16Se4)](CF$_3$SO$_3$)$_2$[60] (21). To $Cu(CF_3SO_3)_2$ (35 mg, 0.097 mmol) in dry acetone (1 ml) was added 16Se4 (48 mg, 0.099 mmol) in dry acetone (0.5 ml). The mixture was stirred for 5 min at ambient temperature and then cooled to 0 °C with an ice bath. Dry diethyl ether (2 ml) was added to the above dark brown solution to give black crystals. The crystals were collected by decanting the solution and washed with ether. Recrystallization by diethyl ether vapor diffusion into a CH_3NO_2 solution afforded 55 mg (67% yield) of the crystals.

[Cu(12Se4)]CF$_3$SO$_3$ (45). To $Cu(SO_3CF_3)_2$ (20 mg, 0.046 mmol) in dry acetone (0.5 ml) was added 12Se4 (16.7 mg, 0.046 mmol) in CH_2Cl_2 (1 ml). A white precipitate was formed immediately with the addition of the 12Se4 solution. The precipitate (10 mg, 34% yield) was collected by filtration. Anal. Calc. for $CuC_9H_{16}F_3SSe_4O_3$: C, 16.87; H, 2.52; Found: C, 16.90; H, 2.40.

[Cu(16Se4(OH)$_2$)](SO$_3$CF$_3$)$_2$ (39). To $Cu(CF_3SO_3)_2$ (10 mg, 0.028 mmol) in dry CH_3NO_2 (2 ml) was added 16Se4(OH)$_2$ (14.3 mg, 0.028 mmol) in dry CH_2Cl_2 (1 ml). A dark brown solution was formed which was stirred for 5 min at ambient temperature and then cooled to 0 °C with an ice bath. Diffusion of diethyl ether vapor into the brown solution yielded [Cu(16Se4(OH)$_2$)](CF$_3$SO$_3$)$_2$ (12 mg, 49% yield) as dark brown crystals. UV (CH_2Cl_2). $\lambda(\varepsilon)$ 464 nm (11920), 310 nm (2267). Anal. Calc. for $CuC_{14}H_{24}F_6O_8S_2Se_4$: C, 19.16; H, 2.70. Found: C, 19.34; H, 2.63.

[Cu(14Se4)](SO$_3$CF$_3$)$_2$ (44). To $Cu(CF_3SO_3)_2$ (22 mg, 0.061 mmol) in dry acetone solution (0.5 ml) was added 14Se4 (27 mg, 0.059 mmol) in CH_2Cl_2 (0.5 ml) at 0 °C. The mixture was stirred at -20 °C for 1.5 h. After the addition of 2 ml dry Et$_2$O, the solution was kept in a freezer (-25 °C) for 48 h. A brown precipitate (32 mg, 64% yield) was collected by decanting the solvent. UV (CH_2Cl_2). $\lambda(\varepsilon)$ 554 nm (1362), 418 nm (7670).

[Cu(8Se2OH)$_2$][CF$_3$SO$_3$]$_2$ (41). To a solution of 8Se2OH (46 mg, 0.178 mmol) in CH$_3$NO$_2$ (2.5 ml) was added Cu(SO$_3$CF$_3$)$_2$ (33 mg, 0.091 mol) in CH$_3$NO$_2$ (2.5 ml). The reaction mixture was stirred for 10 min at ambient temperature and then was cooled to -10 °C. Dark brown crystals (45 mg, 61% yield) were collected by decanting the mother liquor. UV (CH$_2$Cl$_2$). λ(ε) 571 nm (8116), 386 nm (7905). Anal. Calc. for CuC$_{14}$H$_{24}$F$_6$O$_8$S$_2$Se$_4$: C, 19.16; H, 2.76. Found: C, 19.36; H, 2.66.

[Cu(16Se2S2)](CF$_3$SO$_3$)$_2$ (42). To Cu(CF$_3$SO$_3$)$_2$ (20 mg, 0.056 mmol) in dry acetone (0.5 ml) was added 16Se2S2 (22 mg, 0.056 mmol) in dry acetone (0.5 ml). The mixture was cooled to 0 °C with an ice bath and stirred for 5 min. Vapor diffusion of diethyl ether into the solution resulted in the deposition of dark brown crystals which were collected by decanting the mother liquor and were washed with ether. The crystal for x-ray crystallography was prepared by diffusion of diethyl ether vapor into a nitromethane and dichloromethane (2 : 1, v/v) solution of [Cu(16Se2S2)][CF$_3$SO$_3$]$_2$, at ambient temperature. Dark brown needle crystals (20 mg, 47% yield) were formed. UV (CH$_2$Cl$_2$). λ(ε): 570 nm (900), 456 nm (6870), 280 nm (450). Anal. Calc. for CuC$_{14}$H$_{24}$F$_6$O$_6$S$_4$Se$_2$: C, 22.37; H, 3.20. Found: C, 22.49; H, 3.19.

[Cu(16Se2S2)]CF$_3$SO$_3$ (43). [Cu(16Se2S2)](CF$_3$SO$_3$)$_2$ crystals (15 mg) were dissolved in acetone (0.6 ml) and ether vapor was allowed to diffuse into the solution. White needle crystals were formed in 24 h at ambient temperature. X-ray crystallography showed the white crystal was the complex [Cu(16Se2S2)]CF$_3$SO$_3$. Anal. Calc. for CuC$_{14}$H$_{24}$F$_6$O$_6$S$_4$Se$_2$: C, 25.91; H, 3.99. Found: C, 25.99; H, 4.01.

[Pd(16Se4)](BF$_4$)$_2$[*] (34). To PdCl$_2$ (16.4 mg, 0.092 mmol) in CH$_3$CN/CH$_2$Cl$_2$ (4 ml, 2:1, v/v), NaBF$_4$ (13 mg, 0.12 mmol) was added under N$_2$. The solution was heated, stirred for 10 min and cooled to ambient temperature. 16Se4 (23.8 mg, 0.049 mmol) in CH$_3$CN/CH$_2$Cl$_2$ (2 ml, 2:1, v/v) was added to the above solution and

---

[*] The synthetic method was first developed by J. H. Gu in the group

was stirred for 30 min at ambient temperature. Then, the solution was filtered. Ether vapor diffusion into the yellow filtrate gave yellow crystals (21 mg, 57% yield). UV (CH3CN), $\lambda(\varepsilon)$: 314 (26758), 210 (8409). Anal. Calc. for $PdC_{12}H_{24}Se_4B_2F_8$: C, 18.86; H, 3.16. Found: C, 19.10; H, 3.11.

[Pd(16Se4)Cl]BF$_4$ (35). To $PdCl_2$ (8.7 mg, 0.049 mmol) in CH_3CN/CH_2Cl_2 (2 ml, 2:1, v/v), $NaBF_4$ (13 mg, 0.12 mmol) was added under N_2. The solution was heated, stirred for 5 min and cooled to ambient temperature. 16Se4 (44.8 mg, 0.092 mmol) in CH_3CN/CH_2Cl_2 (2 ml, 2:1, v/v) was added to the solution and the mixture was stirred for 15 min at ambient temperature. Then, the solution was filtered. Ether vapor diffusion into the red filtrate gave red crystals (35 mg, 54% yield). Data for **35**: UV (CH3CN). $\lambda(\varepsilon)$: 314 (19949), 210 (6548). Anal. Cal. for $PdC_{12}H_{24}Se_4ClBF_4$: C, 20.22; H, 3.39. Found: C, 20.28; H, 3.28.

[Pd$_2$24Se6(Cl)$_2$](BF$_4$)$_2$* (36). To $PdCl_2$ (12.7 mg, 0.071 mmol) in CH_3CN/CH_2Cl_2 (2 ml, 2:1, v/v), $NaBF_4$ (20 mg, 0.18 mmol) was added under N_2. The solution was heated, stirred for 5 min and then cooled to ambient temperature. 24Se6 (26.0 mg, 0.035 mmol) in CH_3CN/CH_2Cl_2 (2 ml, 2:1, v/v) was added to the above solution and the mixture was stirred for 5 min at ambient temperature. Then the solution was filtered. Ether vapor diffusion into the yellow filtrate gave yellowish orange crystals (34.8 mg, 82.2% yield). Data for **36**: UV (CH3CN). $\lambda(\varepsilon)$: 366 (4837), 294 (24838), 216 (13145). Anal. Calc. for $Pd_2C_{18}H_{36}Se_6Cl_2B_2F_8$: C, 18.26; H, 3.06. Found: C, 18.12; H, 3.00.

8Se2(SO$_3$CF$_3$)$_2$ (33). To $Cu(CF_3SO_3)_2$ (410 mg, 1.14 mmol) in dry CH_3CN and CH_2Cl_2 (0.5 ml, 2:1 v/v) was added 8Se2 (48 mg, 0.099 mmol) in dry acetone (0.5 ml). After the addition, white crystals were observed in the solution. The mixture was stirred for 5 min at ambient temperature and then cooled to 3 ^oC for overnight. The white crystals were collected by filtration and recrystallized from CH_3CN (234 mg). Data for **33**: mp 167-168 ^oC (decomp.). ^1H NMR (100 MHz, CD$_3$CN): δ: 3.0-3.7 (m, 4H,

SeCH$_2$CH$_2$CH$_2$Se), 3.9-4.3 (m, 8H, SeCH$_2$CH$_2$CH$_2$Se). ^{13}C NMR (100 MHz, CDCl$_3$): δ: 36.1 (SeCH$_2$CH$_2$CH$_2$Se); 52.3 (SeCH$_2$CH$_2$CH$_2$Se). Anal. Calc. for C$_8$H$_{12}$F$_6$S$_2$Se$_2$O$_6$: C, 17.25; H, 2.219. Found: C, 17.53; H, 2.370.

Detection of radical cations

UV-visible spectra of radical cations of selenium coronands were recorded with a Hewlett Packard 89500 UV/VIS Chem Station and HP 8452 Diode Array Spectrophotometer. The temperature was controlled at 25 °C with a thermostat.

An NOBF$_4$ stock solution was prepared with freshly distilled CH$_3$CN in a glove bag filled with N$_2$. Selenium coronand stock solutions were prepared with dried CH$_3$CN in 10-ml volumetric flasks.

For each individual selenium coronand, 3 ml of selenium coronand solution was transferred with a pipette into a quartz uv-cell which was then sealed with a wired septum. N$_2$ was bubbled through the solution for 15 min to drive off the O$_2$. The NOBF$_4$ acetonitrile solution was added to the stirred coronand solution with a 25 µl syringe. When the half of the NOBF$_4$ solution in the syringe was added, the repetitive scanning of the spectrum was started at 4, 60 and 300-second intervals according to the stability of the radical cation.

7.3. Kinetics

The instrument for the kinetic measurements was a Hewlett Packard 89500 UV/VIS Chem Station and HP 8452 Diode Array Spectrophotometer which has kinetics software. Except in variable temperature experiments, the temperature was kept at 25 °C with a thermostat.

In order to avoid the interference of O$_2$, flasks for preparing solutions were flushed with N$_2$ before use, and CH$_2$Cl$_2$ was distilled from P$_2$O$_5$ under N$_2$. The copper (II) complex solutions in uv-cells were sealed with a wired septum and bubbled with N$_2$ for 15

min. The selenium coronand solution was also kept in a vial and sealed with a wired septum.

The reaction was initiated by injecting the coronand solution with a 25 μl syringe into the copper (II) complex solution being stirred in the uv-cell. When half of the 16Se4 solution in the syringe was added to the copper (II) complex solution, the data collection was started and this point was taken as time zero in the data treatment. The spectroscopic scan was over the range of interest; therefore, the absorption intensity variations of the complex and the intermediate with time were followed. The variations of complex absorption maximum and intermediate absorption maximum versus time were recorded with the help of a cursor. Subsequently, the data were substituted into equations (see Chapter 5) for kinetic analyses. Three runs were performed for each concentration of a substrate.

7.4. Electrochemical Experimental

7.4.1. Cyclic Voltammetry

Cyclic voltammograms were recorded on a PAR^{TM} Model 170 Electrochemistry System or a PAR^{TM} Model 173/175 Electrochemistry System, both of which have a build in positive feed back IR compensation. Cyclic voltammetry was carried out with a three-electrode device. The reference electrode was an aqueous saturated calomel electrode (SCE) with a Luggin capillary. The tip of the Luggin capillary was located about 0.5 cm from the working electrode. The working electrode was a platinum plane electrode and the counter electrode was a platinum wire. Before potential scanning, the solution was bubbled with N_2 for 15 min to drive off the O_2. An N_2 flow was kept above the surface of the solution after bubbling to maintain a nitrogen atmosphere. The cyclic voltammograms used for kinetic analysis were obtained from a single scan for every concentration and every scan rate, and the surface of the electrode was cleaned with a tissue after every scan.
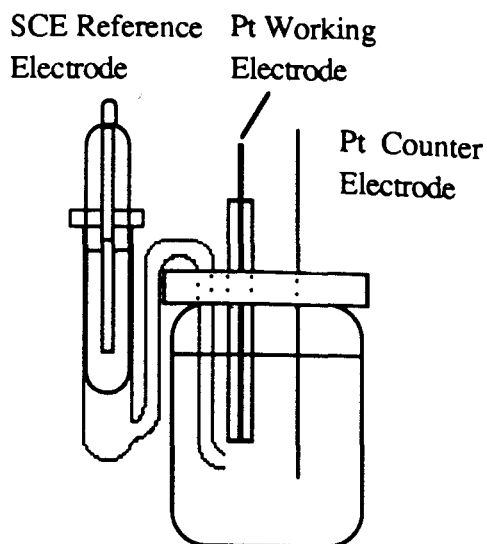
Figure 7.4.1. Experimental set-up for cyclic voltammetry.

7.4.2. Calibration of Reference Electrode for Liquid Junction

In the three-electrode cell, cyclic voltammetric scans were performed on ferrocene $(4.34 \times 10^{-3}$ M) in CH_3CN at different rates. Redox potentials, $E_{1/2}$, of each scan rate were determined vs SCE. The averaged experimental redox potential was 0.369 V. In comparison with the data in the literature, $E_{1/2}$ of ferrocene is 0.307 V[114] vs SCE (in CH_3CN, 0.1 M TEAP); therefore the difference is 0.062 V. Redox potentials determined from cyclic voltammetry in this thesis were corrected by subtracting 0.062 V.

Table 7.4.1 Cyclic Voltammetric Data of Ferrocene

υ (mV/s)	E_{pc}^a (V)	E_{pa}^a (V)	$E_{1/2}^b$ (V)	ΔE_p (V)
10	0.330	0.401	0.366	0.071
20	0.330	0.405	0.369	0.075
50	0.335	0.405	0.370	0.070
100	0.335	0.405	0.370	0.070
200	0.332	0.405	0.369	0.073
500	0.325	0.420	0.372	0.095

a. Versus SCE

b. $E_{1/2} = (E_{pa} + E_{pc})/2$

7.4.3. Electrolysis

The electrolysis was carried out in a two-compartment electrochemical cell. The compartments were partitioned by a sintered glass disk. The working and counter electrodes were Pt gauze electrodes. The reference electrode was an aqueous saturated calomel electrode (SCE) with a Luggin capillary to prevent water from going into the organic solution. TEAP was used as the electrolyte. The solution was purged with the N_2 for 15 min before the electrolysis and the N_2 flow was kept bubbling during electrolysis. The species produced from electrolysis was characterized by uv spectroscopy by withdrawing the electrolyte with a syringe, and transferring into a uv cell. During the electrolysis, the solution was always stirred.

The coulometer was calibrated with ferrocene. Ferrocene in different concentrations (in CH_3CN) was electrolyzed. Tetraethylammonium perchlorate (0.1 M) was used as the electrolyte. The electric charge displayed on the coulometer was compared with the calculation to check if they were consistent. When a concentration of electroactive species was electrolyzed, a parallel experiment, the electrolysis of the blank solution, was performed for as long as the electrolysis of the substrate in low concentration. The electric charge passing through a blank solution was recorded and subtracted from the total electric charge measured from the electrolysis of the substrate to correct for the blank current drifting.

SCE Reference
Electrode

Pt Working
Electrode

Pt Counter
Electrode
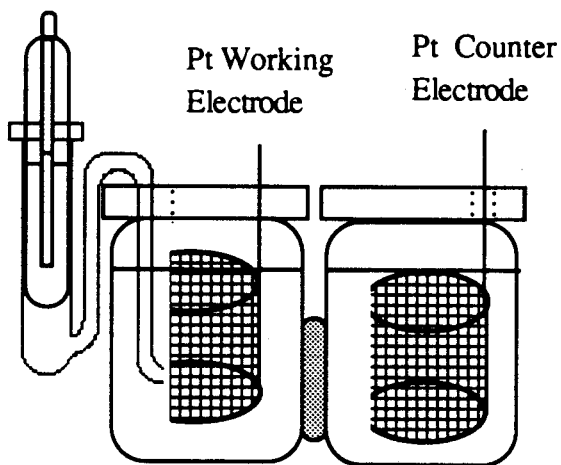
Figure 7.4.2. Experimental set-up for controlled
potential electrolysis.

Table 7.4.2. Data for Electrolysis of Selenium Coronands

Compounds	Solvent ([TEAP])	Applied Potential[b]	Calc. (Coulomb)	Found (Coulomb)
16Se4 (30 mg)	CH$_3$CN (0.1 M)	0.8	5.98[c]	6.0
16Se4 (30 mg)	CH$_3$CN (0.1 M)	2.0	12.0[d]	12
8Se2 (14.7 mg)	CH$_3$CN (0.1 M)	1.0	11[d]	9.7
14Se4 (16 mg)	CH$_3$CN (0.1 M)	1.1	6.8[d]	7.3

Table 7.4.3. Data for Electrolysis of Metal Ion Complexes of Selenium Coronands

Compounds (M)	Solvent ([TEAP])[a]	Applied Potential[b]	Calculation (Coulomb)	Found (Coulomb)	No. of e
[Pd$_2$(24Se6)Cl$_2$]$^{2+}$ (25 mg)	CH$_3$CN (0.1 M)	-0.7	4.5[d]	4.4	2e
[Pd(16Se4)Cl]$^+$ (22.9 mg)	CH$_3$CN (0.1 M)	-0.7	3.1[c]	3.4	1e
Cu(SO$_3$CF$_3$)$_2$ (9.4 mg)	CH$_3$NO$_2$ (0.1 M)	0.0	2.5[c]	2.2	1e
[Cu(16Se4)]$^{2+}$ (10.8 mg)	CH$_2$Cl$_2$ (0.05 M)	0.0	1.2[c]	1.1	1e
[Cu(16S2Se2)]$^{2+}$ (21 mg)	CH$_2$Cl$_2$ (0.05 M)	0.0	2.2[c]	2.1	1e
[Cu(16Se4(OH)$_2$)]$^{2+}$ (6.9 mg)	CH$_3$NO$_2$ (0.1 M)	0.0	0.77[c]	0.81	1e

a. TEAP is tetraethylammonium perchlorate.

b. The potential was referenced to SCE.

c. Calculated by 1e-transfer.

d. Calculated by 2e-transfer.

7.4.4. Cyclic Voltammetry under Electrolysis

Cyclic voltammetry under electrolysis was carried out in the two-compartment cell shown in Figure 6.4.2. Two potentiostats were used: a PAR^{TM} Model 170 Electrochemistry System was used for electrolysis; a PAR^{TM} Model 173/175 Electrochemistry System was used for cyclic voltammetry. The working electrode and counter electrode for electrolysis were both Pt gauze electrodes. In the compartment where the working electrode for electrolysis was placed, another Pt electrode for cyclic voltammetry and a saturated calomel electrode (SCE) were placed.

Two potentials, 1.2 V and 1.8 V were applied separately on the Pt gauze electrodes for the electrolysis of 16Se4 (3.3 mM in CH_3CN). After bubbling N_2 through the solution for 15 min, the potential for electrolysis (1.2 or 1.8 V vs SCE) was applied. The electrolyte was spectroscopically monitored by withdrawing the electrolyte into a uv-cell with a syringe. When the desired absorption maximum became the predominant peak, the cyclic voltammetric scan was started.

7.4.5. Convolutional Analysis

Convolutional analysis was carried out on the Macintosh Plus Computer. The computing program[114] was written in the Microsoft Basic language (Appendix).

Cyclic voltammogram data were digitized manually on a TALOS digitizer that was located at the computing center. The digitized data were saved as MTS files. Then, through the Kermit program, the MTS files were down-loaded and converted to Macintosh files. The format of the data was a column of data pairs, X and Y, which were separated by a space. The data were read and treated by the program.

7.5. Spectroelectrochemistry.

7.5.1. Preparation of an Optically Transparent Pt Film Electrode[216-218]

A quartz plate (4" × 4" × 1/16" CFQT, 20 Suprasil) was purchased from Heraeus Amersil Inc. Platinum powder (99.99%) was purchased from Aldrich.

The quartz plate was boiled in detergent, rinsed, reheated in distilled water and then stored in isopropyl alcohol. The cleaned quartz plate was held on an aluminum plate holder that had filaments underneath to heat the quartz plate, because Pt deposits better on a hot surface[218] Then the holder was placed in a vacuum bell jar (CHA Industries SE-600-RAP Vacuum Evaporator, which was housed in Department of Physics); the quartz plate was facing down towards to the tungsten evaporation filament. This prevented molten metal droplets from falling on the quartz plate. The tungsten evaporation filament was a 1 × 8 cm tungsten plate with a dent in it for holding the Pt powder. The distance between the quartz plate and the Pt powder was approximately 10 cm. Pt was evaporated at a rate of 100 Å/min for 3-5 min at a vacuum of 2×10^{-5} torr. A thin Pt film was formed on the quartz plate. The Pt film was annealed in a muffle furnace at 550 °C for 2 h. Then the electrode was made by cutting the quartz plate into 9 × 30 mm pieces, so that they could be placed in a uv cuvette. Figure 6.5.1 shows the uv-visible spectrum of the optically transparent Pt electrode, which had a broad window for uv-visible light (200-800 nm, absorbance = 0.5) after annealing.

7.5.2. Preparation of AgI/Ag Reference Electrode

In a crucible, AgI (Aldrich) was heated to melt with a tirrill burner. A thin silver plate was dipped into the melted AgI so that a thin film of AgI was coated on the Ag plate.

7.5.3. *Spectroelectrochemistry*

The potentiostat was a PAR^{TM} Model 170 Electrochemistry System or a PAR^{TM} Model 173/175 Electrochemistry System, both of which have a built in positive feed back iR compensation, or a Pine RDE4 bipotentiostat. The spectrophotometer was a Hewlett Packard 89500 UV/VIS Chem Station and a HP 8425 Diode Array Spectrophotometer.

The electrolysis was carried out in a uv cuvette. The electrode was a thin Pt wire curled into a web shape or an optically transparent platinum electrode. The reference electrode was a thin Ag plate coated with a thin layer of AgI. The counter electrode was a platinum wire kept in a glass tube which had a sintered end to prevent the species that is generated on the counter electrode from interfering with the observation of the species produced on the working electrode.

Before the potential was applied to the electrodes, the solution was bubbled with N_2 for 15 min to drive off the O_2 then an N_2 flow was kept, maintaining a blanket of N_2 above the surface of the solution. The uv-visible spectroscopic scan was started as soon as the potential that was determined by cyclic voltammetry of the particular compound was applied to the electrodes. The uv-visible spectroscopic scan was repetitive.
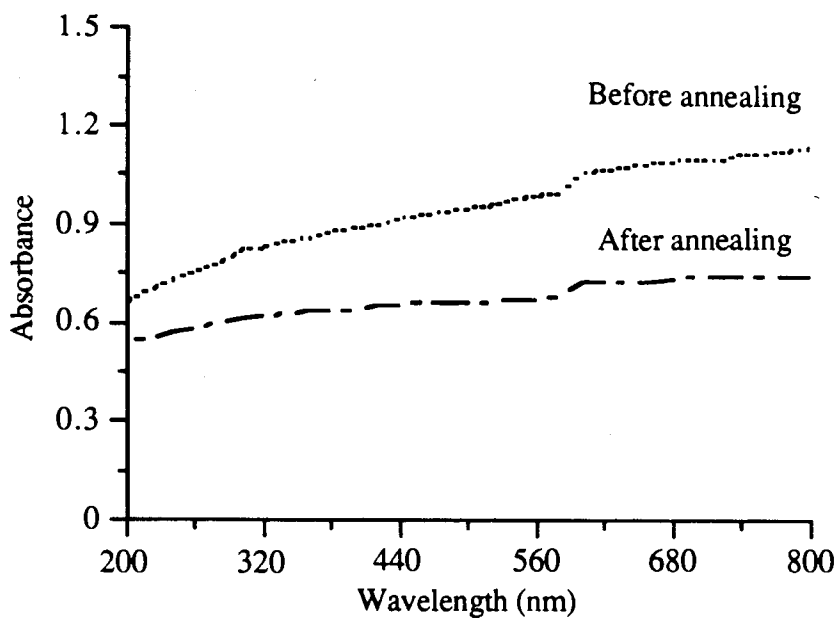
Figure 7.5.1. UV-visible spectrum of an optically transparent Pt electrode.
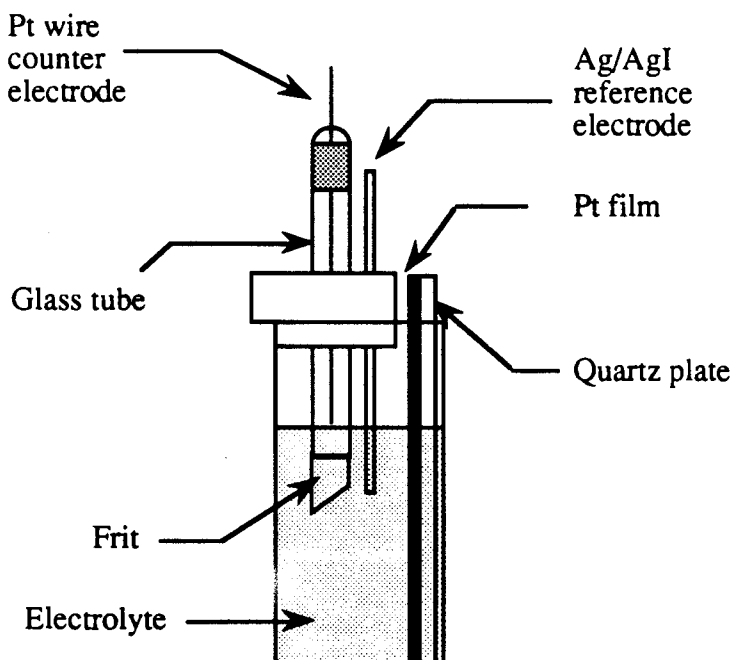
Figure 7.5.2. Experimental setup for spectroelectrochemistry.

Table 7.5.1. Spectroelectrochemistry Data

Compounds	Conc. (M)	Solvent	Potential[a] (Volt)	Observation λ_{max} (nm)
16Se4	1.02×10^{-3}	CH_3CN	1.0	320, 256
	1.02×10^{-4}	(0.1 M TEAP)		256
14Se4	9.87×10^{-4}	CH_3CN	1.2	258
	9.87×10^{-5}	(0.1 M TEAP)		258
8Se2	1.86×10^{-3}	CH_3CN	0.8	428, 250
	1.86×10^{-4}	(0.1 M TEAP)		250
[Cu(16Se4)][SO$_3$CF$_3$]$_2$	1.28×10^{-4}	CH_2Cl_2 (0.05 M TEAP)	0.0	466[b]

a. Potentials are referenced to a Ag thin plate coated with AgI.

b. The peak was decreasing with time.

APPENDIX

A.1. Program for Convolutive Transformation of CV Data

Equation A-1 is the expression for the convolutive transformation. The numerical algorithm[114] for A-1 is given in A-2 and it corresponds to the bracketed term in A-1. The following is the program for carrying out the convolutive transformation of cyclic voltammetric data based on Equation A-2.

$$C_O(0,t) = C_O^* - \frac{1}{nFAD_O^{1/2}} \left[\frac{1}{\pi^{1/2}} \int_0^t \frac{i(u)}{(t-u)^{1/2}} du \right] \qquad \textbf{(A-1)}$$

$$I(k\Delta t) = \frac{1}{\pi^{\frac{1}{2}}} \sum_{j=1}^{j=k} \frac{\Gamma(k-j+\frac{1}{2})}{(k-j)!} \Delta t^{\frac{1}{2}} i(j\Delta t) \qquad \textbf{(A-2)}$$

Variables in the program (on the right of the equations) are explained as follows,

$I(k\Delta t) = I(k)$ Transformed current response

$\Gamma(k-j+1/2) = F1(N-K)$ Γ function, where $\Gamma(1/2) = \pi^{1/2}$, $\Gamma(3/2) = 1/2\pi^{1/2}$, $\Gamma(5/2) = 3/21/2\pi^{1/2}$, etc.

$(k-j)! = E(N-K)$ A factorial

$i(j\Delta t) = J(K)$ Cyclic voltammetric data

$\Delta \tau = \Delta T$ Time

When the program is activated, the computer will prompt with the question "DATAFILE NAME ?". A name corresponding to the data file name should be entered. Then the computer will demand a scan rate and scan range. Enter these parameters. The computer will do the calculation and save the data to a file with the name designated by the operator. The output files are used for plotting.

```
REM THIS PROGRAM IS FOR SEMI-INTEGRAL METHOD
REM THE DATA IS FROM THE DATA FILE
REM ********************************************************
REM **  C = THE CONCENTRATION OF THE ELECTROACTIVE
SPECIES
REM **  n = THE NUMBER INVOLVED IN HETEROELECTRON
TRANSFER
REM **  F = 964509 FARADAI CONSTANT        **
REM **  D = THE DIFFUSION COEFFICIENT       **
REM **  A = THE AREA OF THE ELECTRODE       **
REM **  v = THE SCAN RATE,VOLT=THE SCAN RANGE, ..**
REM **  N=THE NUMBER OF THE DIVISIONS       **
REM **  DT=THE UNIT OF EACH DIVISION        **
REM **  I(k),I1(K) ARE TRANSFORMED CURRENTS   **
REM **  FOR FORWARD AND BACKWARD       **
REM **  T(M) = the experimental value of volt    **
REM **  J(500),J1(500) ARE EXPERIMENTAL CURRENTS  **
REM **  F1(K) AND F(k), E(k) for calculation    **
REM **  J(k),T(K) FOR INPUT; G(k),P(k) FOR out put.  **
REM ******************************************************
DEFDBL Z, E,F,I 'those variables are defined as double
precision=DEFDBL
DIM I1(500), I(500),t(500),F(500), E(500) 'define the size of arrays
DIM J(500),J1(500),CURRENT(500), P(500),F1(500) 'define the size of
arrays
SETDATA:
```

```
F(1)=0

E(0)=1

Z=1

I(K)=0

INPUT"DATAFILE NAME: data#";D$ 'this is to let the program know the
name of the data file

INPUT"THE SCAN RATE IN V/s";V      'enter the scan rate

INPUT"THE SCAN RANGE IN V";VOLT 'enter the scan range in volt

INPUT"P(0)=";P(0) 'enter the initial potential

OPEN "I",1,D$ 'OPEN DATA  FILE

PRINT "contents of file :"

PRINT

M=0

READDATA:

5 IF EOF(1) <0 THEN 10 'to determine the end of the data

INPUT#1, t(M),J(M) 'read data from a file

PRINT "M"M,t(M),J(M) 'print the  data from data file

M=M+1 'to determine how many pairs of data

GOTO 5 'repeat the reading

10 CLOSE 1 'after all the data read the file closed

N=M/2 'calculation of the number of divisions in the scan range

DT=VOLT/(N*V)' to calculate the the smallest unit of a division

F1(0)=3.1415926#^.5

F1(1)=F1(0)*.5

PRINT M

REM ********************************************************
```

REM IN THIS SECTION IS TO CREATE A DATA FILE AFTER READING

THE DATA

REM WHEN THE DATA IS ENTERED BY KEYBOARD IN ORDER TO

AVOID REPEAT KEY IN THE DATA. USUALLY NOT NECESSARY.

'INPUT"the Name of the datafile";D$

'OPEN "O",1,D$

Again:

'FOR I=0 TO M

'PRINT#1, T(I),J(I)

'NEXT I

'GOTO Again

STEP3:

'CLOSE 1

REM **

PRINT "DT   N" 'print the results

PRINT DT,N   'print the results

GOSUB 100   'go to the subroutine for calculation of gama function

GOSUB 200 'go to the subroutine for calculation of factorial

REM **

REM THIS SECTION IS TO CALCULATION OF THE ALGORITHM OF

THE SEMI-INTEGRAL

FOR K=1 TO M 'N-1

FOR L=1 TO K

J1(L)=J(N+L+1)

I(K)=I(K)+F1(K-L)*DT^.5*J(L)/E(K-L)

PRINT "*********"

PRINT "K-L"K-L,"J(L)"J(L)

```
PRINT "********"

NEXT L

CURRENT(K)=.56419*I(K)' EQUAL TO I(t) or m(t) in the literature

PRINT "CURRENT",CURRENT(K)

NEXT K

REM ****************************************************

'OUTPUT:

INPUT"FILENAME FOR OUTPUT";D$'to let the program know the name

of the output file

OPEN "O",1,D$'open the file

'OPEN "O",1,"CLIP:"'for output to clipboard

PRINT t(0),I(0)

FOR I=0 TO M

PRINT t(I),CURRENT(I)'print out the results

PRINT#1, t(I),CURRENT(I)'write into a data file

NEXT I

CLOSE 1

END

Subroutines:

'THIS SUBROUTINE IS FOR GAMA FUNCTION

100   FOR J=2 TO M

Q=J-.5

F1(J)=F1(J-1)*Q

NEXT J

RETURN

REM

REM FOLLOWING SUBROUTINE IS FOR CALCULATION OF THE
```

```
REM  FACTORIAL
REM  IN THE EQUATION
200   FOR J=1 TO M
Z=Z*J
E(J)= Z
NEXT J
RETURN
```

A.2.   *Plots of Kinetics*

The following figures are the plots using all the experimental data of kinetics under the conditions listed in Table 2.   They show that the redox reaction is a simple 2nd order reaction when up to 62% of $[Cu(16Se4)][SO_3CF_3]_2$ (22) has been consumed.
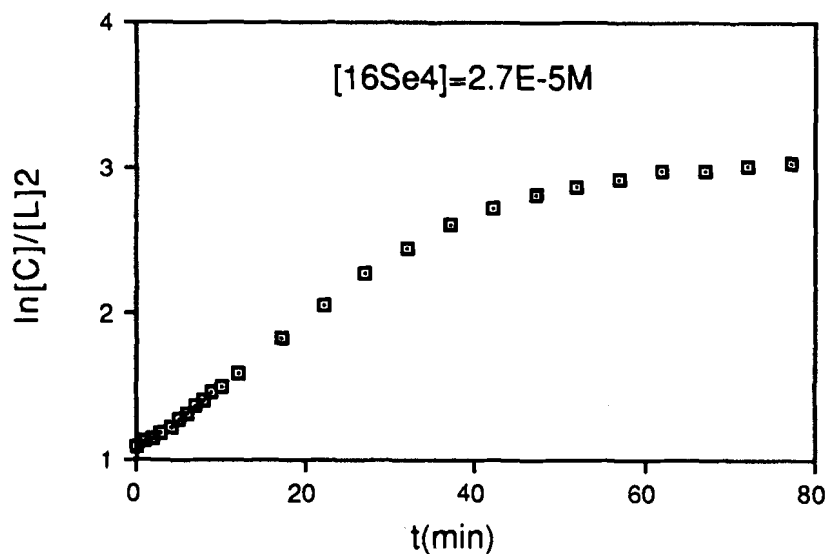

Figure 1. $[Cu(II)16Se4]$ = 7.8E-5 M, $[16Se4]$ = 2.7E-5M.

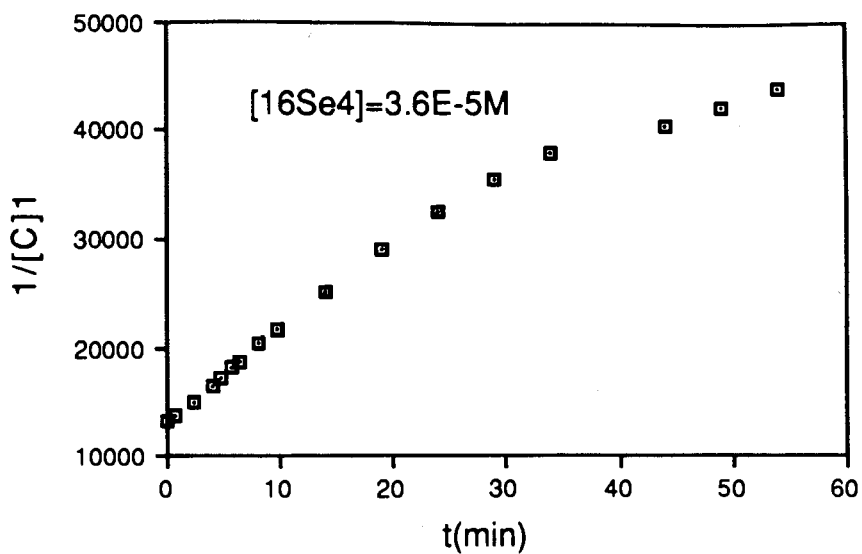**Figure 2.**   [Cu(II)16Se4] = 7.8E-5 M, [16Se4] = 3.6E-5M.

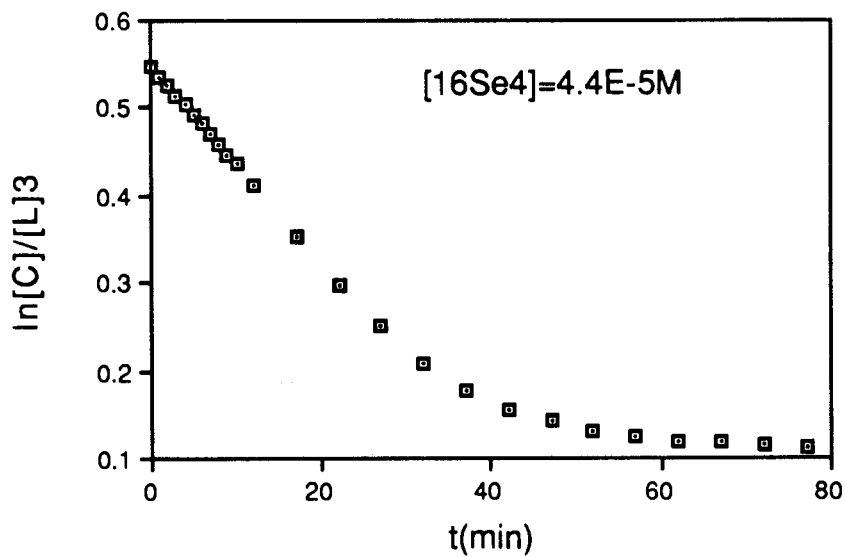**Figure 3.**   [Cu(II)16Se4] = 7.8E-5 M, [16Se4] = 4.4E-5M.

REFERENCES

(1) Blake, A. J.; Schröder, M. In *Advances in Inorganic Chemistry*; A. G. Sykes, Ed.; Academic: New York, 1990; Vol. 35; pp 2-80.

(2) Cooper, S. R.; Rawle, S. C. *Struct. Bonding (Berlin)* **1990**, *72*, 1-72.

(3) Rorabacher, D. B.; Bernardo, A. M.; Vande Linde, A. M. Q.; Leggett, G. H.; Westerby, B. C.; Martin, M. J.; Ochrymowycz, L. A. *Pure & Appl. Chem.* **1988**, *60*, 501-508.

(4) Solomon, E. I.; Pendield, K. W.; Wilcox, D. E. *Struct. Bonding (Berlin)* **1983**, *53*, 1-57.

(5) McCormick, D. B.; Griesser, R.; Sigel, H. *Met. Ions Biol. Syst.* **1973**, *1*, 213.

(6) Collman, P. M.; Freeman, H. C.; Guss, J. M.; Murata, V. A.; Norris, V. A.; Ramshaw, J. A. M.; Venkatappa, M. P. *Nature* **1978**, *272*, 319-324.

(7) Rorabacher, D. B. In *Copper Coordination Chemistry: Biochemical and Inorganic Perspectives*; K. D. Karlin and J. Zubieta, Ed.; Adenine: New York, 1983; pp 167-202.

(8) William, E. B.; Anderson, B. F.; Lewandoski, D. A.; Norris, G. E.; Baker, E. N. *J. Am. Chem. Soc.* **1990**, *112*, 1817-1819.

(9) Vallee, B. L.; Williams, R. J. P. *Proc. Natl. Acad. Sci., U.S.A.* **1968**, *59*, 498-505.

(10) Williams, R. J. P. *Inorg. Chim. Acta Rev.* **1971**, *5*, 137-155.

(11) Patterson, G. S.; Holm, R. H. *Bioinorg. Chem.* **1975**, *4*, 257-275.

(12) Rorabacher, D. B.; Jones, T. E.; Ochrymowycz, L. A. *J. Am. Chem. Soc.* **1975**, *97*, 7485-7486.

(13) Abel, E. W.; Bhargava, S. K.; Kite, K.; Orrell, K. G.; Sik, V.; Williams, B. L. *Polyhedron* **1982**, *1*, 289.

(14) Rorabacher, D. B.; Meagher, N. E.; Juntunene, K. L.; Robandt, P. V.; Leggett, G. H.; Salhi, C. A.; Dunn, B. C.; Schroeder, R. R.; Ochrymowycz, L. A. *Pure & Appl. Chem.* **1993**, *65*, 573-578.

(15) Rorabacher, D. B.; Martin, M. J.; Endicott, J. F.; Ochrymowycz, L. A. *Inorg. Chem.* **1987**, *26*, 3012-3022.

(16) Addison, A. W.; Carpenter, M.; Lau, L. K.-M.; Wicholas, M. *Inorg. Chem.* **1978**, *17*, 1545-1552.

(17) Addison, A. W.; Rao, T. N.; Sinn, E. *Inorg. Chem.* **1984**, *23*, 1957-1967.

(18) Schröder, M. *Pure & Appl. Chem.* **1988**, *60*, 517-527.

(19) Cooper, S. R. *Acc. Chem. Res.* **1988**, *21*, 141-146.

(20) Cooper, S. R.; Rawle, S. C.; Yagbasan, R.; Watkin, D. J. *J. Am. Chem. Soc.* **1991**, *113*, 1600-1604.

(21) Schriver, G. W.; Thomas, T. A. *J. Am. Chem. Soc.* **1987**, *109*, 4121-4123.

(22) Blake, A. J.; Halcrow, M. A.; Schröder, M. *J. Chem. Soc., Dalton Trans.* **1992**, 2803-2808.

(23) Blake, A. J.; Reid, G.; Schröder, M. *J. Chem. Soc., Dalton Trans.* **1990**, 3363-3373.

(24) Blake, A. J.; Reid, G.; Schröder, M. *J. Chem. Soc., Dalton Trans.* **1989**, 1675-1680.

(25) Schröder, M.; Blake, A. J.; Gould, R. O.; Lavery, A. J. *Angew. Chem. Int. Ed. Engl.* **1986**, *25*, 274-275.

(26) Schröder, M.; Atkinson, N.; Blake, A. J.; Drew, M. G. B.; Forsyth, G.; Lavery, A. J.; Reid, G. *J. Chem. Soc., Chem. Commun.* **1989**, 984-986.

(27) Schröder, M.; Blake, A. J.; Gould, R. O.; Holder, A. J.; Hyde, T. I. *Polyhedron* **1989**, *8*, 513-518.

(28) Schröder, M.; Blake, A. J.; Gould, R. O.; Greig, J. A.; Holder, A. J.; Hyde, T. I. *J. Chem. Soc., Chem. Commun.* **1989**, 876-878.

(29) Schröder, M.; Reid, G.; Blake, A. J.; Hyde, T. I. *J. Chem. Soc., Chem. Commun.* **1988**, 1397-1399.

(30) Cooper, S. R.; Hartman, J. R. *J. Am. Chem. Soc.* **1986**, *108*, 1202-1208.

(31) Cooper, S. R.; Rawle, S. C.; Hartman, J. R.; Hintsa, E. J.; Admans, G. A. *Inorg. Chem.* **1988**, *27*, 1209-1214.

(32) Cooper, S. R.; Watkin, D. J.; Hartman, J. R.; Rawle, S. C. *J. Chem. Soc., Chem. Commun.* **1986**, 1083-1084.

(33) Rorabacher, D. B.; Pett, V. B.; Diaddario, Jr., L. L.; Dockal, E. R.; Corfield, P. W.; Glick, M. D.; Ceccarelli, C.; Ochrymowycz, L. A. *Inorg. Chem.* **1983**, *22*, 3661-3670.

(34) Rorabacher, D. B.; Leggett, G. H.; Cooper, T. H.; Reed, P. R.; Situmeang, D.; Ochrymowycz, L. A. *Inorg. Chem.* **1988**, *27*, 2164-2169.

(35) Rorabacher, D. B.; Corfield, P. W. R.; Ceccarelli, C.; Glick, M. D.; Moy, I. W.-Y.; Ochrymowycz, L. A. *J. Am. Chem. Soc.* **1985**, *107*, 2399-2404.

(36) Cooper, S. R.; Wolf, J., R. E.; Hartman, J. R.; Storey, J. M. E.; Foxman, B. M. *J. Am. Chem. Soc.* **1987**, *109*, 4328-4335.

(37) Cooper, S. R.; Hartman, J. R.; Wolf, R. E.; Foxman, B. M. *J. Am. Chem. Soc.* **1983**, *105*, 131-132.

(38) Rorabacher, D. B.; Bernardom, M. M.; Heeg, M. J.; Schroeder, R. R.; Ochrymowycz, L. A. *Inorg. Chem.* **1992**, *31*, 191-198.

(39) Cooper, S. R.; Hartman, J. R.; Hintsa, E. J. *J. Am. Chem. Soc.* **1986**, *108*, 1208-1214.

(40) Weissflog, V. E. Z. *Anorg. Allg. Chem.* **1982**, *60*, 488.

(41) Hojjatie, M.; Muralidharan, M.; Freiser, H. *Tetrahedeon* **1989**, *45*, 1611-1622.

(42) Mitchell, R. H. *Can. J. Chem.* **1980**, *58*, 1398-1406.

(43) Mitchell, R. H.; Weerawarna, K. S. *Tetrahedron Lett.* **1988**, *29*, 5587-5588.

(44) Higuchi, H.; Misumi, S. *Tetrahedron Lett.* **1982**, *23*, 5571-5574.

(45) Mitchell, R. H.; Weerawarna, K. S.; Bushnell, G. W. *Tetrahedron Lett.* **1987**, *28*, 5119-5120.

(46) Higuchi, H.; Tani, K.; Sakata, Y.; Misumi, S. *Bull. Chem. Soc. Jpn.* **1987**, *60*, 4027-4036.

(47) Vogel, E.; Röhrig, P.; Sicken, M.; Knipp, B.; Herrmann, A.; Pohl, M.; Schmickler, H.; Lex, J. *Angerw. Chem. Int. Ed. Engl.* **1989**, *28*, 1651-1655.

(48) Ulman, A.; Manassen, J.; Frolow, F.; Rabinovich, D. *Tetrahedron Lett.* **1978**, 167-170.

(49) Kumagai, T.; Akabori, S. *Chem. Lett.* **1989**, 1667-1670.

(50) McDaniel, C. W.; Bradshaw, J. S.; Tarbetb, K. H.; Lindh, B. C.; Izatt, R. M. *J. Inclusion Phenom. Mol. Recognit. Chem.* **1989**, *7*, 545-548.

(51) Mazouz, A.; Bodiguel, J.; Meunier, P.; Gautheron, B. *Phosphorus, Sulfur, Silicon Relat. Elem.* **1991**, *61*, 247-249.

(52) Xu, H.; Li, W.; Liu, X. *Youji Huaxue* **1993**, *13*, 52-7.

(53) Pedersen, C. J. In *Synthesis Multidentate Macrocyclic Compounds*; R. M. Izatt, Ed.; Academic: New York, 1978; pp 1.

(54) Lehn, J.-M. *Acc. Chem. Res.* **1978**, *11*, 49-57.

(55) Vögtle, F.; Webber, E. In *Host Guest Complex Chemistry Macrocycles Synthesis, Structures, Applications*; F. Vögtle and E. Webber, Ed.; Springer-Verlag: Berlin, 1985; pp 3-41.

(56) Lindoy, L. F. *The Chemistry of Macrocyclic Ligand Complexes*; Cambridge University: Cambridge, 1989.

(57) Melson, G. A. In *Coordination Chemistry of Macrocyclic Compounds*; G. A. Melson, Ed.; Plenum: New York, 1979; pp 2.

(58) Murray, S. G.; Hartley, F. R. *Chem. Rev.* **1981**, *81*, 365-414.

(59) Hope, E. G.; Levason, W. *Coord. Chem. Rev.* **1993**, *122*, 109-170.

(60) Batchelor, R. J.; Einstein, F. W. B.; Gay, I. D.; Gu, J. H.; Pinto, B. M.; Zhou, X.-M. *J. Am Chem. Soc.* **1990**, *112*, 3706-3707.

(61) Batchelor, R. J.; Einstein, F. W. B.; Gay, I. D.; Gu, J.-H.; Pinto, B. M. *J. Organomet. Chem.* **1991**, *411*, 147-157.

(62) Levason, W.; Gulliver, D. J.; Murray, S. G.; Marshall, G. L. *J. Chem. Soc., Dalton Trans.* **1985**, 1265-1269.

(63) Levason, W.; Gulliver, D. J.; Hope, E. G.; Murray, S. G.; Potter, D. M.; Marshall, G. L. *J. Chem. Soc., Perkin Trans. 2* **1984**, 429-434.

(64) Levason, W.; Hope, E. G.; Murray, S. G.; Webster, M. *J. Chem. Soc., Dalton Trans.* **1986**, 1003-1009.

(65) Pearson, R. G. *J. Am. Chem. Soc.* **1963**, *85*, 3533-3539.

(66) Porterfield, W. W. *Inorganic Chemistry A Unified Approach*; Addison-Wesley: Reading, Massachusetts, 1989.

(67) Duffy, J. A. *Bonding, Energy Levels and Bands in Inorganic Solids*; Longman Scientific & Technical: Harlow, Essex, 1990, pp 80.

(68) Parr, R. G.; Donnelly, R. A.; Levy, M.; Palke, W. E. *J. Chem. Phys.* **1978**, 3801-3807.

(69) Parr, R. G.; Bartolotti, J. *J. Am. Chem. Soc.* **1982**, *104*, 3801-3803.

(70) Parr, R. G.; Pearson, R. G. *J. Am. Chem. Soc.* **1983**, *105*, 7512-7516.

(71) Pearson, R. G. *J. Chem. Educ.* **1987**, 561-567.

(72) Orrell, K. G. *Coord. Chem. Rev.* **1989**, *96*, 1-48.

(73) Günther, W. H. H. In *Organic Selenium Compounds: Their Chemistry and Biology*; D. L. Klayman and W. H. H. Günther, Ed.; John Wiley & Sons: New York, 1973; pp 1-12.

(74) Luthra, N. P.; Odom, J. D. In *The Chemistry of Organic Selenium and Tellurium Compounds*; S. Patai and Z. Rapporort, Ed.; Jogn Wiley & Sons: New York, 1986; Vol. 1.

(75) Batchelor, R. J.; Einstein, F. W. B.; Gay, I. D.; Gu, J. H.; Johnston, B. D.; Pinto, B. M. *J. Am Chem. Soc.* **1989**, *111*, 6582-6591.

(76) DeSimone, R. E.; Glick, M. D. *J. Am. Chem. Soc.* **1975**, *97*, 942-943.

(77) DeSimone, R. E.; Glick, B. D. *J. Am. Chem. Soc.* **1976**, *98*, 762-767.

(78) Abel, E. W.; Bhargava, S. K.; Orrell, K. G. In *Progress in Inorganic Chemistry*; S. J. Lippard, Ed.; John Wiley & Sons: New York, 1984; Vol. 32; pp 1-118.

(79) Frieden, E. *J. Chem. Educ.* **1985**, *62*, 917-923.

(80) Rorabacher, D. B.; Zimmer, L. L.; Jones, T. E.; Sokol, L. S. W. L.; Bernardo, A. M.; Yee, E. L.; Ochrymowycz, L. A. *J. Am. Chem. Soc.* **1979**, *101*, 3511-3520.

(81) Musker, W. K.; Olmstead, M. M.; Kessler, R. M. *Inorg. Chem.* **1984**, *23*, 1764-1768.

(82) Kellogg, R. M.; Buter, J.; Bolhuis, F. V. *J. Chem. Soc., Chem. Commun.* **1990**, 282-284.

(83) Kimura, E.; Kurogi, Y.; Tojo, T.; Shionoya, M.; Shiro, M. *J. Am. Chem. Soc.* **1991**, *113*, 4857-4864.

(84) Nabeshima, T.; Nishijima, K.; Tsukada, N.; Furusawa, H.; Hosoya, T.; Yano, Y. *J. Chem. Soc., Chem. Commun.* **1992**, 1092-1094.

(85) Loeb, S. J.; Groot, B. D.; Jenkins, H. A. *Inorg. Chem.* **1992**, *31*, 203-208.

(86) Musker, W. K.; Roush, P. B. *J. Am. Chem. Soc.* **1976**, *98*, 6745-6746.

(87) Musker, W. K.; Wolford, T. L. *J. Am. Chem. Soc.* **1976**, *98*, 3055-3056.

(88) Asmus, K.-D. *Acc. Chem. Res.* **1979**, *12*, 436-442.

(89) Williams, F.; Nishikida, K. *Chem. Phys. Lett.* **1975**, *34*, 302-306.

(90) Furukawa, N.; Fujihara, H.; Akaishi, R.; Erata, T. *J. Chem. Soc., Chem. Comm.* **1989**, 1789-1790.

(91) Furukawa, N.; Fujihara, H.; Erata, T.; Akaishi, R. *J. Chem. Soc., Chem. Commun.* **1989**, 1789-1790.

(92)   Furukawa, N.; Fujihara, H.; Mima, H.; Chiu, J.-J. *Tetrahedron Lett.* **1990**, *31*, 2307-2310.

(93)   Furukawa, N.; Fujihara, H.; Akaishi, R. *Chem. Lett.* **1990**, 549-550.

(94)   Sandman, D. J.; Allen, G. W.; Acampora, L. A.; Stark, J. C.; Jansen, S.; Jones, M. T.; Ashwell, G. J.; Forman, B. M. *Inorg. Chem.* **1987**, *26*, 1664-1669.

(95)   Lindgren, B. *Acta Chem. Scand., Ser. B* **1977**, *31*, 1-6.

(96)   Lindgren, B. *Tetrahedron Lett.* **1974**, 4347-4350.

(97)   Lindgren, B. *Acta Chem. Scand., Ser. B* **1976**, *30*, 941-947.

(98)   Ochrymowycz, L. A.; Mak, C.; Michna, J. D. *J. Org. Chem.* **1974**, *39*, 2079-2084.

(99)   VandenHoven, E.; Cordova, E. I.; Mohammed, A.; Pinto, B. M., in preparation.

(100) Clarembeau, M.; Cravador, A.; Dumont, W.; Hevesi, L.; Krief, A.; Lucchetti, J.; Van Ende, D. *Tetrahedron* **1985**, *41*, 4793.

(101) Pinto, B. M.; Johnston, B. D.; Nagelkerke, R. *Heterocycles* **1989**, *28*, 389.

(102) Günther, H. H.; Mautner, H. G. *J. Med. Chem.* **1964**, *7*, 229.

(103) Silverstein, R. M.; Bassler, G. C.; Morrill, T. C. *Spectrometric Identification of Organic Compounds*; John Wiley & Sons: New York, 1981.

(104) Musker, W. K.; Olmstead, M. M.; Kessler, R. M. *Acta Crystallogr., Sect C* **1984**, *40*, 1172-1175.

(105) Dalley, N. K.; Jiang, W.; Olsher, U. *J. Inclusion Phenom. Mol. Recognit. Chem.* **1992**, *12*, 305-312.

(106) Durrant, M. C.; Richards, R. L.; Firth, S. *J. Chem. Soc., Perkin Trans. 2* **1993**, 445-450.

(107) Rawle, S. C.; Admans, G. A.; Cooper, S. R. *J. Chem. Soc., Dalton Trans.* **1988**, 93-96.

(108) Holdcroft, S.; Pinto, B. M.; Hu, H.; Reyes, I. C. In *76th Canadian Society for Chemistry Conference and Exhibition*; Sherbrooke (Quebec), Centre des congres, 1993; pp 301.

(109) Harris, R. K. *Nuclear Magnetic Resonance Spectroscopy A Physicochemical View*; Longman Scientific & Technical: Burnt Mill, 1986.

(110) Dixon, W. T. *J. Chem. Phys.* **1982**, *77*, 1800-1809.

(111) Lardon, M. A. In *Organic Selenium Compounds: Their Chemistry and Biology*; D. L. Klayman and W. H. H. Günther, Ed.; John Wiley & Sons: New York, 1973; pp 933-939.

(112) Furukawa, N.; Fujihara, H.; Akaishi, R.; Iwasaki, F.; Toyoda, M. *Bull. Chem. Soc. Jpn.* **1988**, *61*, 2563-2567.

(113) Iwasaki, F.; Morimoto, M.; Yasui, M.; Akaishi, R.; Fujihara, H.; Furukawa, N. *Acta Crystallogr., Sect. C* **1991**, *47*, 1463-1466.

(114) Bard, A. J.; Faulkner, L. R. *Electrochemical Methods: Fundamentals and Applications*; John Wiley & Sons: New York, 1980.

(115) Maloy, J. T. *J. Chem. Educ.* **1983**, *60*, 285-289.

(116) Kissinger, P. T.; Heiniman, W. R. *J. Chem. Educ.* **1983**, *60*, 702-706.

(117) Greef, R.; Peat, R.; Peter, L. M.; Pletcher, D.; Robinson, J. *Instrumental Methods in Electrochemistry*; Southampton Electrochemistry Group/Ellis Horwood: West Sussex, England, 1985.

(118) Nadjo, L.; Saveant, J. M.; Tessier, D. *J. Electroanal. Chem.* **1974**, *52*, 403.

(119) Imbeaux, J. C.; Saveant, J. M. *J. Electroanal. Chem.* **1973**, *44*, 169-187.

(120) Saveant, J. M.; Tessier, D. *J. Electroanal. Chem.* **1975**, *65*, 57-66.

(121) Oldham, K. B. *Anal. Chem.* **1972**, *44*, 196-198.

(122) Oldham, K. B.; Grenness, M. *Anal. Chem.* **1972**, *44*, 1121-1129.

(123) Evans, D. H.; Whitson, P. E.; VandenBorn, H. W. *Anal. Chem.* **1973**, *45*, 1298-1306.

(124) Wilson, G. S.; Swanson, D. D.; Ryan, M. D.; Glass, R. S. *J. Phys. Chem.* **1981**, *85*, 1069-1075.

(125) Musker, W. K.; Surdhar, P. S.; Ahmad, R.; Armstrong, D. A. *Can. J. Chem.* **1984**, *62*, 1874-1875.

(126) Nicholson, R. S.; Shain, I. *Anal. Chem.* **1964**, *36*, 706-723.

(127) Asmus, K.-D; Bahnemann, D.; Fischer, C.; Veltwisch, D. *J. Am. Chem. Soc.* **1979**, *101*, 5322-5329.

(128) Bally, T. In *Radical Ionic Systems-Properties in Condensed Phases*; A. Lund and M. Shiotani, Ed.; Kluwer Academic: Dodrecht, 1991.

(129) Norman, R. O. C.; Gilbert, B. C.; Hodgeman, D. K. C. *J. Chem. Soc., Perkin Trans. 2* **1973**, 1748-1752.

(130) Asmus, K.-D.; Bonifacic, M.; Mockel, H. *J. Chem. Soc., Perkin Trans. 2* **1975**, 675-685.

(131) Asmus, K.-D.; Gills, H. A.; Teather, G. G. *J. Phys. Chem.* **1978**, *82*, 2677-2682.

(132) Asmus, K.-D.; Göbl, M.; Bonifacic, M. *J. Am. Chem. Soc.* **1984**, *106*, 5984-5988.

(133) Asmus, K.-D.; Bonifacic, M. *J. Org. Chem.* **1986**, *51*, 1216-1222.

(134) Asmus, K.-D.; Drewello, T.; Lebrilla, C. B.; Schwarz, H. *Angew. Chem. Int. Ed. Engl.* **1989**, *28*, 1275-1276.

(135) Nelsen, S. F.; Alder, R. W.; Sessions, R. B.; Asmus, K.-D.; Hiller, K.; Göbl, M. *J. Am. Chem. Soc.* **1980**, *102*, 1429-1430.

(136) Anklam, E.; Asmus, K.-D.; Mohan, H. *J. Phys. Org. Chem.* **1990**, *3*, 17-22.

(137) Hiller, K.; Masloch, B.; Göbl, M.; Asmus, K.-D. *J. Am. Chem. Soc.* **1981**, 2734-2743.

(138) Mohan, H.; Asmus, K.-D. *J. Am. Chem. Soc.* **1987**, *109*, 4745-4746.

(139) Asmus, K.-D.; Anklam, E.; Mohan, H. *J. Chem. Soc., Perkin Trans. 2* **1988**, 1297-1302.

(140) Mohan, H.; Asmus, K.-D. *J. Chem. Soc., Perkin Trans. 2* **1987**, 1795-1800.

(141) Musker, W. K.; Wolford, T. L.; Roush, P. B. *J. Am. Chem. Soc.* **1978**, *100*, 6416-6421.

(142) Nelsen, S. F.; Teasley, M. F.; Kapp, D. L.; Kessel, C. R.; Grezzo, L. A. *J. Am. Chem. Soc.* **1984**, *106*, 791-792.

(143) Alder, R. W. *Acc. Chem. Res.* **1983**, *16*, 321-327.

(144) Radom, L.; Gill, P. M. W. *J. Am. Chem. Soc.* **1988**, *110*, 4931-4941.

(145) Clark, T. *J. Am. Chem. Soc.* **1988**, *110*, 1672-1678.

(146) Baird, N. C. *J. Chem. Educ.* **1977**, *54*, 291-293.

(147) Hordvik, A.; Porten, J. A. *Acta Chem. Scand.* **1973**, *27*, 485-492.

(148) Hauge, S. *Acta Chem. Scand., Ser. A* **1979**, *33*, 317-322.

(149) Cohen, M. H. *Phys. Rev.* **1956**, *101*, 1432-1433.

(150) Symons, M. C. R. *Faraday Discuss* **1978**, *No. 63*, 280-281.

(151) Glass, R. S.; Wilson, G. S.; Klug, J. T.; Duchek, J. R. *J. Am. Chem. Soc.* **1977**, *99*, 7349-7350.

(152) Musker, W. K.; Wilson, G. S.; Swanson, D. D.; Klug, J. T.; Ryan, M. D.; Glass, R. S. *J. Am. Chem. Soc.* **1979**, *101*, 1040-1042.

(153) Musker, W. K.; Doi, J. T. *J. Am. Chem. Soc.* **1981**, *103*, 1159-1163.

(154) Furukawa, N.; Fujihara, H.; Akaishi, R. *Tetrahedron Lett.* **1990**, *31*, 6375-6378.

(155) Shain, I.; Polcyn, D. S. *Anal. Chem.* **1966**, *38*, 370-375.

(156) Nadjo, L.; Saveant, J. M. *J. Electroanal. Chem.* **1973**, *48*, 113-145.

(157) Olmstead, M. L.; Hamilton, R. G.; Nicholson, R. S. *Anal. Chem.* **1969**, *41*, 260-276.

(158) Saveant, J. M. *Acta Chem. Scand., Ser. B* **1983**, *37*, 365-378.

(159) Nicholson, R. S.; Shain, I. *Anal. Chem.* **1965**, *37*, 190-195.

(160) Shain, I.; Nicholson, R. S. *Anal. Chem.* **1965**, *37*, 178-190.

(161) Nicholson, R. S. *Anal. Chem.* **1966**, *38*, 1406.

(162) Bernardo, M. M.; Schroeder, R. R.; Rorabacher, D. B. *Inorg. Chem.* **1991**, *30*, 1241-1247.

(163) Musker, N. K.; Gorewit, B. V. *J. Coord. Chem.* **1976**, *5*, 67-69.

(164) Pavlishchuk, V.; Yatsimirskii, K. B.; Strizhak, P. E. *Inorg. Chim. Acta* **1989**, *164*, 65-68.

(165) McCrindle, R.; Ferguson, G.; McAlees, A. J.; Parvez, M.; Ruhl, B. L.; Stephenson, D. K.; Wieckowski, T. *J. Chem. Soc., Dalton Trans.* **1986**, 2351-2359.

(166) Vosburgh, W. C.; Cooper, G. R. *J. Am. Chem. Soc.* **1941**, *63*, 437.

(167) Wilson, J. M.; Newcombe, R. J.; Denaro, A. R.; Rickett, R. M. W. *Experiments in Physical Chemistry;* Second ed.; Pergamon: Oxford, 1968, pp 59-60.

(168) Van Holde, K. E. *Physical Biochemistry*; Prentice-Hall: Englewood Cliffs, 1985, pp 62.

(169) Chadha, R. K.; Chehayber, J. M.; Drake, J. E. *Inorg. Chem.* **1986**, *25*, 611.

(170) Stalhandske, C.; Zintl, F. *Acta Crystallogr., Sect. C* **1986**, *42*, 1449.

(171) Skakke, P. E.; Rasmussen, S. E. *Acta Chem. Scand.* **1970**, *24*, 2634-2640.

(172) McCrindle, R.; Ferguson, G.; McAlees, A. J.; Parvez, M.; Stephenson, D. K. *J. Chem. Soc., Dalton Trans.* **1982**, 1291-1296.

(173) Paulmier, C. *Selenium Reagents and Intermediates in Organic Synthesis*; Pergamon Books: 1986, pp 17.

(174) Alcock, N. W.; Herron, N.; Moore, P. *J. Chem. Soc., Dalton Trans.* **1978**, 394.

(175) Alcock, N. W.; Herron, N.; Moore, P. *J. Chem. Soc., Chem. Commun.* **1976**, 866.

(176) Dockal, E. R.; Diaddario, L. L.; Glick, M. D.; Rorabacher, D. B. *J. Am. Chem. Soc.* **1977**, *99*, 4530-4532.

(177) Sands, R. H. *Phys. Rev.* **1955**, *99*, 1222-1226.

(178) Neiman, R.; Kivelson, D. *J. Chem. Phys.* **1961**, *35*, 156-161.

(179) Batchelor, R. J.; Einstein, F. W. B.; Cordova-Reyes, I.; Gay, I. D.; Gu, J.; Pinto, B. M.; Zhou, X. M., in preparation.

(180) Rorabacher, D. B.; Diaddario, J., L. L.; Dockal, E. R.; Glick, M. D.; Ochrymowycz, L. A. *Inorg. Chem.* **1985**, *24*, 356-363.

(181) Wilkins, R. G. *The Study of Kinetics and Mechanism of Reaction of Transition Metal Complexes*; Allyn and Bacon: Boston, 1974, pp 5.

(182) Musker, W. K.; Olmstead, M. M.; Kessler, R. M. *Inorg. Chem.* **1984**, *23*, 3266.

(183) McMillin, D. R.; Pulliam, E. J. *Inorg. Chem.* **1984**, *23*, 1171-1175.

(184) Groot, B.; Loeb, S. J. *Inorg. Chem.* **1989**, *28*, 3573.

(185) Rorabacher, D. B.; Ferris, N. S.; Woodruff, W. H.; Jones, T. E.; Ochrymowycz, L. A. *J. Am. Chem. Soc.* **1978**, *100*, 5939-5942.

(186) Bosnich, B.; Amundsen, A. R.; Whelan, J. *J. Am. chem. Soc.* **1977**, *99*, 6730-6739.

(187) Lever, A. B. P. *Inorganic Electronic Spectroscopy;* Second ed.; Elsevier Science: Amsterdam, 1984, pp 206.

(188) Nikles, D. E.; Powers, M. J.; Urbach, B. *Inorg. Chim. Acta* **1977**, *37*, L499.

(189) McAuley, A. *Coord. Chem. Rev.* **1970**, *5*, 245-273.

(190) Rorabacher, D. B.; Dockal, E. R.; Jones, T. E.; Sokol, W. F.; Engerer, R. J.; Ochrymowycz, L. A. *J. Am. Chem. Soc.* **1976**, *98*, 4322-4324.

(191) Taube, H.; Scott, N. S. *Inorg. Chem.* **1981**, *20*, 3135-3138.

(192) Mitchell, K. A. R. *Chem. Rev.* **1969**, *69*, 157-178.

(193) Nikles, D. E.; Anderson, A. B.; Urbach, F. L. In *Copper Coordination Chemistry: Biochemical and Inorganic Perspectives*; K. D. Karlin and J. Zubieta, Ed.; Adenine: New York, 1983; pp 203-222.

(194) Contton, F. A.; Wilkinson, G. *Advanced Inorganic Chemistry;* 4th ed.; John Wiley and Sons: New York, 1980, pp 799.

(195) Kraatz, H.; Jacobsen, H.; Ziegler, T.; Boorman, P. M. *Organometallics* **1993**, *12*, 76-80.

(196) Hathaway, B. J.; Billing, D. E. *Coord. Chem. Rev.* **1970**, *5*, 143-207.

(197) Fabbrizzi, L.; Castellani, C. B.; Licchelli, M.; Perotti, A.; Poggi, A. *J. Chem. Soc., Chem. Commun.* **1984**, 806-808.

(198) Sayre, L. M.; Reddy, K. V.; Jin, S.; Arora, P. K.; Sfeir, D. S.; Maloney, S. C. F.; Urbach, F. L. *J. Am. Chem. Soc.* **1990**, *112*, 2332-2340.

(199) Margerum, D. W.; Chellappa, K. L.; Bssu, F. P.; Burce, G. L. *J. Am. Chem. Soc.* **1975**, *97*, 6894-6896.

(200) Margerum, D. W.; Bossu, F. P.; Chellappa, K. L. *J. Am. Chem. Soc.* **1977**, *99*, 2195-2203.

(201) Margerum, D. W.; Neubecker, T. A.; Kirksey, J. S. T.; Chellappa, K. L. *Inorg. Chem.* **1979**, *18*, 444-448.

(202) Margerum, D. W.; Rybka, J. S.; Kurtz, J. L.; Neubecker, T. A. *Inorg. Chem.* **1980**, *19*, 2791-2796.

(203) Steggerda, J. J.; Bour, J. J.; Birker, P. J. M. W. L. *Inorg. Chem.* **1971**, *10*, 1202-1205.

(204) Collins, T. J.; Anson, F. C.; Richmond, T. G.; Santarsiero, B. D.; Toth, J. E.; Treco, B. G. R. T. *J. Am. Chem. Soc.* **1987**, *109*, 2974-2979.

(205) Ashurst, K. G.; Higginson, W. C. E. *J. Chem. Soc.* **1953**, 3044-3049.

(206) Cannon, R. D. *Electron Transfer Reactions*; Butterworth: London, 1980.

(207) Marcus, R. A.; Sutin, N. *Biochim. Biophys. Acta* **1985**, *811*, 265-322.

(208) Addison, A. W.; Sakaguchi, U. *J. Chem. Soc., Dalton Trans.* **1979**, 600-608.

(209) Hathaway, B. J. *Coord. Chem. Rev.* **1981**, *35*, 137-155.

(210) Hathaway, B.; Holah, J. D. H.; Underhill, A. E. *J. Chem. Soc.* **1962**, 2444.

(211) Bax, A.; Griffey, R. H.; Hawkins, B. L. *J. Magn. Res.* **1983**, *55*, 301-315.

(212) Bax, A.; Subramanian, S. *J. Magn. Res.* **1986**, *67*, 565-569.

(213) Denguchi, T. *J. Chem. Phys.* **1960**, *32*, 1584-8.

(214) Still, W. C.; Kahn, M.; Mitra, M. *J. Org. Chem.* **1978**, *43*, 2923.

(215) Moniotte, P. G.; Hubert, A. J.; Teyssie, P. *J. Organomet. Chem.* **1975**, *88*, 115-120.

(216) Winograd, N. In *Laboratory Techniques in Electroanalytical Chemistry*; P. T. Kissinger, Ed.; Marcel Dekker: New York, 1984; pp 321-335.

(217) Kuwana, T.; Darlington, R. K.; Leedy, D. W. *Anal. Chem.* **1964**, *36*, 2023.

(218) Benken, W. von.; Kuwana, T. *Anal. Chem.* **1970**, *42*, 1114-1116.